Composite organic-inorganic membrane as new electrolyte in all solid-state battery

Agathe Naboulsi

Sorbonne Université

ED 397 – Physique et Chimie des Matériaux

Laboratoire de Chimie de la Matière Condensée de Paris and Laboratoire de Physicochimie des Polymères et des Interfaces

Composite Organic-Inorganic membrane as new Electrolyte in All Solid-State Battery

By Agathe Naboulsi

PhD thesis in Chemistry

Directed by Christel Laberty-Robert and Odile Fichet

In front of the jury:

Dr. Fannie ALLOIN	Research Director, UGA, LEPMI	Referee
Prof. Matthieu BECUWE	Professor, U-Picardie, LRCS	Referee
Dr. Hubert PERROT	Research Director, SU, LISE	Examiner
Prof. Sylvain Franger	Professor, U-Paris Sud, ICMMO	Examiner
Dr. Nicolas SANSON	Associate Professor, SU, SIMM	Invited Member
Prof. Christel LABERTY-ROBERT	Professor, SU, LCMCP	Director
Prof. Odile FICHET	Professor, CY, LPPI	Director
Dr. Giao T.M. NGUYEN	Associate Professor, CY, LPPI	Supervisor

Remerciements

En premier lieu, je tiens à remercier mes directrices de thèse, Christel Laberty-Robert et Odile Fichet, pour la confiance qu'elles m'ont accordée et les nombreuses connaissances qu'elles m'ont apportées. Leur rigueur et leur disponibilité ont été un réel moteur professionnel. Sans oublier Giao Nguyen pour son encadrement tout au long de ces trois années.

Je tiens également à remercier l'ensemble des membres du jury. D'une part, le président du jury Hubert Perrot, les rapporteurs Fannie Alloin et Matthieu Becuwe, et pour finir, les examinateurs Sylvain Franger et Nicolas Sanson pour la lecture sans faille de mon manuscrit, mais aussi pour les discussions passionnantes lors de la soutenance.

Merci à la direction du LCMCP, Christian Bonhomme et François Ribot, pour rendre ce lieu de travail où il fait bon vivre. Merci à Hélène et Diana qui nous rendent la vie beaucoup plus facile. Merci à Corinne pour son amitié et nos discussions (et les commandes évidemment).

Merci aux permanents de la team RMES, Natacha, Arnaud et Damien, pour les discussions et leur gentillesse. Aux permanents du LCMCP pour les débats passionnants de la kfet et leur aide scientifique. À tous les membres de la team RMES, présents ou passés, Thibaut, Jérémy, Jason, Ronan, Milad, Adeline, Morgan, Kethso, Bastien, Jamal, Navid et Rémi, pour l'ambiance au labo et les débats scientifiques. Pour finir, merci à tous les membres du laboratoire LCMCP et LPPI pour les moments partagés.

Je souhaite également remercier Léna, Mariette, Isa, Fanny, Vivi et le dernier que nous avons pris sous notre aile, Guillaume, sans qui ces trois années de thèse auraient été moins belles. Merci pour votre soutien, votre amitié, les parties de beer pong, les arènes, les gâteaux et les voyages.

Aux copains de Solvay à qui je me dois de dire merci, Camille, Julien, Arnaud, Thomas, Sandrine, Stéphanie, Typhaine, Diego, Franck, Lama, Laura et bien d'autres… pour avoir suivi la « petiote » toutes ces années, toujours en me motivant et me poussant autour de doux breuvages houblonnés.

Les copains de Toulouse, Elena, Maëva, Sarah, Lulu, Lilya, Momo, Stoub, Valou, Jal, Clémence, Etienne et j'en passe… Merci pour nos années d'amitié. Le Sud me manque et vous aussi.

À Josie et Marie-France, les tantines, merci d'être toujours présentes et de bons conseils.

Merci à Jacky et Babeth, qui m'ont permis de me retrouver en famille dans l'immensité de cette ville. Et surtout pour les super repas !

À Florent et Marine, mon beau-frère et ma belle-sœur, qui sont entrés dans la famille et l'ont égayée par leur présence, merci.

À ma ribambelle de neveux et nièces, je dis merci, Augustin, Gaspard, Lilas et Manon, pour le bonheur qu'ils m'apportent à chaque moment passé à leurs côtés. Même lorsqu'il a fallu changer leurs couches.

Sophie, ma grande sœur, qui a le don d'avoir les bons mots et les bons conseils, merci de me redonner le sourire à n'importe quel moment, cela m'est précieux.

À mon grand frère, Doudou, Ours à ses heures perdues, qui a été un vrai modèle pour sa force et sa ténacité à toute épreuve. Nous sommes depuis quelque temps loin l'un de l'autre, mais cette distance nous a rapproché et nous permet de profiter des moments de retrouvailles. Merci pour tout et pour être toujours présent pour moi.

À Papouni, ça n'a pas toujours été simple, mais si j'en suis ici aujourd'hui, c'est grâce à toi. Tu as permis que je m'épanouisse personnellement comme professionnellement, à toujours épauler mes décisions. Merci pour ta rigueur à l'école et ton amour pour les sciences. Ça m'a beaucoup agacé à l'époque, mais aujourd'hui, j'en suis immensément reconnaissante.

À Mamounie, que j'aurais aimé qu'elle lise ces quelques lignes, sûrement les plus difficiles à écrire sur cette thèse. Merci pour l'amour que tu as su nous donner à tous. Je suis fière de la femme que je suis aujourd'hui, et ça, sans toi, ça n'aurait pas été possible.

A Mamounie et Papouni,

List of Abbreviation

ASSB: All solid-state batterie

SE: Solid electrolyte

SPE: Solid polymer electrolyte

Si-SPE: Single-ion solid polymer electrolyte

SIE: Solid inorganic electrolyte

SCE: Solid composite electrolyte

PEO: poly(ethylene oxide)

RT: room temperature

LLZO: $Li_7La_2Zr_3O_{12}$

LLZTO: Ta doped LLZO

Al-LLZO: Al doped LLZO

t-LLZO: tetragonal LLZO

EIS: Electrochemical impedance spectroscopy

TLM: Transmission Line Model

CSP: Cold-sintering process

T_f : Melting temperature

T_g : glass transition temperature

LiTFSI: Lithium bis(trifluoromethylsulphonyl)imide

Mn: Molecular weight

XRD: X-ray diffraction

NASICON: Sodium Superionic Conductors

LATP: $Li_{1.2}Al_{0.2}Ti_{1.8}(PO_4)_3$

LAGP: $Li_{1.5}Al_{0.5}Ge_{1.5}(PO_4)_3$

ACN: Acetonitrile

DSC: Differential scanning calorimetry

DMTA: Dynamic mechanical thermal analysis

PC: Propylene carbonate

NMR: Nuclear magnetic resonance

BE: Blocking electrode

PEGM: Poly(ethylene glycol)methylether methacrylate

PEGDM: poly(ethylene glycol) dimethacrylate)

LiMTFSI: lithium 3-[(trifluoromethane)sulfonamidosulfonyl]propyl methacrylate

AIBN: 2,2′-azobis(2-methylpropionitrile)

TGA: Thermogravimetric analysis

OCV: Open circuit voltage

CV: Cyclic voltammetry

CCD: Critical current density

T_{α}: α relaxation temperature

E': Storage modulus

E_a: Activation energy

PVP: Poly(vinyl pyrrolidone)

DMF: Dimethylformamide

EtOH: Ethanol

RH: Relative humidity

FEG-SEM: Field Emission Gun - Scanning Electron Microscope

LBO: Li_3BO_3

GB: Grain boundary

HF: Hight frequency

MF: Medium frequency

LF: Low frequency

DX: Distributed extended element

f_c: characteristic frequency

PPC: polypropylene carbonate

Table of Contents

General introduction

In 2015, the Paris Agreement adopted at COP21, involves limiting global warming well below 2 °C by reducing greenhouse gas emissions. Reports from the UN's Intergovernmental Panel on Climate Change (IPCC) indicate that crossing the 1.5 °C threshold is likely to trigger much more severe climate change impacts, including more frequent and severe droughts, heatwaves and precipitation. In 2019, members of the European Parliament therefore adopted a resolution calling on the European Union to set carbon neutrality by 2050 as a long-term climate target under the Paris Agreement. The resolution calls for the emissions reduction target to be raised to 55% by 2030. To this end, the Members of the European Parliament and Member states have agreed to stop the sale of new CO_2 emitting vehicles by 2035. To achieve this goal, it is necessary to develop the fleet of electric vehicles and therefore to design high-performance (non-CO_2 emitting) energy storage systems[1].

Today, Li-ion batteries have become a key technology in the transition to electric vehicles. With an estimated 3.1 million electric vehicles on Europe's roads by 2025, the demand for efficient, sustainable and environmentally-friendly energy storage solutions has never been greater. Today, Li-ion batteries have an energy density of around 300 $Wh.kg^{-1}$, which was unthinkable just ten years ago[2]. Despite this, electric vehicles are not yet competitive with combustion vehicles, with a range of only 100 to 600 km. To solve this issue, it is essential to increase the energy density of Li-ion batteries. Unfortunately, they have reached their limits. One possible strategy for improving energy density is the use of Li-metal technology (to reach 400 $Wh.kg^{-1}$), which would enable the lowest possible potential to be reached (0 V *vs.* Li^+/Li). The integration of Li-metal in Li-ion batteries is not possible, as the use of Li-metal causes the formation of Li dendrites, resulting in short-circuits in the battery. Another strategy for increasing energy density is to augment the potential by using high-potential cathodes materials (4.5 V *vs.* Li^+/Li). However, the liquid electrolyte oxidizes at this potential, and it is then essential to use another electrolyte that can withstand the high potential of the active materials and block/avoid the growth of Li dendrites. Additionally, the liquid electrolytes present flammability problems that cause safety issues[3].

Research has therefore focused on the manufacture of a solid electrolyte (SE) to design all solid-state batteries (ASSB) that would improve safety by being non-flammable and having a wider window of potential. Today, many SEs are referenced generally two families: Solid

Polymer electrolytes (SPE) and Solid Inorganic electrolytes (SIE). Each family has its advantages and disadvantages. The polymer most commonly used is poly(ethylene oxide) (PEO) for its ability to dissolve Li-salts[4]. The corresponding SPEs are easily transposable to current Li-ion battery manufacturing processes, but their ionic conductivity at room temperature (RT) remains limited[5]. SIE are composed of two subfamilies, sulfide and oxide. Both have ionic conductivities comparable to those of liquid electrolytes (10^{-3} S.cm^{-1} at RT)[6]. But, sulfides present problems of moisture stability and give off an extremely dangerous gas (H_2S)[7]. Oxides, on the other hand, are more chemically stable. For example, $Li_7La_2Zr_3O_{12}$ (LLZO) has a wide electrochemical window and is not dangerous when exposed to humidity[8]. Unfortunately, shaping this electrolyte requires costly manufacturing processes, as it has to be sintered at high temperature (± 1000 °C) to achieve its excellent ionic conductivity[9].

As the various families mentioned above do not fully meet the requirements of SEs, a new family of SE has emerged the solid composite electrolytes (SCE). Indeed, by mixing SPE and SIE, it is possible to combine their respective advantages in a positive way, while masking their shortcomings. This opens up the possibility of many new material compositions. SCE can be essentially polymeric or, on the contrary, essentially inorganic. The expectations for these SCE are a conductivity equal to that of current liquid electrolytes (10^{-3} S.cm^{-1} at RT), an electrochemical stability window of higher than 4.5 V *vs.* Li^+/Li, chemical compatibility with the cathode materials, a transport number of 1 to avoid the build-up of the ion concentration gradient and the dendrites growth[10,11] and a manufacturing process that can be transposed to the current fabrication chains of Li-ion battery[2].

When designing an SCE, the key to achieve good performance is the assembly of the inorganic and organic materials. It is important to control interfaces and the (electro)chemical reactivity between the two materials. Thus, understanding the mechanisms of transport at the interface is crucial to designing the best assemblies and thus obtaining the lowest possible resistance to the passage of Li^+ from one material to the other. To address this issue, this PhD will be focused on processing methodology to design SCE and on the understanding of mechanism of Li^+ transport in the SCE by impedance spectroscopy. Depending on processing methodologies, we have designed a predominantly polymeric SCE, or a predominantly inorganic SCE. This work has been funded by the RS_2E (Réseau sur le stockage électrochimique de l'énergie) and RESPORE (Réseau d'excellence en solides poreux) networks, and is being carried out in collaboration between the LCMCP (Laboratoire de Chimie

de la Matière Condensée de Paris) at Sorbonne University and the LPPI (Laboratoire de Physicochimie des Polymères et des Interfaces) at Cergy University.

Chapter I reviews the **state of the art in SCE design**. After a brief introduction on the reasons for the transition from Li-ion batteries to ASSBs, the functioning of the latter has been discussed, as well as the technological challenges involved in the various interfaces present in these batteries. The different families of SEs were examined in detail. This study enabled us to identify PEO for the polymer matrix and the inorganic material, LLZO as good candidates for the development of SCEs. The focus was on SCEs, their assemblies, the mechanisms involved in Li^+ conduction and the study of the PEO||LLZO interface.

To design the SCE with the best performance, the focus was on the manufacture of an original SPE. Chapter II (article submitted at ACS Applied Materials & Interfaces and under revision) describes the solvent-free synthesis and the characterization of SPEs based on **an amorphous PEO network**. Mechanical and thermal properties have been analyzed using dynamic mechanical thermal analysis and differential scanning calorimetry, respectively. Ionic conductivity measurements were carried out using electrochemical impedance spectroscopy (EIS). Finally, the parameters affecting mechanical properties and ionic conductivity were discussed.

The design of a **predominantly polymeric CSE** will be discussed in Chapter III. The SCE based on PEO network and LLZO were elaborated using either a **two-stage manufacturing process** involving electrospinning and impregnation or a **single-stage process**. In the one-step process, LLZO particles were pre-dispersed in the polymer precursors which are then polymerized to give the final CSE. In the two-step process, 3D LLZO scaffold was first synthesized using the electrospinning method, followed by a high-temperature heat-treatment. Different parameters related to electrospinning and post-treatment (temperature and pressure) were studied to produce a continuous and porous LLZO scaffold. This latter was then impregnated by capillary force with the polymer precursor solution. The polymerization was then carried out. The impact of SCE morphology on ionic conductivity was studied using impedance spectroscopy.

Chapter IV, which takes the form of an article, then explores the transport of the Li ion at the **polymer||inorganic interface**. To do this, we specifically designed a multilayer design using *in-situ* or *ex-situ* PEO network synthesis on dense LLZO ceramics. The interfacial response was identified by EIS. Data, were analyzed with an innovative model for multilayers using an element of the Transmission Line Model.

Chapter V is devoted to the fabrication of a **predominantly inorganic SCE** using the cold sintering process (CSP). This process, described as a **'one-pot' approach**, allowed the PEO network in-situ synthesis during powder compaction. EIS was used to estimate the ionic conductivity of this SCE.

Reference

(1) EU Deal to End Sale of New CO2 Emitting Car by 2035, 2022.

(2) Janek, J.; Zeier, W. G. A Solid Future for Battery Development. *Nat. Energy* **2016**, *1* (9), 16141. https://doi.org/10.1038/nenergy.2016.141.

(3) Tarascon, J.-M.; Armand, M. Issues and Challenges Facing Rechargeable Lithium Batteries. *Nature* **2001**, *414* (6861), 359–367. https://doi.org/10.1038/35104644.

(4) Armand, M. The History of Polymer Electrolytes. *Solid State Ion.* **1994**, *69* (3–4), 309–319. https://doi.org/10.1016/0167-2738(94)90419-7.

(5) Zhu, P.; Yan, C.; Dirican, M.; Zhu, J.; Zang, J.; Selvan, R. K.; Chung, C.-C.; Jia, H.; Li, Y.; Kiyak, Y.; Wu, N.; Zhang, X. Li $_{0.33}$ La $_{0.557}$ TiO $_{3}$ Ceramic Nanofiber-Enhanced Polyethylene Oxide-Based Composite Polymer Electrolytes for All-Solid-State Lithium Batteries. *J. Mater. Chem. A* **2018**, *6* (10), 4279–4285. https://doi.org/10.1039/C7TA10517G.

(6) Bachman, J. C.; Muy, S.; Grimaud, A.; Chang, H.-H.; Pour, N.; Lux, S. F.; Paschos, O.; Maglia, F.; Lupart, S.; Lamp, P.; Giordano, L.; Shao-Horn, Y. Inorganic Solid-State Electrolytes for Lithium Batteries: Mechanisms and Properties Governing Ion Conduction. *Chem. Rev.* **2016**, *116* (1), 140–162. https://doi.org/10.1021/acs.chemrev.5b00563.

(7) Cai, Y.; Li, C.; Zhao, Z.; Mu, D.; Wu, B. Air Stability and Interfacial Compatibility of Sulfide Solid Electrolytes for Solid-State Lithium Batteries: Advances and Perspectives. *ChemElectroChem* **2022**, *9* (5), e202101479. https://doi.org/10.1002/celc.202101479.

(8) Manthiram, A.; Yu, X.; Wang, S. Lithium Battery Chemistries Enabled by Solid-State Electrolytes. *Nat. Rev. Mater.* **2017**, *2* (4), 16103. https://doi.org/10.1038/natrevmats.2016.103.

(9) Shimonishi, Y.; Toda, A.; Zhang, T.; Hirano, A.; Imanishi, N.; Yamamoto, O.; Takeda, Y. Synthesis of Garnet-Type Li7−xLa3Zr2O12−1/2x and Its Stability in Aqueous Solutions. *Solid State Ion.* **2011**, *183* (1), 48–53. https://doi.org/10.1016/j.ssi.2010.12.010.

(10) Diederichsen, K. M.; McShane, E. J.; McCloskey, B. D. Promising Routes to a High Li $^{+}$ Transference Number Electrolyte for Lithium Ion Batteries. *ACS Energy Lett.* **2017**, *2* (11), 2563–2575. https://doi.org/10.1021/acsenergylett.7b00792.

(11) Ford, H. O.; Park, B.; Jiang, J.; Seidler, M. E.; Schaefer, J. L. Enhanced Li $^{+}$ Conduction within Single-Ion Conducting Polymer Gel Electrolytes via Reduced Cation–Polymer Interaction. *ACS Mater. Lett.* **2020**, *2* (3), 272–279. https://doi.org/10.1021/acsmaterialslett.9b00510.

Chapter I.

State of the Art

I. Introduction: Transition to All Solid-State Batteries

The first Li-ion battery was commercialized by Sony in 1991. These batteries consist of a positive electrode, a polymer separator and a negative electrode, as well as a liquid electrolyte that transports Li^+ ions. The electrolyte consists of a mixture of organic carbonates in which a Li-salt ($LiPF_6$) is dissolved[1]. The materials found in the positive electrode are lamellar oxide $LiCoO_2$[2] or spinel $LiMn_2O_4$[3] or a polyanionic $LiFePO_4$[4]. The negative electrode is made of graphite[5]. The main problem with Li-ion batteries is the use of liquid electrolyte, which is not only flammable but can also degrade if exposed to moisture and form an extremely toxic gas. It therefore needs to be replaced.

The transition from Li-ion batteries to All Solid-State Batteries (ASSB) represents a significant advancement in the field of energy storage technologies. ASSB use a solid electrolyte (SE), thereby eliminating potential issues related to leakage and flammability. This transition is driven by the search for greater safety, higher energy density (400 $Wh.kg^{-1}$ *vs.* 300 $Wh.kg^{-1}$ for Li-ion), and longer battery life[6]. To increase energy density, one solution is to use Li-metal as a negative electrode but also the assembly of the more compact cells. It is also possible to use high-potential cathode materials that cannot be used in Li-ion batteries due to the electrochemical stability windows of liquid electrolytes. The cathode materials most commonly used in ASSBs are LTO ($Li_4Ti_5O_{12}$), LCO ($LiCoO_2$), NMC ($LiNi_xMn_yCo_zO_2$) and LMO ($LiMn_2O_2^-$)[7].

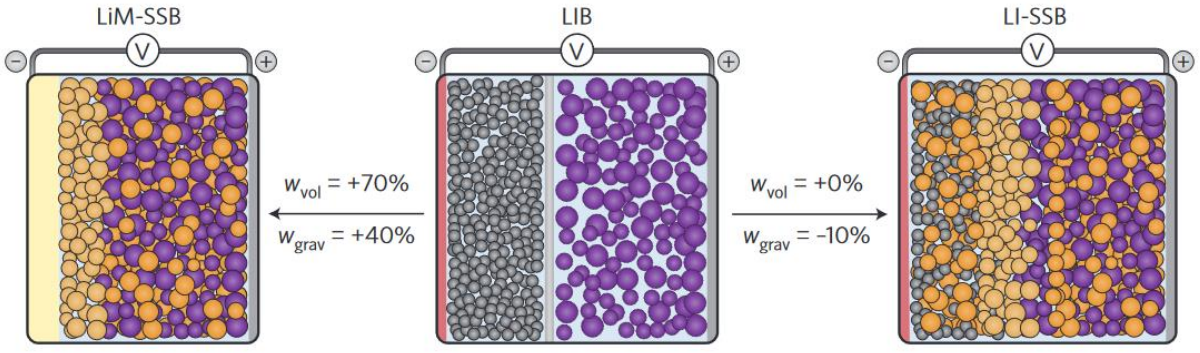

Figure I-1. The architecture of Li-ion batteries (middle), Li-metal solid-state batteries (left), and Li-ion solid-state batteries (right). Purple circles represent cathode materials, grey circles graphite and orange circles SEs[6].

Figure I-1 represents the architecture of Li-ion batteries (middle), it is composed of two porous electrodes filled with liquid electrolyte (discussed above) coated on thin aluminum (positive electrode) and copper (negative electrode) foils, which collects the current. The grey band between the two electrodes represents the separator, which is soaked in the liquid electrolyte. On the right of Figure I-1 is shown the architecture of the Li-ion solid-state battery. The difference with the Li-ion battery is that the liquid electrolyte is replaced by a SE in both electrodes. This SE also takes the place of the separator. Replacing the electrolyte liquid with SE does not change the volumetric energy density. In addition, SEs have a higher density than liquid electrolytes, resulting in a lower gravimetric density. SEs are more chemically resistant to high voltages, which would increase the chemical stability window from 4.2 to 5 V. As far as safety is concerned, it's a mixed subject, because while some SEs are not reactive to air or humidity, others are. The latest architecture shown in the Figure I-1 (left) is the Li-metal solid-state batteries. Compared with the Li-ion solid-state batteries, the negative electrode (composed of graphite) is replaced by a layer of Li-metal. It is this change that will enable a significant increase in energy density, as Li-metal has a very high theoretical energy density (3,700 $mA.g^{-1}$). Its use involves other problems, such as the thermodynamic instability of many SEs with respect to Li-metal. In this work, we will focus on Li-metal solid-state batteries.

Understanding the fundamental workings of ASSBs and the different types of SE is essential to unlocking the potential of next-generation energy storage systems. In the following sections, we will detail the operating mechanisms of ASSBs and the different families of ES presented in the literature, their advantages and limitations.

II. All solid-state batteries

During the operation of the ASSB, for example, during discharge, Li^+ diffuses through the Li-metal||SE interface, along the electrolyte and then to the SE||cathode interface. To ensure electro-neutrality, the simultaneous transport of electrons takes place in an external circuit. During charging, these processes are reversed. The energy source in ASSBs is the oxidation-reduction reactions that take place at the SE||electrode interface. These interfaces are therefore crucial to the performance of ASSBs.

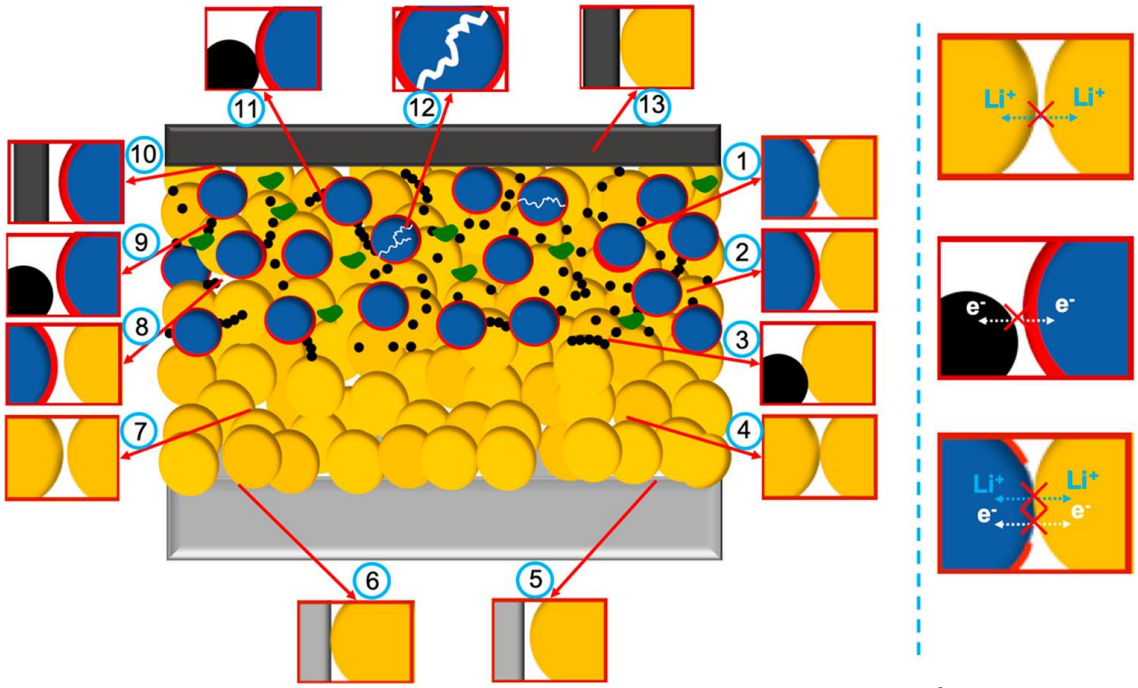

Figure I-2. Illustration of the various interfacial phenomena in ASSBs[8]. The yellow sphere represents the electrolyte, blue is the cathode material and black is the carbon. The grey band represents the Li-metal.

By replacing the liquid electrolyte with SE, the guarantee of good contact between the electrolyte and the electrodes is compromised. Solid||solid contact is trickier to achieve due to the presence of asperities, roughness and irregularities on their surfaces. Figure I-2 is a fairly general representation of the interfacial phenomena that can be encountered during the manufacture of an ASSB. The interface phenomenon that can be encountered in all battery components is the presence of voids, despite the pressure that can be applied when manufacturing the cell, (numbers 5, 7, 8, 9, 10, and 12 in Figure I-2) between the particles, despite the high pressure that can be applied when manufacturing the cell. They can also be created during its operation because some cathode is known to exhibit changes in volume, which can lead to pores, cracks, and loss of contact at the cathode||electrolyte interface but also on the Li-metal side with dendrite growth. This leads to an increase of interfacial resistance[6]. It is possible to observe chemical reactions (numbers 1 and 6 in Figure I-2) at the electrode||electrolyte interface if the materials have different chemical potentials. This will induce the appearance of interphase, which can be beneficial if it conducts Li^+ but not electrons. On the other hand, it can be disadvantageous if it allows both species to pass through. The interface can also be hindered by electrochemical reactions as most SEs have a well-defined electrochemical stability window with respect to the anode and cathode. This can also induce

the appearance of an interphase which will increase the charge transfer resistance (numbers 2, 3, 6, and 13 in Figure I-2). Finally, grain boundaries can also reduce ionic conduction at the interface if two particles are in contact and have different electrochemical potentials (numbers 4 et 11 in Figure I-2). The choice of SE will have a major impact on interfaces. My work focused on the design of an SE. There are several families of SE, which will be discussed in the next section. Depending on their chemical composition, they will have specific properties that can help solve interface problems with electrodes.

III. Solid Electrolyte

Since the manufacture of polyethylene oxide (PEO) materials as SE in the 1980s and the Lithium phosphorus oxynitride (LiPON) in the 1990s, a lot of studies have been devoted to the development of solid electrolytes[9,10]. The target for the ionic conductivity is the one achieved for the current liquid electrolyte in Li-ion batteries (10^{-3} S.cm^{-1} at 25 °C). The SE should also exhibit a sufficiently wide electrochemical stability window (> 4.5 V *vs.* Li^+/Li) to use Li-metal and high-potential positive electrodes. Importantly, they should have sufficiently high mechanical strength to prevent the growth of dendrites (Young modulus > 7 GPa[11]), the lowest value of electrode||electrolyte interface resistance, high thermal stability (> 100 °C), and a manufacturing process that can be transposed to current battery manufacturing methods and at lower cost[12].

In the literature, it can be found different families of solid electrolytes including oxide, sulfur, and polymer (Figure I-3).

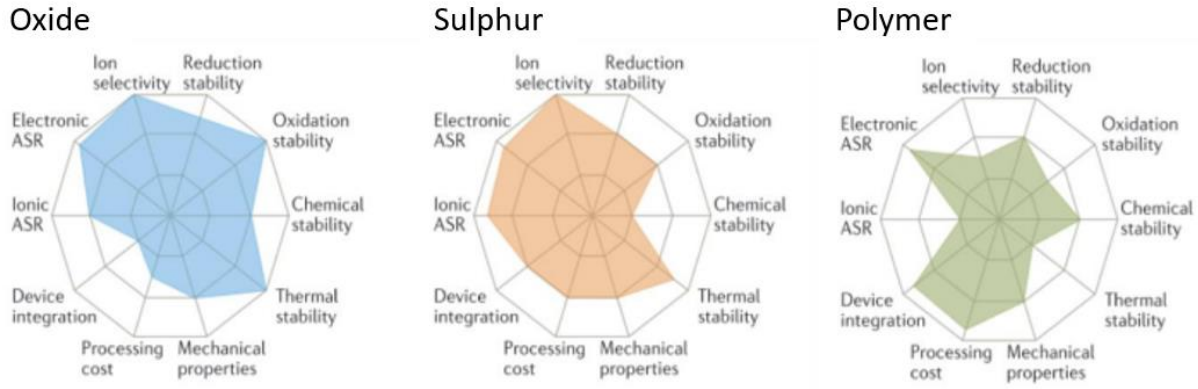

Figure I-3. Performance of different classes of solid electrolyte[13].

Solid inorganic electrolytes (SIE) composed mainly of oxides and sulfides exhibit high ionic conduction at room temperature (RT) (~ 10^{-3} S.cm^{-1})[6]. Oxides are stable over a wide range of temperatures and stable with respect to Li-metal. However, they do have some disadvantages,

as their manufacture requires high temperatures. They are not mechanically soft[14], which is difficult to integrate into current battery manufacturing processes[15]. Finally, despite their rigidity, dendrites can penetrate the joints and cause short circuits[6].

Sulfides have the advantage of being easier to process, but they have very poor chemical stability, being unstable in air and decomposing into a highly toxic gas[16]. Solid polymer electrolytes (SPE) are easy to integrate into existing manufacturing processes. Unfortunately, they have poor conductivity at RT, low chemical, electrochemical, and thermal stabilities. Finally, no SE compound known to date meets all the above expectations.

III.1. Solid Polymer Electrolyte

III.1.1. Linear polymer

Solid polymer electrolytes have played a key role in the development of ASSB. In 1975, Wright et al.[17] demonstrated that PEO was sufficiently solvating to solubilize alkaline salts without the use of solvents. Then in 1978, Armand suggested the possibility of making a SPE from PEO where Li-salts are dissolved[18]. Indeed, PEO is able to solvate Li^+ ions thanks to its ether function[19]. As shown in Figure I-4 the interaction of Li^+ with 4 to 5 oxygens allows dissociation of the salts in the PEO and Li^+ can diffuse within the material by hopping from one chain to another in the polymer[20]. However, this mechanism is only possible if the polymer is in an amorphous state, so it must be used above its melting temperature (T_f) which is around 60 °C[21]. Below 60 °C, PEO is semi-crystalline, and the crystalline domains block ion transfer, thus lowering its ionic conductivity (between 10^{-9}-10^{-6} $S.cm^{-1}$ at RT)[22].

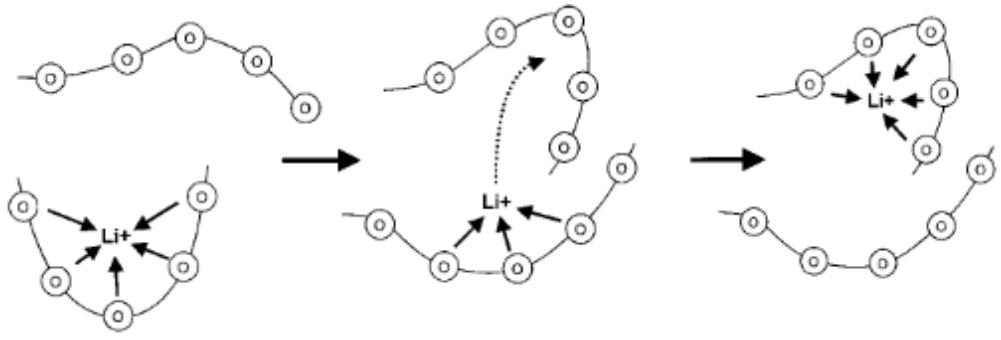

Figure I-4. Schematic of the segmental motion-assisted diffusion of Li^+ in the PEO matrix. The circles represent the ether oxygens of PEO[23].

Bolloré Group has even used a PEO with the Lithium bis(trifluoromethylsulphonyl)imide (LiTFSI) salt in the batteries that equip the BlueCar. However, batteries utilizing PEO-based electrolyte technology operate at high temperatures

because, as explained above, at low temperatures, PEO exhibits crystalline domains that significantly reduce ionic conductivity. In addition, conduction in PEO-based electrolytes depends on numerous parameters affecting the dynamics of the polymer chains[24]. For example, PEOs with high chain mobility have good ionic conductivity but poor mechanical properties. Chain mobility decreases as the molecular weight of PEO increases. There is a critical molecular weight beyond which polymer chains can entangle, known as the critical entanglement mass. When the chains become entangled, the mechanical strength improves, but the chain mobility decreases, resulting in a reduction in ionic conductivity[25]. Studies were carried out to understand the impact of end chain groups and the molar mass of PEO on mechanical properties and ionic conductivity (Figure I-5). Devaux et al.[26] have shown that the conductivity and viscosity of PEO-LiTFSI are dependent on the molecular weight (Mn) as well as the end chain groups. The main impact of end-chain groups is to modify the available free volume, which in turn governs segment dynamics. In addition, they show that at low Mn there is a real impact of end groups on ionic conductivity by modifying the free volume. In contrast, at high Mn, the limiting step is the jump of the Li^+ from one coordination site to another. The segment dynamic decreases with increasing Mn, which leads to a decrease in viscosity and therefore a decrease in mechanical properties. There's a compromise between mechanical strength and ionic conductivity. The higher the molar mass of the PEO the better the mechanical strength, but the lower the ionic conductivity[26].

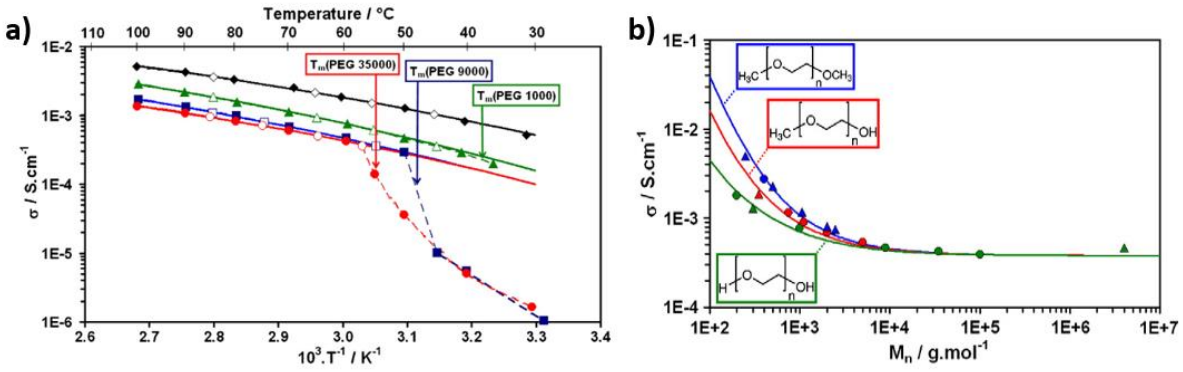

Figure I-5. (a) Ionic conductivities of PEO-LiTFSI (EO/Li = 25) complexes as a function of the inverse of temperature. PEO molecular weights: 200 (diamond). (b) Variations of the ionic conductivity at 60 °C of PEO (green), Poly(ethylene glycol) methyl ether (red), and Poly(ethylene glycol) dimethyl ether (blue) doped with LiTFSI (EO/Li = 25) versus molecular weight.[26]

Another direction of research being investigated to improve the performance of PEO-LiTFSI SPEs is the optimization of the EO/Li ratio. Maurel et al.[27] have studied the impact of

the EO/Li ratio on ionic conductivity as a function of temperature (Figure I-6). They demonstrated that the electrolyte with the best ionic conductivity ($3.8.10^{-6}$ S.cm^{-1} at 20 °C) is for an EO/Li ratio equal to 10. But, the conductivity at RT is still low and the use of PEO-LiTFSI is considered at 90 °C. At this temperature, the best ionic conductivity ($3.9.10^{-4}$ S.cm^{-1}) is achieved for an EO/Li ratio equal to 20. The ionic conductivity as a function of the EO/Li ratio at 90 °C takes the form of a parabola. For a salt concentration higher than EO/Li equal to 20, the conductivity decreases due to reduced ionic mobility caused by the elevated T_g with increasing salt concentration, leading to higher viscosity. Additionally, this reduction is attributed to the formation of ion-ion pairs or triplets. The formation of ion-ion pairs or triplets with LiTFSI refers to the trend of ions present in the electrolyte to associate with each other, thereby forming aggregates of two or three ions[28].

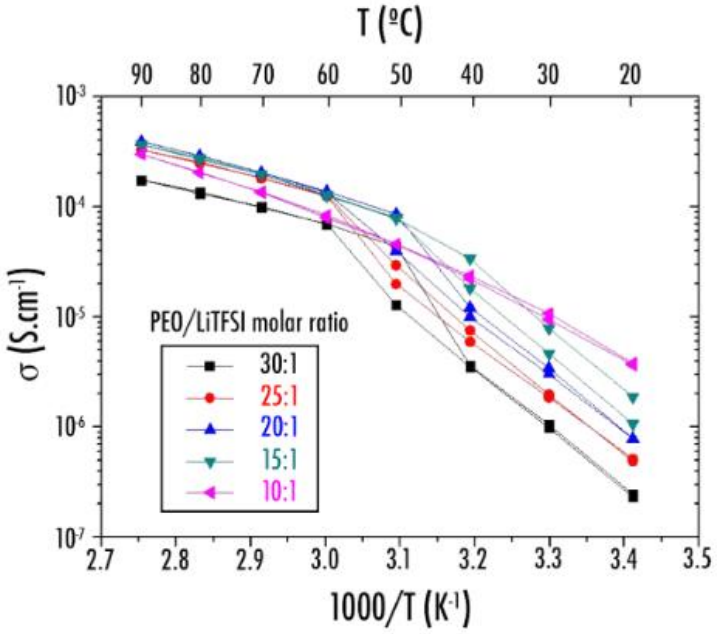

Figure I-6. Arrhenius plots of the ionic conductivity for different EO/Li of PEO-LiTFSI polymer electrolyte.[27]

Other linear polymers have been studied for their use as SPEs such as polyacrylonitrile (PAN)[29], poly(methyl methacrylate) (PMMA)[30,31], poly(vinylidene fluoride) (PVDF), and poly(vinylidene fluoride-co-hexafluoropropylene) (PVDF-HFP)[32]. PAN with its nitrile group (C≡N) has a typical strong electron withdrawing group with high electrochemical stability (4.5 V *vs.* Li$^+$/Li [33]. PMMA provides a stable interface for Li-metal and, thanks to the carbonyl group (C=O), coordination with Li-salts enables rapid transport of Li$^+$[34]. PVDF and PVDF-HFP have functional groups (CF_3) with strong electron-withdrawing which is beneficial for dissolving Li-

salts[35]. Unfortunately, these polymers also present problems of crystallinity or high T_g temperature.

The choice of salt to be used in the PEO matrix was also an important area of research. The focus on designing new Li-salts is to improve the dissociation of the ion pair by delocalizing the negative charge. The greater the dissociation, the better the conductivity performance. The most common being LiTFSI[9], lithium-bis(fluorosulfonyl)imide (LiFSI)[36], and lithium-bis(oxalate)borate (LiBOB) [37]. LiFSI enhances the delocalization of the negative charge as fluorine is directly bonded to SO_2, but it comes with a very high manufacturing cost. LiBOB exhibits adequate delocalization of the negative charge, but it has lower electrochemical stability compared to LiTFSI (4.2 *vs.* 5.0 V respectively).

In conclusion, PEO-LiTFSI has many qualities as a solid electrolyte, but unfortunately, it operates at high temperatures (2.10^{-3} S.cm^{-1} at 100 °C)[38], at which point it loses its mechanical strength. In addition, it is necessary to increase its transport number (t^+). This value represents the mobility of ions within the SE. If the value of t^+ is close to 1, it means that only Li^+ are mobile in the SE. The value of t^+ in a PEO-LiTFSI material can vary from 0.2 to 0.6 depending on its salt concentration. Unfortunately, for t^+ values of 0.6 in these systems, the ionic conductivity is limited (10^{-6} S.cm^{-1} at 100 °C)[39]. In the following, different strategies will be discussed for improving the performance of PEO-based SPEs.

III.1.2. Block copolymer

Block copolymers like SPE have made their emergence to improve mechanical strength. PEO is coupled to one or two other blocks. Polymers studied in diblocks with PEO include alkyl polymethacrylate[40], polyacrylonitrile[41], and poly(4-vinyl pyridine)[42] but the one that has attracted the most interest is polystyrene (PS).

Balsara's group has had a major impact on the study of poly(PEO-*b*-PS). This group studied the impact of molar mass, tortuosity, and domain size (small regions of characteristic size) on ionic conductivity[43–45]. PS is a promising candidate because it has a high T_g and is immiscible with PEO. In contrast to PEO alone, they demonstrated that ionic conductivity improved as the molar mass of PEO in the diblock increased (10^{-5} to 10^{-4} S.cm^{-1} at 100 °C for Mn of PEO ranging from 7 to 98 kg.mol^{-1} respectively)[44]. It has been shown that conductivity decreases as domain size increases (1.10^{-4} to 8.10^{-5} S.cm^{-1} for domain size increases from 20 to 80 nm respectively)[45].

Research has gone one step further by using polymer triblock, bringing even more nanostructuring. The addition of nanostructured domains strengthens the polymer mechanically, thus limiting dendrite growth[46]. Unfortunately, the evolution of these two properties has been shown to be at odds with each other[25,47]. Finally, this diblock and triblock with PEO and PS manufacturing strategy does not significantly increase ionic conductivity and Li transport number (diblock 2.10^{-5} S.cm^{-1} at 60 °C[48] and triblock 2.10^{-4} S.cm^{-1} at 60 °C and t^+ = 0.15 with LiTFSI[47]).

III.1.3. Cross-linking polymer

One of the strategies employed to improve the mechanical properties at high temperatures is the development of cross-linked polymers. Cross-linking produces a 3D network that is mechanically harder than linear PEO. Furthermore, as the cross-linked polymer can be imagined as a "cage", it is possible that it reduces the diffusion of the anion, which has a larger size than Li^+ and therefore improves the number of transports[49]. With the aim of improving both mechanical strength and conductivity, cross-linking strategies have been developed.

Two strategies can then be adopted, the first is the use of a polymer network where the linear PEO chains are dispersed throughout the network, this is a semi-interpenetrating network (semi-IPN). Zeng et al.[50] have developed a semi-IPN with promising conductivity ($2.2.10^{-4}$ S.cm^{-1} at 25 °C), high Young's modulus (12 GPa), and Li transport number (t^+ = 0.65) thanks to the cross-linking of branched acrylate and the dispersion of PEO chains within. The use of the branched acrylate prevents crystallization of the PEO and thus improves t^+ and ionic conductivity at RT. Mechanical properties are improved (12 GPa *vs.* 0,1 to 2 GPa for PEO) by the fact that poly(ether-acrylate) is rigid.

The second strategy is to integrate the PEO chain into the network by cross-linking them. Zhang et al.[51] produced a low-PEO network with tetraglyme (TEGDME), tetraethylene glycol dimethacrylate (TEGDMA), and with addition of LiTFSI (Figure I-7). To achieve this network, a dual *in-situ* reaction is conducted. Ultra-violet (UV) exposure induces the auto-polymerization of the methacrylate of TEGDMA. Simultaneously, the photo-initiator is activated to attract protons from the methylene groups of PEO and TEGDME (or TEGDMA). This generates free radicals that can link different compounds to another. As a result, it triggers the rearrangement of PEO chains, the cross-linking of PEO and TEGDME.

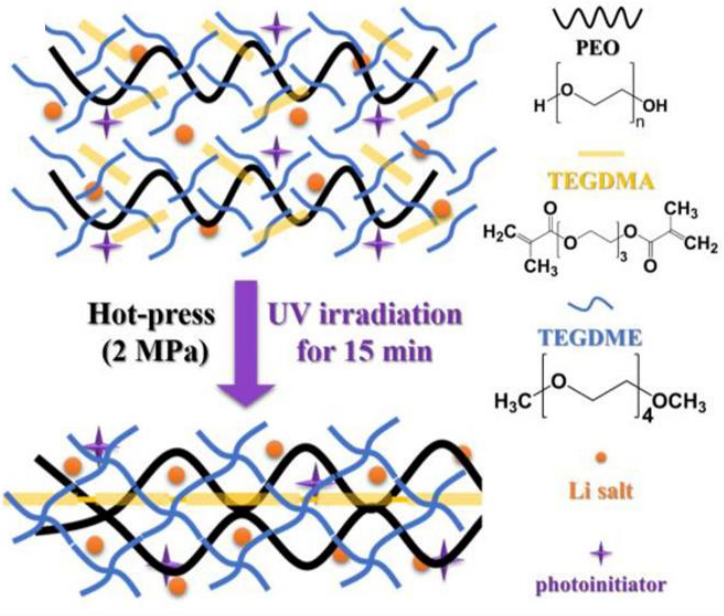

Figure I-7. Diagrams of the IPN structure[51].

This made it possible to reduce the crystallinity of PEO with TEGDME, while retaining the strength mechanics with TEGDMA. The formation of this network results in a highly disordered structure, with a decrease in PEO crystallinity due to the cross-linking reaction, shown by X-ray diffraction (XRD). At the same time, the formation of an oligomer by the self-polymerization of TEGDMA could preserve the (unquantified) mechanical strength of the solid polymer electrolyte (SPE) without compromising ionic conductivity. The result is a conductivity of $2.7.10^{-4}$ S.cm^{-1} at 24 °C and a t^+ of 0.56, thanks to the decrease in T_g (-78 °C). In addition, the stability window is increased to 5 V *vs*. Li^+/Li.

These networks have improved the RT conductive and mechanical properties of PEO-based SPEs. The number of transports has been increased, but has not yet reached 1. To achieve this, another strategy has emerged.

III.1.4. Single ion polymer

This new mono-ionic electrolyte, called single-ion SPE (si-SPE), has been the subject of much research for use in ASSBs. Si-SPEs have the anion grafted to the polymer chains and therefore a t^+ close to 1, thus avoiding concentration gradient build-up and limiting dendrite growth[52,53].

Bouchet et al.[54] have developed a triblock copolymer combining poly(styrene trifluoromethane-lithium sulfonylimide) (P(STFILi)) with a central block of PEO chains (Figure I-8).

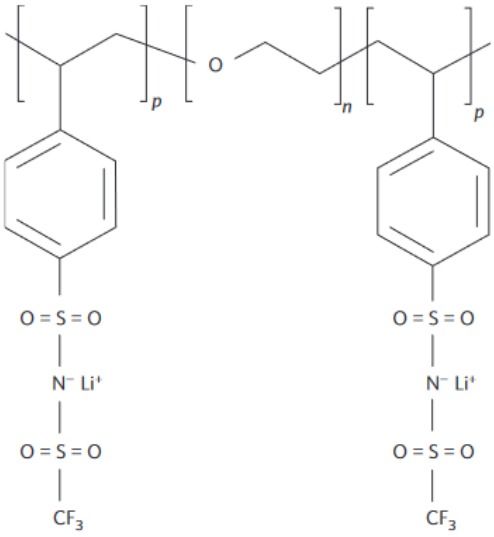

Figure I-8. Chemical structure of the single-ion conductor triblock copolymer[54].

The t^+ of up to 0.85 is very promising because it is higher than the systems studied previously. Unfortunately, the copolymer shows a low ionic conductivity of $1.5.10^{-5}$ $S.cm^{-1}$ at 60 °C. Unfortunately, attaching the anion greatly reduces ionic dissociation, which in turn decreases conductivity. Similarly, Porcarelli et al.[55] have developed a cross-linked polymer based on a PEO-based with a t^+ of around 0.9 at 70°C. If unity is not reached for t^+, this can be explained by the short-range motion of the anion's carrier chain, as well as the motion of the negative charges, which may be due to the segmental motion of the polymer backbone, as the measurements were taken above T_g (-69 °C). However, they obtained a better ionic conductivity than the previous study (~10^{-4} $S.cm^{-1}$ at 25 °C) with the addition of propylene carbonate, which acts as a plasticizer. Numerous other studies have been carried out on si-SPEs, but will be discussed in greater depth in Chapter II. The grafting of the anion therefore implies a drop in ionic conductivity, and to compensate for this it is necessary to add solvents or plasticizers. The ability to modulate ionic conductivity, while maintaining a transport number close to unity, and the possibility of integrating the single ion strategy into the different groups of polymers mentioned above (diblock, triblock, cross-linked) make it very attractive in SPE manufacture.

III.2. Solid Inorganic Electrolyte

It exists several families of SIEs including LISICON, Argyrodite, Garnet, NASICON, Li-Nitride, Li-hydride, Perovskite, and Li-Halide.[56] Figure I-9 shows the ionic conductivities of several electrolytes. It can be seen that the highest conductivities are achieved for the sulfide (Argyrodite) one. In addition to their high ionic conductivity, sulfide electrolytes can easily

accommodate volume changes in electrode materials due to their Young modulus (10-30 GPa) and their elastic behavior[57]. In 2011 Kamaya et al.[58] proposed the $Li_{10}GeP_2S_{12}$ (LGPS) component that exhibits a conductivity of $1.2.10^{-2}$ $S.cm^{-1}$ at RT and a Young modulus of 20 GPa. This component has the best ionic conductivity reported so far. However, LGPS is not stable in the air and has a narrow electrochemical stability window (1.7 to 2.1 V *vs.* Li^+/Li)[59].

Argyrodites containing halide (Li_6PS_5X with X=Cl, Br or I) are very good conductors (7.10^{-3} $S.cm^{-1}$)[60], with a Young modulus of around 20 GPa, and compared with LGPS, they exhibit a wider stability window (0 - 7 V *vs.* Li^+/Li)[61]. Unfortunately, their chemical instability in the air makes them difficult to handle and manufacture. Their synthesis and processing require work in an inert environment[62]. Accordingly, works have been devoted to oxide-based families that are more stable in air.

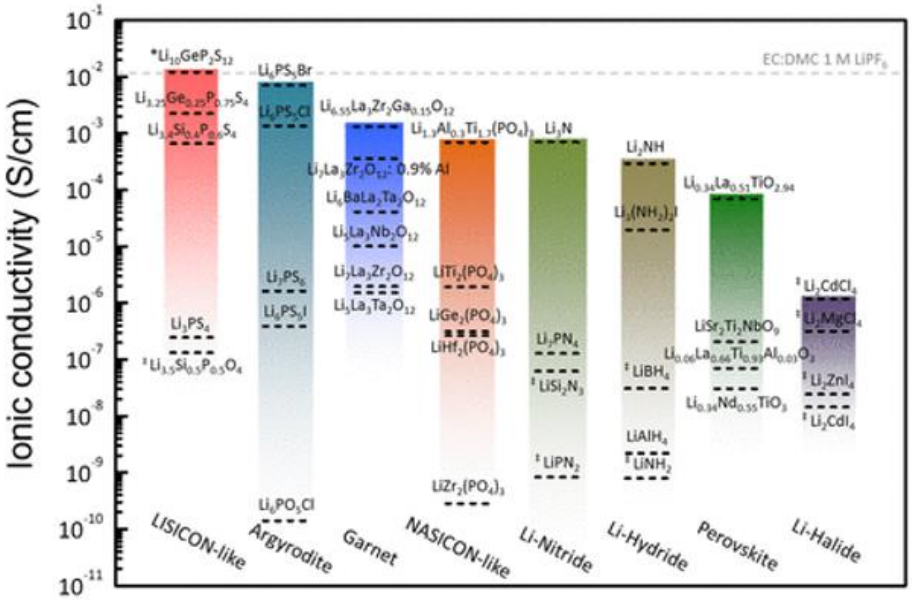

Figure I-9. Reported total ionic conductivity of SIE at RT[56].

What distinguishes the oxide family from the sulfide family is its well-ordered crystalline structure compared to the amorphous or partially ordered structure of sulfides, which results in a higher Young's modulus (100 – 200 MPa). Additionally, oxides have a non-hazardous nature when exposed to air. The family of oxides can be divided into several families, most of which will be discussed briefly below.

Sodium Superionic Conductors (NASICON): a superconductor of sodium ions with structure $NaM_2(PO_4)_3$ (M = Ge, Ti, Zr), was introduced by Goodenough et al.[63] in 1976. Later on, the substitution of Na by Li was explored aiming to develop advanced Li-ion conductors. The most known are $Li_{1.2}Al_{0.2}Ti_{1.8}(PO_4)_3$ (LATP) and $Li_{1.5}Al_{0.5}Ge_{1.5}(PO_4)_3$ (LAGP). The

migration of Li^+ in these compounds occurs via a jump between the two coordination sites that Li can occupy in the structure. The partial occupation of Li^+ at these two sites is crucial for rapid Li^+ conduction, especially as vacancies are required at the intersection of the conduction pathways to give access to three-dimensional diffusion in the structure[56]. LATP has a conductivity of up to 10^{-3} S.cm^{-1} at RT and a Young modulus of 115 GPa but can undergo a reduction reaction in the presence of Li-metal. LAGP has a lower conductivity of 10^{-4} S.cm^{-1} at RT and 125 GPa but greater electrochemical stability (6 V *vs.* Li^+/Li)[64,65].

Another family of oxides is the perovskites, with the formula ABO_3 (A = Nd or La and B = Al or Ti). Li^+ can diffuse by jumping in the plane to an adjacent vacancy through a square-planar bottleneck made of oxygen forming the corners of the octahedra. The best known in this family is $La_{0.67-x}Li_{3x}TiO_3$ (LLTO), with an ionic conductivity of up to $1.53.10^{-3}$ S.cm^{-1} at RT[66] and high Young modulus (200 GPa), but it faces the same problem of reduction of Ti^{4+} to Ti^{3+} as LATP[67].

The garnet oxides are derived from the ideal formula $A_3B_2(XO_4)_3$ with A = Ca, Mg, Y; B = Al, Fe, Ga, Ge, Mn, Ni, V and C = Al, As, Fe, Ge, Si. Where A, B, and C are eight, six, and four oxygen-coordinated cation sites, which crystallize in a face-centered cubic structure. Another unique and crucial aspect is ionic conduction. Commonly studied garnets typically contain five to seven Li atoms per formula unit, they have more Li than that can be accommodated at the tetrahedral sites, leaving excess Li which occupy the octahedral sites in the garnet structure. This class of SIE has a Young modulus of around 150 GPa. To obtain appreciable ionic conductivity at RT, Li can be added into the structure by adjusting the valence of the A and B cations, leading to several stoichiometries of Li-conducting garnets such as $Li_5La_3M_2O_{12}$ (M = Nb, Ta, Sb) or $Li_7La_3M_2O_{12}$ (M = Zr, Sn) (non-exhaustive list)[68]. These compounds have demonstrated very good stability with respect to Li-metal, a stability range of up to (> 6 V *vs.* Li^+/Li), and higher conductivities (10^{-3} S.cm^{-1} at 25 °C) for $Li_{6.4}La_3Zr_{1.4}Ta_{0.6}O_{12}$[69].

In the garnet family, the $Li_7La_3Zr_2O_{12}$ (LLZO) phase was first mentioned in 2007 by Murugan et al.[70]. This SIE exhibits an ionic conductivity of $7.74.10^{-4}$ S.cm^{-1} at 25 °C. LLZO is known in two crystallographic forms (Figure I-10), the non-conducting tetragonal phase (10^{-6} S.cm^{-1}) and the conducting cubic phase (10^{-4} S.cm^{-1}). The transition between these two phases generally occurs between 200-700 °C[71]. The parameters for obtaining the cubic phase will be detailed in Chapter V.

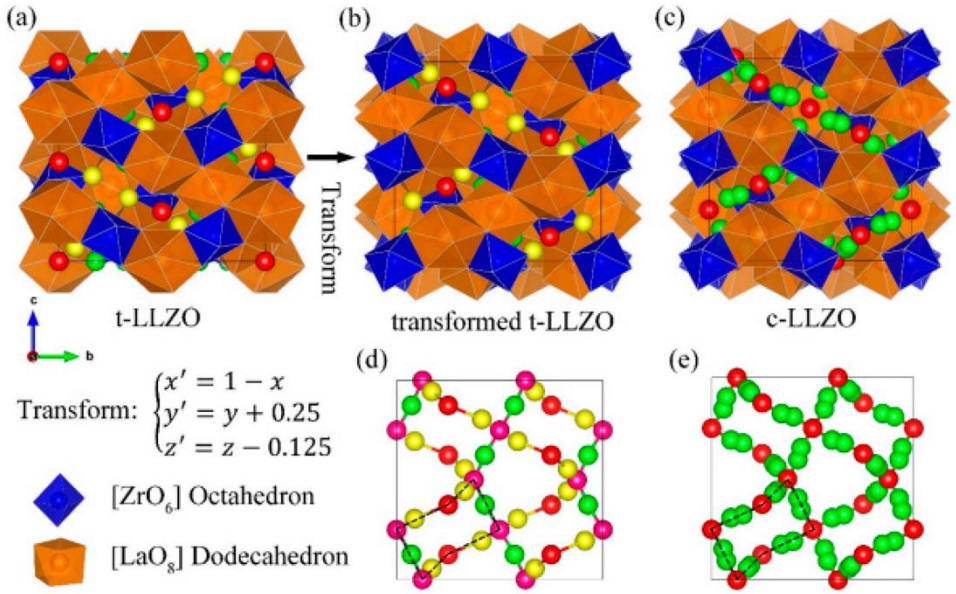

Figure I-10. Crystal structures of (a) tetragonal phase, (b) transformed tetragonal phase, and (c) cubic phase LLZO where the blue and brown polyhedral indicate six- and eight-fold coordination sites, respectively. The distribution of Li in tetragonal phase (d), and cubic phase (e).[72]

Two factors are crucial for obtaining LLZO with the best performance: its synthesis and its densification. Various synthesis methods exist for the preparation of LLZO, the most common being the solid-state method[73]. This technique involves mixing the precursors in a ball milling, i.e. grinding the powders using a ball mill or planetary machine. Other studies have reported the sol-gel method for the synthesis of LLZO. One of the last possible processes is the Pechini method, which introduces an acid that chelates the metal ions. The manufacturing process will have an impact not only on the densification temperature of the LLZO but also on its particle size distribution.

After a solid-state method, a pellet is usually produced and then it is sintered at high temperature for a relatively long time (<1230 °C for 36 h) to obtain a dense ceramic[70]. It has been shown that in this approach, it is difficult to obtain the desired stoichiometric composition. Additionally, the high sintering temperature introduces impurities accompanied by Li loss[74,75]. The sol-gel method allows the fabrication of LLZO at lower temperatures (800-900 °C), impeding the Li loss and the formation of impurities in the powders. Shimonichi et al.[76] have developed sol-gel LLZO allowing its sintering at 1180 °C for 35 h. They achieve a conductivity of $1.6.10^{-4}$ $S.cm^{-1}$ at RT. Regarding the Pechini method, Jin et al.[77] have densified Al-doped LLZO at 1200 °C for 6 h and they achieved finer particles than solid state processing and a conductivity of $2.0.10^{-4}$ $S.cm^{-1}$ at RT.

LLZO densification is essential to obtain a porosity-free ceramic with the best conduction properties. One strategy is to add additives to improve densification during heat treatment. Janani et al.[78] studied the influence of the addition of various additives (Li_3BO_3, Li_3PO_4, and Li_4SiO_4) on the density of the LLZO pellet after a heat treatment at 900 °C and 1200 °C. With a heat treatment at 900 °C, the introduction of Li_3BO_3 showed the best relative density (76%) with a conductivity of $1.3.10^{-5}$ $S.cm^{-1}$ at 33 °C. At 1200 °C, the addition of Li_4SiO_4 showed the best relative density (96%) and ionic conductivity ($6.1.10^{-4}$ $S.cm^{-1}$ at 33 °C).

To obtain LLZO compounds with a high relative density and therefore high ionic conductivity, it is necessary to sinter the LLZO at high temperature or/and to dope the material to obtain the cubic phase, which is the most conductive. Unfortunately, high-temperature treatment often induces the loss of Li and thus the formation of impurities at the grain boundary[74]. These impurities can hinder ionic conductivity. What's more, ceramic-based SIE is generally thick (~1 mm) and therefore difficult to integrate into ASSB devices. With this in mind, they can be integrated into the design of composite materials.

III.3. Solid Composite Electrolyte

As we have seen in the previous sections, the two families of SE have different advantages, but their limitations hinder their use in ASSB systems. Composite solid electrolyte (SCE) design has therefore emerged to mix different types of electrolytes, which would make it possible to combine the advantages of both families, such as improving oxide manufacturing processes and improving the electrochemical properties of polymers[13]. This would combine the advantages of both electrolyte types while compensating for their drawbacks. SCE is a heterogeneous assembly or mixture of at least two materials, whether conductive or not (Figure I-11)

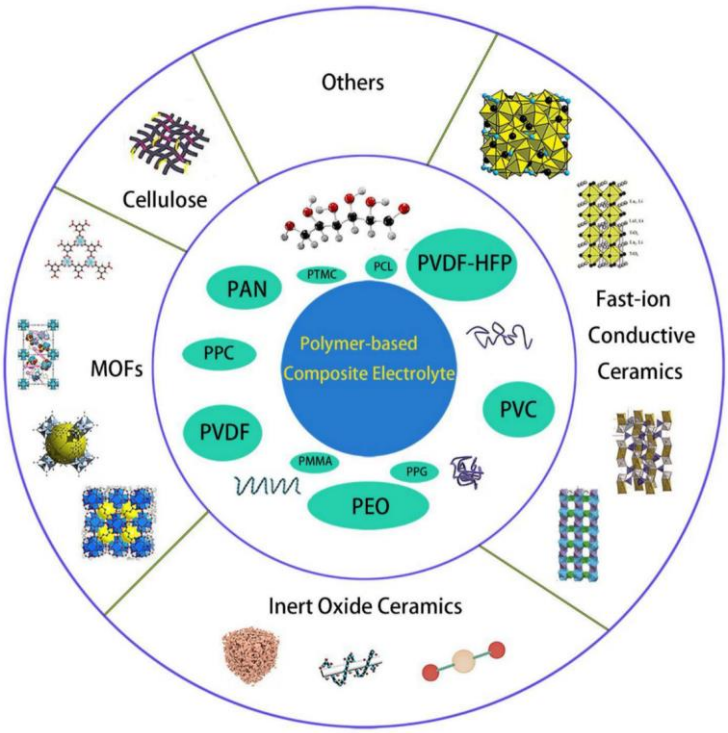

Figure I-11. Categories of the existing materials for SCE[79].

Depending on their inorganic and polymer contents, SCEs can be divided into two categories. The first is a predominantly polymeric SCE, where the inorganic filler, whether conductive or not, mainly improves the mechanical properties of the polymer phase, which in turn is conductive to Li^+ ions. The second class is a predominantly inorganic SCE, where a conductive or non-conductive polymer phase is added to mainly improve the material's flexibility and processability. The manufacturing processes for SCEs are essential to obtain the best electrochemical performance and the lowest possible resistance at the interface of the two materials. In the literature, we find 3 classes of processes for SCE manufacturing. The first is known as solution casting, the second as mechanochemical casting, and the third as electrospinning. SCE design can involve a number of different processes: the inorganic filler can be nanoparticles or nanofibers, in which case the casting process is the most common. On the other hand, inorganic fillers can take the form of 3D networks, and so the processes used can be impregnation if the 3D network is inorganic, or electrospinning if the 3D network is a combination of polymer and inorganic materials. The different ways of preparing SCE will be discussed throughout this section. In addition, for this section, we'll focus on composites based on PEO-like polymers and oxide for the inorganic part.

III.3.1. Non-conductive filler

In section III.1.1, we noted that it was necessary to increase the mechanical properties of the SPE. In addition to the cross-linking and copolymerization strategies, it is possible to incorporate inorganic fillers into the polymer matrix to reinforce it. Inert inorganic fillers are introduced in small quantities so as not to interfere with Li^+ conduction in the polymer matrix, preventing percolation of the inorganic network. Different types of oxide were studied, with different morphologies and structures. Inorganic oxides such as aluminum oxide (Al_2O_3) and titanium oxide (TiO_2) are used as mechanical reinforcements. Silicon oxides (SiO_2), on the other hand, were initially used for mechanical reinforcement, but also to improve electrochemical properties by reducing the crystallinity of PEO chains.

It was in 1982 that Weston et al.[80] first reported the incorporation of Al_2O_3 into a PEO-LiTFSI matrix. They demonstrated that the addition of 10 vol% Al_2O_3 had a negligible impact on the polymer's ionic conductivity but improved its mechanical stability at temperatures above 100 °C. Indeed, it was not possible to measure conductivities above 110 °C for PEO-LiTFSI without Al_2O_3 as they tend to short-circuit, probably due to excessive softening of the amorphous polymer. For the solid electrolytes with 10 vol% Al_2O_3, no evidence of deformation is observed up to 120 °C. In 1999, Croce et al.[81] used Al_2O_3 and TiO_2 as agents in PEO-LiX matrices to improve mechanical stability (not quantify) in the 30-80 °C temperature range. In these examples, the inorganic fillers act more as "solid plasticizers" to reduce the crystallinity of the SPE[82]. It was later (2002) that Shin et al.[83] demonstrated the benefits of incorporating non-conductive inorganic fillers on electrochemical properties. In a PEO-$LiCF_3SO_3$ system with micron-sized TiO_2 particles, they described the possibility of improving the electrolyte||Li-metal interface by reducing the contact area between the Li-metal and the electrolyte while maintaining a conductivity of $2.16.10^{-4}$ $S.cm^{-1}$ for 15 wt% of TiO_2.

This study has opened up a new area of research into the use of inorganic fillers, not only to improve the mechanical properties of SPEs but also to improve their electrochemical performance.

Ji et al.[84], studied the evolution of the conductivity at 25 °C of a PEO-$LiClO_4$ SPE as a function of the SiO_2 nanoparticle (~12 nm) concentration. In Figure I-12, it can be seen that adding 10 wt% SiO_2 to the SPE increases the ionic conductivity by two orders of magnitude. The SPE without SiO_2 crystallizes around 32 °C, remaining in an amorphous state above this temperature. This explains its low conductivity at 25 °C. When 10 wt% of SiO_2 is added, the

electrolyte exhibits very few crystalline domains in amorphous matrix. When conductivity is measured at 25°C, an increase of two-order of magnitude in conductivity is observed, due to the fact that at this temperature the electrolyte has amorphous domain. Unlike other electrolytes, where the crystallization temperature is higher than 25 °C, crystalline phases are present when measuring conductivity (at 25°C), thus reducing Li^+ diffusion. The authors propose that the increase in the degree of crystallization observed with the addition of 10 wt% SiO_2 may be attributed to the role of the filler as a potential crystallization site or to its ability to induce molecular interactions between polymer chains, leading to a reduction in chain mobility.

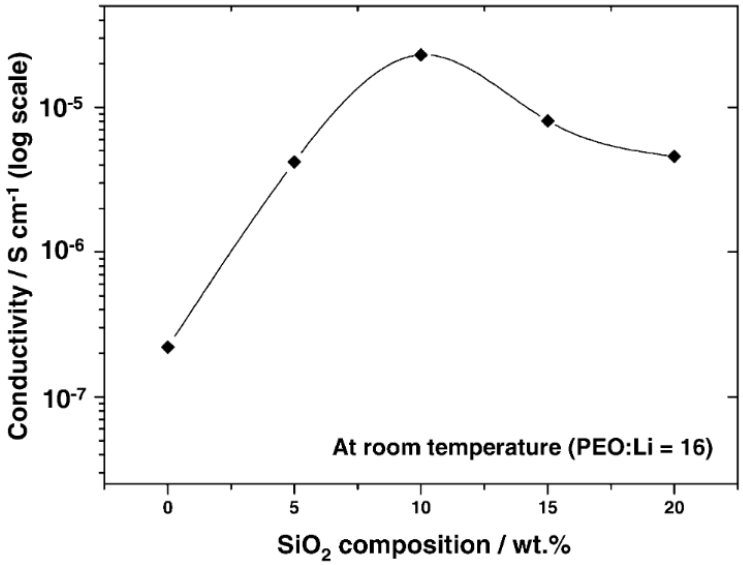

Figure I-12. Evolution of ionic conductivity at 25 °C in PEO-$LiClO_4$ with SiO_2 weight proportion[84].

The use of non-conductive inorganic fillers improves the mechanical properties by strengthening the SPE but also increases its ionic conductivity by reducing or eliminating its crystallinity.

III.3.2. Conductive filler

Conductive fillers Li-rich have been also investigated in order to improve the performances of the SPE. In their papers, Wang et al.[85] introduced a comparative study on the effects of the chemistry of the different types of particles in SPE PEO-$LiClO_4$, including from 5 to 20 wt% of LATP, SiO_2, and TiO_2. The best result in conductivity is obtained for 10 wt% of LATP ($1.7.10^{-4}$ $S.cm^{-1}$ at 20 °C). This study demonstrates the positive impact of adding Li-

rich inorganic fillers to the SCE design. For the conception of this SCE, the authors have used the solution casting method.

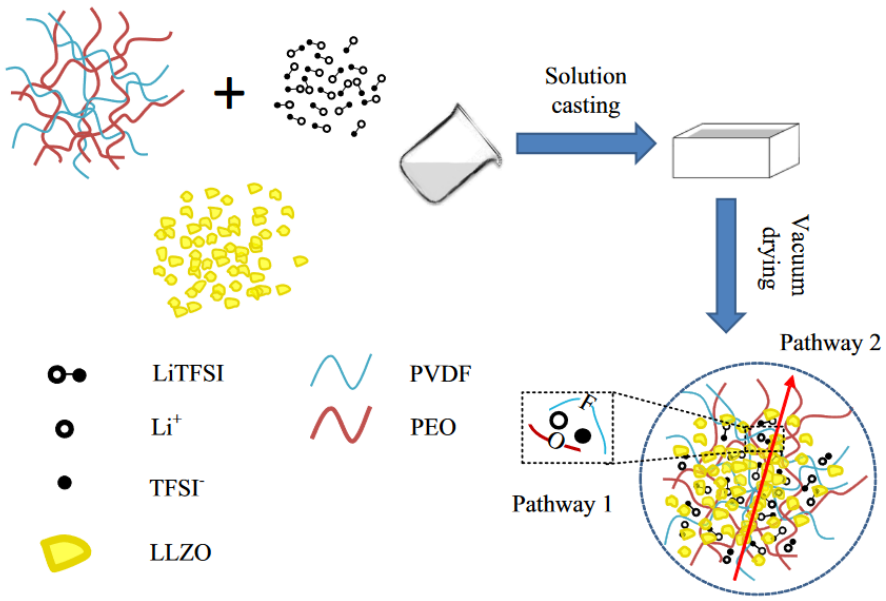

Figure I-13.Schematic representation of SCE fabrication using solution casting process[86].

This method is represented in Figure I-13 and is the most common. Using a liquid solution that can be applied in a wide range of shaping processes, such as deposition in a Teflon mold or tape casting (doctor blade). This method involves mixing polymer precursors, salts, and inorganic fillers in a solvent. This mixture is then deposited using the chosen method and the solvent is evaporated to obtain the SCE. This method produces thin objects, is low cost, and scalable.[87] The important thing with this method is to choose a good solvent. It must be inert to the electrolyte used but also volatile to allow easy evaporation. One of the most commonly used solvents is acetonitrile (ACN, boiling temperature at 82°C) because PEO has good solubility in this solvent and most of the ceramics are stable in it. Li et al.[86] used the sol-gel method for the fabrication of LLZO nanoparticles and obtained the cubic phase. They prepared a SCE using the casting solution method, mixing 10 wt% LLZO in an ACN/PVDF/PEO/LiTFSI solution (Figure I-13). They measured almost the same ionic conductivity of $4.2.10^{-5}$ $S.cm^{-1}$ *vs.* 3.10^{-5} $S.cm^{-1}$ at 30 °C for SPE. In contrast with this work, other studies have shown a clear improvement. Chen et al.[88] used the solid-state method for LLZO fabrication and obtained micrometer particles. They reported the manufacture of a SCE based on PEO-LiTFSI (~10^{-5} $S.cm^{-1}$ at 30 °C) and an optimum of 7.5 wt% LLZO with an ionic conductivity of $5.5.10^{-4}$ $S.cm^{-1}$ at 30 °C. To understand this increase, it is necessary to monitor the crystallinity rate in the SCE. The electrolyte without LLZO has a crystallinity ratio of 54%, with the addition of 7.5

wt% LLZO this rate decreases to 22%. As the crystalline domains are less present, Li^+ diffuses more easily into the SCE. Surprisingly, the latter articles show an order of magnitude higher ionic conductivity than the Li et al. article[86]. The differences that can be noted between these two articles are the presence of PVDF in the first, the size of LLZO (particles nanometer *vs*. micrometer), and the slight difference in the proportion of LLZO mass introduced (10 wt% *vs*. 7.5 wt%).

In section III.3.1, the use of nanoparticles appeared to be favorable to achieving an ionic conductivity of the order of 10^{-4} $S.cm^{-1}$, so we can deduce that this parameter is not the one that influences this result. To understand whether the transition from 7.5 wt% to 10 wt% of LLZO is the cause of the drop-in conductivity, it is essential to examine higher weight proportions.

Choi et al.[89], measured an ionic conductivity of $1.0.10^{-5}$ $S.cm^{-1}$ at 35 °C by incorporating 52.5 wt% LLZO in a PEO-$LiClO_4$ (~ 10^{-8} $S.cm^{-1}$ at 35 °C) matrix. LLZO was synthesized by the Pechini method and a tetragonal phase was obtained. Using Differential Scanning Calorimetry (DSC) analysis, the authors demonstrate the shift (65°C to 50°C for 0 to 52.5 wt% of LLZO, respectively), at lower temperatures, of the endothermic reaction with increasing LLZO content. This means that the addition of LLZO maintains the SCE in an amorphous state at lower temperatures and therefore higher conductivity. According to the latter article, the weight proportion of LLZO could be the reason for the order-of-magnitude difference in ionic conductivity. However, one aspect that has not been addressed is the difference in morphology of LLZO particles. Unfortunately, to our knowledge, no studies has been carried out on the impact of LLZO morphology. On the other hand, it is possible to examine another SCE manufacturing process that uses LLZO fibers.

At the beginning of section III.3, we briefly discussed the fabrication of continuous 3D LLZO arrays using the electrospinning method. This method is widely used for the fabrication of SCEs. This method can be used in two different ways (Figure I-14).

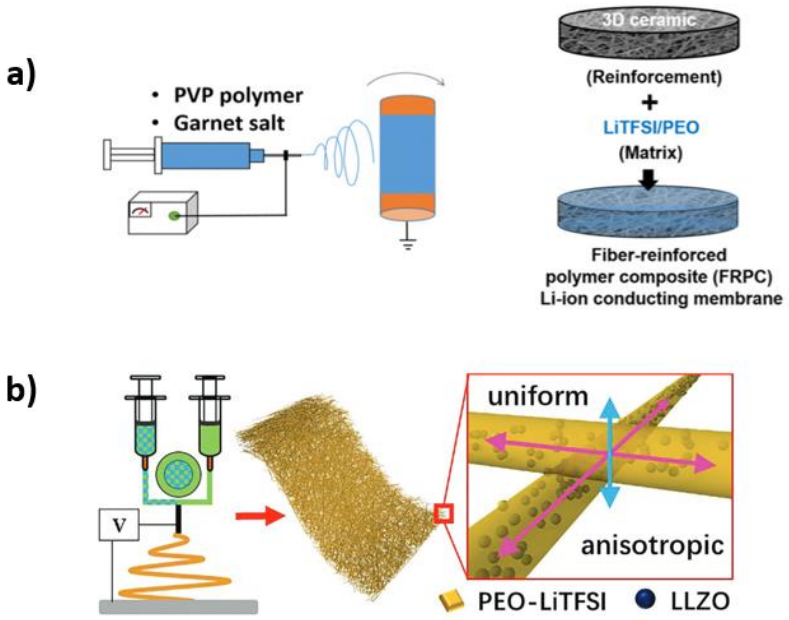

Figure I-14. Schematic representation of the use of the electrospinning method in SCE design for (a) structure before impregnation[90] and (b) total design[91].

The first (Figure I-14a) is to fabricate the 3D LLZO fiber network by electrospin the precursor of LLZO followed by heat treatment. Once the network of LLZO has been obtained, it can then be impregnated with the polymer solution. Fu et al.[90] used this method, they dropped the 3D LLZO cubic network with a solution of PEO/LiTFSI/ACN. A SCE with 20 wt% LLZO was obtained and showed a thickness of 40-50 µm. An ionic conductivity of $2.5.10^{-4}$ $S.cm^{-1}$ at RT was measured. Unfortunately, the increase in conductivity compared with PEO alone is not explained. DSC analyses that could allow us to see the impact of the addition of the 3D LLZO network on crystallinity are not given. In view of the results previously presented with LLZO powder, we can assume that 3D LLZO reduces the crystallinity of PEO and therefore improves its conductivity at RT.

The second option (Figure I-14b) is to electrospun the LLZO/PEO-LiTFSI mixture directly. Guo et al.[91] presented the use of a core-shell nozzle in which a solution of LLZO/PEO/LiTFSI/ACN is present in the core and PEO/LiTFSI/ACN in the shell. These two mixtures are electrospun to produce PEO-LiTFSI fibers containing around 11 wt% of LLZO particles. This technique produces objects with a thickness of 135 µm to 200 µm. What's interesting about this article is that it compares SCE obtained by electrospinning to SCE obtained by tape casting. They observe by DSC that the PEO melting peak shifts towards the lowest temperatures, from PEO-LiTFSI alone (67.9 °C), to tap-casting (64.8 °C) and finally to SCE made by electrospinning (62.9 °C), explained by the authors, as different degrees of

crystallinity which is in accordance with the XRD. SCE made by electrospinning has the lowest melting temperature, an ionic conductivity ($1.5.10^{-4}$ $S.cm^{-1}$ at 35 °C) almost two orders of magnitude higher than PEO-LiTFSI, indicating a lower degree of crystallinity. Furthermore, Stress-strain curves obtained by Dynamic mechanical thermal analysis (DMTA) have enabled to measure of tensile strength. The SCE fabricated using the electrospinning method achieves the best result (7.46 MPa), higher than the PEO-LiTFSI (2.62 MPa), and the SCE prepared by the tap-casting method (5.94 MPa). They explain that this improvement can be attributed to the mechanical reinforcement effect of uniformly dispersed LLZO and interwoven microfibers.

The two manufacturing processes using the electrospinning method ultimately give similar conductivities.

Finally, whether LLZO particles, LLZO fibers, or SCE fibers are used, the ionic conductivity is between 10^{-5} and 10^{-4} $S.cm^{-1}$ at RT. It is difficult to understand why there is an order of magnitude between the different articles quoted above. However, it is important to remember that the addition of LLZO generally improves ionic conductivity in most cases compared with the polymer alone. This highlights the good synergy between PEO and LLZO.

Another method for manufacturing SCE is to use mechanochemical processes. This technique includes two processes, the first is ball-milling (Figure I-15), which is generally used before tape-casting, and the second is the cold-sintering process (CSP), which is used to obtain SCE directly. CSP was introduced by Randall et al.[92] and is used to obtain dense ceramics at low temperature under axial pressure, it was subsequently used to manufacture SCE. CSP will be detailed in Chapter V.

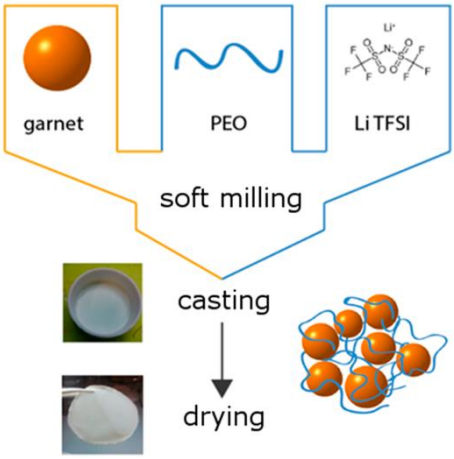

Figure I-15.Schematic view of the SCE preparation using a ball milling[93].

As mentioned earlier, ball-milling is used before the casting methods studied above. This will improve the contact between the two electrolytes. Zagórski et al.[93] studied the

manufacture of SCE with 10 vol% LLZO doped with Gallium in PEO-LiTFSI. They used the ball-milling process to mix LLZO/PEO/LiTFSI/ACN and then poured the slurry into a Teflon mold or carried out tape-casting. They measure a slightly lower conductivity for SCE than PEO-LiTFSI ($4.5.10^{-4}$ $S.cm^{-1}$ than $7.0.10^{-4}$ $S.cm^{-1}$ respectively at 70 °C). This result is in contradiction with previously reported results, where the addition of inorganic filler improves ionic conductivity. The authors explain that this may be due to the PEO chosen as a reference and indicate that their values are often underestimated. On the other hand, SCE shows a much lower interfacial resistance with Li-metal electrodes for SCE than PEO-LiTFSI (33 *vs.* 300 $\Omega.cm^2$ respectively).

In section III.1.4, we discussed the advantages of using si-SPEs to increase the number of transport and avoid the growth of dendrites[52]. Unfortunately, the grafting of the anion to the polymer network greatly reduces the conductivity of the system[54], so they are very interesting candidates for the manufacture of SCEs, where the inorganic would improve conductivity performance by creating an interface between the two electrolytes more favorable to Li^+ diffusion. Yu et al.[94] have developed a SCE based on a 3D-LATP network produced using the electrospinning method. The polymer matrix is a si-SPE composed of poly[bis(2-(2-methoxyethoxy)ethoxy)phosphazene] (MEEP) and LiTFSI containing 86 wt% Ethylene carbonate/Dimethyl carbonate (EC/DMC). The homogeneous solution of LiTFSI, MEEP, benzophenone (UV initiator), ACN, and LATP was sandwiched between Mylar foil, pressed to the desired thickness, and in-situ polymerization through UV light exposure was carried out. They obtained a self-standing film of 150 - 250 µm with a volume ratio of LATP and polymer solution is about 4:1 (approximately 33 wt% of LATP). The composite electrolyte exhibits an ionic conductivity of $2.3.10^{-4}$ $S.cm^{-1}$ at 20 °C which is slightly lower than for si-SPE for a single-ion (around 3.10^{-4} $S.cm^{-1}$), probably due to the lower amount of plasticizer (32 wt% EC/DMC) in the composite membrane than in the si-SPE membrane (86 wt% EC/DMC). A t^+ of 0.94 for SCE (*vs.* 0.93 for si-SPE) is measured and the electrochemical window is improved from 4.9 to 5.4 V (*vs.* Li^+/Li) when LATP is added to the polymer.

Lechartier et al.[95] produced a SCE based on LLZO particles (400-600 nm size) in a single ion polymer matrix. Single ion polymer is composed of crosslinking polymer (Poly(ethylene glycol) methyl ether methacrylate and poly(ethylene glycol) dimethacrylate) and plasticizer (propylene carbonate; PC). Using the casting method in Teflon mold and in-situ UV-photopolymerization, they obtained a flexible, self-supporting film 1mm thick containing up to 50 wt% LLZO. They obtained the best conductivity ($1.1.10^{-4}$ $S.cm^{-1}$ at 25 °C) for SCE

with 40 wt% LLZO *vs.* $4.8.10^{-5}$ $S.cm^{-1}$ for the polymer. Here too, it is necessary to add a plasticizer to obtain such a high ionic conductivity (30 wt% PC) with a single-ion polymer (3.10^{-7} $S.cm^{-1}$ at 20°C for the polymer without PC[55]). Interestingly, they found a decrease of t^+ from 0.73 for si-SPE to 0.57 for SCE at 26 wt% LLZO. Although they cannot unequivocally explain this decrease, they assume the presence of anionic impurities from the LLZO or poor grafting of the anion to the polymer network.

We can see that different processes are used to manufacture SCE. Whether by solvent evaporation or in-situ polymerization, the processes have a crucial role to play in the performance of SCE.

IV. Mechanism of conduction for Li ion in SCE

Previous results have shown an improvement in the ionic conductivity performance by adding conductive or non-conductive fillers. The mechanism conducting to this augmentation of the ionic conductivity is not always discussed and understood. But it is very important to know how the Li^+ moves in these composites in order to design the best SCE.

To study the diffusion mechanism of Li^+ in SCE, Yang et al.[96] used solid-state Li Nuclear magnetic resonance (NMR) with selective ^{6}Li-isotope labeling and a ^{6}Li–^{7}Li isotope-replacement strategy. To determine the different Li ion pathways, a symmetrical cell made from ^{6}Li leaflets and deposited on SCE was electrochemically cycled (^{6}Li/SCE/^{6}Li). During cycling, the ^{6}Li ions were removed from the electrode and then diffused into the electrolyte to be deposited on the second electrode. As cycling proceeds, the ^{6}Li ions replace the ^{7}Li ions in the electrolyte, revealing the Li ion diffusion pathway (Figure I-16c). By analyzing the NMR spectra obtained from the reference materials (LLZO nanowires and PAN-$LiClO_4$) they were able to identify the ^{6}Li peaks characteristic of each material (2.4 and 0.9 ppm respectively; Figure I-16b). On the SCE NMR spectrum, in addition to the peak at 0.9 ppm, they observed the appearance of a new peak at 0.85 ppm, which they attributed to $LiClO_4$ within the PAN with a local structural environment that is modified by the LLZO nanowires. Quantification of the Li NMR spectrum of the SCE reveals that 37.4% of the Li resonates at 0.85 ppm and 62.6% of the Li at 0.90 ppm, which suggests that 37.4% of the PAN polymer matrix is modified by the LLZO nanowires. To determine the diffusion phase of Li ions, they look at the evolution of the NMR spectrum after 10 galvanostatic cycles of the cell described above. They show that the intensity of the peak at 0.85 ppm increases, while that at 0.9 ppm remains unchanged. They conclude that Li^+ prefers to diffuse through the modified regions of the PAN than through the

unmodified regions. For them, this result demonstrates that a small amount of LLZO (5 wt%) is required to significantly modify the local Li^+ environment in the polymer phase and improve conductivity by $4.06.10^{-7}$ $S.cm^{-1}$ for PAN-$LiClO_4$ to $1.31.10^{-4}$ $S.cm^{-1}$ at 20 °C for SCE with 5 wt% of LLZO nanowires. They explain that the increase in conductivity is not due, not like with PEO, to a decrease in crystallinity, but by increasing the dissociation of Li^+ and the ClO_4^- anion, which in turn increases the concentration of free Li^+ in the SCE. This dissociation is made possible by LLZO's high dielectric constant (40-60) and Lewis's base surface groups with a high affinity for the anion. This was supported by a comparative study, replacing LLZO with Al_2O_3 nanowires (non-conductive), the latter with a dielectric constant of 9, which is lower than LLZO. The conductivity of SCE Al_2O_3 is an order of magnitude lower than that of SCE LLZO. This demonstrates that a high dielectric constant promotes salt dissociation and hence ionic conductivity.

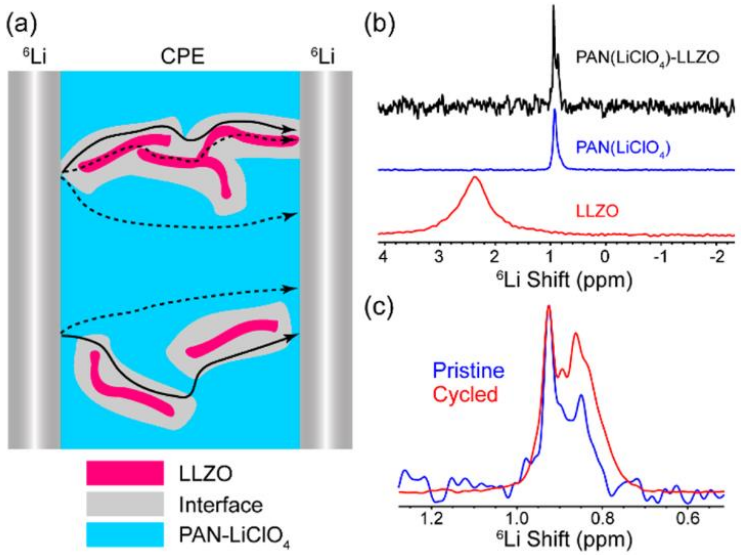

Figure I-16. (a) Schematics of the symmetrical $^6Li/SCE/^6Li$ cell and possible Li transport pathways during battery cycling. (b) ^6Li NMR spectra of the SCE sample, a blank sample with only PAN and $LiClO_4$, and undoped LLZO NW powder. (c) ^6Li NMR spectra comparison between the as-made (pristine) and cycled SCEs[96].

Interestingly, Wang et al.[85] carried out a parametric study of the impact of the weight proportion of LATP (65 nm of average particle size) in cation transport properties. Maximum conductivity is obtained for 10 wt% (4 vol%) of LATP, i.e. a concentration at which percolation via LATP particles involving direct contact is unlikely. However, based on a phase distribution calculation model, they deduce that the maximum conductivity observed is compatible with percolation through the interphase. They also show that above a certain percentage of inorganic

content (10 wt%), ionic conductivity decreases. This decrease is thought to be due to the agglomeration of the LATP particles, which reduces the interphase volume fraction. This opens the way to different conduction mechanisms depending on the volume fraction of inorganic filler.

Zheng et al.[97] used high-resolution solid-state ^{6,7}Li NMR to understand the Li diffusion pathway in an SCE composed of a PEO-$LiClO_4$ matrix with 50 wt% LLZO. They have used a similar approach like Yang et al.[96]. First, the individual materials are studied. A single ^{6}Li resonance at 0.2 ppm was observed for $LiClO_4$ within the PEO polymer matrix and at 2 ppm for pure cubic LLZO. In the SCE NMR spectrum, the two characteristic peaks of the raw materials are found, plus a shoulder at 1.4 ppm. This peak is attributed to Li at the PEO-LLZO interface. The resonance of interfacial Li is significantly broader than that of LLZO and $LiClO_4$ in PEO, indicating a high degree of structural disorder at the interface. The chemical shift of interfacial Li (1.4 ppm) is closer to that of LLZO Li (2.0 ppm), suggesting that interfacial Li originates from the LLZO surface and is strongly affected by the PEO matrix.

After cycling the ^{6}Li/SCE/^{6}Li cell, it shows a significant increase in the LLZO peak (39%) and a slight increase in the interfacial Li resonance (6%) (Figure I-17). This means that a large amount of ^{7}Li has been replaced by ^{6}Li in the LLZO, confirming that Li^+ mainly diffuses through the LLZO particles.

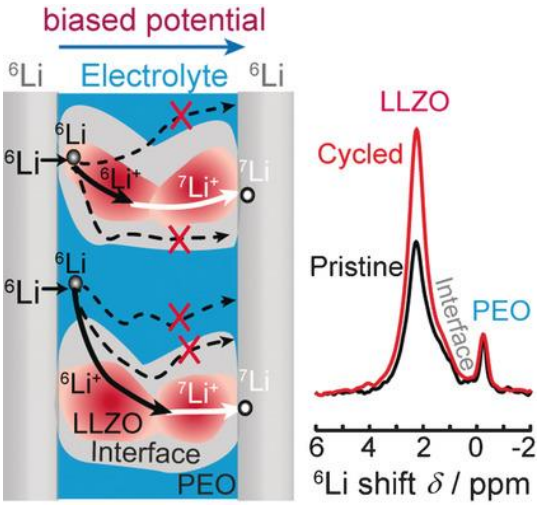

Figure I-17. Schematics of the symmetrical ^{6}Li/SCE/^{6}Li cell and possible Li transport pathways during battery cycling. Comparison of the NMR spectra of battery before and after cycling[97].

The same team therefore investigated the compositional dependence of the three factors that determine ionic conductivity, including ion mobility, ion transport pathways, and the concentration of active ions in SCE with PEO-LiTFSI and LLZO[98]. They illustrated the conduction pathways of Li ions in Figure I-18. They explained that for a low LLZO content

(<20 wt%) the SCE behaves like a polymer electrolyte but differently because it is modified by the LLZO particles. As the weight proportion of LLZO increases (≥ 50 wt%), a critical point is reached where the LLZO particles are percolated and the SCE conduction functions like a ceramic electrolyte. However, LLZO particles are diluted by the polymer matrix, so LLZO particles have a much lower ionic conductivity than dense ceramic pellets.

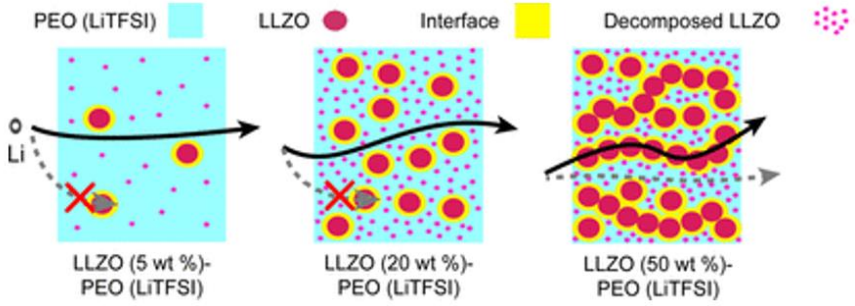

Figure I-18. Schematics of Li-ion diffusion pathways in PEO(LiTFSI)/LLZO SCEs for different LLZO weight proportion[98].

In conclusion, the understanding of Li ion diffusion in SCE is the subject of much research. It is important to note that, depending on the quantity of inorganic introduced into the polymer phase, the diffusion mechanisms differ. Analytical techniques such as NMR or impedance spectroscopy are therefore essential for understanding diffusion phenomena. It has been shown that when the inorganic content is less than 20%, Li ion diffusion occurs mainly through the polymer phase. However, this can be modified by the presence of the inorganic filler, which makes it more conductive, either by improving the dissociation of Li^+ and the anion or by reducing the crystalline domains of the polymer. On the other hand, at a high level of inorganic charge (50 wt%), the LLZO lattice percolates and becomes the diffusion route for Li ions. To our knowledge, no study to date has shown the passage of Li^+ from one phase to the other.

V. Interface PEO||LLZO

When designing the SCE, it is important to understand the interface between the two components. As mentioned earlier, to our knowledge, no study demonstrates the migration of Li^+ ions between the LLZO and the polymer matrix, and vice versa. Some studies have designed multilayer structures to induce the transfer from one matrix to the other and investigate the interfacial resistance. Chapter IV will be dedicated to this investigation, so we won't go into detail in this section.

Gupta et al.[99] designed a tri-layer cell to analyze the interfacial kinetics of Ta-doped LLZO (LLZTO) with PEO (Figure I-19).

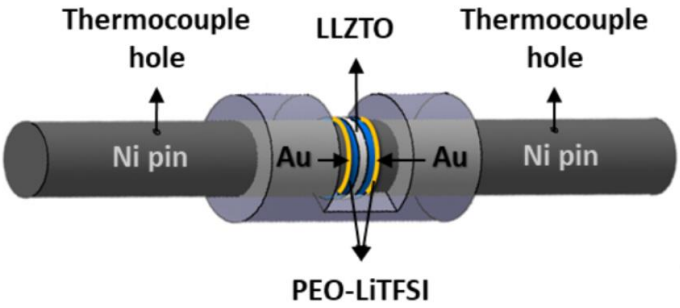

Figure I-19. Schematic of a three-layer cell Au/PEO-LiTFSI/LLZTO/PEO-LiTFSI/Au[99].

By using EIS measurements and deconvolution of each phenomenon occurring in this tri-layer setup, it is possible to determine the interfacial resistance ($R_{interfacial}$) between the two electrolytes and the parameters influencing it. The tri-layer structure consists of a LLZTO pellet, sintered at high temperature, sandwiched between two PEO-LiTFSI membranes. By knowing the EIS response of each electrolyte and employing a defined electronic circuit, it is possible to measure the value of $R_{interfacial}$. They demonstrate that the LLZTO||PEO-LiTFSI interface is the limiting factor for the ionic conductivity of the tri-layer structure. This LLZTO||PEO-LiTFSI interface can be affected by the presence of impurities on the surface of the LLZTO pellet and also by the difference in Li^+ concentration ($[Li^+]$) of the two electrolytes. They explain that impurities, such as Li_2CO_3, can lead to an increase in $R_{interfacial}$ because it is highly resistive. Moreover, Li_2CO_3 increases the oxygen density on the surface of the LLZTO, which induces electrostatic repulsion with the oxygen in the PEO, resulting in a higher hopping distance for Li^+. By applying a second heat treatment to the pellet to remove the Li_2CO_3 layer, they observed a decrease in $R_{interfacial}$ from 14.57 to 0.20 $k\Omega.cm^2$ for the untreated pellet *vs.* the retreated pellet at 700 °C respectively. To demonstrate the influence of the Li^+ concentration gradient on the value of $R_{interfacial}$, the authors prepared several batches of PEO-LiTFSI, with different [EO]:[Li] ratios. After EIS measurements, they observe that $R_{interfacial}$ first decreases to reach a minimum (0.44 $k\Omega.cm^2$) at a ratio of 15:1 and then increases again (Figure I-20). Ideally, as the $[Li^+]$ increases, the difference in concentration between the two electrolytes would decrease and so would $R_{interfacial}$. But this is not the case, and they explain this by the precipitation of the Li-salt in the PEO, so it does not participate in conduction.

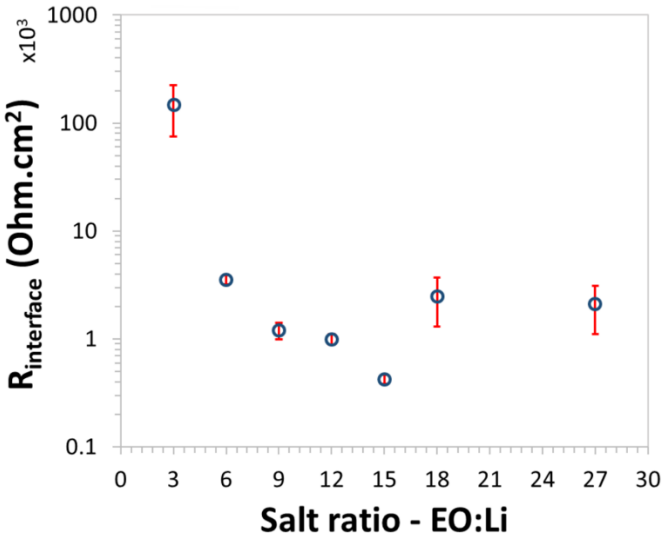

Figure I-20. Effect of EO:Li in the PEO-LiTFSI electrolyte on the PEO-LiTFSI||LLZTO interfacial impedance[99].

Langer et al.[100] carried out a similar study on a tri-layer of LLZO and PEO-$LiClO_4$. Using the same methodology as the authors previously cited, the EIS measurements made it possible to determine the factors influencing the value of $R_{interfacial}$. In this study, what it denotes from the previous one is the integration in the electronic circuit of an element accounting for the roughness of the LLZO pellet. By fitting the impedance data with a Levie element, the two contributions of the pores and the ionic transition across the phase boundary can be separated. This study revealed that ionic movement across the interface is an obstacle.

EIS measurements and the use of electronic circuits are powerful tools for defining and deconvoluting the phenomena occurring at the interface of the two electrolytes. This has enabled the interfaces to be optimized. Kuhnert et al.[101] have investigated the modification of the LLZO surface to reduce $R_{interfacial}$ with respect to PEO. To do this, they treated the LLZO by plasma etching and, using a sol-gel reaction, created a covalent bond with a spacer that would enable the PEO to be bound to the LLZO surface. The use of this spacer avoids electrostatic repulsion between the oxygens on the surface of the LLZO and the oxygen in the PEO. This reduced the value of $R_{interfacial}$.

The manufacture of an SCE today is currently very promising for their use in ASSBs. However, the interfaces between the two electrolytes need to be fully understood in order to optimize their manufacture.

VI. Conclusion and thesis perspectives

As studied previously, electrolytes are an essential component in the emergence of ASSBs. SPEs have the advantage of being easily integrated into the current Li-ion battery manufacturing process. Unfortunately, these batteries operate at high temperatures (>60 °C), so the energy produced in the battery is also used to heat the system, which reduces their performance. At RT, SPEs have low conductivity ($<10^{-6}$ S.cm^{-1}). In addition, SPEs have poor mechanical properties, which can cause issues when batteries operate at high temperatures. SIE, on the other hand, has better conductivity performance at RT (10^{-3}-10^{-4} S.cm^{-1}). Sulfur electrolytes, which have demonstrated high performance and ductility that makes them easy to densify and compensates changes in volume in electrode, make them very attractive. Unfortunately, these materials are less chemically stable and give off dangerous gases when exposed to humidity. This means that great care needs to be taken when developing them, and makes battery manufacturing processes difficult. Oxides, on the other hand, show a high ionic conductivity at RT and much better chemical stability with respect to Li-metal or humidity. But the high Young's modulus indicates that the materials are very brittle and it is difficult to use them in thin layers. In addition, their synthesis and densification require very high temperatures, which would imply a very high-cost manufacturing process. And it would not be possible to incorporate them into current battery manufacturing processes.

To overcome the problems presented by SPE and SIE, a new category has been created. SCEs combine the advantages of both families while reducing their shortcomings. The manufacture of SCEs nevertheless involves optimizing the mixing process so that it is as ideal as possible for the conduction of Li ions. In addition, a great deal of work needs to be done on the proportions of each of the components in the SCE so as not to hamper conduction and mechanical properties. It is also necessary to understand the phenomena involved in conduction in SCE.

In this work, we have therefore chosen to manufacture a SCE based on a PEO network and LLZO. The interest of this work is, first, to study the synthesis of a SPE network (Chapter II). We will then study the factors influencing the thermal and mechanical properties of a cross-linked network. In order to be able to compare with the literature, we will contrast a SPE containing the LiTFSI additive with a si-SPE to observe the impact of anion grafting on ionic conductivity and electrochemical properties.

Once the SPE had been studied, it was possible to use it into a SCE. To understand the interfacial phenomena of these two components, an electrochemical impedance analysis study was carried out on multilayers (Chapter IV). The impact of in-situ polymerization on the interfacial resistance between PEO and LLZO will be demonstrated.

Following the example of the studies presented in section IV, we have chosen to design, manufacture and characterize a panel of SCE compositions. To produce a predominantly polymeric SCE, we have chosen to fabricate an LLZO network by electrospinning, which will be impregnated with a capillary SPE solution and then subjected to in-situ polymerization (Chapter III). In contrast, for a predominantly inorganic compound, we explored cold-sintering coupled with in-situ polymerization to form the polymer network (Chapter V).

References

(1) Xu, K. Nonaqueous Liquid Electrolytes for Lithium-Based Rechargeable Batteries. *Chem. Rev.* **2004**, *104* (10), 4303–4418. https://doi.org/10.1021/cr030203g.

(2) Ozawa, K. Lithium-Ion Rechargeable Batteries with LiCoO2 and Carbon Electrodes: The LiCoO2/C System. *Solid State Ion.* **1994**, *69* (3–4), 212–221. https://doi.org/10.1016/0167-2738(94)90411-1.

(3) Nitta, N.; Wu, F.; Lee, J. T.; Yushin, G. Li-Ion Battery Materials: Present and Future. *Mater. Today* **2015**, *18* (5), 252–264. https://doi.org/10.1016/j.mattod.2014.10.040.

(4) Yamada, A.; Chung, S. C.; Hinokuma, K. Optimized LiFePO4 for Lithium Battery Cathodes. *J. Electrochem. Soc.*

(5) de Klerk, N. J. J.; Wagemaker, M. Space-Charge Layers in All-Solid-State Batteries; Important or Negligible? *ACS Appl. Energy Mater.* **2018**, acsaem.8b01141. https://doi.org/10.1021/acsaem.8b01141.

(6) Janek, J.; Zeier, W. G. A Solid Future for Battery Development. *Nat. Energy* **2016**, *1* (9), 16141. https://doi.org/10.1038/nenergy.2016.141.

(7) Paul, P. P.; Chen, B.-R.; Langevin, S. A.; Dufek, E. J.; Nelson Weker, J.; Ko, J. S. Interfaces in All Solid State Li-Metal Batteries: A Review on Instabilities, Stabilization Strategies, and Scalability. *Energy Storage Mater.* **2022**, *45*, 969–1001. https://doi.org/10.1016/j.ensm.2021.12.021.

(8) Banerjee, A.; Wang, X.; Fang, C.; Wu, E. A.; Meng, Y. S. Interfaces and Interphases in All-Solid-State Batteries with Inorganic Solid Electrolytes. *Chem. Rev.* **2020**, *120* (14), 6878–6933. https://doi.org/10.1021/acs.chemrev.0c00101.

(9) Armand, M.; Gauthier, M.; Muller, D. Nouveau Materiau a Conduction Ionique Constitué Par Un Sel En Solution Dans Un Électrolyte Liquide, 1988.

(10) Bates, J. B.; Dudney, N. J.; Gruzalski, G. R.; Zuhr, R. A.; Choudhury, A.; Luck, C. F.; Robertson, J. D. Fabrication and Characterization of Amorphous Lithium Electrolyte Thin Films and Rechargeable Thin-Film Batteries. *J. Power Sources* **1993**, *43* (1–3), 103–110. https://doi.org/10.1016/0378-7753(93)80106-Y.

(11) Tikekar, M. D.; Choudhury, S.; Tu, Z.; Archer, L. A. Design Principles for Electrolytes and Interfaces for Stable Lithium-Metal Batteries. *Nat. Energy* **2016**, *1* (9), 16114. https://doi.org/10.1038/nenergy.2016.114.

(12) Zheng, Y.; Yao, Y.; Ou, J.; Li, M.; Luo, D.; Dou, H.; Li, Z.; Amine, K.; Yu, A.; Chen, Z. A Review of Composite Solid-State Electrolytes for Lithium Batteries: Fundamentals, Key Materials and Advanced Structures. *Chem. Soc. Rev.* **2020**, *49* (23), 8790–8839. https://doi.org/10.1039/D0CS00305K.

(13) Kerman, K.; Luntz, A.; Viswanathan, V.; Chiang, Y.-M.; Chen, Z. Review—Practical Challenges Hindering the Development of Solid State Li Ion Batteries. *J. Electrochem. Soc.* **2017**, *164* (7), A1731–A1744. https://doi.org/10.1149/2.1571707jes.

(14) Sakuda, A.; Hayashi, A.; Takigawa, Y.; Higashi, K.; Tatsumisago, M. Evaluation of Elastic Modulus of Li_2S–P_2S_5 Glassy Solid Electrolyte by Ultrasonic Sound Velocity Measurement and Compression Test. *J. Ceram. Soc. Jpn.* **2013**, *121* (1419), 946–949. https://doi.org/10.2109/jcersj2.121.946.

(15) Wang, C.; Fu, K.; Kammampata, S. P.; McOwen, D. W.; Samson, A. J.; Zhang, L.; Hitz, G. T.; Nolan, A. M.; Wachsman, E. D.; Mo, Y.; Thangadurai, V.; Hu, L. Garnet-Type Solid-State Electrolytes: Materials, Interfaces, and Batteries. *Chem. Rev.* **2020**, *120* (10), 4257–4300. https://doi.org/10.1021/acs.chemrev.9b00427.

(16) Reddy, M. V.; Julien, C. M.; Mauger, A.; Zaghib, K. Sulfide and Oxide Inorganic Solid Electrolytes for All-Solid-State Li Batteries: A Review. *Nanomaterials* **2020**, *10* (8), 1606. https://doi.org/10.3390/nano10081606.

(17) Wright, P. V. Electrical Conductivity in Ionic Complexes of Poly(Ethylene Oxide). *Br. Polym. J.* **1975**, *7* (5), 319–327. https://doi.org/10.1002/pi.4980070505.

(18) Armand, M. The History of Polymer Electrolytes. *Solid State Ion.* **1994**, *69* (3–4), 309–319. https://doi.org/10.1016/0167-2738(94)90419-7.

(19) Johansson, P. First Principles Modelling of Amorphous Polymer Electrolytes: Li+–PEO, Li+–PEI, and Li+–PES Complexes. *Polymer* **2001**, *42* (9), 4367–4373. https://doi.org/10.1016/S0032-3861(00)00731-X.

(20) Borodin, O.; Smith, G. D. Mechanism of Ion Transport in Amorphous Poly(Ethylene Oxide)/LiTFSI from Molecular Dynamics Simulations. *Macromolecules* **2006**, *39* (4), 1620–1629. https://doi.org/10.1021/ma052277v.

(21) Bresser, D.; Passerini, S.; Scrosati, B. Recent Progress and Remaining Challenges in Sulfur-Based Lithium Secondary Batteries – a Review. *Chem. Commun.* **2013**, *49* (90), 10545. https://doi.org/10.1039/c3cc46131a.

(22) Zhu, P.; Yan, C.; Dirican, M.; Zhu, J.; Zang, J.; Selvan, R. K.; Chung, C.-C.; Jia, H.; Li, Y.; Kiyak, Y.; Wu, N.; Zhang, X. Li $_{0.33}$ La $_{0.557}$ TiO $_3$ Ceramic Nanofiber-Enhanced

Polyethylene Oxide-Based Composite Polymer Electrolytes for All-Solid-State Lithium Batteries. *J. Mater. Chem. A* **2018**, *6* (10), 4279–4285. https://doi.org/10.1039/C7TA10517G.

(23) Meyer, W. H. Polymer Electrolytes for Lithium-Ion Batteries. *Adv. Mater.* **1998**, *10* (6), 439–448. https://doi.org/10.1002/(SICI)1521-4095(199804)10:6<439::AID-ADMA439>3.0.CO;2-I.

(24) Shi, J.; Vincent, C. The Effect of Molecular Weight on Cation Mobility in Polymer Electrolytes. *Solid State Ion.* **1993**, *60* (1–3), 11–17. https://doi.org/10.1016/0167-2738(93)90268-8.

(25) Niitani, T.; Shimada, M.; Kawamura, K.; Kanamura, K. Characteristics of New-Type Solid Polymer Electrolyte Controlling Nano-Structure. *J. Power Sources* **2005**, *146* (1–2), 386–390. https://doi.org/10.1016/j.jpowsour.2005.03.102.

(26) Devaux, D.; Bouchet, R.; Glé, D.; Denoyel, R. Mechanism of Ion Transport in PEO/LiTFSI Complexes: Effect of Temperature, Molecular Weight and End Groups. *Solid State Ion.* **2012**, *227*, 119–127. https://doi.org/10.1016/j.ssi.2012.09.020.

(27) Maurel, A.; Armand, M.; Grugeon, S.; Fleutot, B.; Davoisne, C.; Tortajada, H.; Courty, M.; Panier, S.; Dupont, L. Poly(Ethylene Oxide)−LiTFSI Solid Polymer Electrolyte Filaments for Fused Deposition Modeling Three-Dimensional Printing. *J. Electrochem. Soc.* **2020**, *167* (7), 070536. https://doi.org/10.1149/1945-7111/ab7c38.

(28) Lascaud, S.; Perrier, M.; Armand, M.; Prud'homme, J.; Kapfer, B.; Vallée, A.; Gauthier, M. Evidence for Ion Pairs and/or Triple Ions from Transport Measurements in Mixed-Alkali Polyether Electrolytes. *Electrochimica Acta* **1998**, *43* (10–11), 1407–1414. https://doi.org/10.1016/S0013-4686(97)10076-7.

(29) Appetecchi, G. B.; Scrosati, B. A Lithium Ion Polymer Battery. *Electrochimica Acta* **1998**, *43* (9), 1105–1107. https://doi.org/10.1016/S0013-4686(97)10117-7.

(30) Quartarone, E.; Tomasi, C.; Mustarelli, P.; Appetecchi, G. B.; Croce, F. Long-Term Structural Stability of PMMA-Based Gel Polymer Electrolytes. *Electrochimica Acta* **1998**, *43* (10–11), 1435–1439. https://doi.org/10.1016/S0013-4686(97)10080-9.

(31) Appetecchi, G. B.; Croce, F.; Scrosati, B. Kinetics and Stability of the Lithium Electrode in Poly(Methylmethacrylate)-Based Gel Electrolytes. *Electrochimica Acta* **1995**, *40* (8), 991–997. https://doi.org/10.1016/0013-4686(94)00345-2.

(32) Judez, X.; Zhang, H.; Li, C.; Eshetu, G. G.; González-Marcos, J. A.; Armand, M.; Rodriguez-Martinez, L. M. Review—Solid Electrolytes for Safe and High Energy Density

Lithium-Sulfur Batteries: Promises and Challenges. *J. Electrochem. Soc.* **2018**, *165* (1), A6008–A6016. https://doi.org/10.1149/2.0041801jes.

(33) Hu, P.; Chai, J.; Duan, Y.; Liu, Z.; Cui, G.; Chen, L. Progress in Nitrile-Based Polymer Electrolytes for High Performance Lithium Batteries. *J. Mater. Chem. A* **2016**, *4* (26), 10070–10083. https://doi.org/10.1039/C6TA02907H.

(34) Rajendran, S.; Mahendran, O.; Kannan, R. Characterisation of [(1 2 x)PMMA±xPVdF] Polymer Blend Electrolyte with Li1 Ionq. **2002**.

(35) Manuel Stephan, A. Review on Gel Polymer Electrolytes for Lithium Batteries. *Eur. Polym. J.* **2006**, *42* (1), 21–42. https://doi.org/10.1016/j.eurpolymj.2005.09.017.

(36) Zhang, H.; Liu, C.; Zheng, L.; Xu, F.; Feng, W.; Li, H.; Huang, X.; Armand, M.; Nie, J.; Zhou, Z. Lithium Bis(Fluorosulfonyl)Imide/Poly(Ethylene Oxide) Polymer Electrolyte. *Electrochimica Acta* **2014**, *133*, 529–538. https://doi.org/10.1016/j.electacta.2014.04.099.

(37) Appetecchi, G. B.; Zane, D.; Scrosati, B. PEO-Based Electrolyte Membranes Based on LiBC4O8 Salt. *J. Electrochem. Soc.*

(38) Vallée, A.; Besner, S.; Prud'Homme, J. Comparative Study of Poly(Ethylene Oxide) Electrolytes Made with LiN(CF3SO2)2, LiCF3SO3 and LiClO4: Thermal Properties and Conductivity Behaviour. *Electrochimica Acta* **1992**, *37* (9), 1579–1583. https://doi.org/10.1016/0013-4686(92)80115-3.

(39) Pożyczka, K.; Marzantowicz, M.; Dygas, J. R.; Krok, F. IONIC CONDUCTIVITY AND LITHIUM TRANSFERENCE NUMBER OF POLY(ETHYLENE OXIDE):LiTFSI SYSTEM. *Electrochimica Acta* **2017**, *227*, 127–135. https://doi.org/10.1016/j.electacta.2016.12.172.

(40) Olivetti, E. A.; Kim, J. H.; Sadoway, D. R.; Asatekin, A.; Mayes, A. M. Sol−Gel Synthesis of Vanadium Oxide within a Block Copolymer Matrix. *Chem. Mater.* **2006**, *18* (12), 2828–2833. https://doi.org/10.1021/cm060119s.

(41) Yuan, F.; Chen, H.-Z.; Yang, H.-Y.; Li, H.-Y.; Wang, M. PAN–PEO Solid Polymer Electrolytes with High Ionic Conductivity. *Mater. Chem. Phys.* **2005**, *89* (2–3), 390–394. https://doi.org/10.1016/j.matchemphys.2004.09.032.

(42) Seo, J. A.; Koh, J. K.; Lee, K. B.; Kang, S. W.; Kim, J. H. Poly(Oxyethylene Methacrylate)–Poly(4-Vinyl Pyridine) Comb-like Polymer Electrolytes for Solid-State Dye-Sensitized Solar Cells. *J. Solid State Electrochem.* **2012**, *16* (2), 513–520. https://doi.org/10.1007/s10008-011-1360-5.

(43) Teran, A. A.; Balsara, N. P. Thermodynamics of Block Copolymers with and without Salt. *J. Phys. Chem. B* **2014**, *118* (1), 4–17. https://doi.org/10.1021/jp408079z.

(44) Panday, A.; Mullin, S.; Gomez, E. D.; Wanakule, N.; Chen, V. L.; Hexemer, A.; Pople, J.; Balsara, N. P. Effect of Molecular Weight and Salt Concentration on Conductivity of Block Copolymer Electrolytes. *Macromolecules* **2009**, *42* (13), 4632–4637. https://doi.org/10.1021/ma900451e.

(45) Chintapalli, M.; Chen, X. C.; Thelen, J. L.; Teran, A. A.; Wang, X.; Garetz, B. A.; Balsara, N. P. Effect of Grain Size on the Ionic Conductivity of a Block Copolymer Electrolyte. *Macromolecules* **2014**, *47* (15), 5424–5431. https://doi.org/10.1021/ma501202c.

(46) Schauser, N. S.; Harry, K. J.; Parkinson, D. Y.; Watanabe, H.; Balsara, N. P. Lithium Dendrite Growth in Glassy and Rubbery Nanostructured Block Copolymer Electrolytes. *J. Electrochem. Soc.* **2015**, *162* (3), A398–A405. https://doi.org/10.1149/2.0511503jes.

(47) Devaux, D.; Glé, D.; Phan, T. N. T.; Gigmes, D.; Giroud, E.; Deschamps, M.; Denoyel, R.; Bouchet, R. Optimization of Block Copolymer Electrolytes for Lithium Metal Batteries. *Chem. Mater.* **2015**, *27* (13), 4682–4692. https://doi.org/10.1021/acs.chemmater.5b01273.

(48) Young, W.-S.; Epps, T. H. Ionic Conductivities of Block Copolymer Electrolytes with Various Conducting Pathways: Sample Preparation and Processing Considerations. *Macromolecules* **2012**, *45* (11), 4689–4697. https://doi.org/10.1021/ma300362f.

(49) Carvalho, L. M. Variation of the Mesh Size of PEO-Based Networks ®lled with TFSILi: From an Arrhenius to WLF Type Conductivity Behavior. *Eur. Polym. J.* **2000**.

(50) Zeng, X.-X.; Yin, Y.-X.; Li, N.-W.; Du, W.-C.; Guo, Y.-G.; Wan, L.-J. Reshaping Lithium Plating/Stripping Behavior via Bifunctional Polymer Electrolyte for Room-Temperature Solid Li Metal Batteries. *J. Am. Chem. Soc.* **2016**, *138* (49), 15825–15828. https://doi.org/10.1021/jacs.6b10088.

(51) Zhang, Y.; Lu, W.; Cong, L.; Liu, J.; Sun, L.; Mauger, A.; Julien, C. M.; Xie, H.; Liu, J. Cross-Linking Network Based on Poly(Ethylene Oxide): Solid Polymer Electrolyte for Room Temperature Lithium Battery. *J. Power Sources* **2019**, *420*, 63–72. https://doi.org/10.1016/j.jpowsour.2019.02.090.

(52) Diederichsen, K. M.; McShane, E. J.; McCloskey, B. D. Promising Routes to a High Li^+ Transference Number Electrolyte for Lithium Ion Batteries. *ACS Energy Lett.* **2017**, *2* (11), 2563–2575. https://doi.org/10.1021/acsenergylett.7b00792.

(53) Ford, H. O.; Park, B.; Jiang, J.; Seidler, M. E.; Schaefer, J. L. Enhanced Li^+ Conduction within Single-Ion Conducting Polymer Gel Electrolytes via Reduced Cation–Polymer

Interaction. *ACS Mater. Lett.* **2020**, *2* (3), 272–279. https://doi.org/10.1021/acsmaterialslett.9b00510.

(54) Bouchet, R.; Maria, S.; Meziane, R.; Aboulaich, A.; Lienafa, L.; Bonnet, J.-P.; Phan, T. N. T.; Bertin, D.; Gigmes, D.; Devaux, D.; Denoyel, R.; Armand, M. Single-Ion BAB Triblock Copolymers as Highly Efficient Electrolytes for Lithium-Metal Batteries. *Nat. Mater.* **2013**, *12* (5), 452–457. https://doi.org/10.1038/nmat3602.

(55) Porcarelli, L.; Shaplov, A. S.; Bella, F.; Nair, J. R.; Mecerreyes, D.; Gerbaldi, C. Single-Ion Conducting Polymer Electrolytes for Lithium Metal Polymer Batteries That Operate at Ambient Temperature. *ACS Energy Lett.* **2016**, *1* (4), 678–682. https://doi.org/10.1021/acsenergylett.6b00216.

(56) Bachman, J. C.; Muy, S.; Grimaud, A.; Chang, H.-H.; Pour, N.; Lux, S. F.; Paschos, O.; Maglia, F.; Lupart, S.; Lamp, P.; Giordano, L.; Shao-Horn, Y. Inorganic Solid-State Electrolytes for Lithium Batteries: Mechanisms and Properties Governing Ion Conduction. *Chem. Rev.* **2016**, *116* (1), 140–162. https://doi.org/10.1021/acs.chemrev.5b00563.

(57) Boaretto, N.; Garbayo, I.; Valiyaveettil-SobhanRaj, S.; Quintela, A.; Li, C.; Casas-Cabanas, M.; Aguesse, F. Lithium Solid-State Batteries: State-of-the-Art and Challenges for Materials, Interfaces and Processing. *J. Power Sources* **2021**, *502*, 229919. https://doi.org/10.1016/j.jpowsour.2021.229919.

(58) Kamaya, N.; Homma, K.; Yamakawa, Y.; Hirayama, M.; Kanno, R.; Yonemura, M.; Kamiyama, T.; Kato, Y.; Hama, S.; Kawamoto, K.; Mitsui, A. A Lithium Superionic Conductor. *Nat. Mater.* **2011**, *10* (9), 682–686. https://doi.org/10.1038/nmat3066.

(59) Han, F.; Zhu, Y.; He, X.; Mo, Y.; Wang, C. Electrochemical Stability of $Li_{10}GeP_2S_{12}$ and $Li_7La_3Zr_2O_{12}$ Solid Electrolytes. *Adv. Energy Mater.* **2016**, *6* (8), 1501590. https://doi.org/10.1002/aenm.201501590.

(60) Deiseroth, H.-J.; Kong, S.-T.; Eckert, H.; Vannahme, J.; Reiner, C.; Zaiß, T.; Schlosser, M. Li6PS5X: A Class of Crystalline Li-Rich Solids With an Unusually High Li+ Mobility. *Angew. Chem. Int. Ed.* **2008**, *47* (4), 755–758. https://doi.org/10.1002/anie.200703900.

(61) Boulineau, S.; Courty, M.; Tarascon, J.-M.; Viallet, V. Mechanochemical Synthesis of Li-Argyrodite Li6PS5X (X=Cl, Br, I) as Sulfur-Based Solid Electrolytes for All Solid State Batteries Application. *Solid State Ion.* **2012**, *221*, 1–5. https://doi.org/10.1016/j.ssi.2012.06.008.

(62) Cai, Y.; Li, C.; Zhao, Z.; Mu, D.; Wu, B. Air Stability and Interfacial Compatibility of Sulfide Solid Electrolytes for Solid-State Lithium Batteries: Advances and Perspectives. *ChemElectroChem* **2022**, *9* (5), e202101479. https://doi.org/10.1002/celc.202101479.

(63) Goodenough, J. B.; Hong, H. Y.-P.; Kafalas, J. A. Fast Na+-Ion Transport in Skeleton Structures. *Mater. Res. Bull.* **1976**, *11* (2), 203–220. https://doi.org/10.1016/0025-5408(76)90077-5.

(64) Thokchom, J. S.; Gupta, N.; Kumar, B. Superionic Conductivity in a Lithium Aluminum Germanium Phosphate Glass–Ceramic. *J. Electrochem. Soc.* **2008**, *155* (12), A915. https://doi.org/10.1149/1.2988731.

(65) Cruz, A. M.; Ferreira, E. B.; Rodrigues, A. C. M. Controlled Crystallization and Ionic Conductivity of a Nanostructured LiAlGePO4 Glass–Ceramic. *J. Non-Cryst. Solids* **2009**, *355* (45–47), 2295–2301. https://doi.org/10.1016/j.jnoncrysol.2009.07.012.

(66) Harada, Y.; Ishigaki, T.; Kawai, H.; Kuwano, J. Lithium Ion Conductivity of Polycrystalline Perovskite La0.672xLi3xTiO3 with Ordered and Disordered Arrangements of the A-Site Ions. *Solid State Ion.* **1998**.

(67) Xu, L.; Feng, T.; Huang, J.; Hu, Y.; Zhang, L.; Luo, L. Structural Heterogeneity Induced Li Dendrite Growth in $Li_{0.33}La_{0.56}TiO_3$ Solid-State Electrolytes. *ACS Appl. Energy Mater.* **2022**, *5* (3), 3741–3747. https://doi.org/10.1021/acsaem.2c00181.

(68) Thangadurai, V.; Narayanan, S.; Pinzaru, D. Garnet-Type Solid-State Fast Li Ion Conductors for Li Batteries: Critical Review. *Chem. Soc. Rev.* **2014**, *43* (13), 4714. https://doi.org/10.1039/c4cs00020j.

(69) Chen, X.; Vereecken, P. M. Solid and Solid-Like Composite Electrolyte for Lithium Ion Batteries: Engineering the Ion Conductivity at Interfaces. *Adv. Mater. Interfaces* **2019**, *6* (1), 1800899. https://doi.org/10.1002/admi.201800899.

(70) Murugan, R.; Thangadurai, V.; Weppner, W. Fast Lithium Ion Conduction in Garnet-Type Li7La3Zr2O12. *Angew. Chem. Int. Ed.* **2007**, *46* (41), 7778–7781. https://doi.org/10.1002/anie.200701144.

(71) Bernstein, N.; Johannes, M. D.; Hoang, K. Origin of the Structural Phase Transition in Li 7 La 3 Zr 2 O 12. *Phys. Rev. Lett.* **2012**, *109* (20), 205702. https://doi.org/10.1103/PhysRevLett.109.205702.

(72) Cao, S.; Song, S.; Xiang, X.; Hu, Q.; Zhang, C.; Xia, Z.; Xu, Y.; Zha, W.; Li, J.; Gonzale, P. M.; Han, Y.-H.; Chen, F. Modeling, Preparation, and Elemental Doping of Li7La3Zr2O12

Garnet-Type Solid Electrolytes: A Review. *J. Korean Ceram. Soc.* **2019**, *56* (2), 111–129. https://doi.org/10.4191/kcers.2019.56.2.01.

(73) Raju, M. M.; Altayran, F.; Johnson, M.; Wang, D.; Zhang, Q. Crystal Structure and Preparation of Li7La3Zr2O12 (LLZO) Solid-State Electrolyte and Doping Impacts on the Conductivity: An Overview. *Electrochem* **2021**, *2* (3), 390–414. https://doi.org/10.3390/electrochem2030026.

(74) Liu, K.; Ma, J.-T.; Wang, C.-A. Excess Lithium Salt Functions More than Compensating for Lithium Loss When Synthesizing Li6.5La3Ta0.5Zr1.5O12 in Alumina Crucible. *J. Power Sources* **2014**, *260*, 109–114. https://doi.org/10.1016/j.jpowsour.2014.02.065.

(75) Rangasamy, E.; Wolfenstine, J.; Sakamoto, J. The Role of Al and Li Concentration on the Formation of Cubic Garnet Solid Electrolyte of Nominal Composition Li7La3Zr2O12. *Solid State Ion.* **2012**, *206*, 28–32. https://doi.org/10.1016/j.ssi.2011.10.022.

(76) Shimonishi, Y.; Toda, A.; Zhang, T.; Hirano, A.; Imanishi, N.; Yamamoto, O.; Takeda, Y. Synthesis of Garnet-Type Li7−xLa3Zr2O12−1/2x and Its Stability in Aqueous Solutions. *Solid State Ion.* **2011**, *183* (1), 48–53. https://doi.org/10.1016/j.ssi.2010.12.010.

(77) Jin, Y.; McGinn, P. J. Al-Doped Li7La3Zr2O12 Synthesized by a Polymerized Complex Method. *J. Power Sources* **2011**, *196* (20), 8683–8687. https://doi.org/10.1016/j.jpowsour.2011.05.065.

(78) Janani, N.; Deviannapoorani, C.; Dhivya, L.; Murugan, R. Influence of Sintering Additives on Densification and Li $^{+}$ Conductivity of Al Doped Li $_{7}$ La $_{3}$ Zr $_{2}$ O $_{12}$ Lithium Garnet. *RSC Adv* **2014**, *4* (93), 51228–51238. https://doi.org/10.1039/C4RA08674K.

(79) Yao, P.; Yu, H.; Ding, Z.; Liu, Y.; Lu, J.; Lavorgna, M.; Wu, J.; Liu, X. Review on Polymer-Based Composite Electrolytes for Lithium Batteries. *Front. Chem.* **2019**, *7*, 522. https://doi.org/10.3389/fchem.2019.00522.

(80) Weston, J.; Steele, B. Effects of Inert Fillers on the Mechanical and Electrochemical Properties of Lithium Salt-Poly(Ethylene Oxide) Polymer Electrolytes. *Solid State Ion.* **1982**, *7* (1), 75–79. https://doi.org/10.1016/0167-2738(82)90072-8.

(81) Croce, F.; Curini, R.; Martinelli, A.; Persi, L.; Ronci, F.; Scrosati, B.; Caminiti, R. Physical and Chemical Properties of Nanocomposite Polymer Electrolytes. *J. Phys. Chem. B* **1999**, *103* (48), 10632–10638. https://doi.org/10.1021/jp992307u.

(82) Strauss, E.; Golodnitsky, D.; Ardel, G.; Peled, E. Charge and Mass Transport Properties of LiI-P(EO)n-Al2O3-Based Composite Polymer Electrolytes. *Electrochimica Acta* **1998**, *43* (10–11), 1315–1320. https://doi.org/10.1016/S0013-4686(97)10036-6.

(83) Shin, J. H.; Kim, K. W.; Ahn, H. J.; Ahn, J. H. Electrochemical Properties and Interfacial Stability of (PEO)10LiCF3SO3Á/TinO2n(1 Composite Polymer Electrolytes for Lithium/Sulfur Battery. *Mater. Sci. Eng. B* **2002**.

(84) Ji, K.-S.; Moon, H.-S.; Kim, J.-W.; Park, J.-W. Role of Functional Nano-Sized Inorganic Fillers in Poly(Ethylene) Oxide-Based Polymer Electrolytes. *J. Power Sources* **2003**, *117* (1–2), 124–130. https://doi.org/10.1016/S0378-7753(03)00159-9.

(85) Wang, W.; Yi, E.; Fici, A. J.; Laine, R. M.; Kieffer, J. Lithium Ion Conducting Poly(Ethylene Oxide)-Based Solid Electrolytes Containing Active or Passive Ceramic Nanoparticles. *J. Phys. Chem. C* **2017**, *121* (5), 2563–2573. https://doi.org/10.1021/acs.jpcc.6b11136.

(86) Li, J.; Zhu, K.; Yao, Z.; Qian, G.; Zhang, J.; Yan, K.; Wang, J. A Promising Composite Solid Electrolyte Incorporating LLZO into PEO/PVDF Matrix for All-Solid-State Lithium-Ion Batteries. *Ionics* **2020**, *26* (3), 1101–1108. https://doi.org/10.1007/s11581-019-03320-x.

(87) Liang, J.; Luo, J.; Sun, Q.; Yang, X.; Li, R.; Sun, X. Recent Progress on Solid-State Hybrid Electrolytes for Solid-State Lithium Batteries. *Energy Storage Mater.* **2019**, *21*, 308–334. https://doi.org/10.1016/j.ensm.2019.06.021.

(88) Chen, F.; Yang, D.; Zha, W.; Zhu, B.; Zhang, Y.; Li, J.; Gu, Y.; Shen, Q.; Zhang, L.; Sadoway, D. R. Solid Polymer Electrolytes Incorporating Cubic Li7La3Zr2O12 for All-Solid-State Lithium Rechargeable Batteries. *Electrochimica Acta* **2017**, *258*, 1106–1114. https://doi.org/10.1016/j.electacta.2017.11.164.

(89) Choi, J.-H.; Lee, C.-H.; Yu, J.-H.; Doh, C.-H.; Lee, S.-M. Enhancement of Ionic Conductivity of Composite Membranes for All-Solid-State Lithium Rechargeable Batteries Incorporating Tetragonal Li7La3Zr2O12 into a Polyethylene Oxide Matrix. *J. Power Sources* **2015**, *274*, 458–463. https://doi.org/10.1016/j.jpowsour.2014.10.078.

(90) Fu, K. (Kelvin); Gong, Y.; Dai, J.; Gong, A.; Han, X.; Yao, Y.; Wang, C.; Wang, Y.; Chen, Y.; Yan, C.; Li, Y.; Wachsman, E. D.; Hu, L. Flexible, Solid-State, Ion-Conducting Membrane with 3D Garnet Nanofiber Networks for Lithium Batteries. *Proc. Natl. Acad. Sci.* **2016**, *113* (26), 7094–7099. https://doi.org/10.1073/pnas.1600422113.

(91) Guo, Z.; Pang, Y.; Xia, S.; Xu, F.; Yang, J.; Sun, L.; Zheng, S. Uniform and Anisotropic Solid Electrolyte Membrane Enables Superior Solid-State Li Metal Batteries. *Adv. Sci.* **2021**, *8* (16), 2100899. https://doi.org/10.1002/advs.202100899.

(92) Guo, J.; Guo, H.; Baker, A. L.; Lanagan, M. T.; Kupp, E. R.; Messing, G. L.; Randall, C. A. Cold Sintering: A Paradigm Shift for Processing and Integration of Ceramics. *Angew. Chem. Int. Ed.* **2016**, *55* (38), 11457–11461. https://doi.org/10.1002/anie.201605443.

(93) Zagórski, J.; López del Amo, J. M.; Cordill, M. J.; Aguesse, F.; Buannic, L.; Llordés, A. Garnet–Polymer Composite Electrolytes: New Insights on Local Li-Ion Dynamics and Electrodeposition Stability with Li Metal Anodes. *ACS Appl. Energy Mater.* **2019**, *2* (3), 1734–1746. https://doi.org/10.1021/acsaem.8b01850.

(94) Yu, S.; Xu, Q.; Lu, X.; Liu, Z.; Windmüller, A.; Tsai, C.-L.; Buchheit, A.; Tempel, H.; Kungl, H.; Wiemhöfer, H.-D.; Eichel, R.-A. Single-Ion-Conducting "Polymer-in-Ceramic" Hybrid Electrolyte with an Intertwined NASICON-Type Nanofiber Skeleton. *ACS Appl. Mater. Interfaces* **2021**, *13* (51), 61067–61077. https://doi.org/10.1021/acsami.1c17718.

(95) Lechartier, M.; Porcarelli, L.; Zhu, H.; Forsyth, M.; Guéguen, A.; Castro, L.; Mecerreyes, D. Single-Ion Polymer/LLZO Hybrid Electrolytes with High Lithium Conductivity. *Mater. Adv.* **2022**, *3* (2), 1139–1151. https://doi.org/10.1039/D1MA00857A.

(96) Yang, T.; Zheng, J.; Cheng, Q.; Hu, Y.-Y.; Chan, C. K. Composite Polymer Electrolytes with $Li_7La_3Zr_2O_{12}$ Garnet-Type Nanowires as Ceramic Fillers: Mechanism of Conductivity Enhancement and Role of Doping and Morphology. *ACS Appl. Mater. Interfaces* **2017**, *9* (26), 21773–21780. https://doi.org/10.1021/acsami.7b03806.

(97) Zheng, J.; Tang, M.; Hu, Y.-Y. Lithium Ion Pathway within Li7La3Zr2O12-Polyethylene Oxide Composite Electrolytes. *Angew. Chem.* **2016**, *128* (40), 12726–12730. https://doi.org/10.1002/ange.201607539.

(98) Zheng, J.; Hu, Y.-Y. New Insights into the Compositional Dependence of Li-Ion Transport in Polymer–Ceramic Composite Electrolytes. *ACS Appl. Mater. Interfaces* **2018**, *10* (4), 4113–4120. https://doi.org/10.1021/acsami.7b17301.

(99) Gupta, A.; Sakamoto, J. Controlling Ionic Transport through the PEO-LiTFSI/LLZTO Interface. *Electrochem. Soc. Interface* **2019**, *28* (2), 63–69. https://doi.org/10.1149/2.F06192if.

(100) Langer, F.; Palagonia, M. S.; Bardenhagen, I.; Glenneberg, J.; La Mantia, F.; Kun, R. Impedance Spectroscopy Analysis of the Lithium Ion Transport through the $Li_7La_3Zr_2O_{12}$/$P(EO)_{20}Li$ Interface. *J. Electrochem. Soc.* **2017**, *164* (12), A2298–A2303. https://doi.org/10.1149/2.0381712jes.

(101) Kuhnert, E.; Ladenstein, L.; Jodlbauer, A.; Slugovc, C.; Trimmel, G.; Wilkening, H. M. R.; Rettenwander, D. Lowering the Interfacial Resistance in Li6.4La3Zr1.4Ta0.6O12|Poly(Ethylene Oxide) Composite Electrolytes. *Cell Rep. Phys. Sci.* **2020**, *1* (10), 100214. https://doi.org/10.1016/j.xcrp.2020.100214.

Chapter II.

Correlation between Ionic and Mechanical Properties of Solid PEO Polymer Electrolyte

Buildings points:

- Designing PEO networks through a straightforward and solvent-free copolymerization process
- Understanding the correlation between storage modulus, glass transition temperature, and ionic conductivity
- Determining the transport number using electrochemical (Bruce-Vincent) method and diffusion coefficient measurement (NMR)
- Investigation and comparison of electrochemical properties between networks with Li-salt and Li-monomer

Résumé

L'étude des électrolytes solides polymères à base de poly(éthylène oxide) pour les batteries tout solide est très prometteuse et suscite de nombreuses recherches. Les électrolytes polymères présentent l'avantage d'être facilement mis en forme et transposables aux procédés de fabrication actuels des batteries Li-ion. Malheureusement, les conductivités à température ambiante restent limitées (10^{-6} – 10^{-9} S.cm^{-1}). De plus, les électrolytes à base de PEO présentent des nombres de transport faibles (t^+ ~ 0,3). Bien qu'à des températures plus élevées (> 60°C), ces électrolytes montrent des conductivités acceptables (~ 10^{-3} S.cm^{-1}), cela entraîne une dégradation des propriétés mécaniques. Une des solutions pour atténuer cette perte mécanique consiste à utiliser des polymères réticulés plutôt que des polymères linéaires.

Ce chapitre présente la synthèse et la caractérisation d'une série de réseau PEO, dans l'un des cas contenant un sel de Li, et dans l'autre, un monomère de Li dont le contre-anion peut être greffé aux chaînes de PEO. La synthèse de ces réseaux a été réalisée en utilisant deux précurseurs polymères liquides et commerciaux, ce qui a permis d'effectuer une copolymérisation sans solvant et d'obtenir un réseau amorphe. Ceci permet de s'affranchir des problèmes de cristallinité causant généralement la chute de la conductivité ionique à température ambiante. Pour confirmer le greffage de l'anion aux chaînes PEO, la mesure de la fraction soluble a été employée. Les analyses des propriétés mécaniques et thermiques ont démontré l'homogénéité des membranes polymères.

Une étude portant sur l'impact de la densité de réticulation sur la température de transition vitreuse (T_g), le module de stockage (E') ainsi que sur la conductivité ionique a révélé une corrélation entre ces trois paramètres. Lorsque la densité de réticulation augmente, une diminution de la conductivité ionique est observée, accompagnée d'une hausse de la T_g et de E'. Cela confirme le rôle de la mobilité des chaînes PEO. De manière intéressante, la valeur unitaire de 1 a été mesurée pour le nombre de transport selon deux méthodes (électrochimique et mesure des coefficients de diffusion) pour le réseau contenant l'anion greffé. De plus, sa stabilité électrochimique a été repoussée à des valeurs de potentiel élevé (6 V) ouvrant ainsi la possibilité d'utiliser ces polymères dans la formulation de cathode à haut potentiel. Cependant, la conductivité de ce réseau demeure insuffisante (10^{-7} S.cm^{-1}). Par conséquence, il est nécessaire d'améliorer la chimie de réticulation afin de réduire le module de stockage et d'augmenter la conductivité ionique.

Correlation between Ionic and Mechanical Properties of Solid PEO Polymer Electrolyte

The article was submitted to ACS Applied Materials & Interfaces and is under revision.

Abstract

Poly(ethylene oxide) (PEO) networks with or without anionic bis(trifluoromethanesulfonyl)imide (TFSI) grafted groups are promising electrolytes for Li-metal all solid-state batteries. However, the current state of knowledge about the physico-chemical characteristics of the polymer networks needs to improve to achieve both the mechanical and ionic properties required for electrolyte materials of Li batteries. To address this issue, we aim to identify the effect of the crosslinking density of the PEO network and the ethylene oxide/lithium ratio on the mechanical properties (glass transition temperature, storage modulus) and the ionic conductivity. A series of cross-linked PEO polymer (si-SPE for single ion Solid Polymer Electrolyte) was synthesized through a solvent-free radical copolymerization initiated thermally of commercially available lithium 3-[(trifluoromethane)sulfonamidosulfonyl]propyl methacrylate (LiMTFSI), Poly(ethylene glycol)methylether methacrylate (PEGM) and (poly(ethylene glycol) dimethacrylate) (PEGDM). Instead of LiMTFSI as an ionic species, a series of cross-linked PEO polymers (SPE for Solid Polymer Electrolyte) have been synthesized with LiTFSI. Most of the polymer films synthesized are flexible, homogeneous and thermally stable. Interestingly, a correlation between ionic conductivity and mechanical properties was highlighted in both SPE and si-SPE series. Ionic conductivity increases with a decrease of glass transition, α relaxation temperature and storage modulus, attesting that Li^+ transport depends on the polymer chain flexibility and the Li^+/EO interaction.

Keywords

Cross-linked polymer network – Solid Polymer Electrolyte – Single ion conductor – Transport number – Mechanical properties

I. Introduction

Growing demand for portable energy storage urges researchers to improve the storage capacity of the batteries. While Li-ion technology approaches the limit of their capacities, research efforts are devoted to the next generation of Li batteries[1]. Li-metal is an anode of choice thanks to its high theoretical capacity but it suffers from security issues due notably to the formation of dendrites. The latter results from irregular metallic Li electrodeposits induced by, the formation of the solid electrolyte interphase (SEI) layer, coming from the contact of Li-metal with organic liquid electrolyte[2,3]. On the other hand, polymer-based Solid-State Batteries (SSBs) have attracted great attention in recent years due to their enhanced safety over conventional liquid electrolytes in terms of electrolyte leakage, wide operation temperature, and dendrite growth[3–5]. In these systems, the classical polymer electrolyte is based on polyethylene oxide (PEO), due to its excellent capability to dissolve Li-salts, thanks to the complexation of Li^+ with ethylene oxide sites and its interesting ionic conductivity yet at relatively high temperatures (> 60 °C). More specifically, the PEO/lithium bis(trifluoromethanesulfonyl) imide (LiTFSI) system has been widely studied because of the high dissociation and plasticizing capabilities of LiTFSI, that which lead to better ionic conductivities compared to other salts[6,7]. However, the high crystallinity and the low mechanical strength of PEO are still issues to be improved[8]. Specifically, its crystallization at ambient temperature limits its ionic conductivity, due to the reduction of amorphous conductivity pathways caused by the spherulitic growth[9].

Many strategies have been explored to enhance the ionic conductivity of solid polymer electrolytes (SPE) based on PEO (Table II-1).

Among them, adding a plasticizer into the PEO matrix allowed the suppression of its crystallinity as well as decreasing ion-pairing of the Li-salt, increasing ionic mobility. Aprotic organic solvent and low molecular weight PEO have been added to the PEO-LiX matrices. Even though the ionic conductivity value of 10^{-4} S.cm^{-1} has been reached at room temperature, a loss of mechanical properties has also been observed with a liquid plasticizer. On the other hand, while propylene carbonate (PC) and ethylene carbonate improved ionic conductivity but unexpectedly reduced the Li transport number of the plasticized polymer electrolyte[10]. Another strategy encountered is to increase the oxygen ether sites in order to increase the matrix polarity, thus the ionic mobility[11]. Balsara's group has extensively explored this strategy based on the synthesis of poly- (1,3,6-trioxocane) (P(2EO-MO)), a polyether containing two ethylene oxides

and one methylene oxide in their units[11,12]. The ionic conductivity of the resulting SPE with LiTFSI is lower than that the same electrolyte based on PEO, interestingly with an improvement in Li transport number from 0.08 to 0.2. Additionally, by blending the P(2EO-MO) with PEO led to a new matrix for SPE, with however a similar ionic transport property as the conventional PEO matrix with best results solely reporting an ionic conductivity around 10^{-4} $S.cm^{-1}$, even at temperatures as high as 60 °C.

Table II-1. Main characteristics of PEO-based SPEs reported in the literature.

PEO-based polymer matrix	**Additive/ Solvent**	**Ionic conductivity ($S.cm^{-1}$)**	**Electro-chemical windows**	**t^+ Transport number**	**Authors/Ref**
Linear polymer					
PEO Linear	LiTFSI	10^{-3}@60°C		0.15-0.44 @90°C	Devaux and al.[13]
Polymer blend					
PEO-P(2EO-MO)	LiTFSI/ THF	10^{-3} @90°C		0.08 to 0.2 @90°C	Gao and al.[12]
PEO–PFSILi	MeCN	2.10^{-4}@80°C	0-5.5V	0.9	Shi and al.[14]
Phenylsulfonyl(trifluoromethyl-sulfonyl)imide lithium salt / PEO	MeCN/H_2O	2.10^{-4}@90°C		0.90-0.92 @90°C	Nguyen and al.[15]
LiPSsTFSI-PEO	DMF	1.10^{-4}@90°C	0-4.5V	0.91@60°C	Ma and al.[6]
Copolymer					
combPEO	LiTFSI/ $CH_2Cl/MeCN$	10^{-4} @60°C	0-4.5V	0.15@90°C	Devaux and al.[16]
P(STFSILi)-b-PEO-b-P(STFSILi)	Dioxane	1.10^{-5}@60°C	0-6.5V	0.85@90°C	Bouchet and al.[2]
Li[PSTFSI-*co*-MPEGA]	DMF or MeOH	8.10^{-6}@25°C		0.94@60°C	Feng and al.[17]
PS-*b*-P(MALi-*co*-OEGMA)	THF/MeOH	2.10^{-5}@20°C	0-5V	0.84@90°C	Rolland and al.[18]
PEO–PSLiTFSI	DMF	3.10^{-8}@25°C		0.95@90°C	Inceoglu and al.[19]
poly(PEGM)-*b*-poly(LiMTFSI)	DMF	2.10^{-6}@25°C	0-4.5V	0.83@70°C	Porcarelli and al.[20]
PMATFSI-b-PEO-b-PMATFSI	Dioxane	3.10^{-6}@60°C	0-4V	0.8-0.92 @90°C	Devaux and al.[21]
Network					
PEGM-PEGDM	LiTFSI/PC	2.10^{-3}@25°C		0.14@70°C	Lechartier and al.[22]
PEGM-PEGDM-LiMTFSI	PC	1.10^{-4}@25°C	0-5.5V	0.89-0.91 @70°C	Porcarelli and al.[23]
PEGM-PEGDM-LiMTFSI	PC	5.10^{-5}@25°C		0.73@60°C	Lechartier and al.[22]
Lithium poly (bisphenol A borate) / PEO	MeCN	2.10^{-7}@25°C	0-5.5V	0.92@60°C	Zhang and al.[24]
Lithiated mimic neurons in PEGMA	Acetone	1.10^{-4}@25°C		0.974	Li and al.[25]

The design of nanostructured block copolymer electrolytes (BCEs)[2,26–28], generally with PEO blocks, has been proposed to improve the mechanical properties of the SPE, typically at

temperatures higher than the melting temperature of PEO. For instance, Bouchet *et al.*[16] have designed a large number of BCEs based on either 1/ linear polyethylene oxide (PEO) or 2/ combination of PEO as the ionic conductor block, and poly(styrene) as the structural block (combPEO), using LiTFSI as electrolyte. The authors concluded that combPEO blocks allow the suppression of PEO crystallization and mechanical properties of the BCEs depend only on the molecular weight ($M_{n)}$ and the volume fraction of the polystyrene block. Finally, these self-standing BCEs were obtained with a typical ionic conductivity of PEO/LiTFSI systems, ca. 10^{-4} $S.cm^{-1}$ at 60 °C for the optimized design.

To obtain self-standing and highly conducting SPE at room temperature, Mecerreyes *et al.*[23] have reported the synthesis of single-ion conducting polymer electrolyte gel via an in situ radical copolymerization of PEGM and PEGDM in the presence of PC. These self-standing materials showed a combination of high Li transport number (0.86 ± 0.02 at 25 °C) and high ionic conductivity at ambient temperature ($\sigma \approx 10^{-4}$ $S.cm^{-1}$) but required the presence of carbonate solvent.

In these various works, the materials are mainly characterized by their ionic conductivity, often measured at different temperatures, which makes them difficult to compare. Transport numbers are rarely mentioned, as the potential stability range of the materials. Finally, the characterization of the mechanical properties is only very little approached. Thus, the relationships between these different properties are rarely studied.

The present work reports a simple design of SPE combining (i) PEO network for both self-standing characteristics and crystallization suppression with (ii) LiMTFSI monomer for single-ion conducting properties. A systematic investigation on the effects of the crosslinking density of the PEO network and the ethylene oxide/lithium (EO/Li) ratio on the glass transition temperature (T_g), storage modulus (E') and the ionic conductivity of electrolyte materials has been carried out. PEGM and PEGDM were selected as precursors of PEO networks because they are liquid and allow a solvent-free synthesis. The variation of the proportions between the two precursors allows for modifying the crosslinking density. The EO/Li ratio was modulated by dissolving different amounts of methacrylate salts (LiMTFSI) in the PEGDM/PEGM mixtures with which they were then copolymerized to graft the anion on the PEO network. The Li transport numbers and the electrochemical stability window of the most promising samples were then evaluated. All these properties were systematically compared with those of the polymer network with un-grafted anions, synthesized by replacing methacrylate salt with LiTFSI additive.

II. Experimental

II.1. Materials

Poly(ethylene glycol) methyl ether methacrylate (PEGM, Mn = 500 $g.mol^{-1}$, Sigma Aldrich), poly(ethylene glycol) dimethacrylate (PEGDM, Mn=750 $g.mol^{-1}$, Sigma Aldrich) and lithium 3-[(trifluoromethane)sulfonamidosulfonyl]propyl methacrylate (LiMTFSI, Specific Polymer). 2,2′-azobis(2-methylpropionitrile) (AIBN, initiator, 98%, Sigma Aldrich) was recrystallized in methanol before used. Bis(trifluoromethylsulfonyl) amine lithium salt (LiTFSI, > 99%, Sigma Aldrich) and lithium metal (99.9% Sigma Aldrich) were kept in the glove box (H2O < 0.1 ppm).

II.2. Materials synthesis

Single-ion solid polymer electrolyte (si-SPE) synthesis: PEGM, PEGDM and LiMTFSI were introduced in a vial according to the desired proportions (Table II-2) and stirred at room temperatures until LiMTFSI was completely dissolved (2 h). 2% of AIBN was added to the mixture, which was then degassed and flushed with nitrogen until the AIBN was dissolved (2-3 h). The mixture was poured into a mold made with two glass plates separated by a Teflon gasket. The gasket thickness was 125 µm or 500 µm. The molds were then placed in an oven at 70 °C for 2 h and then at 90 °C for 1 h. The resulting polymer membranes were dried under vacuum (10-15 mbar) at 70 °C in a glass oven (BUCHI B-585) for 12 h. The membranes were kept in a glove box (at ambient temperature and H_2O < 0.1 ppm) until their characterization.

SPE-synthesis: PEGM, PEGDM and AIBN were introduced in a vial at the desired quantities (Table II-2). The vial was then placed in a glove box (H_2O < 0.1 ppm) and the required amount of LiTFSI was added to the mixture. The mixture was stirred until the LiTFSI was dissolved (1 h). The SPE membranes were synthesized using the same mold, the same synthesis and storage protocol as those for the si-SPE.

The samples were named respectively si-$SPE_{x.y}$ and $SPE_{x.y}$, where *x* is the LiMTFSI or LiTFSI weight proportion in the material and *y* is the PEGDM weight proportion. The 80:20 PEGM:PEGDM ratio without LiMTFSI or LiTFSI was used as the reference and was noted pristine (Table II-2).

Table II-2.Sample Compositions and main characteristics of $SPE_{x.y}$ and si-$SPE_{x.y}$ polymer electrolyte.

Sample	LiTFSI	LiMTFSI	PEGM	PEGDM	PEGM: PEGDM	[EO]/Li	[Li] (10^{-4} mol/g)	Tg (°C) ± 4°C	Soluble fraction (%wt)	Appearance	Conductivity (S/cm) at 25°C
PRISTINE	-	-	80	20	80:20	-	-	-60	2	flexible	7.10^{-10}
SPE											
$SPE_{5.19}$	5	-	76	19	80:20	99	1.7	-55	5	flexible	$2.10^{-6} \pm 1.10^{-6}$
$SPE_{6.19}$	6	-	75	19	80:20	82	2.1	-54	7	flexible	$5.10^{-6} \pm 1.10^{-6}$
$SPE_{10.18}$	10	-	72	18	80:20	47	3.5	-55	11	flexible	$5.10^{-6} \pm 2.10^{-6}$
$SPE_{18.16}$	18	-	66	16	80:20	24	6.3	-56	21	flexible	$1.10^{-5} \pm 3.10^{-6}$
$SPE_{34.13}$	34	-	53	13	80:20	10	11.8	-42	32	flexible	$3.10^{-6} \pm 1.10^{-6}$
$SPE_{18.0}$	18	-	82	0	100:0	24	6.3	-52	17	gel	2.10^{-5}
$SPE_{18.4}$	18	-	78	4	95:5	24	6.3	-54	16	difficult to handle	$1.10^{-5} \pm 3.10^{-6}$
$SPE_{18.41}$	18	-	41	41	50:50	24	6.3	-40	17	hard	3.10^{-6}
$SPE_{18.82}$	18	-	0	82	0:100	24	6.3	-31	19	hard	2.10^{-7}
si-SPE											
si-$SPE_{5.19}$	-	5	76	19	80:20	119	1.4	-52	2	flexible	$2.10^{-7} \pm 1.10^{-7}$
si-$SPE_{7.19}$	-	7	74	19	80:20	83	2.0	-53	3	flexible	$2.10^{-7} \pm 5.10^{-8}$
si-$SPE_{11.18}$	-	11	71	18	80:20	51	3.2	-50	3	flexible	$2.10^{-7} \pm 1.10^{-7}$
si-$SPE_{21.16}$	-	21	63	16	80:20	24	6.1	-41	2	flexible	$2.10^{-7} \pm 9.10^{-8}$
si-$SPE_{40.12}$	-	40	48	12	80:20	9	11.6	-29	6	flexible	$4.10^{-9} \pm 1.10^{-9}$
si-$SPE_{21.0}$	-	21	79	0	100:0	24	6.1	-40	7	gel	4.10^{-7}
si-$SPE_{21.4}$	-	21	75	4	95:5	24	6.1	-46	2	difficult to handle	4.10^{-7}
si-$SPE_{21.40}$	-	21	39.5	39.5	50:50	24	6.1	-39	1	hard	3.10^{-8}
si-$SPE_{21.48}$	-	21	31.5	47.5	40:60	24	6.1	-33	4	hard	4.10^{-8}
si-$SPE_{21.79}$	-	21	0	79	0:100	24	6.1	-19	2	hard	2.10^{-8}

II.3. Characterization

The soluble fraction of the different materials was quantified by solid/liquid extraction of a known weight (W_0) sample with an automated Soxhlet extractor BUCHI SPEED-EXTRACTOR E-914 and methanol as extraction solvent. For extraction, 3 cycles of 10 min were carried out at 80 °C under 100 bars. After extraction, the samples were dried under vacuum (10-15 mbar) at 60 °C until constant weight and then weighted (W_e). The soluble fraction was calculated as follows:

$$\% \text{ soluble fraction} = \frac{W_0 - W_E}{W_0} * 100 \qquad \text{Equation 1}$$

Differential Scanning Calorimetry (DSC) measurements were performed on a DSC Q20 (TA Instruments). Samples from 10 mg to 20 mg were introduced in an aluminum capsule. They were first cooled to -80 °C and, after an isotherm of 1 min, a temperature ramp was applied (10 °C.min^{-1}) up to 150 °C. Then, an isotherm at 150 °C was applied for 1 min, and the temperature was decreased to -80 °C with a cooling rate of 10 °C.min^{-1}. This cycle was repeated twice. The glass transition temperature (T_g) was measured on the second cycle, with the TA *Universal Analysis* software, by drawing the tangents to the heat flow curve at temperatures above and below the glass transition. The accuracy on T_g is ± 4 °C.

Dynamic mechanical thermal analysis (DMTA) was carried out with a DMA3200 (TA Instruments) operating in tensile mode (strain: 0.05%, pre-tension: 0.01 N). The measurements were typically performed on 10 x 7 x 0.5 mm (length x width x thickness) samples at a frequency of 1 Hz and ranging from -80 °C to 150 °C (after a 1 minute isotherm at -80 °C) with a 3 °C.min^{-1} heating rate. The setup provided the storage and loss moduli (E' and E''). The damping parameter or loss factor (tan δ) was calculated as tan δ = E''/E'. Tα corresponds to the temperature where tan δ is maximum.

Thermogravimetric analysis (TGA) was performed using a NETZSCH STA 409 PC/PG. Samples with an average weight ca. 20 mg were placed in a platinum pan and heated from 30 °C to 900 °C at 10 °C.min^{-1}. Synthetic air with a flow rate of 60 mL.min^{-1} was used as the sweeping gas. The thermal stability of $SPE_{18.16}$ and si-$SPE_{21.16}$ was analyzed by TGA (Figure SI.II-1), they do not exhibit any degradation up to 200 °C which is highly satisfactory for electrolytes.

Electrochemical impedance spectroscopy (EIS) was carried out using a 1260 Solartron FRA device between 10^7 Hz and 10^{-1} Hz, with a perturbation of 100 mV at the open circuit voltage (OCV). The sample was assembled in a Swagelok-type cell using two stainless-steel blocking

electrodes. The contact pressure was maintained with a spring (0.4 MPa). Data quality was evaluated using the Lin-KK Tool. [29–31] The distribution of relaxation time (DRT) analysis was performed using the MATLAB toolbox DRTtools.

To estimate the ionic conductivity of the samples, the intercept of the first semicircle in EIS measurements was considered to correspond to the bulk resistance (R_{bulk}) from which the conductivity was estimated using the following relation:

$$\sigma = \frac{e}{R_{bulk} * S} \qquad \text{Equation 2}$$

where *e* is the thickness and *S* is the surface area of the sample. The measurement was carried out every 10 °C between 20 and 80 °C. The temperature was controlled using an environmental simulation chamber (Memmert). Cells were allowed to reach the thermal equilibrium for at least 1h before each test.

The Li transport number, the stability in potential and stripping plating measurements were carried out on a Bio-logic SP300 with a Swagelok-type cell. All cells were assembled in a glove box under argon (H_2O < 0.1 ppm). A Li-metal/polymer electrolyte/Li-metal cell was assembled and subjected to a 60 mV polarization bias (ΔV) to determine the initial ($i°$) and steady state (i^{∞}) currents. EIS was performed by applying a 100 mV perturbation between 10^6 Hz and 0.1 Hz at the OCV. In addition, the bulk resistance corresponds to the first semi-circle according to the characteristic frequencies. The values are ~ 10^6 Hz for SPE and ~10^4 Hz for si-SPE @ 25 °C (5.10^6 Hz for $SPE_{18,16}$ and 6.10^5 Hz for si-$SPE_{21,16}$ @ 80 °C)[16,21]. The bulk resistance was measured before (R^0_{bulk}) and after (R^{∞}_{bulk}) polarization. t_{Li+} was calculated using the following equation[17]:

$$t_{Li+} = \frac{i^{\infty} * R^{\infty}_{bulk} * (\Delta V - i^0 * R^0_{int})}{i^0 * R^0_{bulk} * (\Delta V - i^{\infty} * R^{\infty}_{int})} \qquad \text{Equation 3}$$

Note that the second cycle at low frequency corresponds to the response of the Li/polymer interface before (R^0_{int}) and after polarization (R^{∞}_{int}), according to their characteristic frequencies (~ few Hz).

Cyclic voltammetry (CV) was used to determine the electrochemical stability window of the solid polymer electrolytes at 70 °C. The electrochemical cell was assembled by sandwiching the block copolymer between the working electrode, and a metal Li foil as a reference and counter electrode, simultaneously. Stainless steel and copper were used as the working electrode during anodic and cathodic stability measurements, respectively. Potential scans were carried out between OCV and 7 V versus Li^+/Li at a constant scan rate of 1 $mV.s^{-1}$ to determine the anodic limit.

Galvanostatic cycling was employed to evaluate the critical current density (CCD). The symmetric cells were assembled in a Swagelok-type cell. The contact pressure of 0.4 MPa was maintained with a spring. First, the CCD value was estimated. To do so, the starting current density was 0.01 $mA.cm^{-2}$ and the current was subsequently increased up to 0.08 $mA.cm^{-2}$. An increase of the current by 0.04 $mA.cm^{-2}$ was selected for each step. The plating and stripping were performed for 1h and separated by a rest period of 5 min, respectively. The measurement was stopped when the potential reached 4.5 V according to the working conditions of the cathode materials. After determining the CCD, the current density was fixed just below the CCD value, i.e. 0.2 $mA.cm^{-2}$ for si-$SPE_{21.16}$ and 0.12 $mA.cm^{-2}$ for $SPE_{18.16}$, for a period of 100 cycles of stripping and plating (200 h) to study the stability of the polymer against Li-metal electrode.

Li and TFSI diffusion coefficients were measured by NMR spectroscopy. Experiments were performed on a Bruker Av^{III} 300 spectrometer, operating at 116.64 MHz for ^{7}Li and 282.38 MHz for ^{19}F, equipped with a 5 mm BBFO probe (z gradient, G_{max}=49.7 $G.cm^{-1}$) or a 5 mm DIFF30 probe (z gradient, G_{max}=1200 $G.cm^{-1}$) associated to a $^{7}Li/^{2}D$ or $^{19}F/^{2}D$ insert. Measurements were made at 84° ± 1 °C on a stripe of polymer electrolytes (~20 x 4 x 0.3 mm^3), introduced in a 5mm standard NMR tube. A pulsed field gradient stimulated spin echo sequence, with bipolar gradients and longitudinal eddy current delay (ledbpgp2s, from the Bruker standard library) was used. The eddy current delay was set to 5ms and a smooth square shape (SMSQ10.100) was chosen for the gradient pulses. From 16 to 32 gradient values were used, ranging from 2% to 90% of the maximum gradient strength. The diffusion delay (D20) and the gradient pulse length (P30) were optimized for each sample and nucleus (^{7}Li or ^{19}F) in order to obtain an echo intensity below 10% at the strongest gradient, except for the ^{19}F measurements on the Si-$SPE_{21.16}$ sample in which TFSI is grafted to the polymer network does not diffuse. Measures were performed with at least two different pairs of parameters (D20 and P30) to ensure reliability. The evolution of the echo intensity (or area) as a function of the gradient strength g was fitted with the standard Stejskal-Tanner formula to determine the diffusion coefficient D[32] :

$$\frac{I}{I_0} = \exp(-D(\gamma\delta g)^2\left(\Delta' - \frac{\delta}{3}\right)) \qquad \text{Equation 4}$$

where I_0 is the echo intensity at zero gradient, γ is the gyromagnetic ratio of the observed nucleus (^{7}Li or ^{19}F), δ the bipolar gradient pulse length (2*P30) and Δ' the corrected diffusion delay (D20+P30/24-D16/2, with D16 being the gradient recovery delay that was set at 0.2 ms).

The longitudinal (T_1) and transverse (T_2) relaxation times were measured with inversion recovery and cpmg pulse sequences, respectively.

III. Results and discussion

III.1. Single-ion solid polymer electrolytes polymer network synthesis

A series of single-ion solid polymer electrolytes (si-SPE) has been synthesized in an one-pot and solvent-free reaction from poly(ethylene glycol) methyl ether methacrylate (PEGM, Mn 500 g.mol^{-1}), lithium 3-[(trifluoromethane)sulfonamidosulfonyl]propyl methacrylate (LiMTFSI) and poly(ethylene glycol) dimethacrylate (PEGDM, Mn 750 g.mol^{-1}), used as crosslinker. Another series of solid polymer electrolytes (SPE) was obtained by replacing LiMTFSI monomer with LiTFSI salt. The free-radical polymerization of the methacrylate function was initiated by 2 wt% of 2,2′-azobis(2-methylpropionitrile) (AIBN) concerning the monomers. A thermal curing of 2 h at 70 °C, followed by a post-curing of 1 h at 90 °C, was then applied.[33]. The synthetic scheme of (single-ion) solid polymer electrolytes is presented in Figure II-1 and their composition as well as their main physico-chemical characteristics are summarized in Table II-2. The obtained materials were self-standing and easy to handle in most cases. Depending on their composition, they change from flexible to hard and up to very brittle (Table II-2).

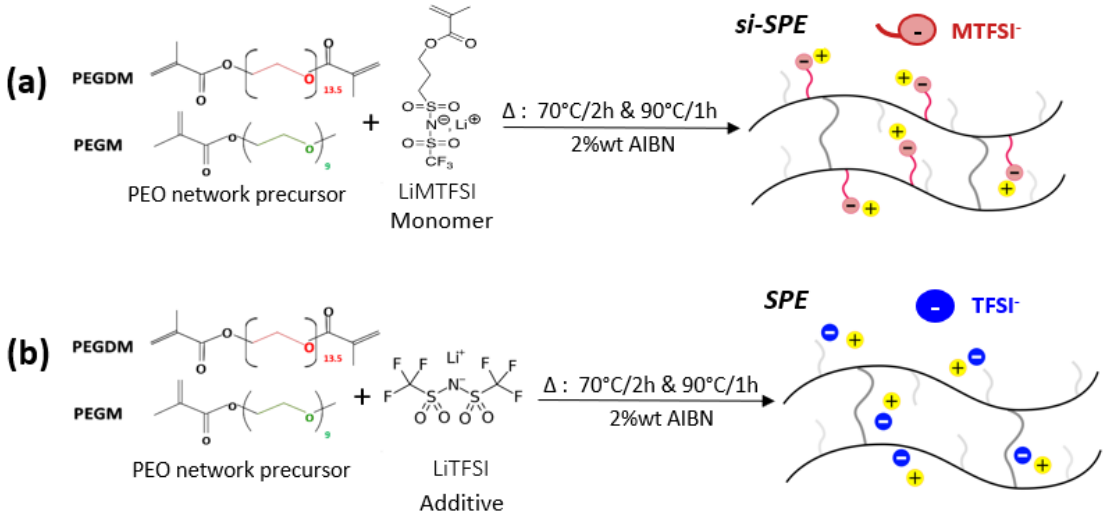

Figure II-1. Synthesis scheme of different (a) single-ion solid polymer electrolyte (si-SPE) and (b) solid polymer electrolyte (SPE).

First, the formation of the polymer networks for SPE and si-SPE samples was verified by the solid/liquid extraction with methanol, which can solubilize all precursors (Figure II-2).

Indeed, if the copolymerization is efficient, only LiTFSI salt can be removed from SPE. The pristine PEGM:PEGDM 80:20 network without Li monomer or Li-salt, contained only 2 wt% of soluble fraction, attesting to the polymer network formation. As expected, the soluble fractions of the SPE samples increase linearly with the weight proportion of LiTFSI salt and they are only slightly higher than the quantity of LiTFSI salt introduced during the synthesis. This result indicates that the addition of LiTFSI into the PEO network precursor does not modify the formation of the PEO network.

On the other hand, the series of si-SPE synthesized from PEGM:PEGDM 80:20 mixture with different contents of LiMTFSI exhibits at most 6 wt% of soluble fraction (Figure II-2), witnessing the efficient copolymerization of the different monomers: the Li-salts monomers (LiMTFSI) are grafted onto the polymer networks.

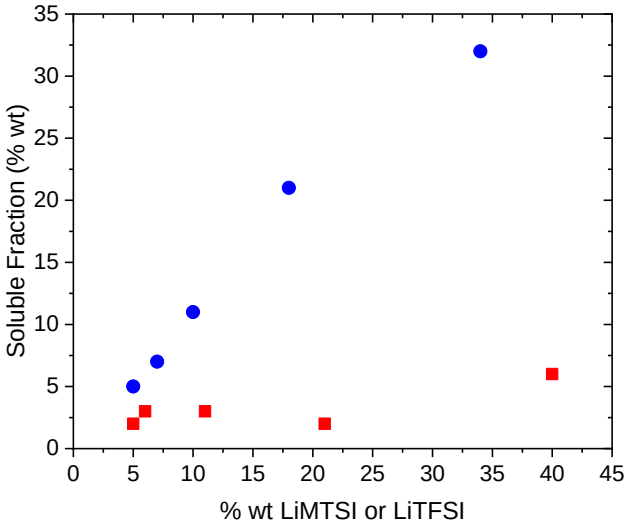

Figure II-2. Soluble fractions si-SPEs (■) and SPEs (●) versus the Li content added in the synthesis while keeping the same weight ratio of PEGM:PEGDM = 80:20.

The copolymerization efficiency was also approved by the absence of polymerization exotherm during the first DSC scan of resulting materials (Figure SI.II-2). Furthermore, the DSC analyses demonstrate the amorphous character of all the synthesized polymers since no crystallization exotherm was detected (Figure SI.II-3). T_g values of the different materials were determined from these DSC thermograms. While the pristine sample exhibits a T_g of -60 °C, the presence of only 5 wt% of Li-salt or Li monomer increases the T_g to -55 or -52 °C, respectively. This increase is linked to the strong interaction of the Li^+ to the PEO chains, as usually reported in the literature[2,34]. This effect is more remarkable with Li monomer, where the T_g reaches -29 °C at 40 wt% of MTFSI. Indeed, in the latter case, not only the interaction

of Li/PEO chains occurs but also the introduction of ionic monomer (MTFSI) within the polymer network rigidifies the network itself, leading to a more pronounced increase in T_g. In addition, the T_g can also be tuned by modulating the weight ratio between the PEGM:PEGDM, thus varying the crosslinking density (Table II-2). Consequently, the T_g can be tuned to -31 °C for SPE and to -19 °C for si-SPE.

III.2. Ionic conduction properties

The Li conductivity of different samples was measured at ambient temperature. The values evolve from 10^{-5} S.cm^{-1} to 10^{-8} S.cm^{-1}, depending on the anionic grafting, the EO/Li ratio, and the cross-linking density. The variation of the Li conductivity was then plotted as a function of T_g and is reported in Figure II-3. It follows a linear variation with T_g, independently to the Li concentration, to the Li source (grafted or un-grafted), and the PEO polymer structure (linear or cross-linked). It should be emphasized that for the conductivity measurements, carried out at 25 °C, the samples are all in the rubbery state since the T_g is lower than -20 °C.

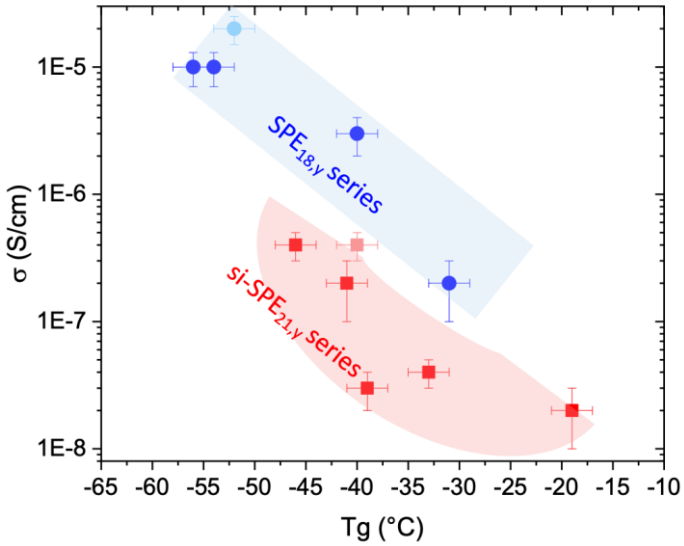

Figure II-3. Ionic conductivity at 25 °C with respect to T_g for $SPE_{18,y}$ series (●) and si-$SPE_{21,y}$ series (■). Linear SPE (●) and linear si-SPE (■) correspond to the samples prepared without PEGDM.

To better understand the dependence of ionic conductivity with T_g, the different parameters (grafting of anionic moiety, cross-linking density, and EO/Li ratio) have been studied separately. First, for a similar T_g, the ionic conductivity is lower by about two orders of magnitude when the anionic moiety is grafted. For example, $SPE_{18.41}$ and si-$SPE_{21.40}$ (T_g around -40 °C) exhibit a conductivity of 3.10^{-6} and 3.10^{-8} S.cm^{-1}, respectively. Second, increasing the cross-linking density (PEGDM proportion) decreases the T_g and induces an important impact

on the ionic conductivity (see si-SPE$_{21.y}$ and SPE$_{18.y}$ series: Figure II-3 and Table II-2). For si-SPE, the highest conductivity value measured at 25 °C is as high as 4 x 10^{-7} S.cm^{-1} and is observed for the sample with the lowest content of cross-linker (si-SPE$_{21.4}$) and thus lowest T_g (-46 °C). Note that the sample without a crosslinker exhibits the same conductivity but with a higher T_g (-40 °C). These results agree with Yu et al.[35] who showed for an electrolyte polymer the lower ionic conductivity is observed for the higher cross-linking agent. Interestingly, introducing more PEGDM increases the crosslink density of the material, which causes an increase of the storage modulus as previously reported in other materials[36]. The medium in which the Li^+ must move becomes more elastic (less viscous). To study this latter parameter, samples containing different proportions of PEGDM were analyzed by DMTA (Figure II-4 and Figure SI.II-4).

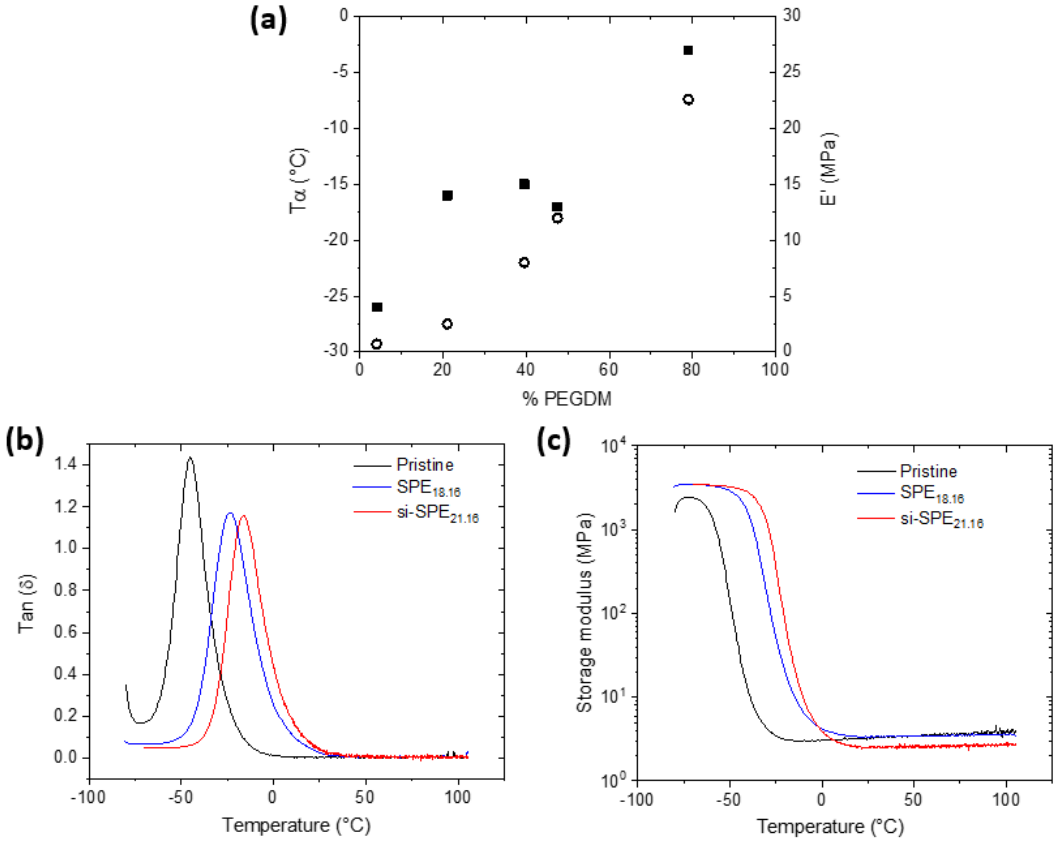

Figure II-4. (a) Dynamic thermomechanical analysis storage modulus (E', O) and T_α (■) as a function of PEGDM wt% for the si-SPE$_{21.y}$ samples; (b) tan(δ) versus T, and (c) storage modulus (E') *vs.* T for pristine network, si-SPE$_{21.16}$ and SPE$_{18.16}$ samples.

As expected, the storage modulus in the rubbery state (above 0 °C) increases from 1 to 20 MPa when the PEGDM proportion increases from 4 to 79 wt%. Simultaneously, the

mechanical relaxation temperature T_α, measured at the maximum of the tanδ peak, increases from -26 for 4 wt% of PEGDM to -3 °C for 79 wt% of PEGDM.

Generally, PEO networks with grafted salts are not always homogeneous. For instance, the free-radical copolymerization of PEGDM:PEGM with 2-acrylamido-2-methyl-1-propanesulfonic acid (AMPS) leads to materials showing a phase separation[37]. DMTA can be used to investigate the homogeneity of LiMTFSI in the si-SPE samples. Indeed, DMTA is often a more sensitive technique than DSC as far as the detection of the occurrence of phase separation is concerned. Thus, the detection of a single peak for the α-relaxation associated with the segmental chain motions can be taken as the characteristic of a homogenous material. The tanδ of different si-$SPE_{21,y}$ samples as a function of temperature exhibits a single peak (Figure SI.II-4a), indicating the absence of phase separation in the synthesized network[38]. Interestingly, it was found that the grafting of the anion (MTFSI) to the pristine polymer induces a significant rise of the α relaxation temperature (T_α) from -45 to -15 °C (Figure II-4b) which is confirmed by a simultaneous increase of the T_g from -60 to -41 °C. The same effect was observed, yet to a lesser extent (shift of T_α from -45 to -23 °C), on the $SPE_{18.16}$ sample, containing the same proportion of Li^+. The augmentation of T_α was related to the decrease of the mobility of the polymer chains upon the anion grafting to the polymer network as well as to the strong interaction of Li^+ with ethylene oxide units in the PEO chains[21].

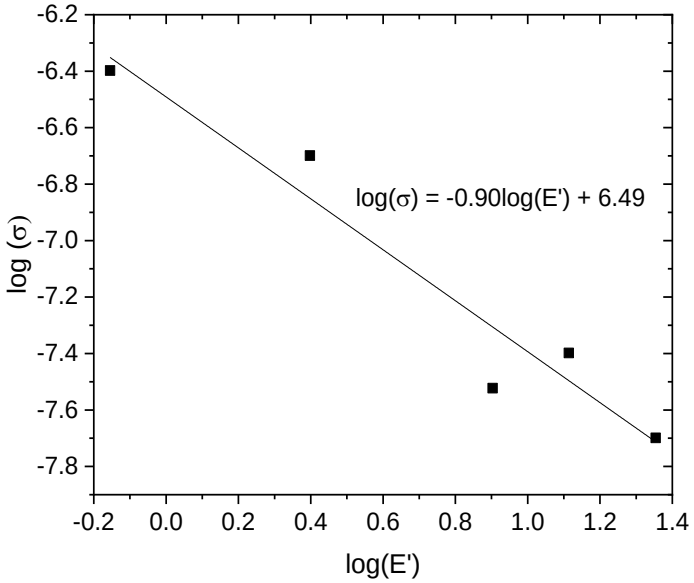

Figure II-5. Logarithm conductivity of si-$SPE_{21,y}$ series as a function of the logarithm of its storage modulus at 25 °C.

Figure II-5 represents the logarithm evolution of the ionic conductivity as a function of the storage modulus (E') for the si-SPE$_{21.y}$ series. It clearly shows that the ionic conductivity is inversely and strongly dependent on the storage modulus. This behavior is very similar to that of the well-known Walden rule relating the equivalent conductivity (Λ) of a liquid electrolyte to its viscosity ($\Lambda\eta$ = constant). The Walden rule has been extended to solid electrolyte by relating the conductivity to the structural (segmental) relaxation based on dielectric spectroscopic data[39]. In that case, the authors concluded that the polyether-Lithium electrolytes (i.e. PEO-Li-salt) present a universal behavior where ion and polymer dynamics are strongly coupled. To our knowledge, the dependence of the viscoelastic properties of a solid to its storage modulus has never been established before. In our case, thanks to the special composition of the samples, critical parameters (ionic concentration, ethylene oxide content) can be kept constant by varying the modulus of the samples solely changing PEGDM:PEGM ratio.

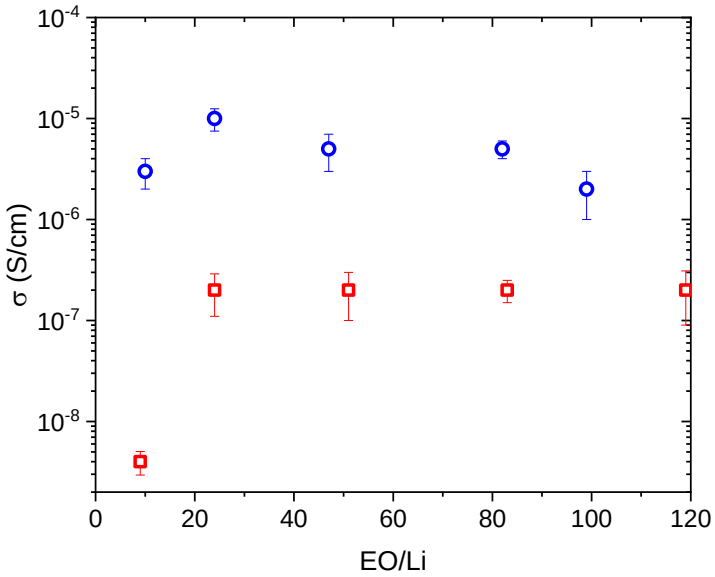

Figure II-6. Variation of the ionic conductivity at 25 °C as a function of EO/Li ratio for SPE (○) and si-SPE (□) electrolytes with a PEGM:PEGDM ratio of 80:20.

Next, the dependence between the conductivity and the Li^+ concentration was investigated while keeping the PEGDM:PEGM ratio constant. Figure II-6 shows the evolution of the ionic conductivity of polymer electrolytes as a function of EO/Li ratio.

For both SPE and si-SPE electrolytes, the ionic conductivity increases with the EO/Li ratio, until it reaches *ca.* 20. For the SPE series, a maximum in conductivity is observed for an EO/Li ratio around 20, similar to those reported in the literature for PEO/Li-salt systems. For the si-SPE series, the conductivity stabilizes for higher ratios. Previously, a decrease of the

conductivity was observed by Mindemark et al.[40] for Li based SPE and by Bouchet et al.[2] for salt-grafted SPE when the EO/Li ratio increases. This behavior is usually attributed to a trade-off between the increase in charge carrier content, the increase in T_g, the crystallization of PEO, and the salt dissociation. For instance, Maurel *et al.* [41] have shown on PEO/LiTFSI samples an optimum in conductivity for an EO/Li ratio of 20. In our case, the EO/Li ratio has little effect on the conductivity. It is likely that at a high concentration of Li (low EO/Li), the high content of complex Li-EO induces an increase in the storage modulus of the material and therefore a simultaneous decrease of the conductivity happens, as shown previously (Figure II-5). At lower concentrations (EO/Li above 20), the stabilization in conductivity in the case of si-SPE is a trade-off between the decrease in Li concentration and the increase in dissociation of Li-salt. On the contrary, the conductivity of SPE tends to decrease with the increase of the EO/Li ratio, due essentially to the decrease in salt concentration, as it is already highly dissociated. This issue will be further discussed in the following part, where the si-$SPE_{21.16}$ and $SPE_{18.16}$ were subjected to different characterizations. These two samples have the same crosslink density, and similar [EO]/[Li] ratios but the anion is grafted at si-$SPE_{21.16}$ but not at $SPE_{18.16}$.

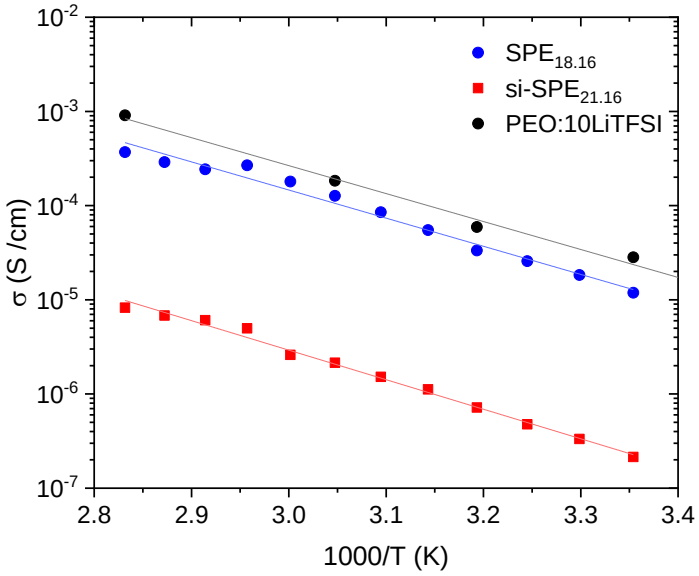

Figure II-7. Arrhenius plot for $SPE_{18.16}$ EO/Li=24 (●) and si-$SPE_{21.16}$ EO/Li =24 (■).

The temperature dependence of the conductivity is depicted in Figure II-7. The si-$SPE_{21.16}$ polymer electrolyte with immobilized anions has a notably lower ionic conductivity than $SPE_{18.16}$, which contains mobile anions, over the entire range of studied temperatures. Interestingly, the absence of any change in the slopes of the ln(σ) *vs.* 1000/T plots (Figure II-7) seems to indicate that both polymer electrolytes do not undergo any crystallization process in the studied temperature range in agreement with the DSC results. The ionic conductivity of

si-SPE$_{21.16}$ and SPE$_{18.16}$ follows Arrhenius model: $\sigma\ (T) = \ \sigma_0 * \exp(-\frac{E_a}{RT})$. From the plot of ln(σ) versus 1000/T, the activation energies (E_a) for SPE$_{18.16}$ and si-SPE$_{21.16}$ have been estimated at 0.64 eV and 0.62 eV, respectively. The similar E_a for both samples demonstrates that the Li^+ ions pathway along the polymer network obeys a similar diffusional mechanism. Compared to literature data on single ion polymer electrolytes[42], this higher activation energy value (0.62 eV compared to 0.22 eV) attests to a different mechanism of Li transport in our polymer matrix.

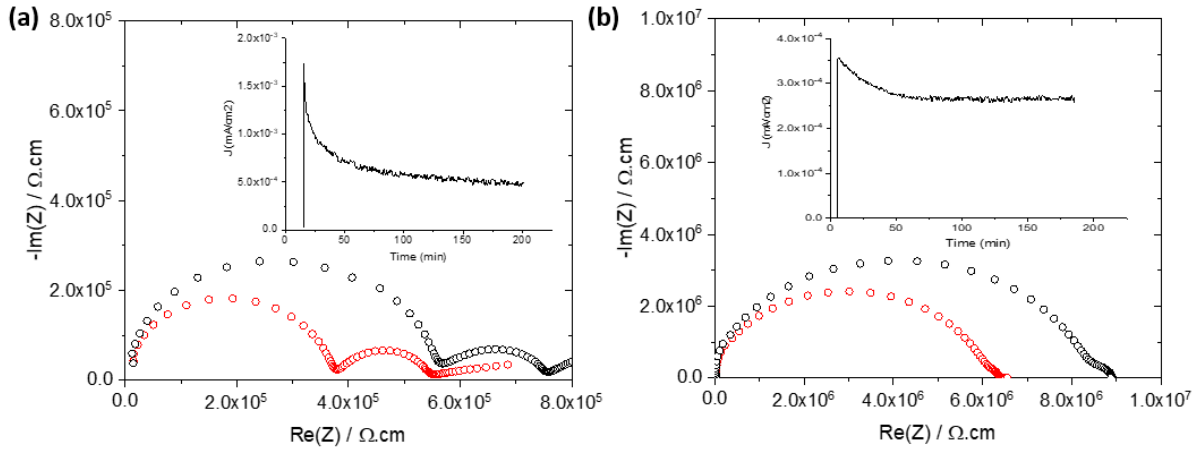

Figure II- 8. Determination of the Li transport numbers by Bruce and Vincent method of (a) Li/SPE$_{18,16}$/Li and (b) Li/si-SPE$_{21,16}$/Li with polarization experiment and EIS spectra before (red) and after (black) polarization.

The Li^+ transport number (t_{Li+}) of both SPE$_{18.16}$ and si-SPE$_{21.16}$ was determined using the method proposed by Bruce and Vincent[43], taking into account also the bulk resistance before and after polarization[17]. The results of EIS and polarization experiments are given in Figure II-8. The transport number was calculated according to Equation 3. The t_{Li+} value was found to be 0.31 for SPE$_{18.16}$ at 25 °C. This low value, classically observed for PEO/Li-salt electrolyte[13], indicates a limitation of Li^+ progression due to its coordination with the EO chains, while $TFSI^-$ is much less influenced[44,45]. For the si-SPE$_{21.16}$ sample, this value is equal to 1.00, confirming the total grafting of the LiMTFSI to the polymer network. This value is an excellent result as the t_{Li+} is generally reported to be close to unity (from 0.83 to 0.96) in most of single-ion conductors (cf Table SI.II-1)[23]. The main difference between the literature results and ours is the presence of solvent. In order to check this assumption, the si-SPE$_{21.16}$ sample was swollen with propylene carbonate. Once swollen, the t^+ of this sample decreases from 1 to 0.7, attesting to the role of PC in the transport of Li^+[22].

To confirm the previous t^+ values, the diffusion coefficients of Li^+ and $TFSI^-$ were measured by pulsed field gradient nuclear magnetic resonance (PFG-NMR) spectroscopy using the ^7Li or ^{19}F signals, which fall around 0 ppm and -78 ppm, respectively[46]. The diffusion coefficients determined at 84± 1 °C for $SPE_{18.16}$ and si–$SPE_{21.16}$ are reported in Table II-3. The main reason for selecting to perform the measurements at this temperature was that the relaxation times (T_2) are too short at room temperature. However, at higher temperatures, relaxation times increase and become compatible with PFG-NMR. The following relaxation times were observed for $SPE_{18.16}$: $T_1(^7Li)$=320 ms, $T_2(^7Li)$=120 ms, $T_1(^{19}F)$=1700 ms and $T_2(^{19}F)$=520 ms; and for si-$SPE_{21.16}$: $T_1(^7Li)$=280 ms, $T_2(^7Li)$=20 ms, $T_1(^{19}F)$=690 ms and $T_2(^{19}F)$=100 ms. In si-$SPE_{21.16}$, the T_2 is notably shorter, in line with a lower local mobility of the species. The transport numbers were then estimated with the following equation[47] :

$$t_{Li+} = \frac{D_{Li}}{D_{Li} + D_{TFSI}}$$

where D_{Li} and D_{TFSI} represent the diffusion coefficient measured in NMR spectroscopy for the Li and TFSI respectively. The obtained transport numbers are presented in Table II-3.

A value of 1.0 was obtained for si-$SPE_{21.16}$ and 0.31 for $SPE_{18.16}$, both in very good agreement with the results obtained by the Bruce and Vincent method. Summarizing, the transport number value of 1.0 confirms that the ionic current in si-$SPE_{21.16}$ is exclusively due to Li^+ and their counter-ions (MTFSI) are covalently grafted to the polymer network (Table II-3).

Table II-3.Diffusion coefficients at 84 °C, transport numbers and molar ionic conductivities of $SPE_{18.16}$ and si-$SPE_{21.16}$.

Sample	D_{Li} ($m^2.s^{-1}$)[a]	D_{TFSI} ($m^2.s^{-1}$)[b]	t^+_{NMR} (84 °C)	t^+_{EI} (25 °C)	[Li] (mol/L)	Λ_{NMR} ($\Omega^{-1}.m^2$)	Λ_{EIS} ($\Omega^{-1}.m^2$)[c]	α $\Lambda_{EIS}/\Lambda_{NMR}$
$SPE_{18,16}$	6.85×10^{-12}	1.54×10^{-11}	0.31	0.31	0.72	6.9×10^{-5}	5.8×10^{-5}	0.84
si-$SPE_{21,16}$	1.05×10^{-12}	$<1\times10^{-15}$	1.00	1.00	0.80	3.1×10^{-6}	2.1×10^{-6}	0.39

[a] uncertainty on D_{Li} is $\pm0.05\text{x}10^{-12}$ $m^2.s^{-1}$; [b] uncertainty on D_{TFSI} is $\pm0.02\text{x}10^{-11}$ $m^2.s^{-1}$ (but for si-$SPE_{21,16}$); [c] based on conductivity values measured at 80 °C

On the other hand, from diffusion coefficient, it is possible to calculate the molar ionic conductivity of the material using the Nernst–Einstein relation:

$$\Lambda_{NMR} = \frac{\sigma_{NMR}}{C} = \frac{N_A e^2}{kT}(D^+ + D^-)$$

with Avogadro's number (N_A), the fundamental charge (e), the Boltzmann constant (k) and the absolute temperature (T). These values can be compared with those obtained from EIS

measurements, through the ratio $\Lambda_{EIS}/\Lambda_{NMR}$, which gives an indication on the proportion of charged species that contribute to ionic conduction. This ratio is considered as ionicity for ionic liquids or the degree of dissociation of liquid electrolytes[48,49]. Table II-3 summarizes the diffusion coefficients and dissociation value (α) of both $SPE_{18.16}$ and si-$SPE_{21.16}$. In our case, the dissociation value of SPE is high, reaching 0.84 which is among the highest values reported in the literature even for liquid electrolytes ($\alpha < 0.8$ for $LiPF_6$ in PC or EC)[50,51]. This result is interesting as it suggests that the incorporation of the Li-salt within this network with dangling PEO chains allows keeping a high level of dissociation with a t^+ value similar to those obtained in the classical liquid electrolyte ($LiPF_6$/carbonate solvent t^+ ~0.3 – 0.4)[52]. The resulting low conductivity in our SPE case is mainly caused by the high viscosity/modulus of the medium, which is unavoidable due to the solid nature of the SPE. The dissociation value of si-SPE (0.39) is slightly higher than values reported in the literature for single-ion conducting solid polymer electrolyte (0.30)[53].

This feature has a considerable advantage over the ungrafted system due to their potential to reduce the build-up of ion concentration gradients, which is especially meaningful for fast charging applications,[52] and suppress Li dendrite growth,[54] which should improve the cycling stability and safety of the device.

The electrochemical stability window of $SPE_{18.16}$ and si-$SPE_{21.16}$ were investigated by cyclic voltammetry (CV) at 70 °C (Figure II-9). Cathodic scans showed a couple of reversible redox peaks between -1.0 V and 7.0 V *vs.* Li at a scan rate of 1 $mV.s^{-1}$. The characteristic at the end of reduction at 0.0 V for si-$SPE_{21.16}$ and -0.5 V for $SPE_{18.16}$ was attributed to the Li deposition on the working electrode. The oxidation peak at 5.5 V for $SPE_{18.16}$ reflects the anodic stability of the electrolytes. The strong increase in current is probably associated with the decomposition of the anion as the anodic stability of the electrolyte is usually linked to the electrochemical stability of the anion[20]. The si-$SPE_{21.16}$ sample exhibits a slight increase of current at high potential, indicating oxidation of the anion grafted to the polymer chains close to the electrode/electrolyte interface.

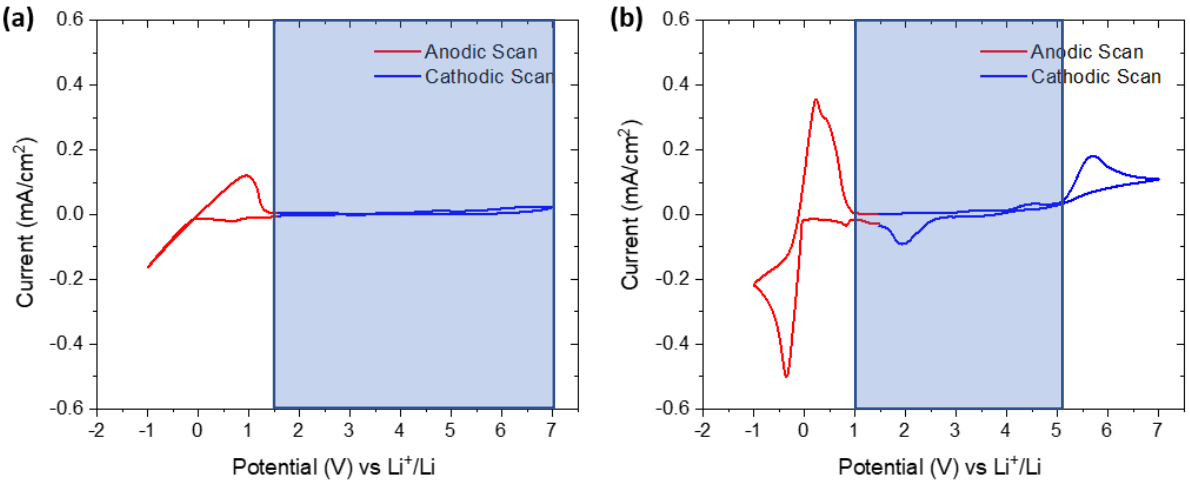

Figure II-9. The electrochemical stability windows for (a) si-SPE$_{21.16}$ and (b) SPE$_{18.16}$ obtained by CV at 70 °C with a scan rate of 1 mV.s^{-1}. (□) Indicates the stability of the polymer *vs.* Li-metal.

The increase in current for SPE$_{18.16}$ appears at a lower potential probably due to the presence of ungrafted anion in the polymer electrolyte. On the contrary for si-SPE$_{21.16}$, as the anions are grafted, anionic stability is postponed to higher potential values (6 V), as solely anions close to the interface can be oxidized [14]. These experiments confirm the importance of using the si-SPE$_{21.16}$ polymer in the formulation of composite positive electrodes with high potential cathode materials, due to its larger potential stability windows[55]. To our knowledge, a such high stability of si-SPE$_{21.16}$ has not been reported for polymer electrolytes, thanks to the grafting of the electrolyte anion as well as the absence of solvent during the whole fabrication process[56].

In order to investigate the possibility of using these electrolytes in Li-metal batteries, the long-term electrochemical stability of both si-SPE$_{21.16}$ and SPE$_{18.16}$ against Li-metal was studied. Symmetric Li/polymer electrolyte/Li cell was cycled at a constant current density of 0.2 mA.cm^{-2} for si-SPE$_{21.16}$ and 0.12 mA.cm^{-2} for SPE$_{18.16}$ at 70 °C (Figure II-10). This current density has been determined according to the value measured in Figure SI.II-6. The voltage of the Li/ SPE$_{18.16}$/Li cell increases to 4.5 V after cycling for 70 h, while the voltage of the Li/si-SPE$_{21.16}$/Li reaches solely 2 V after 200 h of cycling. On the other hand, in contrast to the significant increase of the resistance for the Li/ SPE$_{18.16}$/Li cell from ~ 1.8.10^4 Ω.cm to ~ 4.5.10^5 Ω.cm (Figure II-10d), the Li/si-SPE$_{21.16}$/Li cell showed a slight increase from ~ 2.5.10^5 Ω.cm *vs.* ~ 3.8.10^5 Ω.cm (Figure II-10c), confirming the stability of the si-SPE$_{21.16}$ polymer /Li interface. Accordingly, the grafting of the anion to the network limits an overpotential in the cell, allowing a more stable system over time.

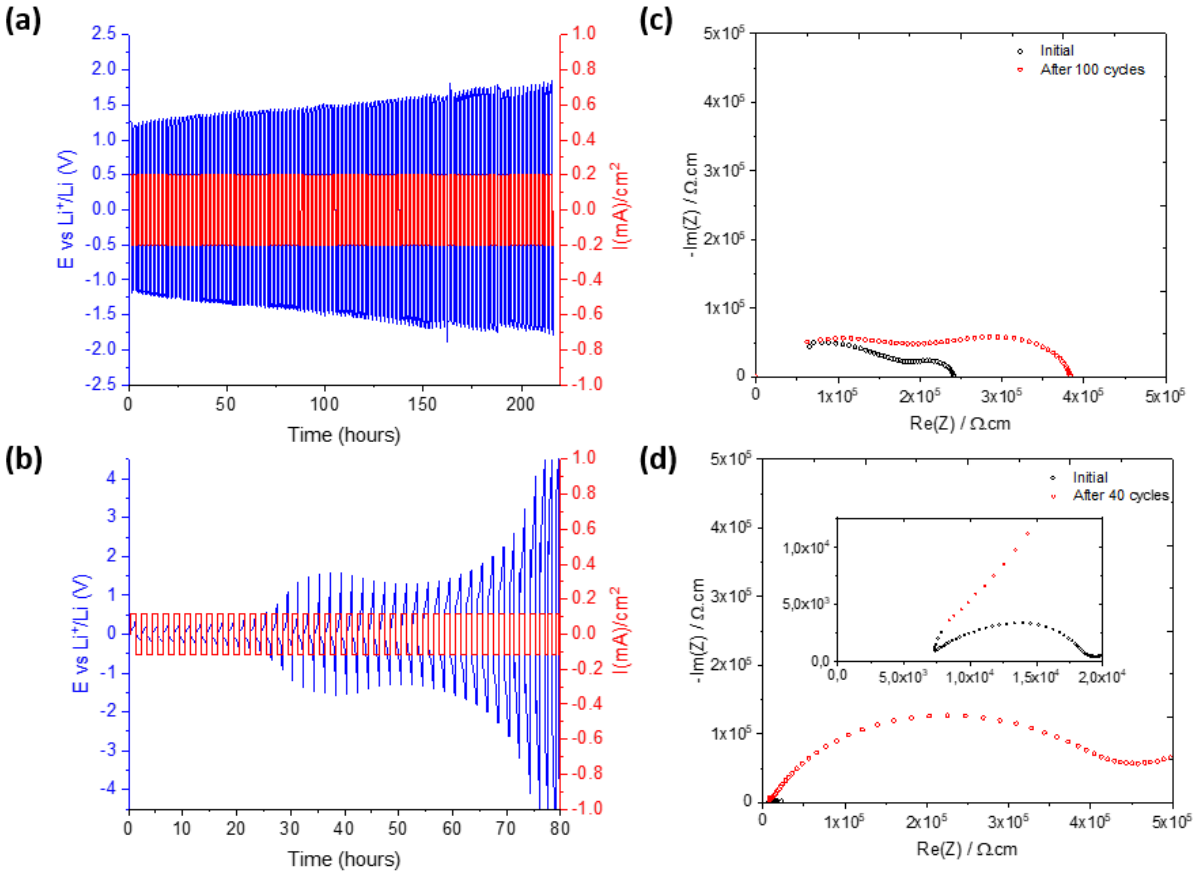

Figure II-10. Galvanostatic cycling at 70 °C of (a)Li/si-$SPE_{21.16}$/Li and (b)Li/$SPE_{18.16}$/Li and (c), (d) Nyquist plots of respective electrolyte before (black) and after (red) cycling. Both electrolytes have a thickness of 250 µm and an area of 0.5 cm^2.

IV. Conclusion

This work reports the synthesis and characterization of a series of cross-linked PEO polymers containing grafted (si-$SPE_{x,y}$) or ungrafted ($SPE_{x,y}$) LiTFSI. The synthesis is a simple *in situ* thermal copolymerization of commercial LiMTFSI, PEGM and PEGDM carried out without solvent. In parallel, a crosslinked PEO polymer network was synthesized, in which LiTFSI salt was dissolved. Flexible free-standing films of amorphous polymer electrolyte were prepared by thermal polymerization of 2 h at 70 °C and 1 h at 90 °C which allows easily varying the composition of $SPE_{x,y}$ and single-ion conducting SPE (si-$SPE_{x,y}$). The measurement of the soluble fraction indicates a satisfying copolymerization of the different monomers. DMTA and TGA analyses demonstrate the homogeneity of the synthesized polymer films and their thermal stability, respectively. The ionic conductivity as well as the T_g and E' modulus for the various polymer electrolytes have been measured, from which a correlation between the ionic conductivity and the mechanical properties (T_g and E') of the solid polymer film have been

demonstrated. The ionic conductivity (σ) decreases with the increase of T_g or T_α and notably of E', confirming the role of the PEO chain flexibility and the Li^+/PEO interaction in the transport of Li^+ in the PEO matrix. The unity value (1.00) of the transport number is confirmed by the electrochemical method and by diffusion coefficients in the case of si-SPE. The si-$SPE_{21.16}$ exhibits a od mechanical robustness: self-standing for a wide range of temperature -70 °C to 100 °C (storage modulus at 25 °C E' = 3 MPa), a low T_g value of around – 40 °C, and a transport number of 1.0, which has never been reported in the literature to our knowledge. In addition, its anionic stability is postponed to higher potential values (6 V). However, its ionic conductivity of 2.10^{-7} $S.cm^{-1}$ at ambient temperature is too low. To improve this value, the storage modulus of the material must be decreased by changing the cross-linking chemistry of the PEO.

Supporting information

DSC thermograms for si-SPE; DMA analysis for si-SPE; TGA thermograms for SPE and si-SPE; NMR experiments Attenuation curve for ^{19}F and ^{7}Li for SPE and si-SPE; Table of comparison of Li transport number; CCD determination at 70 °C for Li/SPE/Li and Li/si-SPE/Li.

References:

(1) Lin, D.; Liu, Y.; Cui, Y. Reviving the Lithium Metal Anode for High-Energy Batteries. *Nat. Nanotechnol.* **2017**, *12* (3), 194–206. https://doi.org/10.1038/nnano.2017.16.

(2) Bouchet, R.; Maria, S.; Meziane, R.; Aboulaich, A.; Lienafa, L.; Bonnet, J.-P.; Phan, T. N. T.; Bertin, D.; Gigmes, D.; Devaux, D.; Denoyel, R.; Armand, M. Single-Ion BAB Triblock Copolymers as Highly Efficient Electrolytes for Lithium-Metal Batteries. *Nat. Mater.* **2013**, *12* (5), 452–457. https://doi.org/10.1038/nmat3602.

(3) Wang, Q.; Wang, H.; Wu, J.; Zhou, M.; Liu, W.; Zhou, H. Advanced Electrolyte Design for Stable Lithium Metal Anode: From Liquid to Solid. *Nano Energy* **2021**, *80*, 105516. https://doi.org/10.1016/j.nanoen.2020.105516.

(4) Li, M.; Wang, C.; Chen, Z.; Xu, K.; Lu, J. New Concepts in Electrolytes. *Chem. Rev.* **2020**, *120* (14), 6783–6819. https://doi.org/10.1021/acs.chemrev.9b00531.

(5) Mauger; Julien; Paolella; Armand; Zaghib. Building Better Batteries in the Solid State: A Review. *Materials* **2019**, *12* (23), 3892. https://doi.org/10.3390/ma12233892.

(6) Ma, Q.; Zhang, H.; Zhou, C.; Zheng, L.; Cheng, P.; Nie, J.; Feng, W.; Hu, Y.-S.; Li, H.; Huang, X.; Chen, L.; Armand, M.; Zhou, Z. Single Lithium-Ion Conducting Polymer Electrolytes Based on a Super-Delocalized Polyanion. *Angew. Chem. Int. Ed.* **2016**, *55* (7), 2521–2525. https://doi.org/10.1002/anie.201509299.

(7) Geiculescu, O. E.; Yang, J.; Zhou, S.; Shafer, G.; Xie, Y.; Albright, J.; Creager, S. E.; Pennington, W. T.; DesMarteau, D. D. Solid Polymer Electrolytes from Polyanionic Lithium Salts Based on the LiTFSI Anion Structure. *J. Electrochem. Soc.* **2004**, *151* (9), A1363. https://doi.org/10.1149/1.1773581.

(8) Tao, C.; Gao, M.-H.; Yin, B.-H.; Li, B.; Huang, Y.-P.; Xu, G.; Bao, J.-J. A Promising TPU/PEO Blend Polymer Electrolyte for All-Solid-State Lithium Ion Batteries. *Electrochimica Acta* **2017**, *257*, 31–39. https://doi.org/10.1016/j.electacta.2017.10.037.

(9) Marzantowicz, M.; Dygas, J. R.; Krok, F.; Łasińska, A.; Florjańczyk, Z.; Zygadło-Monikowska, E.; Affek, A. Crystallization and Melting of PEO:LiTFSI Polymer Electrolytes Investigated Simultaneously by Impedance Spectroscopy and Polarizing Microscopy. *Electrochimica Acta* **2005**, *50* (19), 3969–3977. https://doi.org/10.1016/j.electacta.2005.02.053.

(10) Kim, Y. The Effect of Plasticizers on Transport and Electrochemical Properties of PEO-Based Electrolytes for Lithium Rechargeable Batteries. *Solid State Ion.* **2002**, *149* (1–2), 29–37. https://doi.org/10.1016/S0167-2738(02)00130-3.

(11) Zheng, Q.; Pesko, D. M.; Savoie, B. M.; Timachova, K.; Hasan, A. L.; Smith, M. C.; Miller, T. F.; Coates, G. W.; Balsara, N. P. Optimizing Ion Transport in Polyether-Based Electrolytes for Lithium Batteries. *Macromolecules* **2018**, *51* (8), 2847–2858. https://doi.org/10.1021/acs.macromol.7b02706.

(12) Gao, K. W.; Loo, W. S.; Snyder, R. L.; Abel, B. A.; Choo, Y.; Lee, A.; Teixeira, S. C. M.; Garetz, B. A.; Coates, G. W.; Balsara, N. P. Miscible Polyether/Poly(Ether–Acetal) Electrolyte Blends. *Macromolecules* **2020**, *53* (14), 5728–5739. https://doi.org/10.1021/acs.macromol.0c00747.

(13) Devaux, D.; Bouchet, R.; Glé, D.; Denoyel, R. Mechanism of Ion Transport in PEO/LiTFSI Complexes: Effect of Temperature, Molecular Weight and End Groups. *Solid State Ion.* **2012**, *227*, 119–127. https://doi.org/10.1016/j.ssi.2012.09.020.

(14) Shi, Q.; Xue, L.; Qin, D.; Du, B.; Wang, J.; Chen, L. Single Ion Solid-State Composite Electrolytes with High Electrochemical Stability Based on a Poly(Perfluoroalkylsulfonyl)-Imide Ionene Polymer. *J Mater Chem A* **2014**, *2* (38), 15952–15957. https://doi.org/10.1039/C4TA02810D.

(15) Nguyen, N.; Blatt, M. P.; Kim, K.; Hallinan, D. T.; Kennemur, J. G. Investigating Miscibility and Lithium Ion Transport in Blends of Poly(Ethylene Oxide) with a Polyanion Containing Precisely-Spaced Delocalized Charges. *Polym. Chem.* **2022**, *13* (29), 4309–4323. https://doi.org/10.1039/D2PY00605G.

(16) Devaux, D.; Glé, D.; Phan, T. N. T.; Gigmes, D.; Giroud, E.; Deschamps, M.; Denoyel, R.; Bouchet, R. Optimization of Block Copolymer Electrolytes for Lithium Metal Batteries. *Chem. Mater.* **2015**, *27* (13), 4682–4692. https://doi.org/10.1021/acs.chemmater.5b01273.

(17) Feng, S.; Shi, D.; Liu, F.; Zheng, L.; Nie, J.; Feng, W.; Huang, X.; Armand, M.; Zhou, Z. Single Lithium-Ion Conducting Polymer Electrolytes Based on Poly[(4-Styrenesulfonyl)(Trifluoromethanesulfonyl)Imide] Anions. *Electrochimica Acta* **2013**, *93*, 254–263. https://doi.org/10.1016/j.electacta.2013.01.119.

(18) Rolland, J.; Poggi, E.; Vlad, A.; Gohy, J.-F. Single-Ion Diblock Copolymers for Solid-State Polymer Electrolytes. *Polymer* **2015**, *68*, 344–352. https://doi.org/10.1016/j.polymer.2015.04.056.

(19) Inceoglu, S.; Rojas, A. A.; Devaux, D.; Chen, X. C.; Stone, G. M.; Balsara, N. P. Morphology–Conductivity Relationship of Single-Ion-Conducting Block Copolymer Electrolytes for Lithium Batteries. *ACS Macro Lett.* **2014**, *3* (6), 510–514. https://doi.org/10.1021/mz5001948.

(20) Porcarelli, L.; Shaplov, A. S.; Salsamendi, M.; Nair, J. R.; Vygodskii, Y. S.; Mecerreyes, D.; Gerbaldi, C. Single-Ion Block Copoly(Ionic Liquid)s as Electrolytes for All-Solid State Lithium Batteries. *ACS Appl. Mater. Interfaces* **2016**, *8* (16), 10350–10359. https://doi.org/10.1021/acsami.6b01973.

(21) Devaux, D. Comparison of Single-Ion-Conductor Block-Copolymer Electrolytes with Polystyrene-TFSI and Polymethacrylate-TFSI Structural Blocks. *Electrochimica Acta* **2018**, 12.

(22) Lechartier, M.; Porcarelli, L.; Zhu, H.; Forsyth, M.; Guéguen, A.; Castro, L.; Mecerreyes, D. Single-Ion Polymer/LLZO Hybrid Electrolytes with High Lithium Conductivity. *Mater. Adv.* **2022**, *3* (2), 1139–1151. https://doi.org/10.1039/D1MA00857A.

(23) Porcarelli, L.; Shaplov, A. S.; Bella, F.; Nair, J. R.; Mecerreyes, D.; Gerbaldi, C. Single-Ion Conducting Polymer Electrolytes for Lithium Metal Polymer Batteries That Operate at Ambient Temperature. *ACS Energy Lett.* **2016**, *1* (4), 678–682. https://doi.org/10.1021/acsenergylett.6b00216.

(24) Zhang, Y.; Cai, W.; Rohan, R.; Pan, M.; Liu, Y.; Liu, X.; Li, C.; Sun, Y.; Cheng, H. Toward Ambient Temperature Operation with All-Solid-State Lithium Metal Batteries with a Sp Boron-Based Solid Single Ion Conducting Polymer Electrolyte. *J. Power Sources* **2016**, *306*, 152–161. https://doi.org/10.1016/j.jpowsour.2015.12.010.

(25) Li, Z.; Guo, D.; Li, F.; Hou, G.; Liu, X.; Li, C.; Cao, L.; Wei, R.; Zhou, Z.; Lai, Z. Nerve Network-Inspired Solid Polymer Electrolytes (NN-SPE) for Fast and Single-Ion Lithium Conduction. *Energy Storage Mater.* **2022**, *49*, 575–582. https://doi.org/10.1016/j.ensm.2022.05.003.

(26) Niitani, T.; Shimada, M.; Kawamura, K.; Kanamura, K. Characteristics of New-Type Solid Polymer Electrolyte Controlling Nano-Structure. *J. Power Sources* **2005**, *146* (1–2), 386–390. https://doi.org/10.1016/j.jpowsour.2005.03.102.

(27) Sadoway, D. R. Block and Graft Copolymer Electrolytes for High-Performance, Solid-State, Lithium Batteries. *J. Power Sources* **2004**, *129* (1), 1–3. https://doi.org/10.1016/j.jpowsour.2003.11.016.

(28) Singh, M.; Odusanya, O.; Wilmes, G. M.; Eitouni, H. B.; Gomez, E. D.; Patel, A. J.; Chen, V. L.; Park, M. J.; Fragouli, P.; Iatrou, H.; Hadjichristidis, N.; Cookson, D.; Balsara, N. P. Effect of Molecular Weight on the Mechanical and Electrical Properties of Block Copolymer Electrolytes. *Macromolecules* **2007**, *40* (13), 4578–4585. https://doi.org/10.1021/ma0629541.

(29) Schönleber, M.; Klotz, D.; Ivers-Tiffée, E. A Method for Improving the Robustness of Linear Kramers-Kronig Validity Tests. *Electrochimica Acta* **2014**, *131*, 20–27. https://doi.org/10.1016/j.electacta.2014.01.034.

(30) Boukamp, B. A. A Linear Kronig-Kramers Transform Test for Immittance Data Validation. *J. Electrochem. Soc.* **1995**, *142* (6), 1885–1894. https://doi.org/10.1149/1.2044210.

(31) Schönleber, M.; Ivers-Tiffée, E. Approximability of Impedance Spectra by RC Elements and Implications for Impedance Analysis. *Electrochem. Commun.* **2015**, *58*, 15–19. https://doi.org/10.1016/j.elecom.2015.05.018.

(32) Grosso, D.; Ribot, F.; Boissiere, C.; Sanchez, C. Molecular and Supramolecular Dynamics of Hybrid Organic–Inorganic Interfaces for the Rational Construction of Advanced Hybrid Nanomaterials. *Chem Soc Rev* **2011**, *40* (2), 829–848. https://doi.org/10.1039/C0CS00039F.

(33) Dagousset, L.; Pognon, G.; Nguyen, G. T. M.; Vidal, F.; Jus, S.; Aubert, P.-H. Self-Standing Gel Polymer Electrolyte for Improving Supercapacitor Thermal and Electrochemical Stability. *J. Power Sources* **2018**, *391*, 86–93. https://doi.org/10.1016/j.jpowsour.2018.04.073.

(34) Gauthier, C.; Plesse, C.; Vidal, F.; Pelletier, J.-M.; Chevrot, C.; Teyssié, D. Polybutadiene/Poly(Ethylene Oxide) Based IPNs, Part II: Mechanical Modelling and LiClO4 Loading as Tools for IPN Morphology Investigation. *Polymer* **2007**, *48* (26), 7476–7483. https://doi.org/10.1016/j.polymer.2007.10.035.

(35) Yu, X.; Xiao, M.; Wang, S.; Han, D.; Meng, Y. Fabrication and Properties of Crosslinked Poly(Propylene Carbonate Maleate) Gel Polymer Electrolyte for Lithium-Ion Battery. *J. Appl. Polym. Sci.* **2010**, n/a-n/a. https://doi.org/10.1002/app.32480.

(36) Berrebi, M.; Fabre-Francke, I.; Lavédrine, B.; Fichet, O. Development of Organic Glass Using Interpenetrating Polymer Networks with Enhanced Resistance towards Scratches and Solvents. *Eur. Polym. J.* **2015**, *63*, 132–140. https://doi.org/10.1016/j.eurpolymj.2014.12.010.

(37) Chikh, L.; Girard, S.; Teyssie, D.; Fichet, O. Proton Conducting PAMPS Networks: From Flexible to Rigid Materials. *J. Appl. Polym. Sci.* **2008**, *107* (6), 3672–3680. https://doi.org/10.1002/app.27471.

(38) Szczepanski, C. R.; Pfeifer, C. S.; Stansbury, J. W. A New Approach to Network Heterogeneity: Polymerization Induced Phase Separation in Photo-Initiated, Free-Radical Methacrylic Systems. *Polymer* **2012**, *53* (21), 4694–4701. https://doi.org/10.1016/j.polymer.2012.08.010.

(39) Wang, Y.; Fan, F.; Agapov, A. L.; Yu, X.; Hong, K.; Mays, J.; Sokolov, A. P. Design of Superionic Polymers—New Insights from Walden Plot Analysis. *Solid State Ion.* **2014**, *262*, 782–784. https://doi.org/10.1016/j.ssi.2013.09.026.

(40) Mindemark, J.; Lacey, M. J.; Bowden, T.; Brandell, D. Beyond PEO—Alternative Host Materials for Li + -Conducting Solid Polymer Electrolytes. *Prog. Polym. Sci.* **2018**, *81*, 114–143. https://doi.org/10.1016/j.progpolymsci.2017.12.004.

(41) Maurel, A.; Armand, M.; Grugeon, S.; Fleutot, B.; Davoisne, C.; Tortajada, H.; Courty, M.; Panier, S.; Dupont, L. Poly(Ethylene Oxide)−LiTFSI Solid Polymer Electrolyte Filaments for Fused Deposition Modeling Three-Dimensional Printing. *J. Electrochem. Soc.* **2020**, *167* (7), 070536. https://doi.org/10.1149/1945-7111/ab7c38.

(42) Ahmed, F.; Choi, I.; Rahman, Md. M.; Jang, H.; Ryu, T.; Yoon, S.; Jin, L.; Jin, Y.; Kim, W. Remarkable Conductivity of a Self-Healing Single-Ion Conducting Polymer Electrolyte, Poly(Ethylene- *Co* -Acrylic Lithium (Fluoro Sulfonyl)Imide), for All-Solid-State Li-Ion Batteries. *ACS Appl. Mater. Interfaces* **2019**, *11* (38), 34930–34938. https://doi.org/10.1021/acsami.9b10474.

(43) Bruce, P. Conductivity and Transference Number Measurements on Polymer Electrolytes. *Solid State Ion.* **1988**, *28–30*, 918–922. https://doi.org/10.1016/0167-2738(88)90304-9.

(44) Oradd, G. Diffusion: A Comparison between Liquid and Solid Polymer LiTFSI Electrolytes. *Solid State Ion.* **2002**, *152–153*, 131–136. https://doi.org/10.1016/S0167-2738(02)00364-8.

(45) Edman, L.; Ferry, A.; Orädd, G. Analysis of Diffusion in a Solid Polymer Electrolyte in the Context of a Phase-Separated System. *Phys. Rev. E* **2002**, *65* (4), 042803. https://doi.org/10.1103/PhysRevE.65.042803.

(46) Hayamizu, K.; Seki, S.; Haishi, T. Lithium Ion Micrometer Diffusion in a Garnet-Type Cubic Li $_7$ La $_3$ Zr $_2$ O $_{12}$ (LLZO) Studied Using ^{7} Li NMR Spectroscopy. *J. Chem. Phys.* **2017**, *146* (2), 024701. https://doi.org/10.1063/1.4973827.

(47) Zhao, J.; Wang, L.; He, X.; Wan, C.; Jiang, C. Determination of Lithium-Ion Transference Numbers in LiPF[Sub 6]–PC Solutions Based on Electrochemical Polarization

and NMR Measurements. *J. Electrochem. Soc.* **2008**, *155* (4), A292. https://doi.org/10.1149/1.2837832.

(48) Tokuda, H.; Hayamizu, K.; Ishii, K.; Susan, Md. A. B. H.; Watanabe, M. Physicochemical Properties and Structures of Room Temperature Ionic Liquids. 2. Variation of Alkyl Chain Length in Imidazolium Cation. *J. Phys. Chem. B* **2005**, *109* (13), 6103–6110. https://doi.org/10.1021/jp044626d.

(49) MacFarlane, D. R.; Forsyth, M.; Izgorodina, E. I.; Abbott, A. P.; Annat, G.; Fraser, K. On the Concept of Ionicity in Ionic Liquids. *Phys. Chem. Chem. Phys.* **2009**, *11* (25), 4962. https://doi.org/10.1039/b900201d.

(50) Feng, Z.; Higa, K.; Han, K. S.; Srinivasan, V. Evaluating Transport Properties and Ionic Dissociation of $LiPF_6$ in Concentrated Electrolyte. *J. Electrochem. Soc.* **2017**, *164* (12), A2434–A2440. https://doi.org/10.1149/2.0941712jes.

(51) Hayamizu, K. Temperature Dependence of Self-Diffusion Coefficients of Ions and Solvents in Ethylene Carbonate, Propylene Carbonate, and Diethyl Carbonate Single Solutions and Ethylene Carbonate + Diethyl Carbonate Binary Solutions of $LiPF_6$ Studied by NMR. *J. Chem. Eng. Data* **2012**, *57* (7), 2012–2017. https://doi.org/10.1021/je3003089.

(52) Diederichsen, K. M.; McShane, E. J.; McCloskey, B. D. Promising Routes to a High Li^+ Transference Number Electrolyte for Lithium Ion Batteries. *ACS Energy Lett.* **2017**, *2* (11), 2563–2575. https://doi.org/10.1021/acsenergylett.7b00792.

(53) Borzutzki, K.; Thienenkamp, J.; Diehl, M.; Winter, M.; Brunklaus, G. Fluorinated Polysulfonamide Based Single Ion Conducting Room Temperature Applicable Gel-Type Polymer Electrolytes for Lithium Ion Batteries. *J. Mater. Chem. A* **2019**, *7* (1), 188–201. https://doi.org/10.1039/C8TA08391F.

(54) Ford, H. O.; Park, B.; Jiang, J.; Seidler, M. E.; Schaefer, J. L. Enhanced Li^+ Conduction within Single-Ion Conducting Polymer Gel Electrolytes via Reduced Cation–Polymer Interaction. *ACS Mater. Lett.* **2020**, *2* (3), 272–279. https://doi.org/10.1021/acsmaterialslett.9b00510.

(55) Armand, M.; Tarascon, J.-M. Building Better Batteries. *Nature* **2008**, *451* (7179), 652–657. https://doi.org/10.1038/451652a.

(56) Nguyen, H.-D.; Kim, G.-T.; Shi, J.; Paillard, E.; Judeinstein, P.; Lyonnard, S.; Bresser, D.; Iojoiu, C. Nanostructured Multi-Block Copolymer Single-Ion Conductors for Safer High-Performance Lithium Batteries. *Energy Environ. Sci.* **2018**, *11* (11), 3298–3309. https://doi.org/10.1039/C8EE02093K.

Supporting information

Correlation between Ionic and Mechanical Properties of Solid PEO Polymer Electrolyte

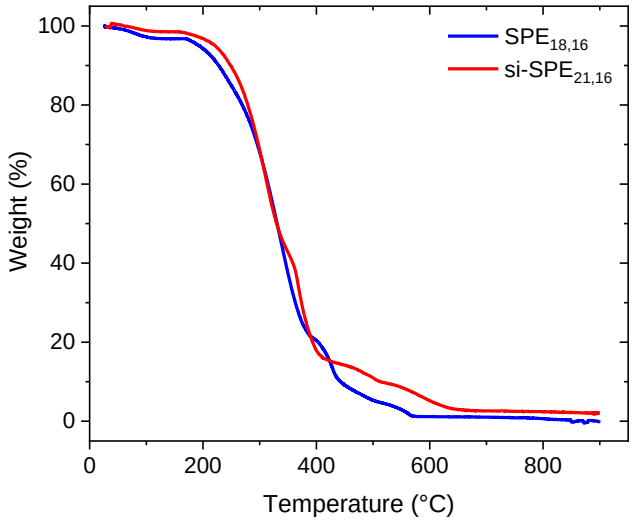

Figure SI.II-1. Thermogravimetric analysis of $SPE_{18,16}$ and $si\text{-}SPE_{21,16}$ under air atmosphere at 10°C.min^{-1}.

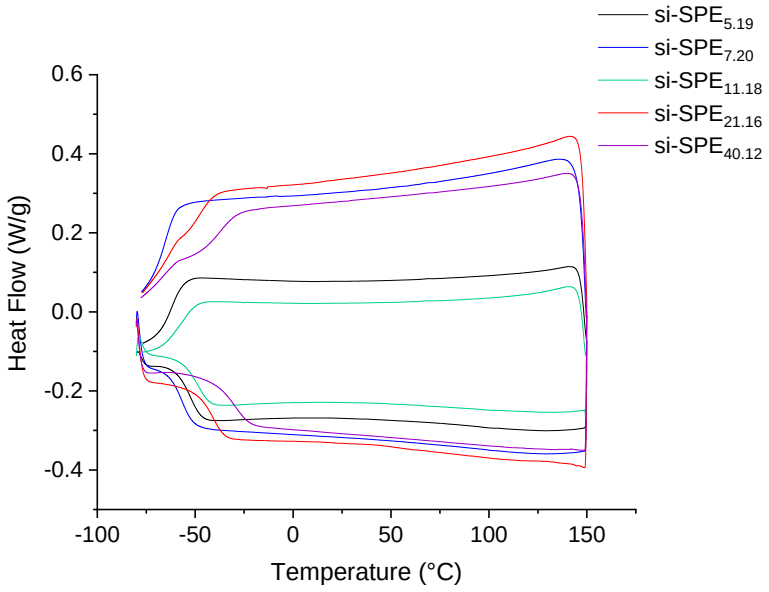

Figure SI.II-2. First DSC scans thermograms recorded on different si-SPE samples showing the absence of polymerization exotherm.

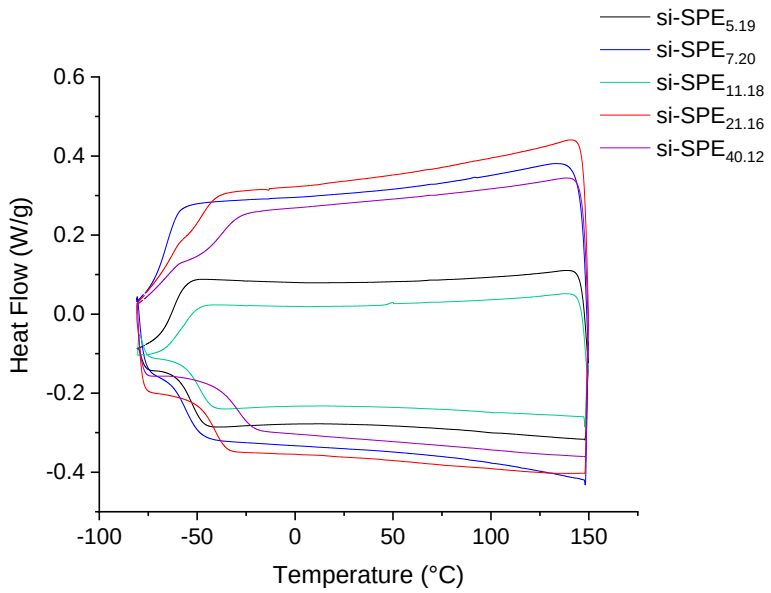

Figure SI.II-3. Second DSC scans recorded on different si-SPE samples showing the absence of crystallization exotherm**.**

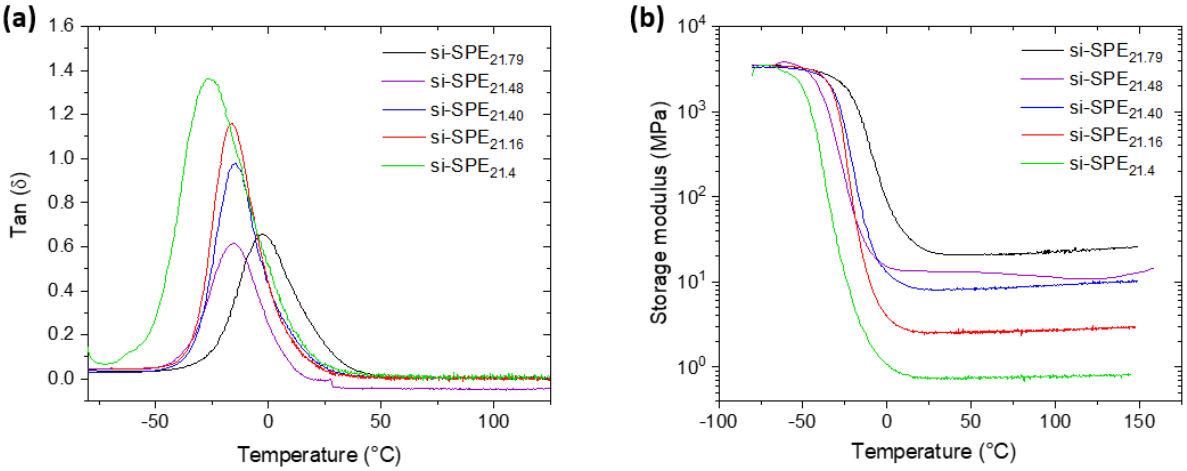

Figure SI.II-4. Tanδ (a) and storage modulus (E') (b) as function of temperature for various si-SPE$_{21,y}$ materials showing the absence of phase separation.

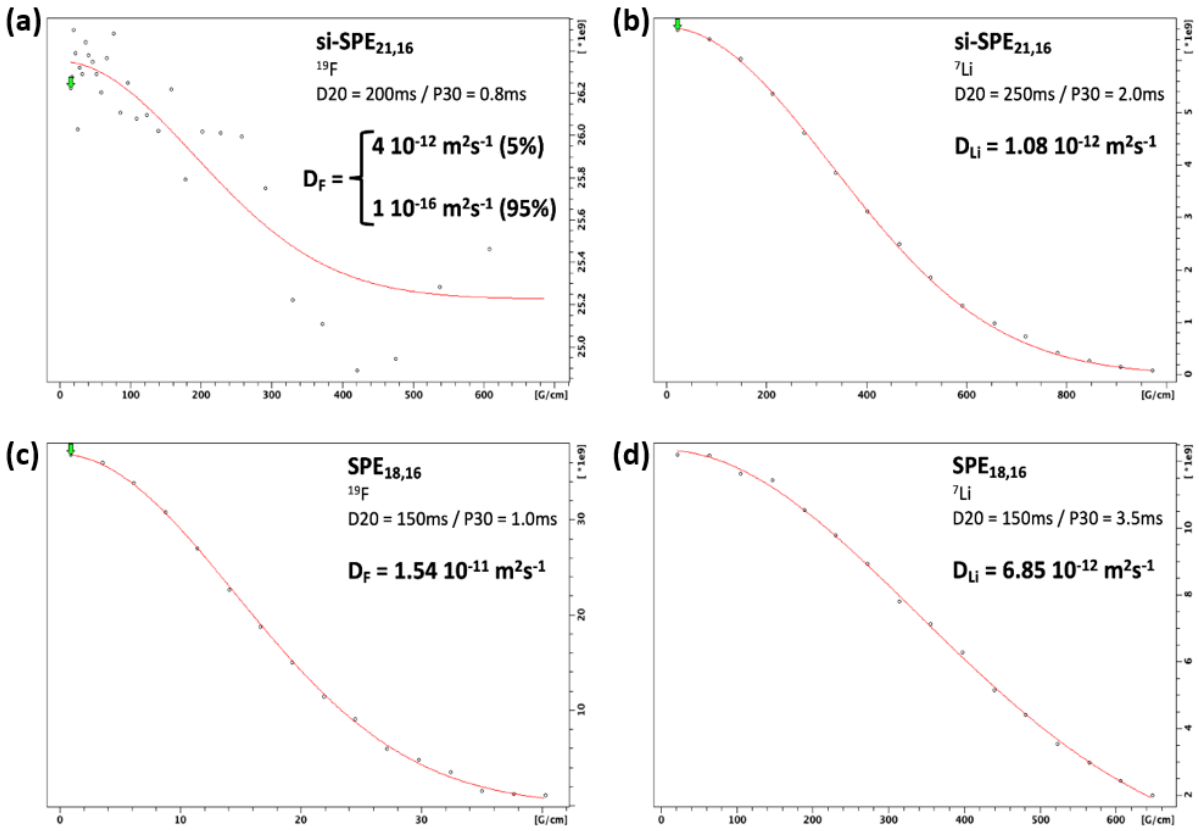

Figure SI.II-5**.** NMR experiments Attenuation curve for (a), (c) ^{19}F signal for si-$SPE_{21,16}$ and $SPE_{18,16}$ respectively and (b); (d) attenuation curve for ^{7}Li signal for si-$SPE_{21,16}$ and $SPE_{18,16}$ respectively.

The attenuation curve observed for the ^{19}F signal in si-$SPE_{21,16}$ (Figure SI-5a) shows almost no decay (~5%). It was yet fitted with 2 components to account for this weak decay. The major component corresponds to a diffusion coefficient that was set at $1.0.10^{-16}$ $m^2.s^{-1}$. It is associated to "immobile" species. The minor component corresponds to a diffusion coefficient of ~ 4.10^{-12} $m^2.s^{-1}$. This small amount of weakly mobile species could correspond to short oligomers or ends of chains.

Table SI.II-1. Comparison of lithium-ion transport number values for single-ion conducting electrolytes reported in literature.

Authors/Ref	**Polymer**	**Solvent**	**t^+**
Nguyen and al.[1]	Li-PVDF	DMF	0.87 ± 0.3
Bouchet and al.[2]	P(STFSILi)-b-PEO-b-P(STFSILi)	Dioxane	0.85
Porcarelli and al.[3]	LiMTFSI-PEGM-PEGDM	PC	0.84-0.91
Borzutzki and al.[4]	Polysulfonylamide (with -C(CF3)) / PVdF-HFP	THF	0.9
Porcarelli and al.[5]	poly(PEGM)-*b*-poly(LiMTFSI)	DMF	0.83
Feng and al.[6]	Li[PSTFSI-*co*-MPEGA]	DMF or MeOH	0.94
Rohan and al.[7]	MTF-Li/PVDF-HFP	DMF	0.88
Zhang and al.[8]	lithium poly (bisphenol A borate) / PEO	MeCN	0.92-0.96
Humbeck and al.[9]	Tetraarylborate polymer	DMSO, DMF, MeOH	0.89-0.93
Rolland and al.[10]	PS-*b*-P(MALi-*co*-POEGMA)	THF/MeOH	0.84
Pan and al.[11]	Lithiated poly(bis(4-carbonyl benzene sulfonyl)imide-co-bis(4-amino benzene sulfonyl)imide) / PVDF-HFP	NMP	0.92
Xu and al.[12]	lithium poly (glutaric acid aluminate)	DMF	0.8
Shi and al.[13]	PEO–PFSILi	MeCN	0.9
Inceoglu and al.[14]	PEO–PSLiTFSI	DMF	0.95
Nguyen and al.[15]	phenylsulfonyl(trifluoromethylsulfonyl)imide lithium salt / PEO	MeCN/H_2O	0.90-0.92
Li and al.[16]	Lithiated mimic neurons in PEGMA	Acetone	0.974

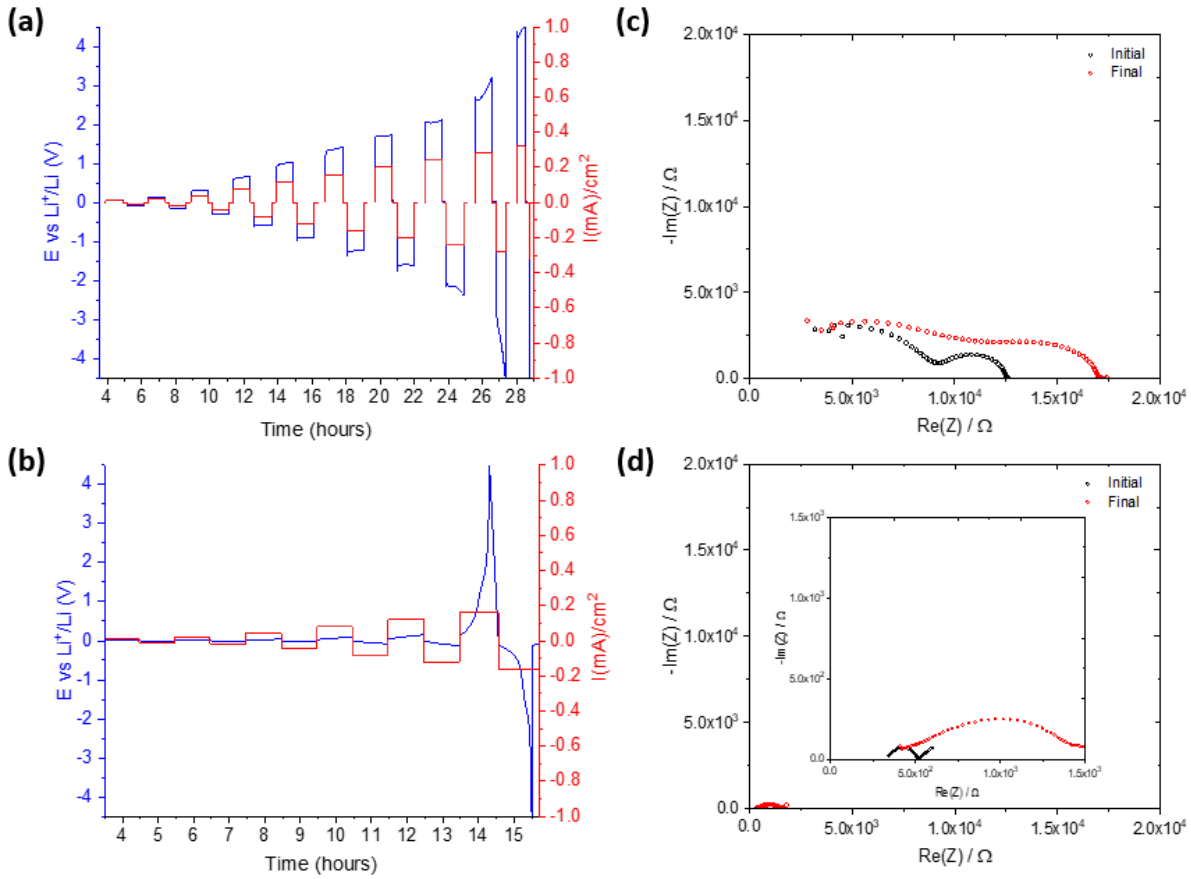

Figure SI.II-6. CCD determination at 70 °C of (a) Li/si-$SPE_{21,16}$/Li and (b) Li/$SPE_{18,16}$/Li and (c), (d) Nyquist plots of respective electrolyte before CCD determination (black) and after CCD determination (red) cycling.

The starting current density was 0.01 $mA.cm^{-2}$ and the current was subsequently doubled to achieve 0.08 $mA.cm^{-2}$ and after ramped by 0.04 $mA.cm^{-2}$ steps. The plating and stripping were performed respectively for 1 h and separated by a rest period of 5 min.

References:

(1) Nguyen, T. K. L.; Lopez, G.; Iojoiu, C.; Bouchet, R.; Ameduri, B. Novel Single-Ion Conducting Electrolytes Based on Vinylidene Fluoride Copolymer for Lithium Metal Batteries. J. Power Sources 2021, 498, 229920. https://doi.org/10.1016/j.jpowsour.2021.229920.

(2) Bouchet, R.; Maria, S.; Meziane, R.; Aboulaich, A.; Lienafa, L.; Bonnet, J.-P.; Phan, T. N. T.; Bertin, D.; Gigmes, D.; Devaux, D.; Denoyel, R.; Armand, M. Single-Ion BAB Triblock Copolymers as Highly Efficient Electrolytes for Lithium-Metal Batteries. Nat. Mater. 2013, 12 (5), 452–457. https://doi.org/10.1038/nmat3602.

(3) Porcarelli, L.; Shaplov, A. S.; Bella, F.; Nair, J. R.; Mecerreyes, D.; Gerbaldi, C. Single-Ion Conducting Polymer Electrolytes for Lithium Metal Polymer Batteries That Operate at Ambient Temperature. ACS Energy Lett. 2016, 1 (4), 678–682. https://doi.org/10.1021/acsenergylett.6b00216.

(4) Borzutzki, K.; Thienenkamp, J.; Diehl, M.; Winter, M.; Brunklaus, G. Fluorinated Polysulfonamide Based Single Ion Conducting Room Temperature Applicable Gel-Type Polymer Electrolytes for Lithium Ion Batteries. J. Mater. Chem. A 2019, 7 (1), 188–201. https://doi.org/10.1039/C8TA08391F.

(5) Porcarelli, L.; Shaplov, A. S.; Salsamendi, M.; Nair, J. R.; Vygodskii, Y. S.; Mecerreyes, D.; Gerbaldi, C. Single-Ion Block Copoly(Ionic Liquid)s as Electrolytes for All-Solid State Lithium Batteries. ACS Appl. Mater. Interfaces 2016, 8 (16), 10350–10359. https://doi.org/10.1021/acsami.6b01973.

(6) Feng, S.; Shi, D.; Liu, F.; Zheng, L.; Nie, J.; Feng, W.; Huang, X.; Armand, M.; Zhou, Z. Single Lithium-Ion Conducting Polymer Electrolytes Based on Poly[(4-Styrenesulfonyl)(Trifluoromethanesulfonyl)Imide] Anions. Electrochimica Acta 2013, 93, 254–263. https://doi.org/10.1016/j.electacta.2013.01.119.

(7) Rohan, R.; Pareek, K.; Cai, W.; Zhang, Y.; Xu, G.; Chen, Z.; Gao, Z.; Dan, Z.; Cheng, H. Melamine–Terephthalaldehyde–Lithium Complex: A Porous Organic Network Based Single Ion Electrolyte for Lithium Ion Batteries. J. Mater. Chem. A 2015, 3 (9), 5132–5139. https://doi.org/10.1039/C4TA06855F.

(8) Zhang, Y.; Cai, W.; Rohan, R.; Pan, M.; Liu, Y.; Liu, X.; Li, C.; Sun, Y.; Cheng, H. Toward Ambient Temperature Operation with All-Solid-State Lithium Metal Batteries with a Sp Boron-Based Solid Single Ion Conducting Polymer Electrolyte. J. Power Sources 2016, 306, 152–161. https://doi.org/10.1016/j.jpowsour.2015.12.010.

(9) Van Humbeck, J. F.; Aubrey, M. L.; Alsbaiee, A.; Ameloot, R.; Coates, G. W.; Dichtel, W. R.; Long, J. R. Tetraarylborate Polymer Networks as Single-Ion Conducting Solid Electrolytes. Chem. Sci. 2015, 6 (10), 5499–5505. https://doi.org/10.1039/C5SC02052B.

(10) Rolland, J.; Poggi, E.; Vlad, A.; Gohy, J.-F. Single-Ion Diblock Copolymers for Solid-State Polymer Electrolytes. Polymer 2015, 68, 344–352. https://doi.org/10.1016/j.polymer.2015.04.056.

(11) Pan, Q.; Zhang, W.; Pan, M.; Zhang, B.; Zeng, D.; Sun, Y.; Cheng, H. Construction of a Lithium Ion Transport Network in Cathode with Lithiated Bis(Benzene Sulfonyl)Imide Based Single Ion Polymer Ionomers. J. Power Sources 2015, 283, 279–288. https://doi.org/10.1016/j.jpowsour.2015.02.137.

(12) Xu, G.; Rohan, R.; Li, J.; Cheng, H. A Novel Sp 3 Al-Based Porous Single-Ion Polymer Electrolyte for Lithium Ion Batteries. RSC Adv. 2015, 5 (41), 32343–32349. https://doi.org/10.1039/C5RA01126D.

(13) Shi, Q.; Xue, L.; Qin, D.; Du, B.; Wang, J.; Chen, L. Single Ion Solid-State Composite Electrolytes with High Electrochemical Stability Based on a Poly(Perfluoroalkylsulfonyl)-Imide Ionene Polymer. J Mater Chem A 2014, 2 (38), 15952–15957. https://doi.org/10.1039/C4TA02810D.

(14) Inceoglu, S.; Rojas, A. A.; Devaux, D.; Chen, X. C.; Stone, G. M.; Balsara, N. P. Morphology–Conductivity Relationship of Single-Ion-Conducting Block Copolymer Electrolytes for Lithium Batteries. ACS Macro Lett. 2014, 3 (6), 510–514. https://doi.org/10.1021/mz5001948.

(15) Nguyen, N.; Blatt, M. P.; Kim, K.; Hallinan, D. T.; Kennemur, J. G. Investigating Miscibility and Lithium Ion Transport in Blends of Poly(Ethylene Oxide) with a Polyanion Containing Precisely-Spaced Delocalized Charges. Polym. Chem. 2022, 13 (29), 4309–4323. https://doi.org/10.1039/D2PY00605G.

(16) Li, Z.; Guo, D.; Li, F.; Hou, G.; Liu, X.; Li, C.; Cao, L.; Wei, R.; Zhou, Z.; Lai, Z. Nerve Network-Inspired Solid Polymer Electrolytes (NN-SPE) for Fast and Single-Ion Lithium Conduction. Energy Storage Mater. 2022, 49, 575–582. https://doi.org/10.1016/j.ensm.2022.05.003.

Chapter III.

Study of *Al*-LLZO morphology impact on ionic conductivity and mechanical properties of solid composite electrolyte

I. Introduction

Li-ion batteries are now the leading technology for energy storage[1]. Unfortunately, this technology uses liquid electrolytes containing inorganic solvents that are flammable and decompose at high voltage. Additionally, Li dendrites are easily formed in the presence of liquid electrolyte, which not only causes safety issues but also limits the use of Li-metal as negative electrode[2]. To circumvent all these limitations, the development of all-solid batteries (ASSB) has attracted a lot of interest[3]. They are considered as the next generation of electrochemical energy storage devices because of their safety and high energy density (400 $Wh.kg^{-1}$)[2]. Nevertheless, one of the challenges in designing ASSB is the development of a solid electrolyte with an ionic conductivity at room temperature (RT) equal to that of the liquid electrolyte (10^{-2} - 10^{-3} $S.cm^{-1}$) and with a wide window of electrochemical stability (> 4.5 V *vs.* Li^+/Li).

In the state of the art of this PhD manuscript (chapter I p.11-31), a variety of solid electrolytes were presented[4]. Briefly, solid polymer electrolytes (SPE) have demonstrated their interest regarding their manufacturing process, which can be easily transposed to the current battery manufacturing process. The most widely studied polymer as an SPE is polyethylene oxide (PEO).Wright et al.[5] has shown that PEO was a good matrix for solubilizing alkaline salts without using solvents. But, SPEs based on PEO exhibit satisfactory conductivity solely at high temperatures (10^{-3} $S.cm^{-1}$ at 60 °C)[6] with poor mechanical strength.[7] On the contrary, $Li_7La_2Zr_3O_{12}$ (LLZO) garnet appears to be a promising candidate because of its high ionic conductivity (~ 1.10^{-3} $S.cm^{-1}$), and its wide electrochemical stability window (0 to ~ 6 V *vs.* Li^+/Li)[8]. But to process it for ASSB, high temperatures (± 1000 °C) are needed to densify it in order to achieve the promising conductivity of 1.10^{-3} $S.cm^{-1}$ at room temperature[9]. This shows that none of the electrolytes pre-cited fulfill all together the criteria of high conductivity and easy processability. To prevent low conductivity of SPE, some strategies have proposed to disperse conductive or non-conductive inorganic particles in the SPE, leading to the synthesis of solid composite electrolyte (SCE)[10]. In the design of SCE, one of the objectives is to break the crystalline domains of the PEO polymer to enhance the ionic conductivity of the solid electrolyte at RT, but also to improve the mechanical properties at higher temperatures (> 60 °C)[11]. Generally, this SCE exhibits a low content in inorganic particles (≤ 30 wt%)[10].

Interestingly, adding inorganic particles in polymer can favor reactivity between the two phases, leading to the formation to solid interface[12]. Some studies have shown that the formation of this interface enhances the ionic conductivity of the SCE. Interestingly, other studies have shown the improvement of the ionic conductivity of the SCE due to a better dissociation of the Li-salt, due to interaction of anion with the LLZO particle[13,14].

In this work, we have chosen to design a predominantly polymeric SCE based on a PEO-LiTFSI network. This PEO network was synthesized from Poly(ethylene glycol) methyl ether methacrylate (PEGM) and Poly(ethylene glycol) dimethacrylate (PEGDM) as commercial liquid precursors. These monomers allow a solvent-free synthesis that will facilitate the impregnation by capillary of the $Li_{6.25}Al_{0.25}La_2Zr_3O_{12}$ (*Al*-LLZO) 3D scaffold, chosen for its ionic conductivity, its chemical stability toward PEO matrix and its wide electrochemical stability (> 6 V *vs.* Li^+/Li). To design the SCE, we have used two different strategies. First, we have dispersed the inorganic particles into the polymer precursor mixture before the polymerization was carried out. Second, we have designed a 3D ionic conductor inorganic scaffold that is further impregnated with the PEO precursor mixture which were then polymerized. The morphology and the microstructure of the SCE have been studied by scanning electron microscopy while the mechanical properties of the SCE by rheology measurements. The ionic conductivity at room temperature has been measured by impedance spectroscopy.

II. State of the art

The synthesis of LLZO particles were presented in Chapter I (p.20). There are three known synthesis methods for LLZO particles: solid-state, sol gel and Pechini method[15]. Another recently developed synthesis method for obtaining a new LLZO morphology is electrospinning, which will be described in detail in this section. We will discuss its definition and the history of the electrospinning method, before focusing on the synthesis of 3D LLZO scaffolds. Next, we will then present the various bibliographic references demonstrating their integration into SCE.

II.1. Electrospinning method and synthesis of LLZO 3D scaffold

II.1.1. Electrospinning: definition and history

Electrospinning (Figure III-1) enables the fabrication of fibers in the nanometer scale. This technique uses electrohydrodynamic processes to stretch and form fibers from a polymer

solution. During electrospinning process, the electrostatic forces overcome the surface tension of the electrospun solution allowing the stretching of the liquid as nanometer-scale fiber diameters. This approach allows the fabrication of nanofiber materials with unique properties and can find application in various fields[16].

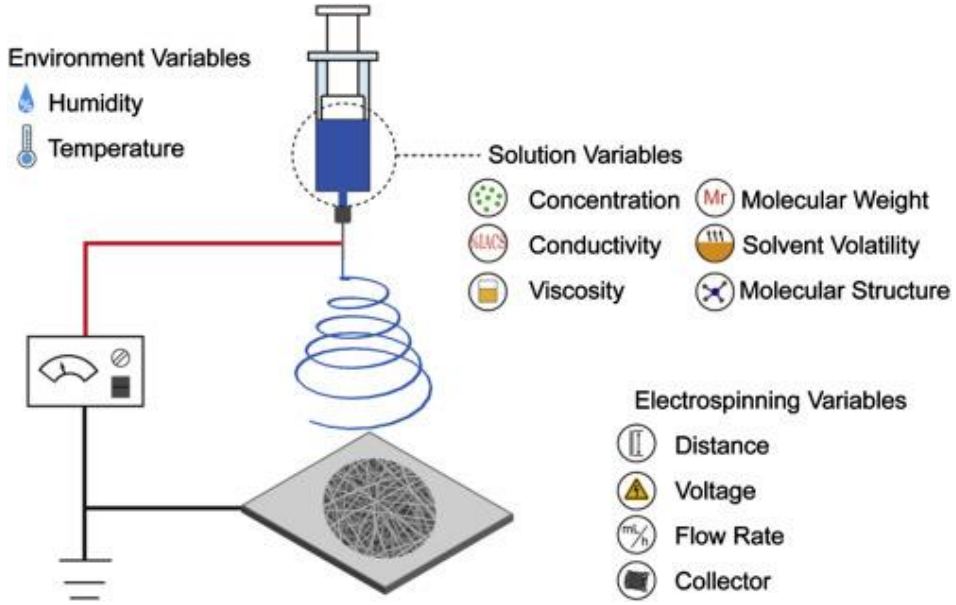

Figure III-1. Schematics of electrospinning set-up[17].

The electrospinning process involves five distinct steps that are summarized below.

- **Electrospinning solution**: A polymer is dissolved in a suitable solvent to form a liquid solution. The development of this solution is a critical parameter because it greatly affects the stretching of the jet. If the polymer concentration is too low, the applied electric field and surface tension cause the entangled polymer chains to break into fragments before reaching the collector. These fragments form beads or beaded nanofibers. Increasing the concentration of the polymer in the solution leads to an increase in viscosity due to the chain entanglements, which overcome the surface tension and ultimately result in uniform electrospun nanofibers. On the other hand, too high a concentration of the polymer solution hinders the flow of the solution through the needle. Depending on the choice of polymer and solvent, the optimal viscosity of the solution is not the same (800-4000 cp with 2.5 – 5 wt% of PEO in aqueous solution [18] or 1.7-215 cp with 7.5 – 20 wt% of polyacrylonitrile (PAN) in Dimethylformamide[19]). This choice is therefore crucial for forming homogeneous fibers. In addition, the choice of polymer and solvent depends on the desired properties of the final fibers, such as chemical composition and mechanical strength.

- **Electrostatic charging:** The polymer solution is placed in a specially designed syringe or reservoir, typically equipped with a fine needle at its tip. An electric voltage is applied between the needle's tip and a collecting surface located at a certain distance. The needle can be replaced by a nozzle or a core-shell reservoir.
- **Formation of the polymer jet**: When the electric voltage reaches a critical threshold, it induces an electric charge on the surface of the polymer liquid. The electrostatic charges repeal the liquid droplets towards the needle, forming a cone at its tip. This cone, known as the Taylor cone, is crucial for the electrospinning process.
- **Liquid Stretching and solvent evaporation**: The Taylor cone undergoes electrohydrodynamic instability, resulting in the stretching and thinning of the polymer liquid into a fine jet. As the jet travels towards the collecting surface, the solvent gradually evaporates, allowing the fiber to solidify and harden.
- **Fiber collection**: The solid, ultrafine, and electrostatically charged fibers are collected on the opposite surface, typically a plate or a rotating drum, forming an as-spun mat of fibers that deposit in a random or ordered manner, depending on the configuration of the collecting surface.

As shown in Figure III-1, many parameters need to be optimized during electrospinning. These parameters can affect the size and the orientation of the fibers, but also the thickness of the mat recovered.

The first patent was issued in 1902 by John Francis Cooley[20]. In 1934, Antonin Formhals invented the process for manufacturing textile yarns from cellulose acetate using an applied voltage of 57 kV and acetone and monomethyl ether as solvents[21]. This was followed by a number of patents, which described the process of preparing fine fibers by drawing spinning solutions through a nozzle using a high electric current.

Today, more than 200 universities and research institutes around the world are studying the electrospinning process, and every year the number of research papers on the electrospinning process increases[22]. Over the last ten years, some 35,000 papers have been published on the subject of electrospinning (Figure III-2).

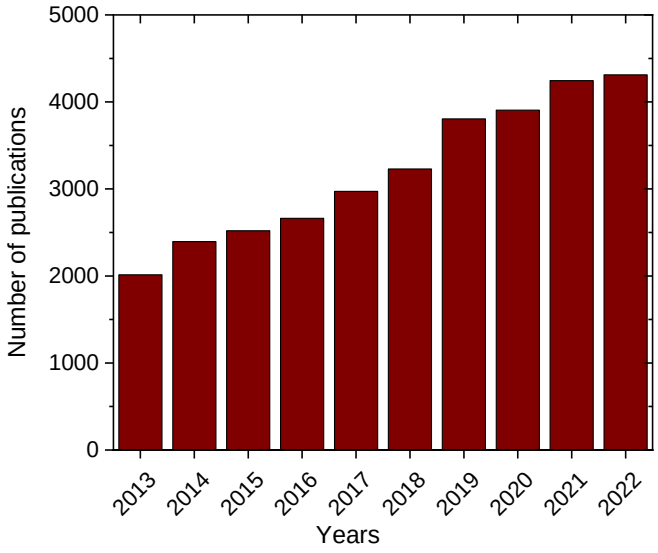

Figure III-2. Number of publications over the last 10 years. Generated from the website: webofscience.com on August 28th 2023.

The electrospinning method is widely used to produce polymer fibers, but has been less studied to form inorganic fibers. To do this, two approaches are used: i/ the inorganic particles are suspended in the polymer solution or ii/ the precursors of the inorganic compound are solubilized with the polymer solution. This method requires post heat-treatment, leading to decomposition of the polymer to form the inorganic scaffold.

II.1.2. Synthesis of oxides 3D scaffold

In early 2000, Li and Xia[23] described the electrospinning synthesis of an amorphous 1D TiO_2 structure, by mixing the inorganic precursors to the polymer solution. TiO_2 nanofibers (20-200 nm length) were prepared by calcining the as-spun mat composed of 3.4 wt% poly(vinyl pyrrolidone) (PVP) and 11 wt% titanium tetraisopropoxide in solution in acetic acid and ethanol.

Since the publication of this result, highly conductive Li ceramics have also been produced using the electrospinning method. In 2015, Yang et al.[24] described the electrospinning of LLZO nanofibers starting from the inorganic precursors. The electrospinning solution is composed of a 1:1 volume ratio between a solution containing Li, La and Zr nitrate precursors dissolved in dimethylformamide (DMF) with acetic acid and a solution with PVP (15 wt%) dissolved in acetic acid. The final solution contained 0.12 $mol.L^{-1}$ of inorganic precursors and 7.5 wt% of PVP. The solution was electrospinned onto a flat stationary collector at 10 cm from the needle, with a voltage of 7 kV and a flow rate of 0.12 $mL.h^{-1}$. The as-spun nanofibers exhibit

a diameter ranging from 100 to 200 nm (not shown). To obtain the cubic LLZO structure, a calcination at 700 °C for 3 or 5 h is necessary. During this treatment, the fibrous structure is lost while the particles seem to be sintered all together (Scanning Electron Microscopy (SEM) images in Figure III-3). This is a promising result, considering that cubic LLZO is typically achieved through a sintering temperature of ± 1000°C[9,25] (densified pellet). Regrettably, the authors did not report the formation of a self-standing membrane.

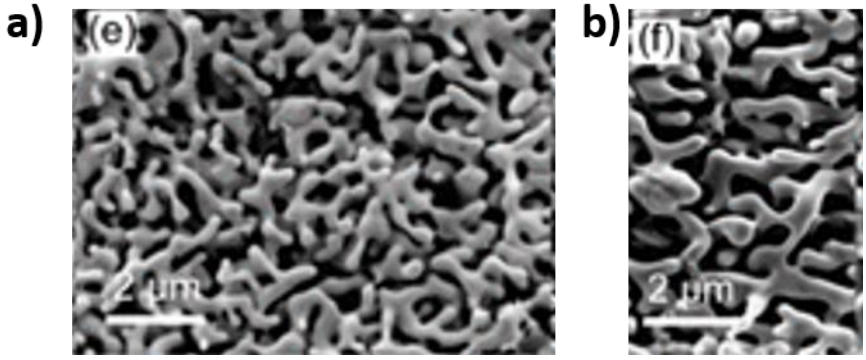

Figure III-3. SEM images of LLZO nanofibers after calcination at 700 °C for (a) 3 h and (b) 5 h[24].

Interestingly, in 2016 Fu et al.[26] reported the fabrication of a 3D percolative scaffold of *Al*-LLZO synthesis A stoichiometric quantity of *Al*-LLZO nitrate precursors was dissolved in dimethylformamide (DMF) with 15 vol% of acid acetic. 10 wt% of PVP was dissolved in DMF. The salt and PVP solutions were mixed at a 1:1 volume ratio. The solution was electrospinned onto drum collector (rotation speed not specified) at 10 cm from the needle and the voltage was high (20 kV). The as-spun nanofibers were then dried under vacuum for 24 h. The nanofiber as-spun mat was then calcinated with a heating rate of 10 °C.min^{-1} at 800 °C for 2 h in flow air to obtained the cubic *Al*-LLZO structure. After thermal treatment, the average diameter of the nanofibers measured by SEM image is 138 nm. According to this work, an inorganic membrane can be preserved as lately they used it as a scaffold for the fabrication of SCE (see section II.2.1). However, in the article, no image of the 3D *Al*-LLZO scaffold was reported.

More recently (2019), Zhao et al.[27] have shown the fabrication of a 3D *Al*-LLZO scaffold from an electrospinning solution using a binary H_2O:EtOH (1:1) mixture, a more friendly solvent (compare to DMF). The electrospun solution was made of 6.5 wt. % of PVP and a PVP:salt mass ratio of 1:4.4. The electrospinning process was carried out with a feed rate of 1 mL.h^{-1}, a voltage of 15 kV and a distance of 15 cm between the needle and the drum collector. The rotation speed was controlled to 60 revolutions per minutes (rpm). Importantly,

the humidity of the electrospinning chamber was close to 45% to control the morphology of the fiber and its solidification[28]. After electrospinning, the as-spun mats were kept in a vacuum oven at 60 °C for 2 h, and then they were calcined with a heating rate of 2 °C.min^{-1} at 800 °C in air for 4 h to obtain the cubic LLZO structure. Following calcination, they successfully obtained the cubic LLZO phase with a minority impurity phase (Figure III-4a). The resulting membrane appears to possess a considerable level of macro-porosity, as seen in Figure III-4b. Based on the SEM and Transmission Electron microscopy (TEM) images (Figure III-4c), the fibers exhibit a diameter of 245 nm and consist of sintered nanoscale particles bound together.

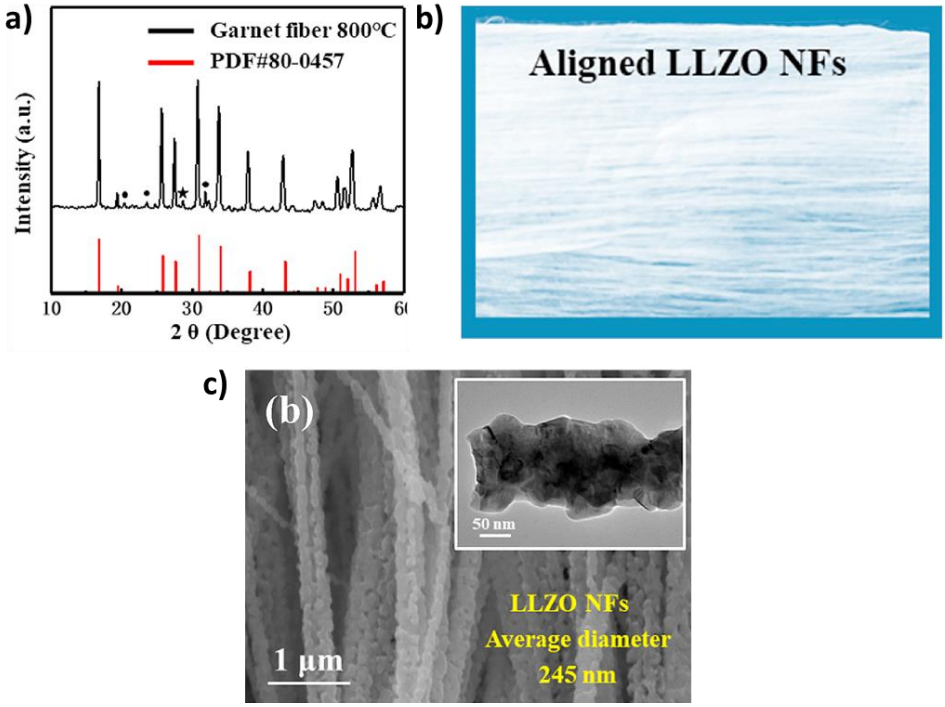

Figure III-4. (a) XRD patterns of LLZO nanofibers with PDF#80-0457 ($Li_5La_2Nb_2O_{12}$) as a reference: (•) unidentified intermediate phase; (★) $La_2Zr_2O_7$. (b) Digital image of the aligned LLZO nanofibers membrane and (c) SEM and TEM image of LLZO nanofibers[27].

According to the literature, fibers of cubic LLZO can be achieved but it seems to be difficult to obtain a self-standing 3D LLZO membrane, as few people have yet demonstrated. Importantly, none of the studies has measured the ionic conductivity of either 3D inorganic LLZO fibers or LLZO fibers pressed as pellets.

II.2. Fabrication of SCE

II.2.1. Fabrication of SCE based on PEO/3D LLZO scaffold

The presence of porosity in the 3D LLZO scaffold makes it possible to incorporate a polymer matrix and thus fabricate an SCE. Interestingly, the continuous 3D LLZO scaffolds may support Li transport in the interconnected LLZO nanofibers.

Fu et al.[26], whose description of the formation of the 3D scaffold is given above, described the preparation of a SCE from the 3D LLZO scaffold. For that, a PEO/LiTFSI/Acetonitrile (ACN) solution was dropped onto the 3D LLZO scaffold in order to impregnate it. After impregnation, the SCE was first dried in air and then under vacuum to fully remove the solvent. To improve both the infiltration of the 3D LLZO scaffold with the polymer and the contact at the nanofiber/PEO-LiTFSI interface, the SCE was heated at 60°C, which is close to the melting temperature (T_m) of the polymer (65 °C). The SPE obtained has a thickness of 40-50 µm, which is relatively thin compared to SIE (~1 mm for LLZO pellet[29]) but close enough to SPE (10-50 µm for BlueCar, Bolloré technology based on PEO/PVDF-HFP[30]). Thermogravimetric analysis (TGA) of the SCE showed that it is composed of around 20 wt% of LLZO. Electrochemical impedance spectroscopy (EIS) measurements showed an ionic conductivity of the SPE of $2.5.10^{-4}$ $S.cm^{-1}$ at RT, which is much lower than the one found classically for PEO-LiTFSI (between 10^{-6}-10^{-9} $S.cm^{-1}$ at RT[31]). Interestingly, this article shows an improvement in ionic conduction compared with the polymer matrix, and the achievement of a thin SCE. However, it was not discussed the impact of the addition of the 3D LLZO scaffold on the crystallinity of the PEO and the mechanism of conduction in this SCE. While the design of PEO-based SCEs with a 3D LLZO scaffold is recent, there are not many studies on the subject.

II.2.2. Fabrication of SCE based on PEO/LLZO particles

On the contrary, the synthesis of SCE from LLZO powder has reported in the literature and results have already been discussed in Chapter I (section III.3.2, p.25). In this part, we will concentrate our discussion on few examples. Chen et al.[11] reported the design of SCE combining PEO-LiTFSI polymer matrix and cubic LLZO particles in one-step using the tape casting process. First, PEO/LiTFSI was dissolved in ACN and then LLZO powder was added in different weight ratios varying from 2.5 to 10 wt%. The solution was poured onto a Teflon

plate and dried at 60 °C under vacuum for 24 hours. A maximum conductivity of $5.5.10^{-4}$ $S.cm^{-1}$ at RT is measured for a content of 7.5 wt% of LLZO and a thickness of 45 µm. The addition of LLZO therefore enabled a slight increase in ionic conductivity compared with the polymer matrix (10^{-5} $S.cm^{-1}$). They explain this gain in conductivity by the decrease in the crystalline phase of PEO due to the addition of inorganic LLZO particles. This is confirmed by differential scanning calorimetry (DSC) analyses, with PEO crystallinity decreasing from 53.83% to 21.63% as the amount of LLZO increases from 0 to 7.5wt% respectively. However, for higher concentration of LLZO (10 wt%), the crystallinity ratio increases compared to 7.5 wt% concentration, due to the difficulty in dispersing the LLZO inorganic particles in the PEO matrix. In addition, they describe a positive synergy between LLZO and PEO-matrix in the transport of Li^+: there is an improvement of the concentration of free Li^+ due to the attraction of the anion $TFSI^-$ with the LLZO surface[14]. In this article, the LLZO inorganic particles were introduced in small quantities, so as they are not percolated and cannot support the Li^+ diffusion through a continuous pathway.

In contrast, Choi et al.[32] studied SCEs with much higher contents of LLZO (42.5 to 82.5 wt%). PEO, $LiClO_4$ and LLZO (tetragonal phase) were mixed in ACN, and the slurry was casted onto a glass plate. The solvent was evaporated at RT in a dry room and the final thickness of SCE is around 100 µm. The highest conductivity obtained was $4.42.10^{-4}$ $S.cm^{-1}$ at 55 °C and around 10^{-5} $S.cm^{-1}$ at 35 °C for an amount of 52.5 wt% of LLZO in SCE. The conductivity increases by three orders of magnitude compared to the one observed for PEO-$LiClO_4$ (around 10^{-8} $S.cm^{-1}$ at 35 °C) and two order of magnitude compared to that of tetragonal LLZO pellet (around 10^{-7} $S.cm^{-1}$ at RT). In this case, we suppose that the LLZO is percolated and can support Li^+ diffusion. Additionally, the increase in conductivity can also be attributed to the decrease of the crystalline phase proportion in the PEO matrix that was confirmed by DSC analysis.

II.3. Conclusion

Finally, whatever the morphology (3D scaffold or particle), the structure (cubic or tetragonal) of the LLZO and the quantity introduced into the SCE, the ionic conductivity is driven by the polymer phase or the LLZO||PEO interface. In general, the improvement in conductivity is due to the reduction in the crystalline domain of PEO matrix with the introduction of LLZO. However, it has been suggested that LLZO can also participate in ionic transport by increasing the concentration of free Li^+ and in a better dissociation of ion pairs.

In Chapter II, we have reported the synthesis of two PEO networks: i/ one contains Li salt (PEO-LiTFSI, called SPE in Chapter II), ii/ the second one is single-ion SPE containing Li^+ as the TFSI counter-anion is grafted onto the PEO chains (si-SPE). Unfortunately, the conductivities of these two PEO networks (10^{-5} and 10^{-7} S.cm^{-1} at RT for PEO-LiTFSI and for si-SPE, respectively) are insufficient to be directly integrated into ASSB. Furthermore, it was difficult to manufacture them as a self-standing membrane with a thickness < 100 µm. In this chapter, we have studied the opportunity to fabricate SCE based on PEO-LiTFSI network and *Al*-LLZO. To control the properties of the SCE, we have proposed to synthesize two different SCE, exhibiting two different microstructures by using different processing methodologies:

i/ an one-step approach that consists in casting a solution containing the pre-dispersed inorganic LLZO particles into a liquid monomer mixture. One of the main benefits of this method is that the monomer mixture can be quickly polymerized without any visual particle sedimentation and the need for additional organic solvent.

ii/ a two-step approach that consists in the synthesis a porous 3D LLZO scaffold that is then impregnated by the liquid monomer mixture. The benefits of using liquid monomer allows an impregnation of the *Al*-LLZO 3D scaffold without solvent. In addition, the in-situ thermal polymerisation leading to the PEO-network is carried out without the addition of organic solvent. These both points are the originality of our work compared to previously studies.

III. Methods

III.1. Materials

Poly(ethylene glycol) methyl ether methacrylate (PEGM, M_n = 500 g.mol^{-1}, Sigma Aldrich) and poly(ethylene glycol) dimethacrylate (PEGDM, Mn=750 g.mol^{-1}, Sigma Aldrich) were dried at 25 °C under vacuum (10-15 mbar) before use. 2,2′-azobis(2-methylpropionitrile) (AIBN, initiator, 98%, Sigma Aldrich) was recrystallized in methanol before use. Bis(trifluoromethylsulfonyl) amine lithium salt (LiTFSI, > 99%, Sigma Aldrich), lithium metal (99.9% Sigma Aldrich, 0.38mm thick) and $Li_{6.25}Al_{0.25}La_2Zr_3O_{12}$ (*Al*-LLZO, 400 to 600 nm D50, Ampcera) were kept in the glove box (H_2O < 0.1 ppm) to avoid any modification.

For the synthesis of 3D *Al*-LLZO scaffold, $LiNO_3$ (99.99% trace metals basis Sigma Aldrich), $La(NO_3)_3.6H_2O$ (99.99% Sigma Aldrich), $Al(NO_3)_3.9H_2O$ (≥ 98%, Sigma Aldrich), $Zr(OCH_2CH_2CH_3)_4$ (Zirconium Propoxide 70wt% in 1-propanol, Sigma Aldrich), Polyvinylpyrrolidone (PVP, $(C_6H_9NO)_n$, M_w 1,300,000, K85-95, Acros), CH_3COOH (Acetic

acid glacial, Carlo Erba Reagents) and EtOH (Absolute, Sigma Aldrich) have been used as received.

III.2. Materials procedure

Procedure for PEO-LiTFSI precursor solution and synthesis of the membranes: detailed can be seen in Chapter II section II.2 (p.59). The PEO-LiTFSI network precursor solution uses PEGM and PEGDM monomers, while the PEO-LiTFSI brush solution uses only the PEGM monomer.

Procedure for producing the electrospinning solution: Only the solution leading to the fabrication of pure 3D *Al*-LLZO will be detailed in this section, while the other tested solutions will be included in the appendix 1. Firstly, 4.4 wt% of PVP were dissolved at RT in a binary EtOH:H_2O (1:1) solvent. In parallel, Zirconium propoxide and 8 equivalents of acetic acid were stirred at RT until the solution becomes milky white (approximately 3-4 h). Then PVP solution was added to it. After, stoichiometric amounts of nitrate salts (Li, La, and Al) were added one by one, ensuring that each salt is completed dissolved before the addition of the next one (approximately 2 h for each salt). The concentration of nitrate salts in the final solution is 1.19 $mol.L^{-1}$ except an excess of 15 wt% of $LiNO_3$ was added to compensate the Li-loss during heat treatment at high temperature[33,34]. The final solution is colorless and slightly viscous.

Procedure for fabrication of 3D *Al*-LLZO scaffold: An industrial-scale electrospinning equipment (Inovenso, Nanospinner) was used. The electrospinning process was carried out at a flow rate of 2 to 3 $mL.h^{-1}$. A voltage between 20-23 kV was applied, and a distance of 15 cm was maintained between the nozzle and the drum collector. The rotation speed was set at 600 rpm, and the humidity level was fixed at ~10% relative humidity (RH). The electrospinning tests were carried out at room temperature (25 ± 5 °C).

The as-spun mats were collected from the drum collector onto an aluminum foil and carefully peeled off to be stored in parchment paper.

For membrane densification, three pieces of as-spun mats were stacked on top of each other and placed between two parchment papers. Using a manual press (Scamex 20T), a pressure of 100 bars at 50 °C was applied for 10 min. The pressed as-spun mats were then recovered and placed in an alumina crucible for calcination. The thermal treatment was conducted in a tubular furnace (Nabertherme) with a dry air flow (0.8 $L.min^{-1}$). A heating program of 200°C for 2h and 850°C for 4h with a ramp rate of 5 $°C.min^{-1}$ between each temperature was applied. The

resulting 3D *Al*-LLZO scaffold is white, very brittle and its thickness varies around 10 - 20 µm (see images Appendix 1, test 7). It was then recovered and stored in a glove box.

Procedure to obtain SCE composed of 3D *Al*-LLZO$_{scaffold}$ and PEO-LiTFSI (network or brush):

In the glove box, the 3D *Al*-LLZO scaffold was placed on a glass plate. Using a glass pipette, drops of the PEO-LiTFSI precursor solution were deposited at the corners of the scaffold. Once it was impregnated (appearing wet), the glass plate was placed on a heating plate with a glass dome covered with aluminum foil. A thermal program of 70 °C for 2 h and 90 °C for 1 h was applied to polymerize the PEO precursor mixture. Once the plate has cooled down to RT, the resulting membrane was stored in the glove box. It retains a white color, is self-supporting and is approximately 20-40 µm thick.

Procedure to obtain SCE composed of *Al*-LLZO$_{particle}$ and PEO-LiTFSI (network or brush): 24 wt% *Al*-LLZO particles were introduced in PEO-LiTFSI precursor solution in a glove box. The mixture was stirred using a magnetic bar for 2 h. The solution was then cast between two glass plates (following the same process as for the fabrication of polymer membranes, Chapter II section II.2 p.59) separated with a Teflon mold of 75 µm and 250 µm thickness. The solution was then polymerized at 70 °C for 2 h and at 90 °C for 1 h in an oven. The resulting SCE were dried under vacuum (10-15 mbar) at 70 °C in a glass oven (BUCHI B-585) for 12 h to avoid any presence of H_2O. The membranes were kept in a glove box (H_2O < 0.1 ppm) upon to their characterization. SCE are named *Al*-LLZO$_{particle}$/PEO-LiTFSI network and *Al*-LLZO$_{particle}$/PEO-LiTFSI brush when the precursor solution used is PEO-LiTFSI network and PEO-LiTFSI brush, respectively. Images of these membranes are shown in Appendix 2.

III.3. Characterizations

Electrochemical impedance spectroscopy (EIS) was carried out using the same methodology as in Chapter II section II.3 (p.61).

When a pressure of more than 0.4 MPa is required, a cell designated for ASSB testing was used (designed by Romain Dugas, College de France). The figure in Appendix 3 shows the structure of this cell. The SCE was placed in the center of this cell and using a set of screws and a dynamo wrench, pressures of up to 110 MPa can be applied.

To estimate the ionic conductivity of the samples, the intercept of the first semicircle (high frequency) was considered and it corresponds to the bulk resistance (R_{bulk}) from which the conductivity was estimated by using the following relation:

$$\sigma = \frac{e}{R_{bulk} * S} \qquad \text{Equation 1}$$

where *e* (cm) is the thickness and *S* (cm^2) the surface area of the sample.

Thermogravimetric analysis (TGA): The thermal properties were performed using same method of Chapter II section II.3 (p.61).

X-ray diffraction (XRD): The identification of crystalline phases was performed using a D8-Advance diffractometer with a Cu-Kα source equipped with a LynxEye detector. X-ray diffraction data were analyzed using the DIFFRAC.EVA software.

Rheological measurements: The shear modulus was estimated from the slope of shear stress as a function of shear strain (first 5 points) obtained by rheological measurement using plate-plate configuration on a rheometer (Anton Paar, MCR 302) with an 8 mm insert. A controlled amplitude oscillatory test was employed, with a linear shear strain ramp ranging from 1% to 10%, while maintaining a constant frequency of 0.01 Hz.

Morphology analysis: To study the morphology of both 3D *Al*-LLZO scaffold and SCE, imaging was performed using a Hitachi FEG-SEM (Field Emission Gun Scanning Electron Microscope) model Su-70 at an acceleration voltage of 10 kV.

The Lithium-ion transport number: the stability in potential and stripping plating measurements were carried using the same method as in Chapter II section II.3 (p.62). On Nyquist plot, the bulk resistance corresponds to the first semi-circle (high frequency) according to the characteristic frequencies of the bulk SPE. The bulk resistance was measured before (R^0_{bulk}) and after (R^∞_{bulk}) polarization. The second cycle at low frequency correspond to the response of the Li||SCE interface before (R^0_{int}) and after polarization (R^∞_{int}), according to their characteristic frequencies of ~ few Hz. t_{Li+} was calculated using the following equation[35]:

$$t_{Li+} = \frac{i^\infty * R^\infty_{bulk} * (\Delta V - i^0 * R^0_{int})}{i^0 * R^0_{bulk} * (\Delta V - i^\infty * R^\infty_{int})} \qquad \text{Equation 2}$$

IV. Results and discussion

SPE based on linear PEO/Li-salt exhibits low conductivity at RT (10^{-6}-10^{-9} $S.cm^{-1}$) mainly due to its semi-crystalline characteristic, reducing the mobility of Li^+ [31]. Chapter II has reported the synthesis of amorphous cross-linked PEO/LiTFSI network having ionic

conductivity of 10^{-5} S.cm^{-1} at 25 °C. But, this conductivity is still low, compared to liquid electrolyte. To implement this SPE in ASSB, different strategies can be envisioned: i/ reduce the thickness of the electrolyte in order to reach low ohmic resistance or ii/ improve the ionic conductivity through a highly advanced strategy that consists in incorporating inorganic particles or 3D inorganic scaffold[10,26].

IV.1. Elaboration of SCE with *Al*-LLZO particles

Lechartier et al.[36] have previously reported the fabrication of a SCE using identical monomer precursors (ratio PEGM :PEGDM, 12 :88 in weight), 5.8 wt% of LiTFSI, 26 wt% of LLZO particles and with the addition of 37.5 wt% of propylene carbonate (PC), which is not our case. Unfortunately, only NMR study are available for this SCE. On the other hand, a more detailed study was carried out in this article, on an SCE replacing LiTFSI with a LiMTFSI monomer (like si-SPE, Chapter II). The ionic conductivity was measured within a range of 5.10^{-5} to 1.10^{-4} S.cm^{-1} at 25 °C for LLZO quantities ranging from 0 to 50 wt%. They have demonstrated interesting ionic conductivity of 1.4 x 10^{-4} S.cm^{-1} at 25 °C for 40 wt% of LLZO and high transference number (t^+ = 0.57 for 26 wt% of LLZO). This value is surprisingly low for an SCE whose anion is supposed to be grafted and therefore non-mobile.

In our study, we have chosen to design SCE electrolyte containing 24 wt% (7 vol%) of *Al*-LLZO with LiTFSI as source of Li in organic phase. This SCE is named *Al*-LLZO$_{particle}$/PEO-LiTFSI network. The polymer precursor solution is prepared following the procedure described in Chapter II and the design of the *Al*-LLZO$_{particle}$/PEO-LiTFSI network is carried out according to the detailed procedure in the section III.2. This SCE is self-standing, flexible and visually homogenous white. It could be manufactured with a thickness of 75 and 250 µm (Appendix 2). FEG-SEM images and EDX mapping (Figure III-5) show good dispersion of LLZO particles across the SCE thickness.

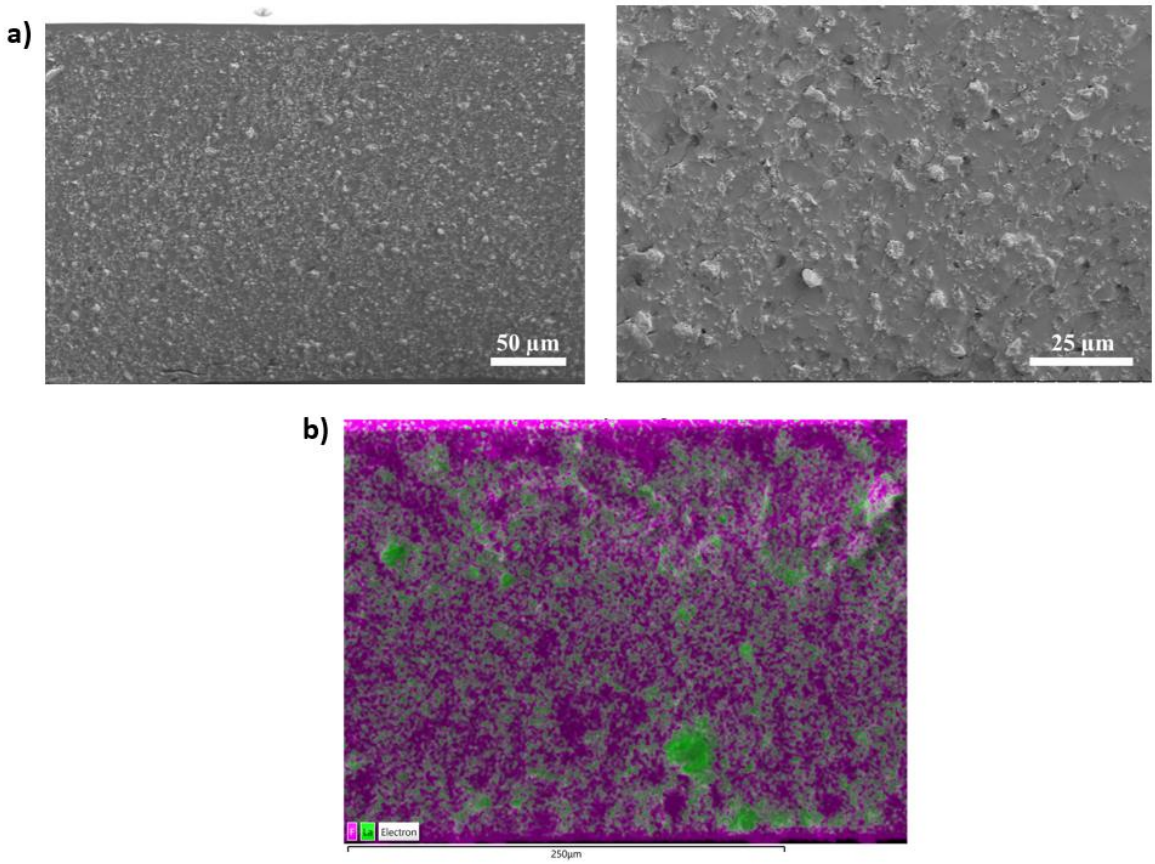

Figure III-5. (a) FEG-SEM images and (b) EDX mapping of *Al*-LLZO$_{particle}$/PEO-LiTFSI network cross-section.

These observations are very encouraging as it was impossible to fabricate self-standing PEO-LiTFSI network with this proportion of PEGM:PEGDM (80:20) with a thickness of 75µm. To confirm these visual observations, the shear moduli were estimated from rheologic measurements. The values of 0.11 and 0.16 MPa are measured for PEO-LiTFSI network and *Al*-LLZO$_{particle}$/PEO-LiTFSI network membrane, respectively. Contrary to their macroscopic mechanic properties, these two materials therefore have the same shear modulus. Similarly, the ionic conductivity of the *Al*-LLZO$_{particle}$/PEO-LiTFSI network (results reported in the Appendix 4) was equal to 8.10^{-6} S.cm^{-1} at 25 °C. This value is close to the one observed for PEO-LiTFSI network, demonstrating that there is no improvement in ionic conductivity in the SCE. Since it was difficult to achieve higher concentration of *Al*-LLZO particles in SCE keeping good homogeneity of membrane and that the quantity of *Al*-LLZO particles added is low to achieve the percolation of the inorganic network, we have decided to synthesize SCE using a continuous *Al*-LLZO scaffold.

IV.2. SCE with 3D *Al*-LLZO$_{scaffold}$

IV.2.1. Elaboration of 3D *Al*-LLZO$_{scaffold}$

IV.2.1.1. Elaboration of as-spun 3D scaffold

Appendix 1 shows the non-exhaustive list of different tests carried out to obtain a self-standing membrane by electrospinning using PVP as supporting polymer. We set the electrospinning voltage to 20-23 kV, the needle distance to the collection drum to 15 cm, and carefully set the collection drum speed to 600 rpm. A binary EtOH:H_2O (1:1) or a tertiary EtOH:DMF:H_2O (0.67:0.22:0.11) mixture was employed as the solvent, based on the works of Zhao et al.[27] or Rosenthal et al[37], respectively. Based on this literature, the inorganic precursor concentrations were set at 1.19 and 0.12 mol.L^{-1} for the tertiary and binary solutions, respectively. Unfortunately, the concentration of 0.12 mol.L^{-1} was not sufficient to achieve a self-supporting membrane after heat treatment (see picture test 1 in Appendix 1). The rest of the study will therefore be carried out with the electrospinning solution having a concentration in inorganic precursor of 1.19 mol.L^{-1} in a binary EtOH:H_2O (1:1) and 4.4 wt% of PVP (test 7 in Appendix 1).

The appearance of the as-spun mat was investigated by FEG-SEM imaging (Figure III-6). A diameter of around 1-3 µm is observed in the FEG-SEM images. This is higher than the diameter measured (577 nm) in the literature[27]. The difference can be linked to the electrospinning parameters that differ (feed rate of 1 mL.h^{-1}; voltage 15 kV; distance of 15 cm; rotation speed of 60 rpm; 45% RH). In this study, the RH imposed during electrospinning is lower (~10% RH), the rotation speed is faster (600 rpm), the voltage is higher (20-23 kV) and as well as the solution flow rate (2-3 mL.h^{-1}).

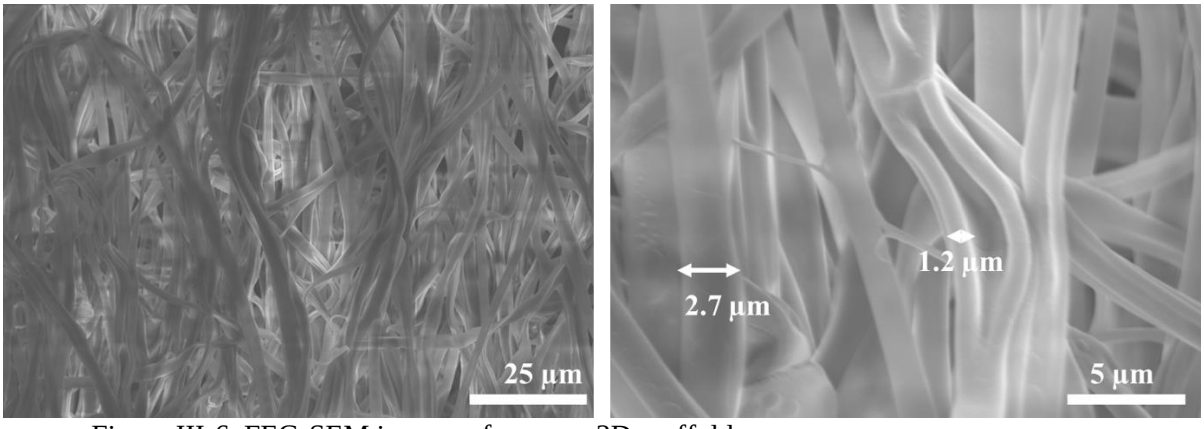

Figure III-6. FEG-SEM images of as-spun 3D scaffold.

IV.2.1.2. Optimisation of the thermal treatment

After selecting the appropriate electrospinning solution, the cubic-LLZO scaffold was obtained by sintering and removing the PVP polymer. The heat-treatment was performed in tubular furnace in dry air (flow 0.8 $L.min^{-1}$). To avoid the formation of Lithium carbonate. A thorough investigation of the heat treatment process was undertaken. The heat-treatment was the following:

- a heating ramp of 5 $°C.min^{-1}$ up to 200°C and a dwelling at this temperature for 2 h, to gently decompose the PVP (TGA analysis, Appendix 5)
- a heating ramp of 5 $°C.min^{-1}$ up to 750°C, 800°C, 850°C, 900°C or 1000°C for 4 hours to nucleate and sinter the LLZO particles.

The XRD analyses (Figure III-7a) were performed to determine the temperature and duration needed to achieve the pure cubic phase.

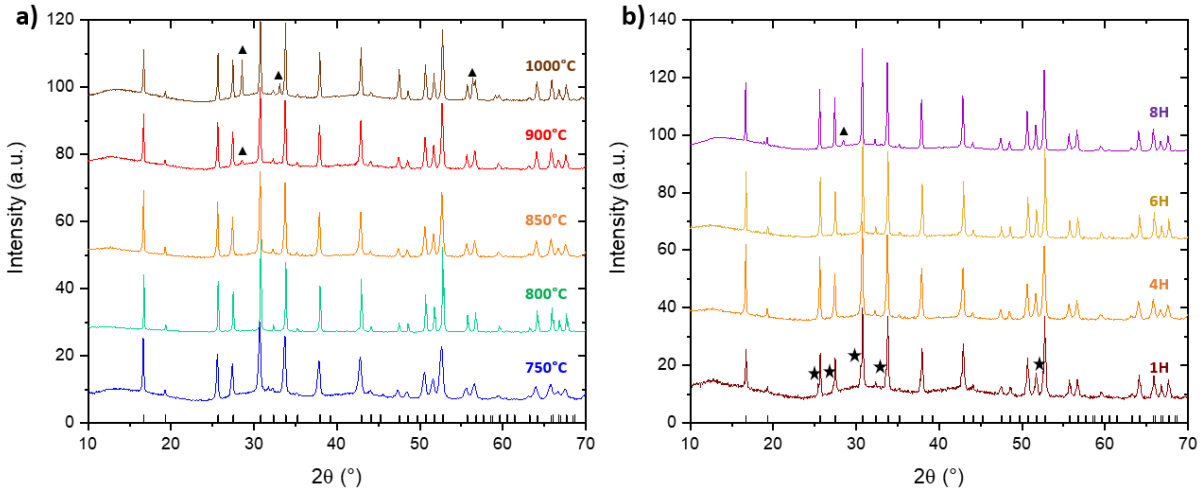

Figure III-7. XRD patterns of the various LLZO scaffold calcination at different (a) temperatures and (b) dwelling time at 850°C. PDF#01-084-7686 (*Al*-LLZO cubic) is used as a reference (|). (▲) $La_2Zr_2O_7$ (Pyrochlore) (★) LLZO tetragonal

Interestingly, the cubic phase is achieved at 750 °C. The attainment of the cubic phase at such a low temperature is likely attributed to the high specific surface area of the 3D *Al*-LLZO membrane compared to conventionally densified pellets[29]. However, for heat-treatment higher than 900 °C, a pyrochlore impurity appears due to lithium loss during the heat treatment[33]. Consequently, the temperature of 850 °°C is chosen to improve sintering between particles and avoid the apparition of secondary phases. In order to optimize sintering between the particles, we have studied the impact of the dwelling time at this temperature (going from

1 h to 8h) and the diffractograms were reported in Figure III-7b. It can be seen i/ the presence of the tetragonal phase with a dwelling time of 1 h and ii/ the appearance of the pyrochlore phase after a dwelling time of 8 h. Accordingly, we have selected the dwelling time of 4 hours. The obtained 3D *Al*-LLZO$_{scaffold}$ is very fragile and exhibit a thickness of 40 µm (see picture Appendix 1, test 7).

The overall morphology of the 3D *Al*-LLZO$_{scaffold}$ has been then studied by FEG-SEM analyses and the results were reported in Figure III-8. The FEG-SEM images reveal that the inorganic scaffold is continuous and retains the three-dimensional structure obtained by electrospinning. The fiber diameters range is around 1-1.5 µm. Interestingly, the fibers appear to be interconnected and consist of sintered *Al*-LLZO microparticles of ~1 µm, which is comparable to the diameter of the fibers. There features are promising as they can provide mechanical support and a continuous pathway for Li^+ transport. Unfortunately, it was not possible to determine the ionic conductivity of this scaffold due to its brittle structure.

Importantly, the significant porosity in the 3D *Al*-LLZO$_{scaffold}$ can be used to efficient infiltrate the monomer mixture for SCE synthesis.

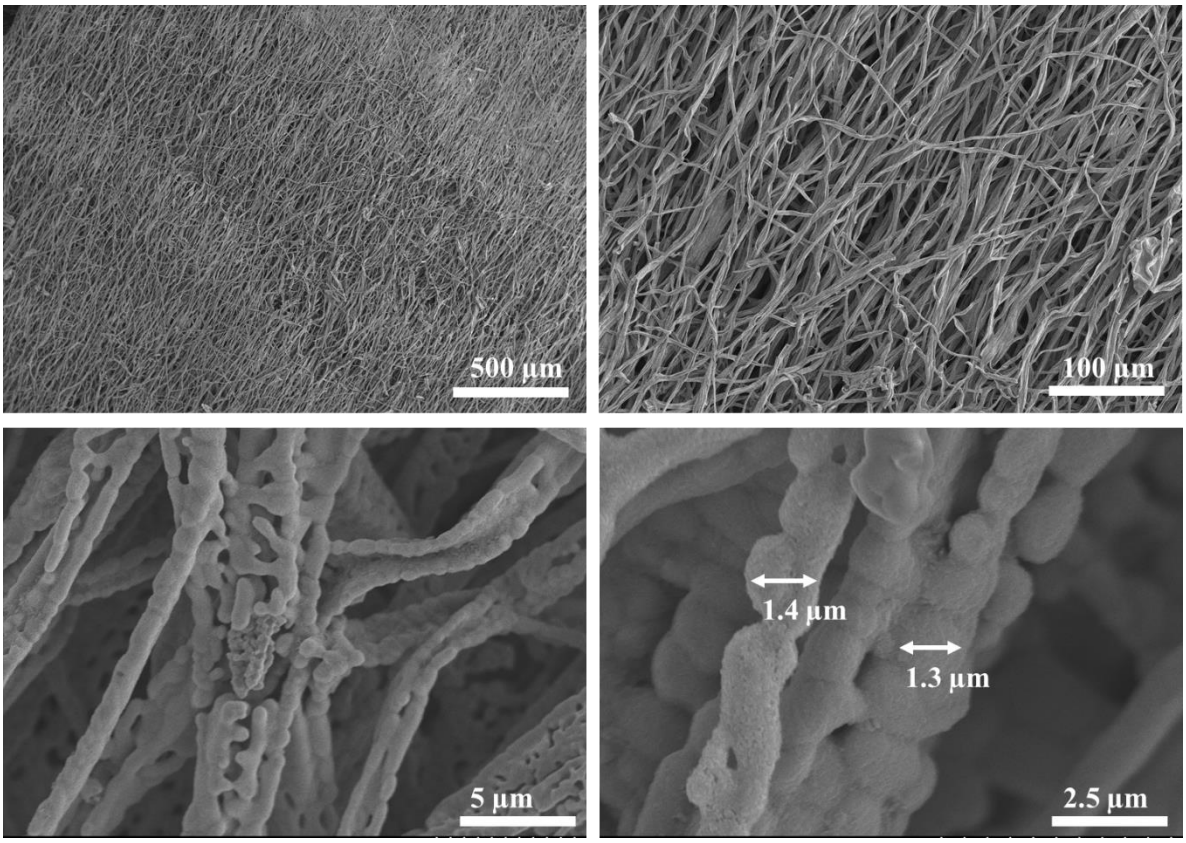

Figure III-8. FEG-SEM images of 3D *Al*-LLZO$_{scaffold}$.

IV.2.2. Elaboration of SCE with 3D *Al*-LLZO$_{scaffold}$

To synthesize the SCE, the 3D *Al*-LLZO scaffold was impregnated with the PEO-LiTFSI network precursor solution through capillary method. The PEO-LiTFSI network precursor solution was deposited drop-by-drop on the 4 corners of the 3D scaffold, enabling the polymer to infiltrate the scaffold's structure. Once the entire scaffold has been wetted by the PEO-LiTFSI network precursor solution, a heat treatment of 70 °C for 2 h and 90°C for 1 h, generally used for the synthesis of the PEO network (Chapter II – section II.2, p.59) was applied on a hot plate with an aluminum-covered glass dome inside a glove box. Finally, we obtain the SCE *Al*-LLZO$_{scaffold}$/PEO-LiTFSI network.

The volumetric concentration of PEO network was estimated by weighing the membrane before and after impregnation. The *Al*-LLZO$_{scaffold}$/ PEO-LiTFSI network contains 30 wt% of *Al*-LLZO (i.e 9 vol%). To confirm this result, we have performed TGA analysis (Appendix 6). The TGA analysis exhibits a one-step degradation process, initiated at around 200°C, that was mostly attributed to the degradation of the polymeric matrix. The residue at 600°C correspond to the composition of the inorganic LLZO content in the SCE. A value of 30 wt% is observed, indicating around 9 vol% of *Al*-LLZO. Accordingly, we have 70 wt% of polymer, if the mass loss of *Al*-LLZO$_{scaffold}$ is not considered. If we consider the mass loss of inorganic (10%), the weight proportion of polymer is 60%. This difference can be explained by adsorption of water and CO_2 at the surface of *Al*-LLZO$_{scaffold}$ during the preparation and stabilization of sample in the TGA.

To observe the morphology of the SCE, FEG-SEM analyses were conducted (Figure III-9). Figure III-9 shows the view of the cross-section (made in liquid nitrogen) and the top view of the composite membrane. It is interesting to note that all the fibers appear to be covered by a layer of polymer, and at the same time, the porosity of the 3D *Al*-LLZO$_{scaffold}$ appears to be appropriately filled. Thus, the polymerization did not degrade the morphology of the fibers. The polymer-coated fibers appear thicker (3 µm) than *Al*-LLZO$_{scaffold}$ fibers. A thickness of 20-30 µm is measured on the cross-section. Importantly, note that the thickness obtained for the composite depends on the thickness of the calcined scaffold as well as volume proportion, which can vary between 9-11.

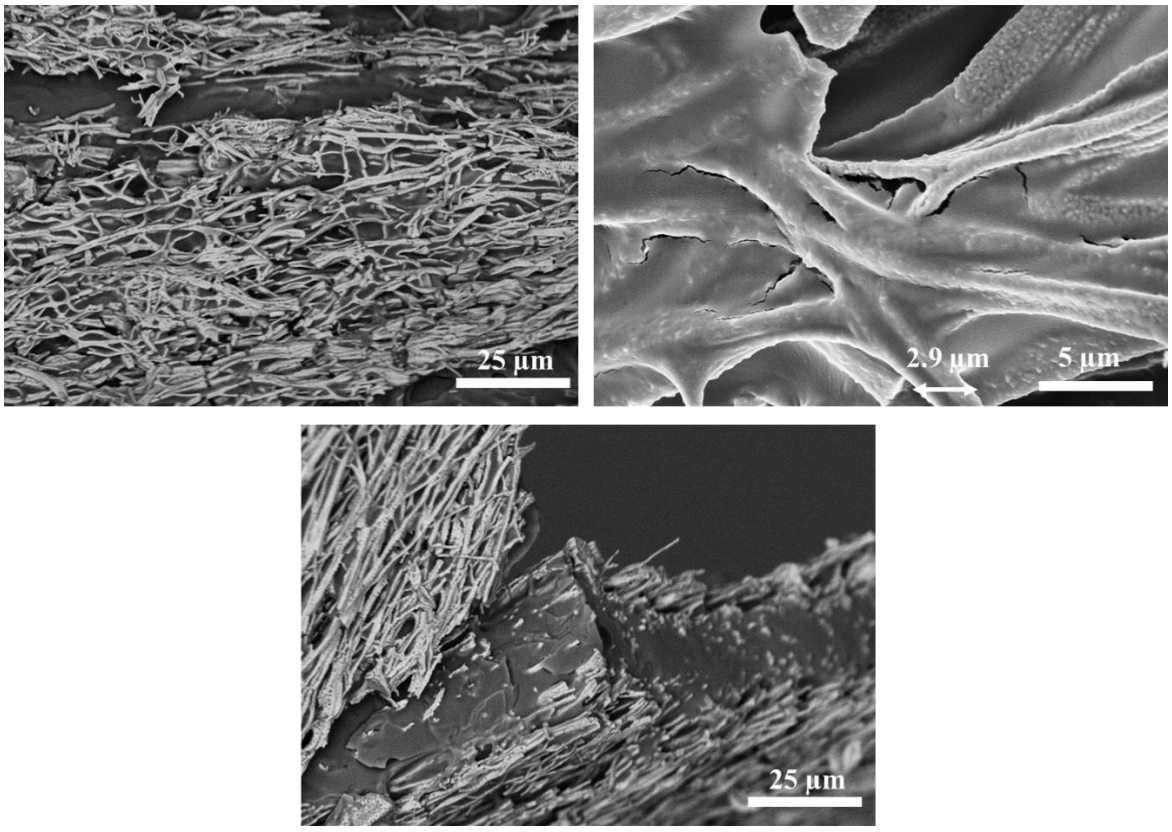

Figure III-9. FEG-SEM images of *Al*-LLZO$_{scaffold}$/PEO-LiTFSI network in top view (up) and cross-section (down).

In contrast to the 3D *Al*-LLZO$_{scaffold}$, the *Al*-LLZO$_{scaffold}$/PEO-LiTFSI network can be manipulated allowing the estimation of its ionic conductivity using EIS. The Nyquist plot was reported in Appendix 7) and exhibit the same behavior of the PEO-LiTFSI network. The obtained conductivity is 1.10^{-5} S/cm at 25 °C which is similar than the one observed for PEO-LiTFSI single network and close to the one observed for the *Al*-LLZO$_{particle}$/PEO-LiTFSI network made of dispersed *Al*-LLZO$_{particle}$ microparticles (8.10^{-6} S.cm^{-1}). Zheng et al.[14] investigated the Li^+ diffusion in LLZO/PEO-$LiClO_4$ composite using NMR and reported that at 20 wt% LLZO content in the composite, conduction occurs primarily through the polymer matrix. However, at 50 wt% and above, Li^+ diffusion is achieved by the LLZO. In our case, at 30 wt%, it appears that we are closer to the 20 wt% scenario.

The incorporation of a 3D *Al*-LLZO$_{scaffold}$ in an SCE does not lead an improvement in ionic conductivity compared to the PEO-LiTFSI network alone. However, it is noteworthy that this approach allowed the production of self-standing and thin objects in the range of a few tens of micrometers in thickness, which is not achievable with the PEO-LiTFSI network alone and *Al*-LLZO alone.

Unfortunately, we were unable to measure amplitude shear oscillation because the *Al*-$LLZO_{scaffold}$/PEO-LiTFSI network is too brittle. Nonetheless, to ascertain whether there is any additional benefit in using 3D *Al*-$LLZO_{scaffold}$ instead of *Al*-LLZO particles, we have decided to impregnate the 3D *Al*-$LLZO_{scaffold}$ with a PEGM-LiTFSI (PEO-LiTFSI brush) polymer precursor solution. PEO-LiTFSI brush is a linear PEO with dangling chains. Nevertheless, this solution resulted in a gel-like rather than a self-standing membrane, making challenging to handle it (see Appendix 2).

IV.3. Contribution of 3D *Al*-$LLZO_{scaffold}$ *vs.* *Al*-LLZO particles in PEO-LiTFSI brush

In Chapter II, have described the manufacture of a PEO-LiTFSI brush material. This electrolyte exhibits a slightly higher ionic conductivity (2.10^{-5} S/cm) compared to a PEO-LiTFSI network (1.10^{-5} S/cm) with the same Ethylene Oxide on Li (EO/Li) ratio. Unfortunately, this material cannot be utilized as a solid electrolyte due to its gel-like behavior. It is therefore interesting to observe the impact of the *Al*-LLZO particles or the 3D *Al*-$LLZO_{scaffold}$ on this type of polymer. Initially, 10 vol% of *Al*-LLZO particles was introduced into the PEO-LiTFSI brush precursor solution, and the material was shaped using the polymer membrane preparation method (Chapter II - section II-2). The standard thermal polymerization program was applied. After polymerization, the set-up was recovered to remove the *Al*-$LLZO_{particle}$/PEO-LiTFSI brush from the mold. Unfortunately, 10 vol% was not enough to obtain a self-supporting membrane (see picture in Appendix 2). When removing from the mold, the material sticks to the glass plates and numerous small bubbles are present. A test with two films of Mylar on the glass plates was tried to prevent the composite from sticking to the glass plates, but gave the same result. So, it is not possible to measure shear modulus or ionic conductivity on this composite.

We then impregnated a 3D *Al*-$LLZO_{scaffold}$ with the PEO-LiTFSI brush precursor solution. Using the same method as described above, i.e. the same protocol of capillary impregnation and polymerization heat treatment, the *Al*-$LLZO_{scaffold}$/PEO-LiTFSI brush composite was prepared. Capillary impregnation is easier with PEO-LiTFSI brush precursor solution, as it is less viscous. The resulting composite is easy to handle, flexible and self-standing (see Appendix 2). *Al*-$LLZO_{scaffold}$/PEO-LiTFSI brush contains approximately 9 vol% *Al*-LLZO, estimated using the same method described for *Al*-$LLZO_{scaffold}$/PEO-LiTFSI network. In order to observe the polymer impregnation into the 3D *Al*-$LLZO_{scaffold}$, FEG-SEM

analyses were carried out (Figure III-10). The thickness of the material is around 40 µm, as estimated by FEG-SEM microscopy (Figure III-10). As before, capillary impregnation fills the pores and coats the LLZO fibers.

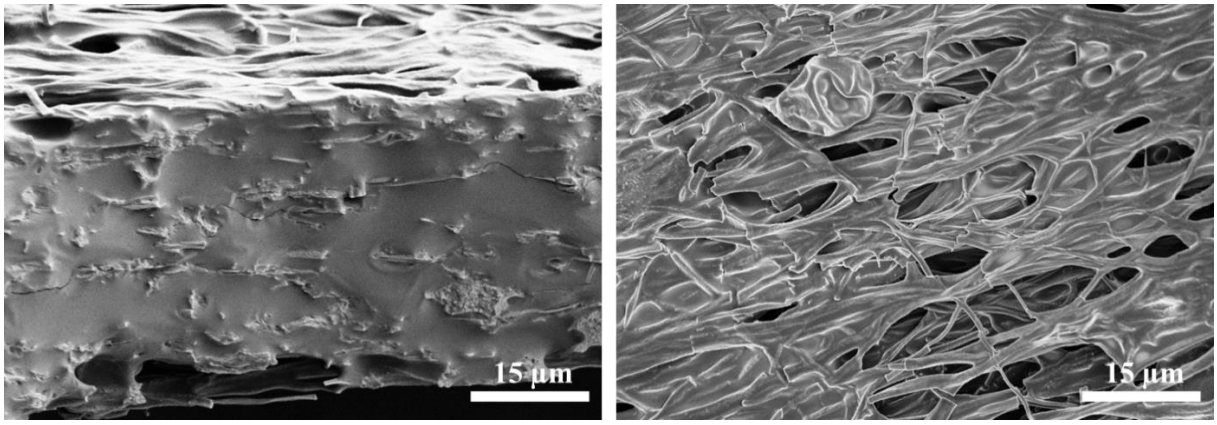

Figure III-10. FEG-SEM images of *Al*-LLZO$_{scaffold}$/PEO-LiTFSI brush in cross-section (left) and top view (right).

Ionic conductivity was determined using EIS (Nyquist plot Figure III-11), and a value close to 1.10^{-5} S.cm^{-1} was measured. This value is comparable to the PEO-LiTFSI brush and both composites produced with PEO-LiTFSI network. These results seem to corroborate the observations reported by Zheng et al.[14]. Below 50wt% (~ 20 vol%) of LLZO, ionic conductivity is mainly governed by the polymer phase.

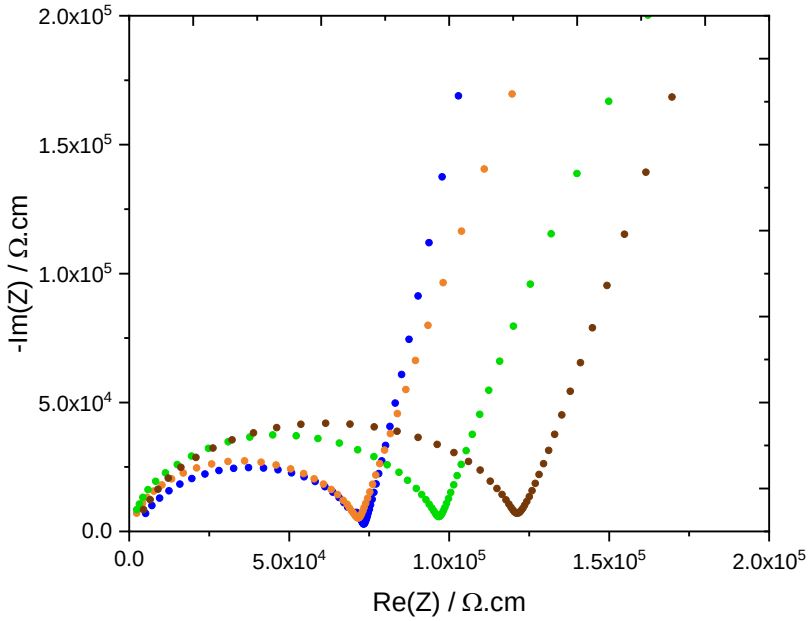

Figure III-11. Nyquist plot at 25°C of (●) PEO-LiTFSI network, (●) *Al*-LLZO$_{scaffod}$/PEO-LiTFSI brush, (●) *Al*-LLZO$_{scaffod}$/PEO-LiTFSI network, and (●) *Al*-LLZO$_{particle}$/PEO-LiTFSI network.

Another way of determining the conductive phase in SCEs is to study the transport number. In ceramics, t^+ is equal to 1 because only Li^+ ions are mobile[2], whereas for PEO-LiTFSI brush, t^+ must be less than 0.5 because both (Li^+ and $TFSI^-$) ions diffuse. In Chapter II, we indicated a t^+ of 0.3 for PEO-LiTFSI network. The transports number (t^+) was measured on the *Al*-$LLZO_{scaffold}$/PEO-LiTFSI brush using the method developed by Bruce and Vincent[38]. The results of the EIS experiment and polarization are presented in Appendix 8. According to Equation 2, a t^+ value of 0.28 was calculated at 25 °C. This result is close to that of the PEO-LiTFSI network and confirms that Li^+ ions diffusion takes place mainly in the polymer matrix of the *Al*-$LLZO_{scaffold}$/ PEO-LiTFSI brush.

This study enabled us to highlight the mechanical contribution of the 3D *Al*-$LLZO_{scaffold}$ that can offer to an SCE. Unfortunately, no improvement in ionic conductivity was measured. Therefore, it is necessary to increase the volume proportion of *Al*-LLZO in the SCE to hope to see its contribution. However, the current 3D *Al*-$LLZO_{scaffold}$ does not allow us to do this, so we need to make it denser. Nonetheless, further experiments exploring the enhancement of the 3D *Al*-$LLZO_{scaffold}$ density are reported in the following section.

IV.4. Prospects for improving the 3D *Al*-LLZO porous scaffold

To increase the density of the 3D *Al*-$LLZO_{scaffold}$, an initial approach involved the modification of the parameters of the electrospinning solution. Unfortunately, as we saw in section IV.2.1.1, increasing the reagent concentrations in the solution did not allow producing a membrane by electrospinning.

Another strategy consists in adding commercial *Al*-LLZO (400-600 nm) particles to the electrospun solution to increase the content of LLZO. However, the sedimentation of the LLZO microparticles was generally observed in the electrospun solution. Thus, this approach only slightly increased the reagent concentration from 1.19 mol/L to 1.20 mol/L and did not improve the densification of the 3D *Al*-LLZO scaffold as it can be seen in Figure III-12. Furthermore, the diameter of the fibers is finally the same as without the addition of Al-LLZO particles (~ 1 µm). As a result, it became necessary at this point to explore alternative techniques for densifying the 3D *Al*-$LLZO_{scaffold}$.

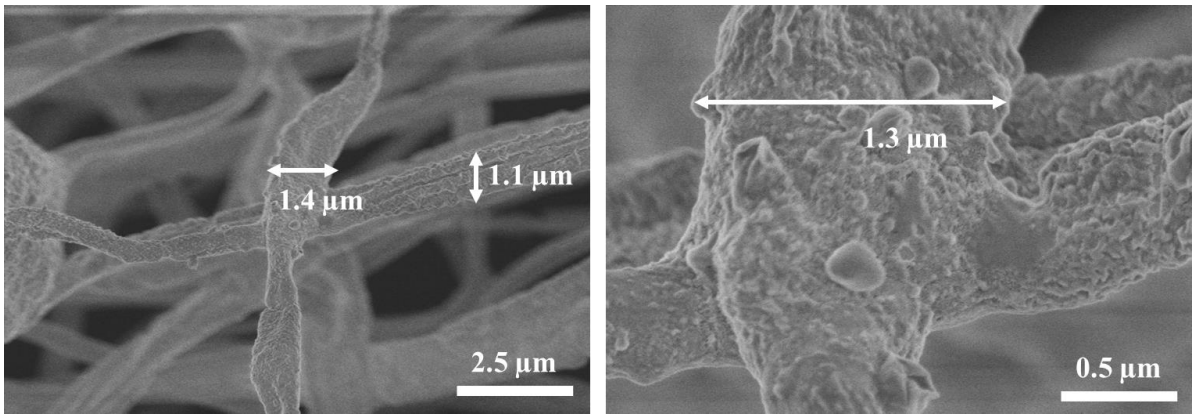

Figure III-12. FEG-SEM images of 3D *Al*-LLZO$_{scaffold}$ elaborated with addition of *Al*-LLZO particles.

Hérou et al.[39] described the densification of a 3D carbon scaffold by pressing the as-spun polymer membrane to increase connectivity between the fibers. To do so, they stacked several as-spun polymer membranes to each other and they applied different pressures. They show that the contact points between the layers of nanofibers increases by bending around each other at 40 bars. Between 60 and 80 bar, the nanofibers begin to fuse and after 80 bar the fibrous morphology disappears.

Based on this paper, 3 pieces of as-spun mat were superimposed and an uniaxial pressure of 100 bar at 50 °C was imposed for 10 min. We chose to apply a pressure of 100 bar to promote fibers fusion. Tests at higher temperatures (80 °C) were tried, but the mat showed brown spots, indicating that the polymer was starting to decompose. By comparison the FEG-SEM analysis of the as-spun mats and the ones pressed at 100 bars at 50°C for 10 min, it can be seen that the quantity of pores decreases and a flattening of the fibers (Figure III-13).

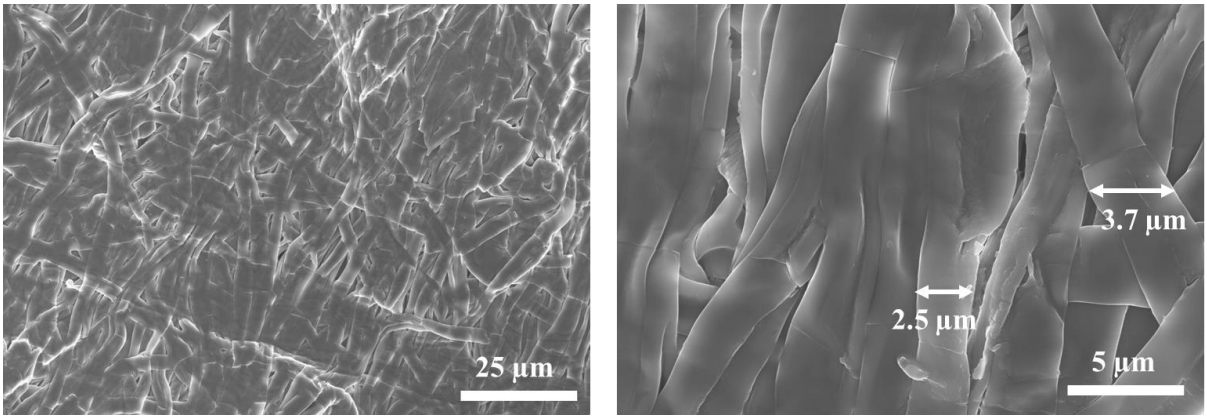

Figure III-13. FEG-SEM images of 3D as spun scaffold after hot pressing at 100 bars at 50°C for 10 min.

We have then applied the same heat treatment (step at 200°C for 2h and 850°C for 4h with 5°C.min^{-1} ramp). FEG-SEM analyses (Figure III-14) show less apparent porosity and the flattening of the fibers. The fibers nevertheless retain a similar diameter of around 3µm. One intriguing observation is that the sintered particles composing the fiber are significantly smaller, with sizes around 120 nm (vs 1 µm for 3D *Al*-LLZO not pressed). To our knowledge, it is difficult to obtain such small particles for LLZO.

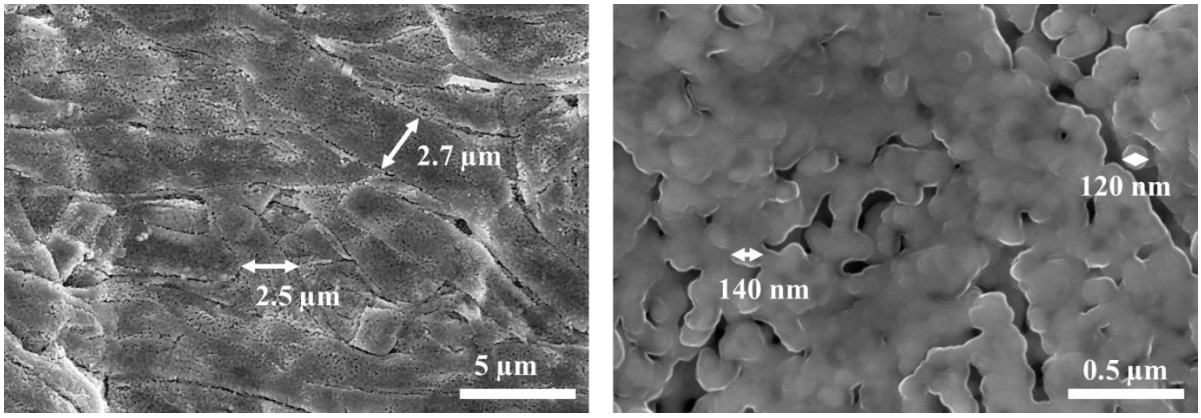

Figure III-14. FEG-SEM images of 3D *Al*-LLZO$_{scaffold}$ after pressing with heating and calcination.

Once the 3D *Al*-LLZO$_{scaffold}$ has been densified (named *Al*-LLZO$_{scaffold-densified}$), it has been impregnated by capillarity with the polymer precursor solution. For this study, we have selected the PEO-LiTFSI network precursor solution, as the use of PEO-LiTFSI brush did not improve ionic conductivity. Same procedure for impregnation was applied: the solution was deposited at the corner of 3D *Al*-LLZO$_{scaffold-densified}$ and let impregnated. First, we observed that the impregnation takes more time (approximately 30 min compared to 10 min), probably due to the change in the porosity of the LLZO scaffold. Polymerization was carried out under the same conditions.

We estimated the amount of *Al*-LLZO by weighing in the SCE to be between 18 and 37% (50 and 72% by weight respectively), assuming that all the pores of the 3D *Al*-LLZO scaffold are filled with polymer. This confirming that the hot-pressing treatment improves the density of the *Al*-LLZO scaffold. Importantly, we note a disparity in the volume fraction of *Al*-LLZO, probably linked to the difficulty in impregnating the 3D scaffold in this case. Interestingly, the increase in the %vol. of *Al*-LLZO can also be seen in the FEG-SEM photographs in Figure III-15. Unfortunately, as the *Al*-LLZO$_{scaffold-densified}$/PEO-LiTFSI network is more brittle than *Al*-LLZO$_{scaffold}$/PEO-LiTFSI network, it was more difficult to do a cross-section in liquid nitrogen as cleanly as previously. For this membrane, thicknesses measured

with the palmer are of the order of 70-80 µm, which is significantly thicker than previously. This was expected, as the 3D *Al*-LLZO$_{scaffold\text{-}densified}$ was thicker than 3D *Al*-LLZO$_{scaffold}$ before impregnation. It is not possible to densify a single piece of 3D *Al*-LLZO$_{scaffold}$, if a self-supporting object is to be obtained after heat treatment.

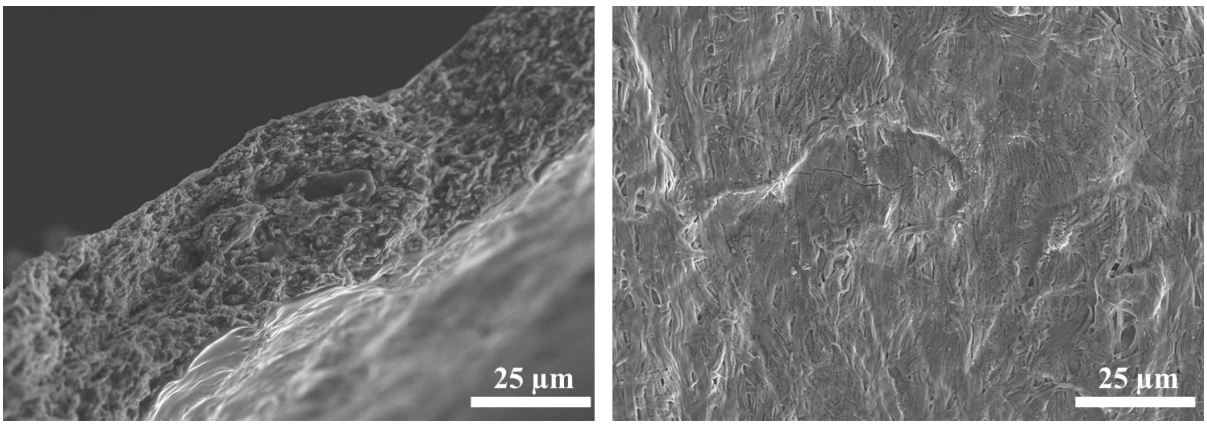

Figure III-15. FEG-SEM images of *Al*-LLZO$_{scaffold\text{-}densified}$/PEO-LiTFSI network in cross-section (left) and top view (right).

The ionic conductivity of the *Al*-LLZO$_{scaffold\text{-}densified}$/PEO-LiTFSI network was measured by EIS using the same set-up as for other SCEs (swagelock, 0.4 MPa). But, a capacitive response was achieved. To check whether the pressure applied was insufficient, another type of set-up was used (see Appendix 3). This cell uses a set of screws to apply different pressures and Nyquist plots were recorded (Figure III-16). A minimum pressure of 63 MPa must be applied to measure an ionic conductivity close to 10^{-6} S.cm^{-1} for the various samples. This value is different from the conductivity of PEO-LiTFSI network (10^{-5} S.cm^{-1}) and high-temperature sintered *Al*-LLZO (10^{-4} S.cm^{-1}). This low conductivity may be explained by the poor connectivity of *Al*-LLZO particles in the LLZO$_{scaffold\text{-}densified}$ as discussed by Zheng et al.[14, 12] or to the orientation of the *Al*-LLZO fibers in the plane of the membrane, i.e. perpendicular to the perturbation during EIS measurement[40]. Another possibility is that the PEO-LiTFSI network is not properly connected due to the reduced pore volume in 3D densified *Al*-LLZO$_{densified}$ or its lower proportion.

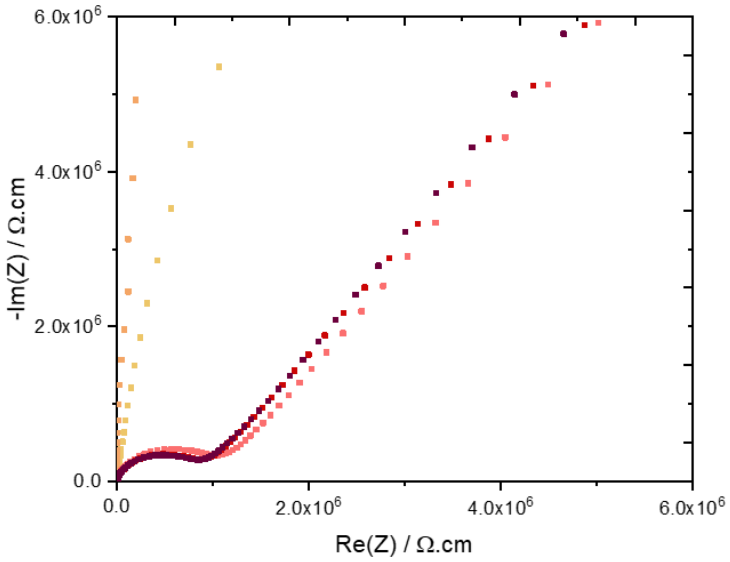

Figure III-16. Nyquist plot at 25 °C of *Al*-LLZO$_{scaffold\text{-}densified}$/PEO-LiTFSI network for at different pressures: (■) 0.4MPa, (■) 38 MPa, (■) 63 MPa, (■) 86 MPa and (■) 111 MPa.

V. Conclusion

We have designed several SCEs using one-step or two-step approaches. The originality of our work is to use a solvent-free mixture of commercially liquid monomers to form the polymer matrix of the SCE by thermal polymerization. In the one-step approach, the LLZO particles were first dispersed in the mixture of the liquid monomers and they were then thermally polymerized, allowing a good dispersion of the LLZO particles. In the two-step approach, the mixture of liquid monomers was used to impregnate a 3D LLZO scaffold, previously synthesized by electrospinning process. The use of liquid precursors allows a better impregnation by capillarity.

In the one-step approach, we have shown the advantage of SCE design in improving the mechanical properties of SCE compared to pure polymer. This is demonstrated by visual observation of SCEs with 7 vol% *Al*-LLZO particles compared to the pure PEO-LiTFSI network. Additionally, the *Al*-LLZO$_{particle}$/PEOLiTFSI membrane is self-standing and exhibits a thickness of 75 µm, which was not possible with the PEO-LiTFSI polymer. Unfortunately, the ionic conductivity of the polymer was not improved, probably due to the low concentration of *Al*-LLZO particles.

For the two-step approach, we have first defined the experimental conditions allowing the synthesis of porous 3D inorganic cubic LLZO scaffold by combining electrospinning and heat-treatment at moderate temperature (850°C, 4 hours). These 3D inorganic LLZO scaffold

was then impregnated by the precursors of either a PEO-LiTFSI network or a PEO-LiTFSI brush. Interestingly, the use of 3D *Al*-LLZO$_{scaffold}$ allows obtaining very thin self-standing membranes (20-40 µm). However, an ionic conductivity of 10^{-5} S.cm^{-1} was achieved at room temperature similar to that of the PEO-LiTFSI network or PEO-LiTFSI brush. This low conductivity was attributed to low content of *Al*-LLZO in the SCE, due to the high porosity of the 3D *Al*-LLZO$_{scaffold.}$

To increase the density of the 3D *Al*-LLZO$_{scaffold}$, we have performed a hot-pressing (50°C at 100 MPa during 10 min) treatment on electrospun membrane. The hot-pressed membrane was then calcined at 850°C during 4 hours to crystallize the cubic *Al*-LLZO$_{scaffold}$ and sinter the particles along the fibers. FEG-SEM images show the densification of the scaffold, which was then confirmed during the impregnation step. Indeed, a volume fraction of 8 and 37 % of LLZO in the SCE was achieved. Unfortunately, this increase in vol. fraction of LLZO did not allow an enhancement of the ionic conductivity as a value of 10^{-6} S.cm^{-1} has been measured at room temperature. This result may be explained by the low connectivity of *Al*-LLZO particles in the membrane, the orientation of *Al*-LLZO fibers in the plane of the membrane and/or the low connectivity of the PEO-LiTFSI network. Efforts will be required to enhance the density and connectivity of particles within the *Al*-LLZO scaffold. Nevertheless, this is a promising avenue for future research.

References:

(1) Armand, M.; Tarascon, J.-M. Building Better Batteries. *Nature* **2008**, *451* (7179), 652–657. https://doi.org/10.1038/451652a.

(2) Janek, J.; Zeier, W. G. A Solid Future for Battery Development. *Nat Energy* **2016**, *1* (9), 16141. https://doi.org/10.1038/nenergy.2016.141.

(3) Mauger; Julien; Paolella; Armand; Zaghib. Building Better Batteries in the Solid State: A Review. *Materials* **2019**, *12* (23), 3892. https://doi.org/10.3390/ma12233892.

(4) Judez, X.; Zhang, H.; Li, C.; Eshetu, G. G.; González-Marcos, J. A.; Armand, M.; Rodriguez-Martinez, L. M. Review—Solid Electrolytes for Safe and High Energy Density Lithium-Sulfur Batteries: Promises and Challenges. *J. Electrochem. Soc.* **2018**, *165* (1), A6008–A6016. https://doi.org/10.1149/2.0041801jes.

(5) Wright, P. V. Electrical Conductivity in Ionic Complexes of Poly(Ethylene Oxide). *Brit. Poly. J.* **1975**, *7* (5), 319–327. https://doi.org/10.1002/pi.4980070505.

(6) Devaux, D.; Bouchet, R.; Glé, D.; Denoyel, R. Mechanism of Ion Transport in PEO/LiTFSI Complexes: Effect of Temperature, Molecular Weight and End Groups. *Solid State Ionics* **2012**, *227*, 119–127. https://doi.org/10.1016/j.ssi.2012.09.020.

(7) Niitani, T.; Shimada, M.; Kawamura, K.; Kanamura, K. Characteristics of New-Type Solid Polymer Electrolyte Controlling Nano-Structure. *Journal of Power Sources* **2005**, *146* (1–2), 386–390. https://doi.org/10.1016/j.jpowsour.2005.03.102.

(8) Thompson, T.; Yu, S.; Williams, L.; Schmidt, R. D.; Garcia-Mendez, R.; Wolfenstine, J.; Allen, J. L.; Kioupakis, E.; Siegel, D. J.; Sakamoto, J. Electrochemical Window of the Li-Ion Solid Electrolyte $Li_7La_3Zr_2O_{12}$. *ACS Energy Lett.* **2017**, *2* (2), 462–468. https://doi.org/10.1021/acsenergylett.6b00593.

(9) Shimonishi, Y.; Toda, A.; Zhang, T.; Hirano, A.; Imanishi, N.; Yamamoto, O.; Takeda, Y. Synthesis of Garnet-Type Li7−xLa3Zr2O12−1/2x and Its Stability in Aqueous Solutions. *Solid State Ionics* **2011**, *183* (1), 48–53. https://doi.org/10.1016/j.ssi.2010.12.010.

(10) Wang, W.; Yi, E.; Fici, A. J.; Laine, R. M.; Kieffer, J. Lithium Ion Conducting Poly(Ethylene Oxide)-Based Solid Electrolytes Containing Active or Passive Ceramic Nanoparticles. *J. Phys. Chem. C* **2017**, *121* (5), 2563–2573. https://doi.org/10.1021/acs.jpcc.6b11136.

(11) Chen, F.; Yang, D.; Zha, W.; Zhu, B.; Zhang, Y.; Li, J.; Gu, Y.; Shen, Q.; Zhang, L.; Sadoway, D. R. Solid Polymer Electrolytes Incorporating Cubic Li7La3Zr2O12 for All-Solid-

State Lithium Rechargeable Batteries. *Electrochimica Acta* **2017**, *258*, 1106–1114. https://doi.org/10.1016/j.electacta.2017.11.164.

(12) Zheng, J.; Tang, M.; Hu, Y.-Y. Lithium Ion Pathway within Li7La3Zr2O12-Polyethylene Oxide Composite Electrolytes. *Angewandte Chemie* **2016**, *128* (40), 12726–12730. https://doi.org/10.1002/ange.201607539.

(13) Yang, T.; Zheng, J.; Cheng, Q.; Hu, Y.-Y.; Chan, C. K. Composite Polymer Electrolytes with $Li_7La_3Zr_2O_{12}$ Garnet-Type Nanowires as Ceramic Fillers: Mechanism of Conductivity Enhancement and Role of Doping and Morphology. *ACS Appl. Mater. Interfaces* **2017**, *9* (26), 21773–21780. https://doi.org/10.1021/acsami.7b03806.

(14) Zheng, J.; Hu, Y.-Y. New Insights into the Compositional Dependence of Li-Ion Transport in Polymer–Ceramic Composite Electrolytes. *ACS Appl. Mater. Interfaces* **2018**, *10* (4), 4113–4120. https://doi.org/10.1021/acsami.7b17301.

(15) Raju, M. M.; Altayran, F.; Johnson, M.; Wang, D.; Zhang, Q. Crystal Structure and Preparation of Li7La3Zr2O12 (LLZO) Solid-State Electrolyte and Doping Impacts on the Conductivity: An Overview. *Electrochem* **2021**, *2* (3), 390–414. https://doi.org/10.3390/electrochem2030026.

(16) Nonnenmacher, W. Stromverteilung in porösen elektroden.

(17) Long, Y.-Z.; Yan, X.; Wang, X.-X.; Zhang, J.; Yu, M. Chapter 2 - Electrospinning: The Setup and Procedure. In *Electrospinning : Nanobabrication and applications*; William Andrew Publishing, 2019; pp 21–52.

(18) Doshi, J.; Reneker, D. H. Electrospinning Process and Applications of Electrospun Fibers. *Journal of Electrostatics* **1995**, *35* (2), 151–160. https://doi.org/10.1016/0304-3886(95)00041-8.

(19) Baumgarten, P. K. Electrostatic Spinning of Acrylic Microfibers. *Journal of Colloid and Interface Science* **1971**, *36* (1), 71–79. https://doi.org/10.1016/0021-9797(71)90241-4.

(20) Cooley, J. F. Apparatus for Electrically Dispersing Fluids, 1902.

(21) Formals, A. Process and Apparatus for Preparing Artificial Threads, 1934.

(22) Bhardwaj, N.; Kundu, S. C. Electrospinning: A Fascinating Fiber Fabrication Technique. *Biotechnology Advances* **2010**, *28* (3), 325–347. https://doi.org/10.1016/j.biotechadv.2010.01.004.

(23) Li, D.; Xia, Y. Fabrication of Titania Nanofibers by Electrospinning. *Nano Lett.* **2003**, *3* (4), 555–560. https://doi.org/10.1021/nl034039o.

(24) Yang, T.; Gordon, Z. D.; Li, Y.; Chan, C. K. Nanostructured Garnet-Type Solid Electrolytes for Lithium Batteries: Electrospinning Synthesis of Li $_{7}$ La $_{3}$ Zr $_{2}$ O $_{12}$ Nanowires and Particle Size-Dependent Phase Transformation. *J. Phys. Chem. C* **2015**, *119* (27), 14947–14953. https://doi.org/10.1021/acs.jpcc.5b03589.

(25) Jin, Y.; McGinn, P. J. Al-Doped Li7La3Zr2O12 Synthesized by a Polymerized Complex Method. *Journal of Power Sources* **2011**, *196* (20), 8683–8687. https://doi.org/10.1016/j.jpowsour.2011.05.065.

(26) Fu, K. (Kelvin); Gong, Y.; Dai, J.; Gong, A.; Han, X.; Yao, Y.; Wang, C.; Wang, Y.; Chen, Y.; Yan, C.; Li, Y.; Wachsman, E. D.; Hu, L. Flexible, Solid-State, Ion-Conducting Membrane with 3D Garnet Nanofiber Networks for Lithium Batteries. *PNAS* **2016**, *113* (26), 7094–7099. https://doi.org/10.1073/pnas.1600422113.

(27) Zhao, Y.; Yan, J.; Cai, W.; Lai, Y.; Song, J.; Yu, J.; Ding, B. Elastic and Well-Aligned Ceramic LLZO Nanofiber Based Electrolytes for Solid-State Lithium Batteries. *Energy Storage Materials* **2019**, *23*, 306–313. https://doi.org/10.1016/j.ensm.2019.04.043.

(28) Haider, A.; Haider, S.; Kang, I.-K. A Comprehensive Review Summarizing the Effect of Electrospinning Parameters and Potential Applications of Nanofibers in Biomedical and Biotechnology. *Arabian Journal of Chemistry* **2018**, *11* (8), 1165–1188. https://doi.org/10.1016/j.arabjc.2015.11.015.

(29) Murugan, R.; Thangadurai, V.; Weppner, W. Fast Lithium Ion Conduction in Garnet-Type Li7La3Zr2O12. *Angew. Chem. Int. Ed.* **2007**, *46* (41), 7778–7781. https://doi.org/10.1002/anie.200701144.

(30) Cotton, F.; Guena, T.; Leblanc, P.; Vallee, A.; Deschamps, M. Electrolyte for Lithium Polymer Batteries, 2009.

(31) Zhu, P.; Yan, C.; Dirican, M.; Zhu, J.; Zang, J.; Selvan, R. K.; Chung, C.-C.; Jia, H.; Li, Y.; Kiyak, Y.; Wu, N.; Zhang, X. Li $_{0.33}$ La $_{0.557}$ TiO $_{3}$ Ceramic Nanofiber-Enhanced Polyethylene Oxide-Based Composite Polymer Electrolytes for All-Solid-State Lithium Batteries. *J. Mater. Chem. A* **2018**, *6* (10), 4279–4285. https://doi.org/10.1039/C7TA10517G.

(32) Choi, J.-H.; Lee, C.-H.; Yu, J.-H.; Doh, C.-H.; Lee, S.-M. Enhancement of Ionic Conductivity of Composite Membranes for All-Solid-State Lithium Rechargeable Batteries Incorporating Tetragonal Li7La3Zr2O12 into a Polyethylene Oxide Matrix. *Journal of Power Sources* **2015**, *274*, 458–463. https://doi.org/10.1016/j.jpowsour.2014.10.078.

(33) Liu, K.; Ma, J.-T.; Wang, C.-A. Excess Lithium Salt Functions More than Compensating for Lithium Loss When Synthesizing Li6.5La3Ta0.5Zr1.5O12 in Alumina

Crucible. *Journal of Power Sources* **2014**, *260*, 109–114. https://doi.org/10.1016/j.jpowsour.2014.02.065.

(34) Rangasamy, E.; Wolfenstine, J.; Sakamoto, J. The Role of Al and Li Concentration on the Formation of Cubic Garnet Solid Electrolyte of Nominal Composition Li7La3Zr2O12. *Solid State Ionics* **2012**, *206*, 28–32. https://doi.org/10.1016/j.ssi.2011.10.022.

(35) Feng, S.; Shi, D.; Liu, F.; Zheng, L.; Nie, J.; Feng, W.; Huang, X.; Armand, M.; Zhou, Z. Single Lithium-Ion Conducting Polymer Electrolytes Based on Poly[(4-Styrenesulfonyl)(Trifluoromethanesulfonyl)Imide] Anions. *Electrochimica Acta* **2013**, *93*, 254–263. https://doi.org/10.1016/j.electacta.2013.01.119.

(36) Lechartier, M.; Porcarelli, L.; Zhu, H.; Forsyth, M.; Guéguen, A.; Castro, L.; Mecerreyes, D. Single-Ion Polymer/LLZO Hybrid Electrolytes with High Lithium Conductivity. *Mater. Adv.* **2022**, *3* (2), 1139–1151. https://doi.org/10.1039/D1MA00857A.

(37) Rosenthal, T.; Weller, J. M.; Chan, C. K. Needleless Electrospinning for High Throughput Production of Li $_7$ La $_3$ Zr $_2$ O $_{12}$ Solid Electrolyte Nanofibers. *Ind. Eng. Chem. Res.* **2019**, *58* (37), 17399–17405. https://doi.org/10.1021/acs.iecr.9b03376.

(38) Bruce, P.; Evans, J.; Vincent, C. A. Conductivity and Transference Number Measurements on Polymer Electrolytes. *Solid State Ionics* **1988**, *28–30*, 918–922. https://doi.org/10.1016/0167-2738(88)90304-9.

(39) Hérou, S.; Bailey, J. J.; Kok, M.; Schlee, P.; Jervis, R.; Brett, D. J. L.; Shearing, P. R.; Ribadeneyra, M. C.; Titirici, M. High-Density Lignin-Derived Carbon Nanofiber Supercapacitors with Enhanced Volumetric Energy Density. *Advanced Science* **2021**, *8* (17), 2100016. https://doi.org/10.1002/advs.202100016.

(40) Lancel, G.; Stevens, P.; Toussaint, G.; Marechal, M.; Krins, N.; Bregiroux, D.; Laberty-Robert, C. Hybrid Li Ion Conducting Membrane as Protection for the Li Anode in an Aqueous Li-Air Battery: Coupling Sol Gel Chemistry and Electrospinning. *Langmuir* **2017**, *33* (37), 9288–9297. https://doi.org/10.1021/acs.langmuir.7b00675.

Chapter IV.

Understanding the Li^+ transport through the PEO network||*Al*-LLZO interface by using Electrochemical Impedance Spectroscopy

Buildings points:

- Formation of *Al*-LLZO/PEO network multilayers through *in-situ* and *ex-situ* polymerization
- Employing electrochemical impedance spectroscopy to discern interface resistances
- Integration of a TLM element accounting for micro and macro transport across *Al*-LLZO||PEO network interface phenomena

Résumé

L'élaboration d'électrolyte composite polymère/inorganique pour les batteries tout-solide nécessite une compréhension approfondie du transport des ions Li^+ aux interfaces entre les deux matériaux. En utilisant la spectroscopie d'impédance électrochimique, il est possible d'appréhender cette problématique. Nous avons opté pour la fabrication de tri-couches afin d'étudier le déplacement des Li^+ aux interfaces. Ces multicouches sont composées de la céramique $Li_{6.25}Al_{0.25}La_3Zr_2O_{12}$ (*Al*-LLZO) en raison de sa conductivité ionique élevée (10^{-4} $S.cm^{-1}$ à température ambiante) et des réseaux polymères, PEO. Les phases polymères sélectionnées (Chapitre II), sont des réseaux poly(éthylène oxyde) (PEO) dotés de chaînes pendantes incorporant un sel de Li (non greffé, 10^{-5} $S.cm^{-1}$) ou un monomère de Li (greffé, 10^{-7} $S.cm^{-1}$), ce qui permet de greffer l'anion au réseau PEO. Cela a permis de modifier à la fois la mobilité et la distribution des Li^+ à l'interface. Pour concevoir les tri-couches, nous avons soit procédé à la polymérisation du réseau PEO sel de Li directement sur les deux faces de la pastille *Al*-LLZO (*in-situ*), soit le contact entre les réseaux PEO (synthétisé en amont) et la pastille *Al*-LLZO est maintenu par un ressort (*ex-situ*). Cela a permis d'évaluer l'impact de la polymérisation *in-situ* sur le transfert des Li^+ mais aussi, d'observer l'influence de la distribution des Li^+ à l'interface en opposant réseau PEO greffé et non greffé (*ex-situ*). En utilisant un circuit équivalent intégrant le Modèle de Ligne de Transmission (TLM) pour interpréter les différentes données d'impédance observées au sein de ces structures multicouches, nous avons pu identifier trois composantes clés influençant le comportement des Li^+ : R_i reflète la résistivité du chemin ionique direct à l'interface réseau PEO||*Al*-LLZO alors que R_t et C_t correspondent à la résistance/capacitance réparties, liées au transfert des Li^+ entre les deux électrolytes. De manière intéressante, la valeur de R_i est plus élevée dans le cas de la polymérisation *in-situ*, probablement dû à une distance de saut plus grande pour le Li^+ entre la phase inorganique et polymère. Cela peut être causé par des réactions secondaire, lors de la polymérisation *in-situ* et/ou une répulsion électrostatique. En revanche, la valeur de R_t semble indépendante de la manière dont le polymère est assemblé sur la surface du *Al*-LLZO et de la manière dont les Li^+ sont introduits dans le réseau PEO (non greffés *vs.* greffés). Cette résistance est attribuée au changement d'environnement des ions Li^+ entre *Al*-LLZO et le réseau PEO. De plus, l'estimation des énergies d'activation de R_i et R_t a permis de mettre en évidence que le passage direct (R_i) des Li^+ est favorisé et de confirmer la modification de l'interface réseau PEO||*Al*-LLZO lors de la polymérisation *in-situ*.

Understanding the Li^+ transport through the PEO network||*Al*-LLZO interface by using Electrochemical Impedance Spectroscopy

Project of Article

Abstract

The design of composite Poly(ethylene oxide) (PEO)-garnet electrolyte for all solid-state batteries requires understanding the transport of Li^+ at the polymer||inorganic interfaces. To do so, we develop a multilayer design to characterize the Li^+ transport at the composite interfaces using impedance spectroscopy. First, $Li_{6.25}Al_{0.25}La_3Zr_2O_{12}$ (*Al*-LLZO) ceramics have been selected because of its ionic conductivity of 10^{-3} $S.cm^{-1}$ at ambient temperature. A polymer network with PEO dangling chains has been chosen as an organic phase because it is easily synthesized from commercially available liquid precursors such as poly(ethylene glycol) methyl ether methacrylate (PEGM) and poly(ethylene glycol) dimethacrylate (PEGDM) via a free radical polymerization. The lithium bis(trifluoromethanesulfonyl)imide (LiTFSI) or lithium sulfonamide methacrylic monomer (LiMTFSI) were included in the PEO network leading to ungrafted and grafted lithium counterions, respectively, to both modify the mobility and the distribution of Li^+ at the interface. The polymerization of the PEO network has also been performed onto the *Al*-LLZO surfaces to study its impact on Li^+ transport. Using the Transmission Line Model to describe the different impedance spectra of these multilayers, we have shown that the Li^+ can be described by two elements: R_i which represents the resistance of the direct ionic path at the PEO network||*Al*-LLZO interface, and R_t and C_t that correspond to the distributed Li^+ transfer resistance/capacitance between the two electrolytes. Finally, R_i is influenced by the polymerization carried out in the presence of *Al*-LLZO, whereas R_t is the same regardless of the strategies used to synthesize the multilayers.

Keywords

Multilayer LLZO/PEO network, Electrochemical impedance spectroscopy, Transmission Line Model

I. Introduction

All-solid-state lithium batteries (ASSBs) are considered as next generation of electrochemical energy storage devices because of their safety and high energy density of up to 400Wh/kg. This is possible through the use of Li-metal as the negative electrode. One critical component in ASSBs is the electrolyte, as none of the existing electrolyte family up to now fulfills all the requirements including ionic conductivity, processability, electrochemical and chemical stabilities toward Li[1]. In this context, the design of composite materials seems to be the most realistic solution in the short term[2]. Usually, the polymer improves the processability of the electrolyte but at the expense of the ionic conductivity while the inorganic materials have better ionic conductivity with poor processability. One of the challenges when designing composite materials is to tune the inorganic||polymer interface since it controls several properties such as the transport of Li^+. Before designing the best composite, it is necessary to understand the experimental conditions favoring the transport of Li^+ at this interface[3,4]. To our knowledge, few studies have been reported on the understanding of the transport of Li^+ at the PEO||ceramic interface. Zheng et al.[5] demonstrated by NMR analysis that the content of LLZO in a PEO-Li salt polymer (made by ball-milling and solution casting) impact Li^+ mobility. On one hand, a composite with a high mass fraction of polymer (80-95 wt%) exhibits ionic conductivity close to that of the polymer (~ 10^{-5} $S.cm^{-1}$). On the other hand, a high mass fraction of LLZO (≥ 50 wt%) leads to lower ionic conductivity (10^{-6} – 10^{-7} $S.cm^{-1}$) attributed to the poor LLZO||LLZO contact that restricts Li^+ transport in the inorganic percolated network. To explain this result, several hypotheses have been drawn including the modification of the crystallinity of the PEO or the transport mechanism along or through the LLZO||polymer interface. The latter has been studied by Brogioli et al.[6] through the estimation of the activation energy of ionic conduction at the interface by impedance spectroscopy. Interestingly, they estimated a high activation energy barrier for Li^+ between the two phases (LLZO-PEO), demonstrating the difficulty of Li^+ in moving from one phase to the other. To overcome this limitation, Kuhnert et al.[7] investigated the surface modification of $Li_{6.4}La_3Zr_{1.4}Ta_{0.6}O_{12}$ (LLZTO) particles by covalently grafting PEO chains. To do so, the surface-terminated oxygen of LLZTO particles is first activated by plasma etching and a sol-gel chemistry reaction was performed with (3-glycidyloxypropyl)trimethoxysilane (Si-R) in order to covalently bonded Si-R layers on top of LLZTO particles. The surface layers terminated by an epoxy group react then with the hydroxyl group of the PEOs, allowing the functionalization of the surface by PEO chains. Interestingly,

this functionalization modifies the charge surface of LLZTO. As a result, the PEO segments organize themselves around the LLZTO particles, in a way that the jump distance of Li^+ between the LLZTO and the PEO polymer is drastically reduced. As a consequence, the Li^+ easily crosses the LLZTO||PEO interface, as shown by the resistance measurement using impedance spectroscopy.

To quantify the interface resistance, Gupta et al.[8] designed a multilayer PEO-LiTFSI/LLZTO/PEO-LiTFSI system and studied the Li^+ transport through these multilayers by impedance spectroscopy. Their interest was the estimation of interface resistance between the two electrolytes (PEO-LiTFSI and LLZTO). The impedance spectra exhibit two distinct frequency-dependent phenomena on the Nyquist representation, corresponding to two semi-circles. The semicircle at high frequency (HF) is attributed to the bulk response corresponding to both the resistance of the PEO-LiTFSI polymer and the bulk LLZTO. The second one at a medium frequency (MF) is attributed to the interface and noted $R_{interface}$. To estimate the value of $R_{interface}$, they proposed the following electronic circuit: $(CPE_{bulk}//R_{bulk}) + (CPE_{interface}//R_{interface}) + M_{Au}$ where $CPE_{bulk}//R_{bulk}$ represents the total capacity and resistance of the 3 electrolytes bulk layers, $CPE_{interface}//R_{interface}$ the capacity and resistance between the two electrolytes and M_{Au} the capacitive phenomenon due to the use of blocking gold electrodes. A $R_{interface}$ of 15 $k\Omega.cm^2$ at 30 °C is estimated. Interestingly, they observe a decrease of this value with the surface cleaning of the LLZTO (0.2 $k\Omega.cm^2$) by heat treatment and with the modification of the concentration of Li^+ in the polymer electrolyte. Increasing the Li^+ concentration in the polymer changes the gradient concentration between the two electrolytes, then favoring Li^+ transport. The same behavior has been observed on multilayers with $Li_{1+x+y}Al_xTi_{2-x}Si_yP_{3-y}O_{12}$ (LATP) and PEO-LiTFSI.[9] Using a methodology comparable to Gupta et al.[8], they demonstrated that the interfacial resistance, R_{ct}, is inversely proportional to the concentration of Li^+ in the polymer in the range of 0.01-2.5 M ($R_{ct} \sim 2.10^3$ $\Omega.cm^2$ and 20 $\Omega.cm^2$ respectively at 70 °C). Finally, in their studies on PEO-$LiClO_4$/LLZO/PEO-$LiClO_4$ multilayers, Langer et al.[10] observed an additional ion transfer process which they attributed to interface processes. To model and to estimate its contribution to the overall response, they proposed to use a de Levie element in their equivalent circuit: $R_{SE} + Z_{deLevie} + CPE_{dl}$ where R_{SE} represents the total resistance of the electrolytes, $Z_{deLevie}$ is used to represent the porous structure of the interface between the two electrolytes and finally CPE_{dl} for the capacitance at the blocking electrodes. Often, $Z_{deLevie}$ is used for porous electrodes to separate contributions of Li^+

diffusing in the pores from the ionic transport across the phase boundary[11,12]. In these conditions, a $R_{interface}$ of 9 kΩ.cm^2 at 70 °C was estimated.

Inspired by these literature studies, we designed a multilayer LiTFSI-PEO network/LLZO/LiTFSI-PEO network to study the transfer of Li^+ at the LLZO||LiTFSI-PEO network interface. Compared to work performed in the literature, we have selected the LiTFSI-PEO network because of its amorphous nature along a wide temperature range and the ability to synthesize directly it on the surface of LLZO pellet by using liquid monomers. Importantly, this LiTFSI-PEO exhibits a conductivity of 10^{-5} S.cm^{-1} at 25 °C[13] which is two orders of magnitude lower than the one measured on dense $Li_{6.4}La_3Zr_2Al_{0.2}O_{12}$ ceramic[14] (10^{-4} S.cm^{-1} at 25 °C). Interestingly, our approach allows eventually the grafting of the PEO network onto the LLZO surface and induces a modification of the free volume at the interface, in comparison with the classical LiTFSI-PEO network system. In addition, it is also possible to graft the lithium counterions to the polymer chains (using MTFSI monomer instead of LiTFSI) allowing control of unbound ion concentration at the interfaces. To characterize diffusion phenomena at the interface, we have implemented in the equivalent circuit the well-known Transition Model Line (TML). This element was first introduced by Euler and Nonnnenmacher[15] to describe the hindered diffusion of Li^+ in pores of classical Li-ion electrodes in contact with liquid electrolyte.

II. Experimental

II.1. Materials

$Li_{6.25}Al_{0.25}La_3Zr_2O_1$ (*Al*-LLZO, 400 to 600nm D50, Ampcera) and Lithium bis(trifluoromethylsulfonyl)imide (LiTFSI, > 99%, Sigma Aldrich) was kept in the glove box (H_2O < 0.1 ppm). Poly(ethylene glycol) methyl ether methacrylate (PEGM, M_n = 500 g.mol^{-1}, Sigma Aldrich) and poly(ethylene glycol) dimethacrylate (PEGDM, Mn=750 g.mol^{-1}, Sigma Aldrich) were dried at 25 °C under vacuum (10-15 mbar) before used. 2,2′-azobis(2-methylpropionitrile) (AIBN, initiator, 98%, Sigma Aldrich) was recrystallized in methanol before used. For the synthesis of Li_3BO_3 (LBO), H_3BO_3 (Alfa Aesar) and LiOH (Alfa Aesar) have been used in stoichiometric proportion.

II.2. Materials synthesis

Synthesis procedure for *Al*-LLZO ceramics: LBO was first synthesized by dissolving H_3BO_3 and LiOH into distilled water in a 1:3 molar ratio and stirred vigorously at 50 °C to make a

homogeneous solution. The solution was then dried at 120 °C and stirred under low rpm. The resulting powder was finally heat-treated at 600 °C for 12 h. *Al*-LLZO ceramics were obtained from commercial *Al*-LLZO powder manually ground with 5wt% of LBO. 1g of the ground powder mixture was then pressed under 296 MPa to achieve 13 mm pellets. Excess of lithium source was adopted to compensate for the lithium loss (volatilization) during sintering. To do so, the pellets were covered in an Al_2O_3 crucible with commercial *Al*-LLZO powder. These pellets were then sintered under air in an alumina crucible with a heating rate of 5 °C.min^{-1} at 780 °C during 5 h and then with a heating rate of 1 °C.min^{-1} at 1150 °C for 12 h in a muffle furnace. The sintered pellets exhibit a thickness of about 2 mm and a diameter of about 10-12 mm. The relative density is about 90%.

Synthesis procedures of polymer electrolyte: Polymer electrolyte syntheses were performed as previously reported in Naboulsi et al.[13].

For LiTFSI/polymer precursors mixture, PEGM, PEGDM and AIBN were introduced into a vial at the desired quantities (ratio PEGM/PEGDM: 80/20 wt/wt, 2 wt% AIBN by respect to the total monomer weight). The precursor solution was stirred until the total solubilization of AIBN then flushed with nitrogen. The vial was then introduced in a glove box (H_2O < 0.1 ppm). Finally, the required amount of LiTFSI (18 wt%, EO/Li = 24) was added to the PEGM/PEGDM solution and stirred until the LiTFSI was completely dissolved.

For single-ion polymer electrolyte, PEGM, PEGDM and LiMTFSI were introduced in a vial according to the desired proportions (ratio PEGM/PEGDM: 80/20 wt%, 21 wt% of LiMTFSI, EO/Li = 24) and stirred until the total solubilization of LiMTFSI (2 h) at room temperature. 2 wt% of AIBN concerning the total weight of PEGM, PEGDM and LiMTFSI were added to the mixture, which was then stirred and flushed with nitrogen until the AIBN was dissolved.

For the synthesis of the polymer membranes, the precursor mixtures were poured into a mold made with two glass plates separated by a Teflon gasket (thickness = 250 µm). The mold was then placed in an oven at 70°C for 2 h and then at 90°C for 1 h. The resulting polymer membranes were then dried under vacuum (10-15 mbar) at 70 °C in a glass oven (BUCHI B-585) for 12 h and then kept in a glove box (H_2O < 0.1 ppm) before use.

Synthesis of the (PEO network||LLZO|| PEO network) multilayers: Two different approaches have been used for the fabrication of the multilayers to control *Al*–LLZO||polymer interface. As a first approach, the polymer layer was synthesized on the surface of the *Al*–LLZO pellet; this approach will be called "*in-situ*" in the rest of the manuscript. In the glove box, the *Al*–LLZO pellet surface was first cleaned on both sides with silicon carbide sanded polishing

paper. A quantity of the chosen precursor mixture is deposited with a micropipette (Vol=10 µL to achieve a final thickness of around 0.2 mm) on one side and spread with the tip of the micropipette on the whole surface (0.99 cm^2). On a hot plate, a thermal curing of 2 h at 70 °C, followed by a post-curing of 1 h at 90 °C was applied to obtain the *Al*–LLZO/polymer bilayer assembly. The assembly was then cooled to room temperature. The second polymer layer was synthesized on the uncovered side of the *Al*–LLZO with the same procedure leading to a multilayer assembly PEO network||LLZO|| PEO network, and called "*in-situ*" multilayer in the rest of the manuscript.

In a second approach, two polymer films (thickness of ~ 0.250 mm) were first prepared as previously described (i.e. synthesis procedure of polymer membrane) and then assembled with *Al*–LLZO pellet to the configuration of PEO network||LLZO|| PEO network in a Swagelok cell and the contact is maintained with a spring (0.4 MPa). This approach is called "*ex-situ"* in the rest of the manuscript. The two multilayers are defined as "*in-situ*" and "*ex-situ*" and are described in Figure IV-1and Table SI.IV-1. Several multilayer tests were carried out to check the reproducibility of the tests, but only three samples will be discussed here.

Testing procedure: The multilayers (*in-situ* and *ex-situ*) and polymer electrolyte were then placed in a Swagelok-type cell using two stainless-steel blocking electrodes (BE). For the *Al*-LLZO, a metallization with 50 nm Au has been performed. For all the cells, the contact was maintained with a spring (0.4 MPa).

II.3. Characterization

Electrochemical impedance spectroscopy (EIS) experiments were carried out using a 1260 Solartron FRA device between 10^7 Hz and 10^{-1} Hz, with a perturbation amplitude of 100 mV at the OCV (open circuit voltage), recording 11 points per decade. The activation energy was estimated from the complex impedance spectra measured every 10 °C from 30 °C to 80 °C. Temperature was controlled using an environmental simulation chamber (Memmert). Cells were allowed to reach the thermal equilibrium for at least 1 h before each measurement.

Calculation of the capacitance from the *Constant Phase Element (*CPE). Using the Zview software for the impedance data refinement, the CPE element includes two components, Q_o and α, respectively. The equivalent capacitance is calculated according to the following equation[16]:

$$C = \frac{(Q_o * R)^{(\frac{1}{\alpha})}}{R} \qquad \text{Equation 1}$$

with R, the resistance in parallel to the CPE element in the electrical equivalent circuit.

III. Results and discussion

To understand the transport of Li^+ into composite electrolytes, it is important to characterize the transport of Li^+ at the interface of the PEO network and *Al*-LLZO ceramics. To do so, we have designed PEO network/*Al*-LLZO/PEO network multilayers (Figure IV-1). Two approaches have been proposed to tune the PEO network||*Al*-LLZO interface. In the "*in-situ*" approach, the PEO network layer is synthesized directly onto the surface of *Al*-LLZO ceramics, while in the "*ex-situ*" one the PEO network layer was first synthesized and then maintained onto the surface of *Al*-LLZO ceramics by applying a constant pressure (0.4 MPa) via a spring.

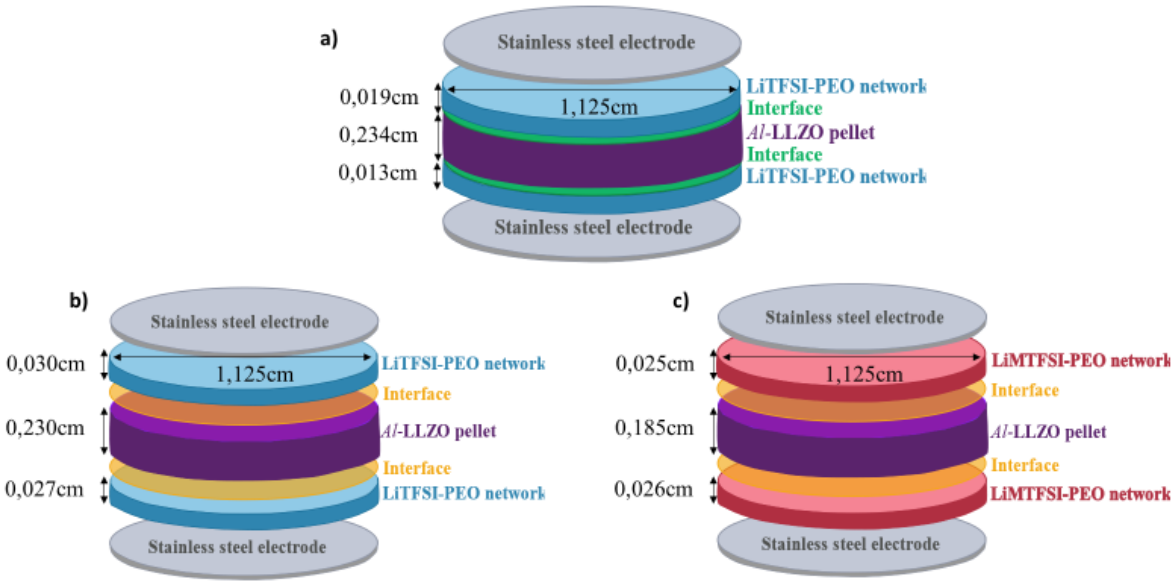

Figure IV-1. Schematic representation of (a) *in-situ* LiTFSI-Multilayer, (b) *ex-situ* LiTFSI-Multilayer and (c) *ex-situ* LiMTFSI-Multilayer.

III.1. Designing the electrical circuit corresponding to describe the PEO network/*Al*-LLZO/PEO network multilayers

Before studying the different multilayers, we have independently characterized the Li^+ transport in the individual electrolytes (LiTFSI-PEO network and *Al*–LLZO ceramics) by using an Au/electrolyte/Au (or BE) cell configuration. The results are reported in Figure SI.IV-1. The values of the different electrical elements used in the model, at all studied temperatures, are summarized in Table SI.IV-2 and

Table SI.IV-3 for the PEO network and *Al*-LLZO, respectively for all the temperatures. According to the literature[17], the BE/LiTFSI-PEO network/BE spectra can be divided into two parts (Figure SI.IV-1a). The ionic motion in the material mainly governs the HF response, while

the low frequency (LF) one is governed by the electrode polarization**.** Indeed, with a LF perturbation signal, Li^+ tends to accumulate at the interface with the blocking electrodes, leading to a depletion of positive charges on the opposite metallic electrodes**.** The LiTFSI-PEO network resistance, $R_{polymer}$, and capacitance**,** $CPE_{polymer}$, were extracted from the impedance data by fitting the spectra using the classical $R_{swagelock}$ + $CPE_{polymer}$//($R_{polymer}$+CPE_{BE}) Debye equivalent circuit shown in the inset of Figure SI.IV-1a. Figure SI.IV-1a shows selected samples and fitted spectra, where CPE was used to take into account the non-ideality of the capacitors (described in the method*),* $R_{swagelock}$ is the resistance of the setup (cell, cables) and CPE_{BE} represents the capacitive response of the blocking electrode.

Table IV- 1. Values of electrical circuit elements at 30 °C for BE/LiTFSI-PEO network/BE and Au/*Al*-LLZO/Au.

Sample	$R_{LLZO\text{-}bulk\ or\ polymer}$ (Ω)	$C_{LLZO\text{-}bulk\ or\ polymer}$ (F)	$R_{LLZO\text{-}gb}$ (Ω)	$C_{LLZO\text{-}gb}$ (F)	**Conductivity (S.cm^{-1}) at 30°C**
Al-LLZO	2830	2.10^{-11}	1306	7.10^{-9}	$5.6.10^{-5}$
LiTFSI-PEO network	1700	6.10^{-11}			$1.9.10^{-5}$

From the modeling of the impedance data of the LiTFSI-PEO network using the classical equivalent circuit, a capacitance value of 6.10^{-11} F (Equation 1) and a conductivity value of $1.9.10^{-5}$ S.cm^{-1} at 30 °C were estimated (Table IV- 1). Figure SI.IV-1b represents the impedance spectra of the Au/*Al*-LLZO/Au cell. This latter exhibits three different domains. According to the literature[18], the first semi-circle at HF is associated with the motion of Li^+ into the bulk *Al*-LLZO grains, since a value of 2.10^{-11} F for the capacitance (Table IV- 1) has been estimated from a $CPE_{LLZO\text{-}bulk}$ of 6.10^{-10} F.cm^{-2} (Equation 1). The second semicircle at MF corresponds to the grain boundaries (GB) response with a capacitance of 7.10^{-9} F (Table IV- 1). Finally, the capacitive response, CPE_{BE}, at LF is attributed to the *Al*-LLZO||Au blocking interface. From the bulk and grain boundaries resistances, an effective ionic conductivity of $5.6.10^{-5}$ S.cm^{-1} was estimated for our *Al*-LLZO ceramic.

We have then studied the *in-situ* LiTFSI-Multilayers by impedance spectroscopy with the same setup configuration and the experimental data (represented in a Nyquist plot) are reported in Figure IV-2.

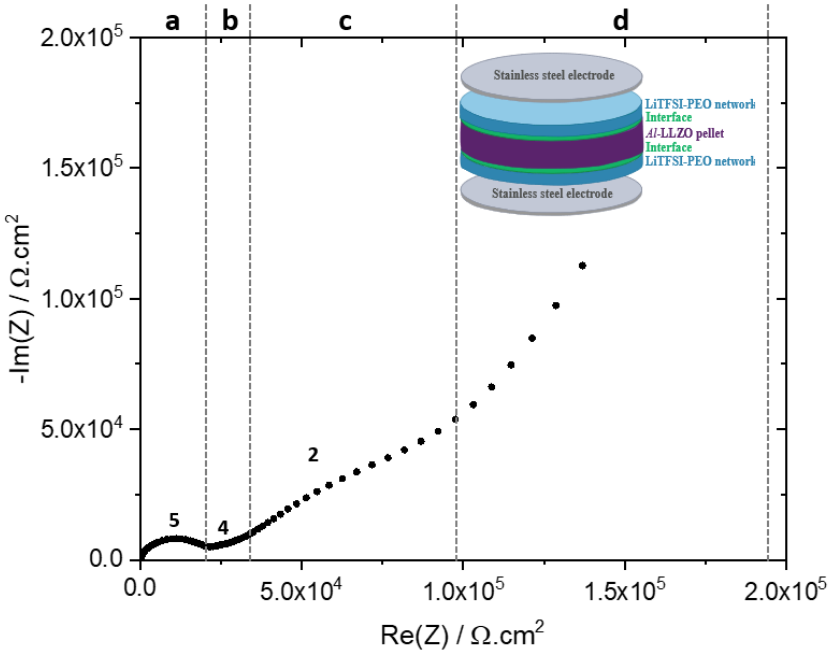

Figure IV-2. Nyquist plot at 30 °C of *in-situ* LiTFSI-Multilayer and its schematic representation. Numbers at the data points indicate the power of frequency. a, b, c and d on top of the Nyquist plot represent the different frequency zones.

The impedance spectrum of this multilayer exhibits four different zones: a semi-circle at HF (4.10^5 Hz, zone a), a contribution at HF-MF (3.10^4 Hz, zone b) followed by a shoulder at MF (200 Hz, zone c), and a capacitive response at LF (zone d) corresponding to the charge accumulation at the blocking electrode surface (modeled by CPE_{BE}). The HF response (10^7-10^5 Hz, zone a) was attributed to the transport of Li^+ into both the LiTFSI-PEO network and LLZO, according to the apparent frequency of the two reference cells for both individual electrolytes (see Figure SI.IV-1a. and 2b). Accordingly, the HF-MF corresponds to the grain boundaries response of the LLZO (zone b), as the apparent frequency corresponds to the one found for LLZO GB (see Figure SI.IV-1b). These different features are modeled by $CPE_{LLZO\text{-}bulk}$ // ($R_{polymer}$ //$CPE_{polymer}$ + $R_{LLZO\text{-}bulk}$ + $R_{LLZO\text{-}gb}$//$CPE_{LLZO\text{-}gb}$). In addition to these, there is a MF contribution superimposed with the LLZO GB, which we have attributed to the LiTFSI-PEO network||Al-LLZO interface as the fit of the impedance spectra with the contribution of solely the two electrolytes in series is poor (Figure IV-3a).

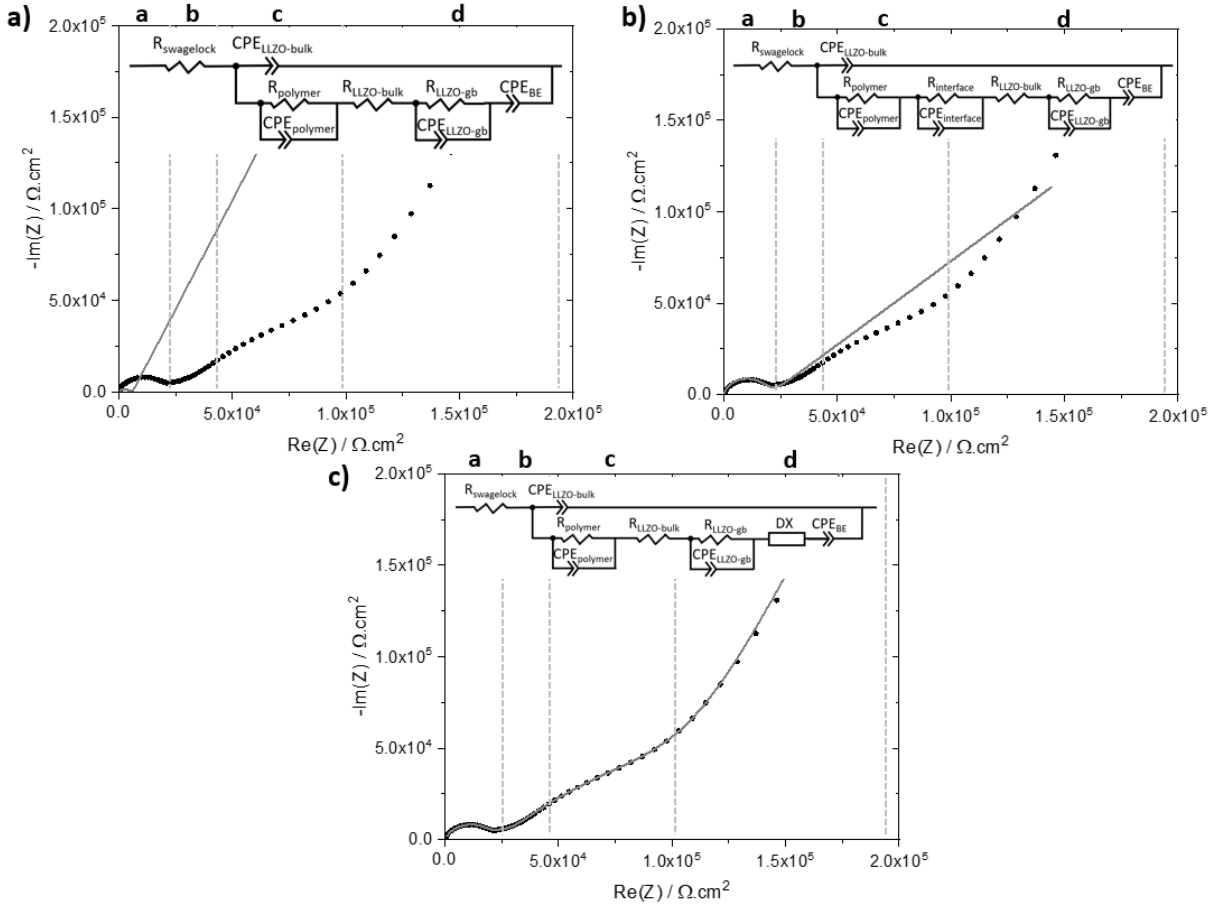

Figure IV-3. Nyquist plot at 30 °C of (●) *in-situ* LiTFSI-Multilayer, (—) fit according to the equivalent circuit presented respectively (a), (b) and (c). a, b, c and d on top of the Nyquist plot represent the different frequency zones.

According to Isaac et al.[9], a resistance in parallel with a constant phase element model this latter contribution. Using the equivalent circuit reported in Figure IV-3b, the result of the fit with the experimental data is very good in the a and b zones, but is poor in zone c, probably because of a non-ideal or more complex interface in our case. To deeper analyze the impedance spectrum, we propose to replace this last contribution with a TLM (represented by DX in the equivalent circuit) element in our equivalent circuit (see Figure IV-3c) in order to better describe the heterogeneity of our LiTFSI-PEO network||*Al*-LLZO interface. In the TLM (see Figure SI.IV-2), R_i translates the resistivity of the ionic path in the pores of the electrode (filled with liquid electrolyte) and R_{ct} and C_{dl} translate the charge transfer resistance and the double layer capacitance[19]. Inspiringly, in our LiTFSI-PEO network||*Al*-LLZO interface, R_i is attributed to the resistivity of the direct ionic path at the LiTFSI-PEO network||*Al*-LLZO interface (facilitated ionic transfer regions), while R_t and C_t correspond to the distributed Li^+ transfer resistance/capacitance between the two electrolytes (hindered ionic transfer regions).

This supplementary distributed $R_t//C_t$ element is the signature of a more tortuous (or an energetically costlier) path for the Li^+. The use of a $Z_{deLevie}$ element, which is equivalent to a TLM, was previously used by Langer et al.[10] to describe the ion-transfer process due to interface processes including distributed Li^+ transition across the interface at the PEO-$LiClO_4$ and LLZO. Finally, the equivalent circuit shown in Figure IV-3c has been proposed to fit our experimental data and the fit (reported in the same figure) is in excellent agreement.

III.2. Understanding and studying PEO network||*Al*-LLZO interface resistance

The LiTFSI-PEO network||*Al*-LLZO interfacial resistance of *in-situ* LiTFSI-Multilayer at 30 °C has been evaluated to be ~ 16 kΩ.cm^2, considering it is mostly coming from R_i in the TLM element (as it gives the amplitude of the real part of the corresponding impedance – zone a in Figure IV-2). The value of interfacial resistance of *in-situ* LiTFSI-Multilayer at 30 °C is higher than the one estimated by Gupta et al. on PEO-LiTFSI/LLZTO/PEO-LiTFSI multilayer ($R_{interface}$ = 0.2 kΩ.cm^2)[8]. The main difference between their study and our work, whether the polymer is linear or reticulated, is that the PEO network is formed *in-situ* on the surface of the *Al*-LLZO. To check whether this implies a difference in resistance of the LiTFSI-PEO network||*Al*-LLZO interface, an *ex-situ* LiTFSI-Multilayer is thus studied. The polymer is formed *ex-situ* and held to the surface of the *Al*-LLZO pellets by pressure during the electrochemical test.

The shape of the impedance plot (Figure IV-4) is similar to the one obtained for *in-situ* polymerization. By using the same equivalent circuit, proposed in Figure IV-3c, the values of R_i and R_t for all studied temperatures, are summarized in Table SI.IV-4 and Table SI.IV-5for *in-situ* LiTFSI-Multilayer and *ex-situ* LiTFSI-Multiplayer. For *ex-situ* LiTFSI-Multilayer, the resistance R_i for the composite interface is ~ 2.3 kΩ.cm^2 at 30 °C.

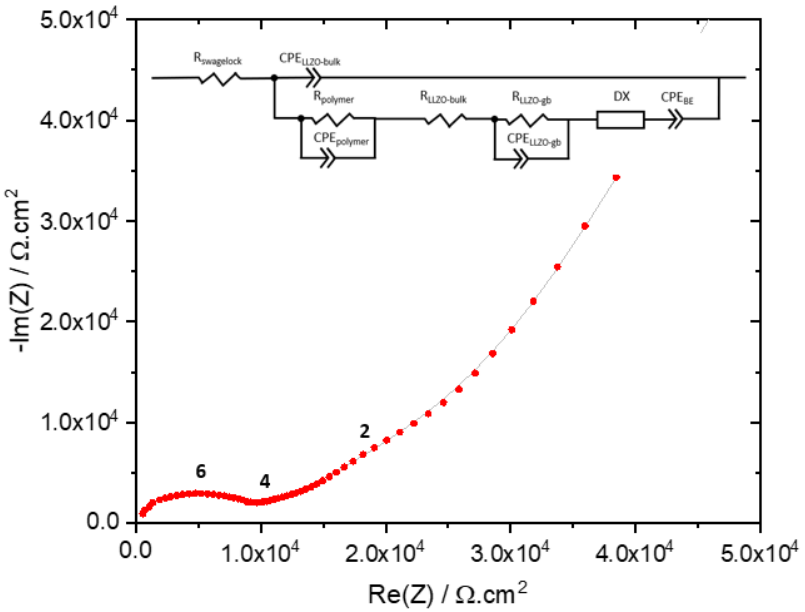

Figure IV-4. Nyquist plot at 30 °C of (●) *ex-situ* LiTFSI-Multilayer, (—) fit according to the equivalent circuit presented. Numbers at the data points indicate the power of frequency.

This value is much lower than the one observed for *in-situ* polymerization (16 kΩ.cm²). However, the main difference between the two multilayer is that the LiTFSI-PEO network is formed *in-situ*, favoring covalent bonding between PEGM-PEGDM and the *Al*-LLZO ceramics through two different possible mechanisms (described in Figure IV-5). In the first mechanism, the free radicals from the initial state of the polymerization can be transferred to the hydroxyl group on the surface of the *Al*-LLZO ceramics that allowing the grafting of PEGM or PEGDM on the ceramics (see Figure IV-5a). In the second one, transesterification could occur between the methacrylate of the precursor PEGM or/and PEGDM and the hydroxyl on the surface of the LLZO (see Figure IV-5b). This covalent bonding probably accentuate the electrostatic repulsion between LLZO and the oxygen of the PEO chain, increasing the distance for Li^+ hopping between the polymer and LLZO[20,21]. The grafted methacrylate function can subsequently participate in the formation of a PEO network grafted on the LLZO surface. IR spectroscopy analyses were carried out to validate the hypothesis of a covalent bond between the PEO network and the *Al*-LLZO ceramic, but unfortunately, the concentration of the PEO chain grafted to the surface of the ceramic is probably too low to be detected due to the 2D morphology of the interface.

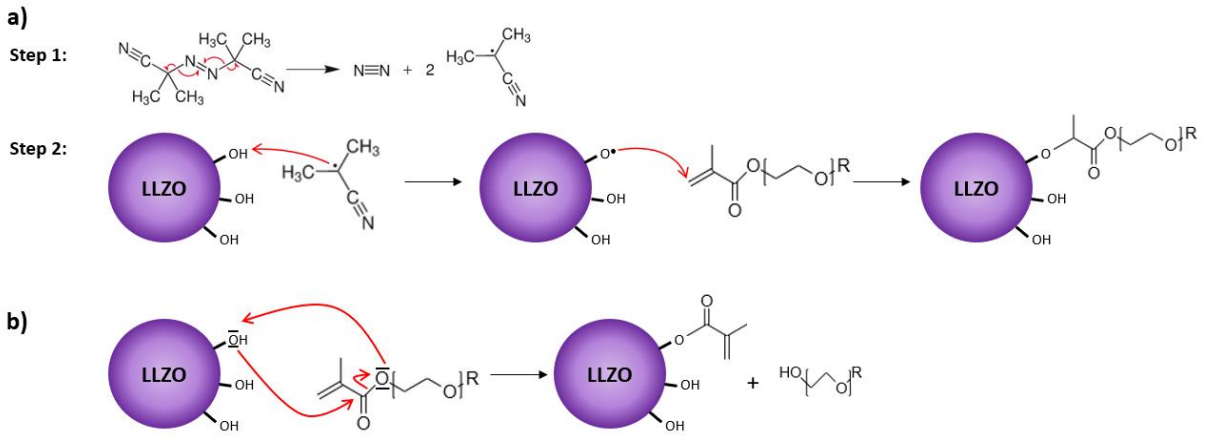

Figure IV-5. (a) Hypothesis on the reaction between *Al*-LLZO and precursor solution LiTFSI-PEO network activated by the free radicals from AIBN, (b) Hypothesis on the reaction between *Al*-LLZO and methacrylate from precursor solution of LiTFSI-PEO network.

The *in-situ* formation of the PEO network does then appear to be less favorable to direct Li^+ ions transport at the LiTFSI-PEO network||*Al*-LLZO interface, in the whole range of temperatures (Figure IV-6a). However, this tendency is not observed for the diffusion phenomena described by R_t in the TML element (Figure IV-6b). R_t represents the transfer of Li^+ ions from the *Al*-LLZO to the PEO network, and its value is influenced by the differences in dielectric constant and Li^+ concentration between the two compounds. The fact that R_t is similar for both *in-situ* and *ex-situ* multilayers is to be expected, as the Li^+ concentration in the two polymer networks is the same and the dielectric constants should be close. This also indicates that *in-situ* polymerization does not macroscopically modify the polymer. Interestingly, the change of R_i between the *in-situ* and the *ex-situ* polymerization approaches is an indication that the PEO chains directly grafted onto the *Al*-LLZO surface induce a distance of jump for Li^+ different, affecting the direct Li^+ transport.[20,21]

Compared with the work performed on the LLZTO||PEO-LiTFSI interface (R_i = 0.2 kΩ.cm^2)[8], the value measured for R_i of our *ex-situ* LiTFSI-Mutlilayer (2.3 kΩ.cm^2) at 30 °C is an order of magnitude higher. This may be due to differences in the conductivity of ceramics (Al-doped LLZO *vs.* Ta-doped LLZO) or to the surface chemistry of LLZO. After high-temperature sintering (1225 °C), a second heat treatment is carried out at 700 °C to remove impurities[8]. Most of the results in the literature are obtained at 70 °C, since the conductivities of PEO at this temperature (10^{-3} S.cm^{-1}) are compatible with batteries application. We have, therefore, compared our R_i values at 70 °C with the literature. A value of ~ 0.2 kΩ.cm^2 was

measured, which is an order of magnitude lower than that of Langer et al.[10] (9 kΩ.cm^2 at 70 °C) measured on a symmetrical multilayer cell with LLZO and PEO-$LiClO_4$.

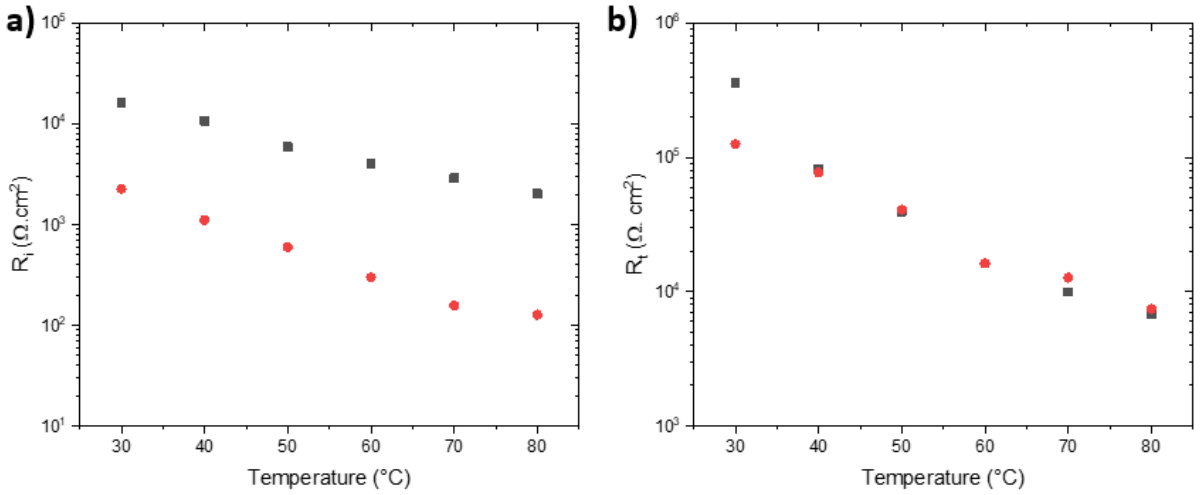

Figure IV-6. Evolution of the interface resistance (a) R_i and (b) R_t as a function of temperature for (■) *in-situ* LiTFSI-Multilayer and (●) *ex-situ* LiTFSI-Multilayer.

To analyze the importance of Li^+ distribution at the interface, and in particular the distance Li^+ has to travel between the polymer EO groups and the Li^+ sites in *Al*-LLZO, the anion was grafted to the polymer chain. The impact of this modification on interfacial processes, including resistive and/or diffusional phenomena, was evaluated. For this purpose, we designed an *ex-situ* LiMTFSI-Mutilayer, comprising two single-ion polymer membranes synthesized according to Naboulsi et al.[13] The results are gathered in Figure IV-7.

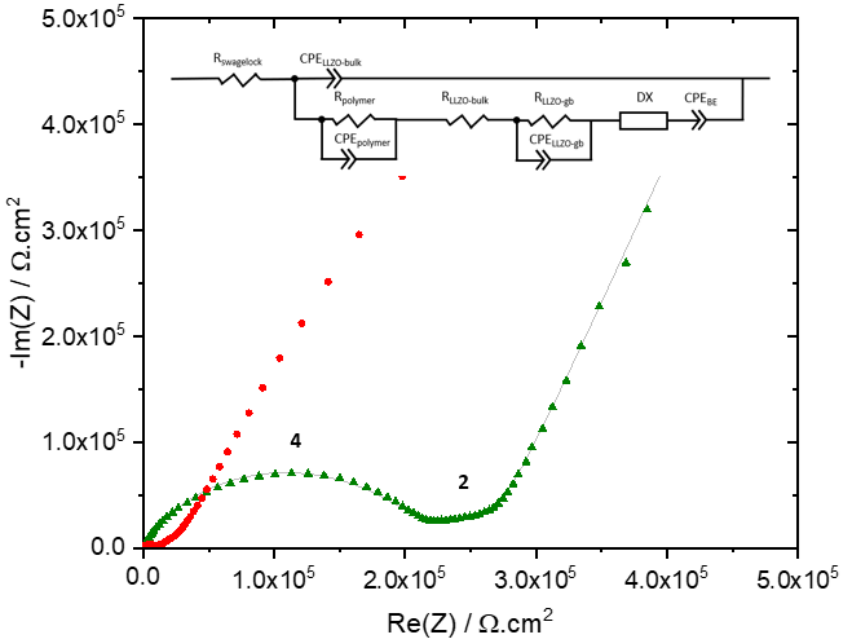

Figure IV-7. Nyquist plot at 30 °C of (●) *ex-situ* LiMTFSI-Multilayer, (—) fit according to the equivalent circuit presented and numbers at the data points indicate the power of frequency for *ex-situ* LiMTFSI-Multilayer and (●) *ex-situ* LiTFSI-Multilayer.

First, the impedance spectra are comparable in shape to *ex-situ* LiTFSI-Multilayers at extremely high and low frequencies. The main differences occur in the impedance values obtained, and at the MF range, where a shoulder appears much more attenuated and flatten. The impedance differences may be related to the high resistance of the single-ion polymer membrane (10^{-7} S.cm^{-1})[13] compared to the polymer membrane with LiTFSI (10^{-5} S.cm^{-1}), inducing than a much larger first semicircle (HF). Using the equivalent circuit of Figure IV-3c, it is then possible to fit the Nyquist plot and estimate the values for R_i and R_t (i.e. Table SI.IV-6)

Figure IV-8a represents the variation of R_i as a function of the temperature. For *ex-situ* LiMTFSI-Multilayer, it can be seen that R_i is an order of magnitude higher than the one observed for *ex-situ* LiTFSI-Multilayer. For *ex-situ* LiMTFSI-Multilayer, the hopping distance for Li^+ to cross the interface is fixed and probably more important as the anion is attached to the polymer chain. Interestingly, R_t (Figure IV-8b) for *ex-situ* LiMTFSI multilayer compares well with the one for *ex-situ* LiTFSI multilayer. R_i and R_t are influenced by the chemical composition of the materials brought into contact and by the energy barrier that Li^+ must overcome to pass from one dielectric material to the other (inorganic and polymer). Given that the polymers are of the same chemical nature, the only difference between the two systems studied is the distribution of Li at the interface. LiTFSI is free in the PEO network whereas

LiMTFSI is grafted to the PEO network, which perhaps implies that more Li is present at the interface for PEO-LiTFSI. This difference in the value of R_i confirms its attribution to the transport of the Li^+ between the *Al*-LLZO and the PEO network.

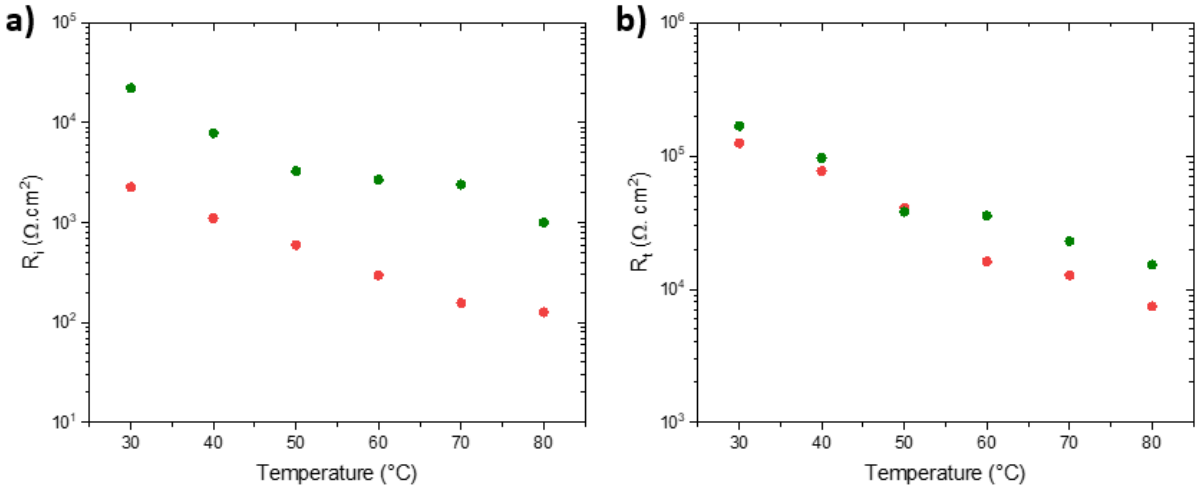

Figure IV-8. (a) Evolution of the interface resistance (a) R_i and (b) R_t as a function of temperature for (●) *ex-situ* LiMTFSI-Multilayer and (●) *ex-situ* LiTFSI-Multilayer.

From the variation of R_i and R_t with temperature, we estimated the activation energy (E_a) for each of these phenomena as a function of the assembly processes (Figure SI.IV-3 and SI.IV-4, Table IV-2). We find that the activation energies for R_i and R_t are comparable in the case of *ex-situ* LiTFSI and LiMTFSI, showing that the energy barrier for the Li^+ to cross the interface by this shaping process is identical. This is because the polymers are held to the surface of the *Al*-LLZO pellet by pressure. Conversely, the activation energies for LiTFSI are different between *in-situ* and *ex-situ*. For R_i, they are lower for the *in-situ* multilayer (0.38 eV for *in-situ* compared with 0.54 eV for *ex-situ*). This suggests a modification of the Li^+ transport mechanism at the interface, probably linked to the assembly process such as the *in-situ* polymerization. Furthermore, in the *in-situ* multilayer, we note that the activation energies for R_i and R_t are different. Just as the values of R_i are lower than R_t. These values tend to show that the preferred transport mechanism is the direct one.

Table IV-2. Activation energy is estimated for interfacial resistances (R_i and R_t) for the three multilayers.

Sample	**E_a (R_i) eV**	**R^2**	**E_a (R_t) eV**	**R^2**
in-situ LiTFSI-Multilayer	0.38	0.99	0.60	0.98
ex-situ LiTFSI-Multilayer	0.54	0.99	0.53	0.98
ex-situ LiMTFSI-Multilayer	0.54	0.96	0.43	0.99

IV. Conclusion

We have studied the transport of Li^+ ions through the cross-linked PEO network||LLZO interface by designing multilayer architectures. Our interest was to understand how Li^+ ion moves through the composite interface in order to define the physical-chemical parameters influencing most of its transport. In this context, we have used our knowledge of the synthesis of cross-linked PEO network from liquid polymer precursor to investigate the impact of grafting cross-linked PEO network to *Al*-LLZO surface, and of the depletion of Li^+ at the interface by grafting anions (TFSI) to the PEO chain. Impedance spectroscopy has been advantageously used for evaluating the various resistances (polymer, *Al*-LLZO and interface) based on an equivalent circuit integrating a TLM element, to better highlight heterogeneities at the interfaces. Interestingly, we found that the R_i representing the direct transport of Li^+ at the composite interface was larger in the case of in situ polymerization, due probably to a larger jump distance of Li^+ between the inorganic and organic phases. On the contrary, the R_t value appears to be independent of the way in which the polymers are assembled onto the *Al*-LLZO surface and the manner that Li^+ is brought to the PEO network (LiTFSI salts *vs.* grafted anion) as this resistance is attributed to the change of environment of Li^+ going from *Al*-LLZO to PEO network. Interestingly, the estimation of the energy of activation from R_i and R_t confirms the modification of the cross-linked PEO network||*Al*-LLZO interface for the assembly by *in-situ* polymerization. In particular, the direct transport of Li^+ appears more favorable.

Supporting information

Table of sample composition and characteristics of the various multilayer designs; Nyquist plot at 30°C of LiTFSI-PEO network, *Al*-LLZO; Table of values of electrical circuit elements at all temperatures for LiTFSI-PEO network, LiMTFSI-PEO network and *Al*-LLZO; Representation of TLM element; Table of values of R_i, CPE_i, α_i and R_t electrical circuit elements at all temperature for *in-situ* LiTFSI-Multilayer, *ex-situ* LiTFSI-Multilayer and *ex-situ* LiMTFSI-Multilayer; Arrhenius plot of the interfacial resistance R_i and R_t for *in-situ* LiTFSI-Multilayer, *ex-situ* LiTFSI-Multilayer and *ex-situ* LiMTFSI-Multilayer.

References:

(1) Janek, J.; Zeier, W. G. A Solid Future for Battery Development. *Nat. Energy* **2016**, *1* (9), 16141. https://doi.org/10.1038/nenergy.2016.141.

(2) Zheng, Y.; Yao, Y.; Ou, J.; Li, M.; Luo, D.; Dou, H.; Li, Z.; Amine, K.; Yu, A.; Chen, Z. A Review of Composite Solid-State Electrolytes for Lithium Batteries: Fundamentals, Key Materials and Advanced Structures. *Chem. Soc. Rev.* **2020**, *49* (23), 8790–8839. https://doi.org/10.1039/D0CS00305K.

(3) Zhao, Y.; Zheng, K.; Sun, X. Addressing Interfacial Issues in Liquid-Based and Solid-State Batteries by Atomic and Molecular Layer Deposition. *Joule* **2018**, *2* (12), 2583–2604. https://doi.org/10.1016/j.joule.2018.11.012.

(4) Weiss, M.; Simon, F. J.; Busche, M. R.; Nakamura, T.; Schröder, D.; Richter, F. H.; Janek, J. From Liquid- to Solid-State Batteries: Ion Transfer Kinetics of Heteroionic Interfaces. *Electrochem. Energy Rev.* **2020**, *3* (2), 221–238. https://doi.org/10.1007/s41918-020-00062-7.

(5) Zheng, J.; Hu, Y.-Y. New Insights into the Compositional Dependence of Li-Ion Transport in Polymer–Ceramic Composite Electrolytes. *ACS Appl. Mater. Interfaces* **2018**, *10* (4), 4113–4120. https://doi.org/10.1021/acsami.7b17301.

(6) Brogioli, D.; Langer, F.; Kun, R.; La Mantia, F. Space-Charge Effects at the $Li_7La_3Zr_2O_{12}$ /Poly(Ethylene Oxide) Interface. *ACS Appl. Mater. Interfaces* **2019**, *11* (12), 11999–12007. https://doi.org/10.1021/acsami.8b19237.

(7) Kuhnert, E.; Ladenstein, L.; Jodlbauer, A.; Slugovc, C.; Trimmel, G.; Wilkening, H. M. R.; Rettenwander, D. Lowering the Interfacial Resistance in Li6.4La3Zr1.4Ta0.6O12|Poly(Ethylene Oxide) Composite Electrolytes. *Cell Rep. Phys. Sci.* **2020**, *1* (10), 100214. https://doi.org/10.1016/j.xcrp.2020.100214.

(8) Gupta, A.; Sakamoto, J. Controlling Ionic Transport through the PEO-LiTFSI/LLZTO Interface. *Electrochem. Soc. Interface* **2019**, *28* (2), 63–69. https://doi.org/10.1149/2.F06192if.

(9) Isaac, J. A.; Mangani, L. R.; Devaux, D.; Bouchet, R. Electrochemical Impedance Spectroscopy of PEO-LATP Model Multilayers: Ionic Charge Transport and Transfer. *ACS Appl. Mater. Interfaces* **2022**, *14* (11), 13158–13168. https://doi.org/10.1021/acsami.1c19235.

(10) Langer, F.; Palagonia, M. S.; Bardenhagen, I.; Glenneberg, J.; La Mantia, F.; Kun, R. Impedance Spectroscopy Analysis of the Lithium Ion Transport through the $Li_7La_3Zr_2O_{12}$ /$P(EO)_{20}$ Li Interface. *J. Electrochem. Soc.* **2017**, *164* (12), A2298–A2303. https://doi.org/10.1149/2.0381712jes.

(11) De Levie, R. The Influence of Surface Roughness of Solid Electrodes on Electrochemical Measurements. *Electrochimica Acta* **1965**, *10* (2), 113–130. https://doi.org/10.1016/0013-4686(65)87012-8.

(12) La Mantia, F.; Vetter, J.; Novák, P. Impedance Spectroscopy on Porous Materials: A General Model and Application to Graphite Electrodes of Lithium-Ion Batteries. *Electrochimica Acta* **2008**, *53* (12), 4109–4121. https://doi.org/10.1016/j.electacta.2007.12.060.

(13) Naboulsi, A.; Chometon, R.; Ribot, F.; Nguyen, G.; Fichet, O.; Laberty-Robert, C. Correlation between Ionic and Mechanical Properties of Solid PEO Polymer Electrolyte. *ACS Appl. Mater. Interfaces* **2023**, *Under revision*.

(14) Chen, Y.; Wen, K.; Chen, T.; Zhang, X.; Armand, M.; Chen, S. Recent Progress in All-Solid-State Lithium Batteries: The Emerging Strategies for Advanced Electrolytes and Their Interfaces. *Energy Storage Mater.* **2020**, *31*, 401–433. https://doi.org/10.1016/j.ensm.2020.05.019.

(15) Nonnenmacher, W. Stromverteilung in porösen elektroden.

(16) Orazem, M. E.; Frateur, I.; Tribollet, B.; Vivier, V.; Marcelin, S.; Pébère, N.; Bunge, A. L.; White, E. A.; Riemer, D. P.; Musiani, M. Dielectric Properties of Materials Showing Constant-Phase-Element (CPE) Impedance Response. *J. Electrochem. Soc.* **2013**, *160* (6), C215–C225. https://doi.org/10.1149/2.033306jes.

(17) Devaux, D.; Bouchet, R.; Glé, D.; Denoyel, R. Mechanism of Ion Transport in PEO/LiTFSI Complexes: Effect of Temperature, Molecular Weight and End Groups. *Solid State Ion.* **2012**, *227*, 119–127. https://doi.org/10.1016/j.ssi.2012.09.020.

(18) Irvine, J. T. S.; Sinclair, D. C.; West, A. R. Electroceramics: Characterization by Impedance Spectroscopy. *Adv. Mater.* **1990**, *2* (3), 132–138. https://doi.org/10.1002/adma.19900020304.

(19) Nara, H.; Mukoyama, D.; Yokoshima, T.; Momma, T.; Osaka, T. Impedance Analysis with Transmission Line Model for Reaction Distribution in a Pouch Type Lithium-Ion Battery by Using Micro Reference Electrode. *J. Electrochem. Soc.* **2016**, *163* (3), A434–A441. https://doi.org/10.1149/2.0341603jes.

(20) Sharafi, A.; Yu, S.; Naguib, M.; Lee, M.; Ma, C.; Meyer, H. M.; Nanda, J.; Chi, M.; Siegel, D. J.; Sakamoto, J. Impact of Air Exposure and Surface Chemistry on Li–$Li_7La_3Zr_2O_{12}$ Interfacial Resistance. *J. Mater. Chem. A* **2017**, *5* (26), 13475–13487. https://doi.org/10.1039/C7TA03162A.

(21) Huo, H.; Luo, J.; Thangadurai, V.; Guo, X.; Nan, C.-W.; Sun, X. Li_2CO_3 : A Critical Issue for Developing Solid Garnet Batteries. *ACS Energy Lett.* **2020**, *5* (1), 252–262. https://doi.org/10.1021/acsenergylett.9b02401.

Supporting information

Understanding the Li^+ transport through the PEO network||*Al*-LLZO interface by using Electrochemical Impedance Spectroscopy

Table SI.IV-1. Sample composition and characteristic of the various multilayer design

Sample	Polymerization	Type of polymer	Thickness (cm)		Area (cm^2)
			Total polymer	LLZO	
in-situ LiTFSI-Multilayer	in-situ	PEGM-PEGDM-LiTFSI	0.032	0.234	0.99
ex-situ LiTFSI-Multilayer	ex-situ	PEGM-PEGDM-LiTFSI	0.057	0.230	0.99
ex-situ LiMTFSI-Multilayer	ex-situ	PEGM-PEGDM-LiMTFSI	0.051	0.185	0.99

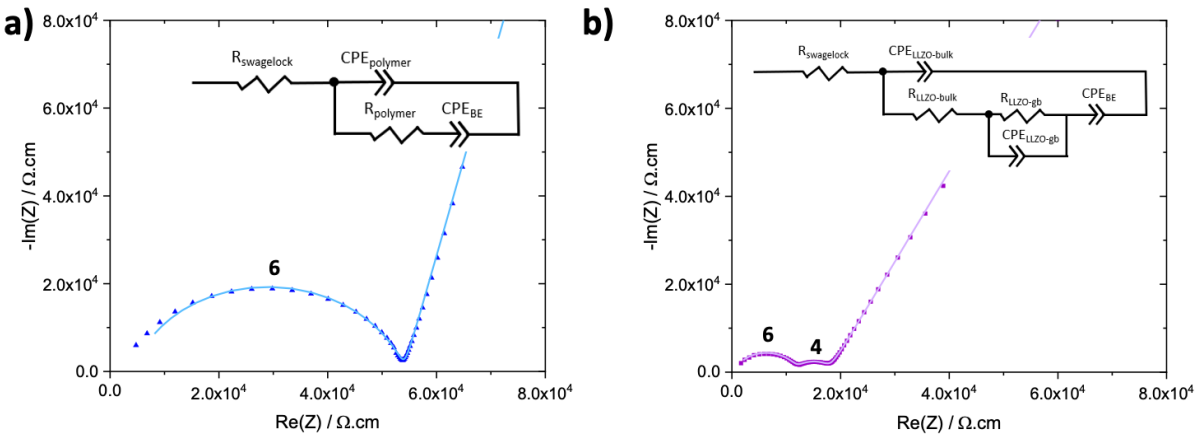

Figure SI.IV-1. Nyquist plot at 30 °C of (a) BE/LiTFSI-PEO network/BE, (b) Au/*Al*-LLZO/Au and (—) fit according to the equivalent circuit presented respectively. Numbers at the data points indicate power of frequency.

Table SI.IV-2. Values of electrical circuit elements at all temperature for BE/LiTFSI-PEO network/BE and BE/LiMTFSI-PEO network/BE.

Temperature (°C)	LiTFSI-PEO network			LiMTFSI-PEO network		
	$R_{polymer}$ (Ω)	$CPE_{polymer}$ ($F.cm^{-2}$)	$\alpha_{polymer}$	$R_{polymer}$ (Ω)	$CPE_{polymer}$ ($F.cm^{-2}$)	$\alpha_{polymer}$
30	1700	$9.0.10^{-10}$	0.83	95327	$1.2.10^{-9}$	0.76
40	850	$6.1.10^{-10}$	0.86	44327	$1.4.10^{-9}$	0.76
50	400	$7.2.10^{-10}$	0.87	20849	$1.8.10^{-9}$	0.76
60	200	$7.0.10^{-10}$	0.91	12170	$2.2.10^{-9}$	0.75
70	100	$5.0.10^{-10}$	0.96	5219	$3.1.10^{-9}$	0.74
80	50	$7.0.10^{-10}$	0.99	3818	$3.7.10^{-9}$	0.74

Table SI.IV-3. Values of electrical circuit elements at all temperature for Au/*Al*-LLZO/Au.

Temperature (°C)	***Al*-LLZO**					
	$R_{LLZO\text{-}bulk}$ (Ω)	$CPE_{LLZO\text{-}bulk}$ ($F.cm^{-2}$)	$\alpha_{LLZO\text{-}bulk}$	$R_{LLZO\text{-}gb}$ (Ω)	$CPE_{LLZO\text{-}gb}$ ($F.cm^{-2}$)	$\alpha_{LLZO\text{-}gb}$
30	2830	$5.5.10^{-10}$	0.80	1306	$1.0.10^{-7}$	0.77
40	1919	$9.6.10^{-10}$	0.77	705	$6.0.10^{-8}$	0.84
50	1291	$2.0.10^{-9}$	0.74	366	$3.6.10^{-8}$	0.90
60	942	$5.0.10^{-9}$	0.69	218	$2.5.10^{-8}$	0.94
70	704	$2.0.10^{-8}$	0.63	111	$1.7.10^{-8}$	0.99
80	460	$8.0.10^{-9}$	0.70	97	$4.8.10^{-8}$	0.88

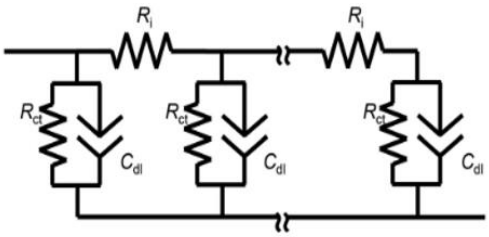

Figure SI.IV-2. Representation of TLM element.

Table SI.IV-4. Values of R_i, CPE_i, α_i and R_t electrical circuit elements at all temperature for BE/*in-situ* LiTFSI-Multilayer/BE.

Temperature (°C)	***in-situ* LiTFSI-Multilayer**			
	R_i ($\Omega.cm^2$)	R_t ($\Omega.cm^2$)	CPE_t (F)	α_t
30	$1.6.10^4$	$3.6.10^5$	$3.1.10^{-8}$	0.83
40	$1.1.10^4$	$8.2.10^4$	$4.6.10^{-9}$	0.85
50	$5.9.10^3$	$3.9.10^4$	$9.0.10^{-8}$	0.77
60	$4.0.10^3$	$1.7.10^4$	$1.0.10^{-7}$	0.78
70	$2.9.10^3$	$9.9.10^3$	$1.1.10^{-7}$	0.78
80	$2.0.10^3$	$6.8.10^3$	$2.3.10^{-7}$	0.72

Table SI.IV-5. Values of R_i, CPE_i, α_i and R_t electrical circuit elements at all temperature for BE/*ex-situ* LiTFSI-Multilayer/BE.

Temperature (°C)	***ex-situ* LiTFSI-Multilayer**			
	R_i ($\Omega.cm^2$)	R_t ($\Omega.cm^2$)	CPE_t (F)	α_t
30	$2.3.10^3$	$1.2.10^5$	$7.3.10^{-8}$	0.73
40	$1.1.10^3$	$7.7.10^4$	$4.9.10^{-8}$	0.76
50	$6.0.10^2$	$4.1.10^4$	$3.9.10^{-8}$	0.79
60	$3.0.10^2$	$1.6.10^4$	$9.8.10^{-9}$	0.92
70	$1.6.10^2$	$1.3.10^4$	$1.0.10^{-8}$	0.87
80	$1.3.10^2$	$7.4.10^3$	$1.1.10^{-8}$	0.88

Table SI.IV-6. Values of R_i, CPE_i, α_i and R_t electrical circuit elements at all temperature for BE/*ex-situ* LiMTFSI-Multilayer/BE.

Temperature (°C)	*ex-situ* LiMTFSI-Multilayer			
	R_i ($\Omega.cm^2$)	R_t ($\Omega.cm^2$)	CPE_t (F)	α_t
30	$2.2.10^4$	$1.7.10^5$	$6.7.10^{-8}$	0.78
40	$7.9.10^3$	$9.7.10^4$	$2.0.10^{-8}$	0.91
50	$3.3.10^3$	$3.8.10^4$	$3.8.10^{-8}$	0.86
60	$2.7.10^3$	$3.6.10^4$	$3.2.10^{-8}$	0.92
70	$2.4.10^3$	$2.3.10^4$	$9.3.10^{-8}$	0.75
80	$1.0.10^3$	$1.5.10^4$	$5.8.10^{-8}$	0.79

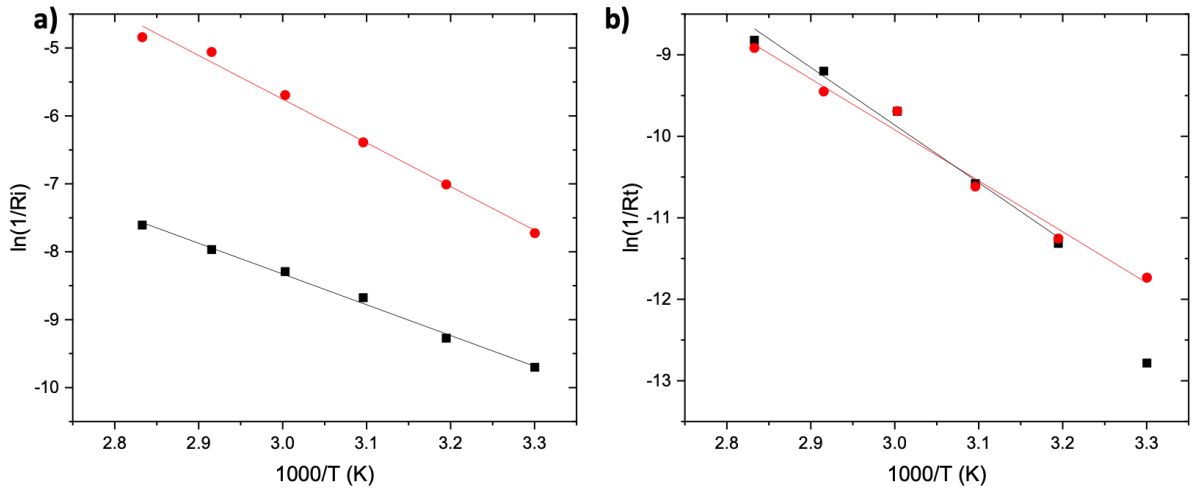

Figure SI.IV-3. Arrhenius plot of the interfacial resistance (a) R_i and (b) R_t for (■) *in-situ* LiTFSI-Multilayer and (●) *ex-situ* LiTFSI-Multilayer.

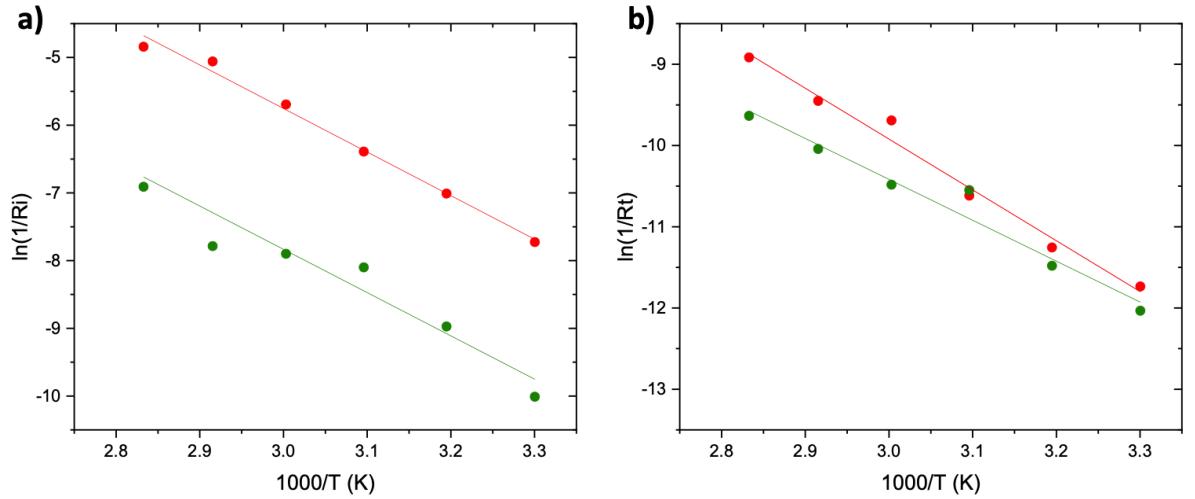

Figure SI.IV-4. Arrhenius plot of the interfacial resistance (a) R_i and (b) R_t for (●) *ex-situ* LiMTFSI-Multilayer and (●) *ex-situ* LiTFSI-Multilayer.

Chapter V.

Improvement of Ionic Conductivity of the *Al*-LLZO composite through *in-situ* synthesis of the PEO networks during the cold-sintering process

Buildings points:

- Fabrication of predominantly inorganic composite electrolytes using the CSP through *in-situ* polymerization and one-pot synthesis
- Enhancement of ionic conductivities in the composites compared to the pure polymer network
- Identification of Li^+ diffusion pathway at the PEO||*Al*-LLZO network interface through the EIS method and measurement of E_a.

Résumé

Pour la conception de batteries tout solide, il est essentiel de concevoir un électrolyte solide offrant les meilleures performances. De nombreuses recherches se sont portées sur les électrolytes composites, car ils permettraient de combiner les avantages des électrolytes inorganique et polymère, tout en masquant leurs défauts respectifs. Pour élaborer un électrolyte composite majoritairement inorganique, l'utilisation du procédé de frittage à froid (cold-sintering process, CSP) s'avère prometteuse. Ce procédé a été développé pour fritter et/ou compacter des céramiques à plus basse température (< 200 °C) que le frittage conventionnel. Les composites ainsi réalisés comprennent comme phase inorganique le grenat $Li_7La_3Zr_2O_{12}$ (LLZO), choisi en raison de sa stabilité à l'air et sa haute conductivité ionique (10^{-3} S.cm^{-1} à température ambiante)[1]. Après une étude détaillée dans le chapitre II, les phases polymères choisies sont composées d'un réseau de polymère doté de chaînes pendantes de poly(éthylène oxyde) (PEO). Ces réseaux sont obtenus via une polymérisation radicalaire thermiquement activée, ce qui permet de réaliser une polymérisation *in-situ* pendant le CSP et d'obtenir l'électrolyte composite par une synthèse one-pot. Nous avons pu étudier l'impact de la nature de la phase polymère (contenant des sels de Li ou non et le greffage du contre anion aux chaînes PEO) sur la conductivité ionique du composite. De plus, d'autre phases inorganiques autres que le LLZO ont également été étudiées. Des nettes améliorations des conductivités ioniques ont été observées lors de la fabrication de pastilles par CSP en comparaison avec les réseaux PEO seuls (sans sel : 10^{-8} *vs.* 10^{-5} S.cm^{-1}, sel de Li : 10^{-5} *vs.* 10^{-4} S.cm^{-1} et greffé : 10^{-7} *vs.* 10^{-5} S.cm^{-1}). En revanche, la nature de la phase inorganique ne semble pas avoir un impact prédominant sur la conductivité des pastilles CSP, tant qu'elle est une source de Li (10^{-5} *vs.* 10^{-8} S.cm^{-1} pour LLZO *vs.* SiO_2). Sur la base de ces observations et du circuit équivalent utilisé pour modéliser les mesures de spectroscopie d'impédance électrochimique, nous avons proposé que le transport des ions Li^+ dans les composites CSP se produit principalement à l'interface du réseau PEO||LLZO. De plus, nous avons démontré une modification de l'assemblage des chaînes PEO à la surface du LLZO par le CSP. Les résultats obtenus mettent en évidence une très faible énergie d'activation (0.1 eV) et une très bonne synergie entre le LLZO et le PEO.

Improvement of Ionic Conductivity of the *Al*-LLZO composite through *in-situ* synthesis of the PEO networks during the cold-sintering process

Project of Article.

Abstract

The design of composite electrolytes for all-solid-state batteries is a subject of extensive research. However, it is challenging to create electrolytes that are predominantly inorganic. To address this, we employed the cold-sintering process (CSP). The ceramic material chosen for this purpose is $Li_{6.25}Al_{0.25}La_3Zr_2O_{12}$ (*Al*-LLZO) due to its high ionic conductivity (10^{-4} $S.cm^{-1}$ at ambient temperature). The polymer phase consists of a network based on poly(ethylene oxide) (PEO) derivatives with dangling chains. The formation of the PEO network is achieved through thermally activated radical polymerization, allowing for an *in-situ* polymerization process and one-pot synthesis of the composite electrolyte during CSP. Interestingly, we demonstrated that the ionic conductivity of the CSP pellet changes with the nature of the polymer 10^{-4} to 10^{-5} $S.cm^{-1}$ for a PEO network with non-grafted and grafted ion pairs, respectively. Furthermore, the diffusion of Li^+ is not influenced by the nature of the inorganic material, as long as it contains Li. A significant increase in ionic conductivity was observed in the composite pellet compared to the pure grafted PEO network (10^{-5} to 10^{-7} respectively). Lastly, the study of electrochemical impedance spectroscopy measurements revealed a modification in the assembly of PEO chains on the surface of *Al*-LLZO during CSP. This was confirmed by the low activation energy value (0.1 eV) measured.

Keywords

Cold sintering process, composite LLZO-PEO network, transmission line element (TLM)

I. Introduction

Recently, solid-state batteries have grown a lot of attention as a feasible alternative to traditional liquid electrolytes in Li-ion batteries (LIBs). The concept of all solid-state batteries has the potential to overcome the electrochemical limits of the standard liquid-based LIBs. It also offers enhanced safety, power and energy density over a wider range of operating voltages and temperatures.[2]. One of the biggest challenge is to design a solid electrolyte (SE) with high ionic conductivity and a wide electrochemical window[3–5]. Among the various electrolytes available in the literature, oxide-based electrolytes including Garnet and NASICON-like meet criteria of conductivity of 10^{-3} S.cm^{-1} at 25 °C[6]. However, the scope of options becomes more limited when the electrochemical stability against lithium metal and high-potential cathode materials is taken into account. Lithium Garnet $Li_7La_2Zr_3O_{12}$ (LLZO) has a high ionic conductivity (1.10^{-3} S.cm^{-1} at 25 °C) and also a wide electrochemical stability window (0 to ~ 6 V *vs.* Li^+/Li), making it a promising electrolyte candidate for the development of solid-state LIBs[7]. Table V-1 shows a non-exhaustive list of different LLZO compositions, their heat treatment and the conductivity obtained.

Table V-1. Comparison of Composition & Crystal structure, Heat treatment and ionic conductivity for LLZO reported in literature.

Authors	Composition & Crystal structure	Heat treatment (sintering)	Conductivity @25°C (S.cm^{-1})
Murugan et al[1]	$Li_7La_3Zr_2O_{12}$ (cubic)	1230°C / 36h	$7.74.10^{-4}$
Awaka et al[8]	$Li_7La_3Zr_2O_{12}$ (tetragonal)	1040°C / 48h	$1.63.10^{-6}$
Kotobuki et al[9]	Al_2O_3-added LLZO	1000°C / 36h	$1.4.10^{-4}$
Mori et al[10]	$Li_{6.25}Ga_{0.25}La_3Zr_2O_{12}$	800-1000°C / 12h	$1.4.10^{-3}$
Xiang et al[11]	$Li_{6.4}Ga_{0.2}La_3Zr_2O_{12}$	1200°C / 18h	$1.09.10^{-3}$
Yoon et al[12]	Ta- $Li_7La_3Zr_2O_{12}$	1000°C / 4h	$2.1.10^{-4}$

In 2007, Murugan et al.[1] have, for the first time, described LLZO crystal structure. The material was synthesized at high temperature (1230 °C) and exhibits a cubic structure with an ionic conductivity of $7.74.10^{-4}$ S.cm^{-1} at 25 °C. Awaka et al.[8] have subsequently reported a tetragonal LLZO phase with an ionic conductivity of $1.63.10^{-6}$ S.cm^{-1} at 25 °C after densification at 980 °C under air. Interestingly, the difference in conductivity between the two

polymorphs is related to the distribution of Li in the different crystallographic sites.[13] Indeed, the distance in the LLZO between two sites of Li is smaller in the cubic phase, consequently increasing its ionic conductivity.[14] In-situ XRD experiments have shown a gradual transformation of tetragonal LLZO into cubic LLZO at about 200 °C [15]. Furthermore, Geiger et al.[14] have studied the influence of the nature of the crucible on the synthesis of the LLZO polymorphs. Thus, the cubic structure is stabilized, through the doping of the Garnet structure by Al coming from the crucible. Using a solid-state synthesis approach, Kotobuki et al.[9] have shown that it is possible to lower the sintering temperature to 1000 °C and to stabilize the cubic polymorph by adding a small amount of Al_2O_3 (1.25 mol%). A maximum of conductivity of $1.4.10^{-4}$ $S.cm^{-1}$ at 30 °C was obtained for the sintered LLZO pellets. Other doping has been studied including Gallium and Tantalum (Table V-1)[13]. For example, Mori et al.[10] have doped LLZO with Ga and achieved a conductivity of 1.10^{-3} $S.cm^{-1}$. Yoon et al.[12] have densified Ta-doped LLZO (LLZTO) ceramic at 1100 °C for 4 h and they achieved an ionic conductivity of $2.1.10^{-4}$ $S.cm^{-1}$ at 25 °C. Ga doping of LLZO gives an order of magnitude higher ionic conductivity than Al or Ta doping. Unfortunately, the electrochemical stability of Ga-substituted LLZO towards Li-metal is much lower than that of Al-substituted LLZO due to the leaching of Ga into the grain boundary when in contact with Li-metal[16]. The integration of LLZO doped with Ta or Al in a Li-metal battery will therefore be easier. If we focus on the price of the dopant, Al is much cheaper than Ta (around 2 *vs.* 250 $\$.kg^{-1}$)[17].

The ionic conductivity is generally measured on LLZO pellets which are usually synthesized following ceramic sintering processes that require long processing times (above 10 h) and high temperatures equal or superior to 1000 °C. Usually, the fabricated pellets have a diameter of 8 to 12 mm at maximum and a thickness in the millimeter range. Generally, a polishing step is required to achieve a smooth surface and to remove degradation residues to improve LLZO|| Li interface and consequently avoid Li dendrite. This polishing step is long and results in a significant waste of raw material, which is a major drawback for the development of solid-state batteries with a lithium Garnet electrolyte. From an industrial outlook, it is thus urgent to investigate alternative fabrication methods for electrolytes that enable larger-scale and faster production at lower costs including lower sintering temperature and shorter time.

In this perspective, Randall et al.[18] reported in 2016 a new processing method called cold-sintering process (CSP) allowing the fabrication of dense materials (90-95.7%) like NaCl, Alkali molybdates and V_2O_5 at extremely low temperatures (< 200 °C) under uniaxial pressure

(100 -800 MPa) within a short time (15 – 60 min). This is possible because of the use of a transient solvent during the processing that facilitates the densification via a judicious coupling of dissolution and precipitation processes. Importantly, temperature and pressure are experimental parameters that govern these two processes. For instance, they have shown a relative densification of 93% at 180 °C under 430 MPa on polycrystalline $BaTiO_3$ nanoceramics using deionized water[19]. Lately, they extended this approach for the densification of ionic conductors including $Li_{1.5}Al_{l0.5}Ge_{1.5}(PO_4)_3$ (LAGP). They achieved densification of 80% with solely a treatment of 120 °C under 400 MPa for 20 min using either ethanol or water as the transient solvent. However, the ionic conductivity of the as-prepared CSP ceramic is low ($3.6.10^{-6}$ S.cm^{-1}) in comparison to high sintered LAGP (10^{-4} S.cm^{-1}). This low conductivity value is related to the presence of an amorphous low conducting phase at the grain boundary (GB) that lower the total conductivity. A post-thermal treatment at 650°C for 5 min allows an increase of ionic conductivity up to $5.4.10^{-5}$ S.cm^{-1} due to the crystallization of more conducting phases in the grain boundaries[20]. To improve ionic conductivity and control the transport of Li^+ ions at the grain boundaries, Li-containing salts were added during the CSP processing to form a composite (LAGP-$LiClO_4$) like electrolyte. The total conductivity reaches a value of $6.35.10^{-5}$ S.cm^{-1}, which is slightly higher than that of $3.79.10^{-5}$ S.cm^{-1} of pure LAGP[21]. An improvement of the ionic conductivity in LAGP and $Li_{1.2}Al_{0.2}Ti_{1.8}(PO_4)_3$ (LATP) ceramic electrolytes is achieved by using bis(trifluoromethanesulfonyl)imide lithium (LiTFSI) salt in aqueous solution as transient solvent. For example, the addition of LiTFSI during CSP led to an increase in the conductivity from $7.6.10^{-6}$ S.cm^{-1} to $1.8.10^{-4}$ S.cm^{-1} for LAGP, and from $2.7.10^{-5}$ S.cm^{-1} to $1.8.10^{-4}$ S.cm^{-1} for LATP[22]. Other salts (LiOH, for example) or a combination of salts (LiOH-$LiNO_3$) have also been tested. For example, it has been shown that the ionic conductivity is highly dependent on the LiOH content: the ionic conductivity evolves from $8.0.10^{-6}$ to $1.8.10^{-5}$ S.cm^{-1} for LiOH content ranging from 0.39 to 0.47 (mol ratio) at room temperature[23].

The densification of LLZO by CSP has also been investigated[24,25]. Wang et al. have demonstrated that the dissolution-precipitation process occurs in LLZO pellet and a density up to 87.7 % was achieved at 350 °C under 350 MPa for 5 min with deionized water or nitric acid aqueous solution[24]. Unfortunately, the dissolution of LLZO was incongruent, leading to a preferential dissolution of Li and Al. Consequently, the non-conducting β-Li_5AlO_4 nanocrystals precipitate in the grain boundaries. This results in a very low conductivity of $3.8.10^{-9}$ S.cm^{-1}, far below the 10^{-4} S.cm^{-1} value found in conventional sintered ceramics[9]. Interestingly, the low

conductivity at the grain boundaries can be readily improved with the addition of low mass fractions of polypropylene carbonate (PPC, 3.2 wt%) and salts (lithium bis(trifluoromethanesulfonyl)imide, LiTFSI or $LiClO_4$, 1.5 wt%). Indeed, the PPC-salt composite favor the transport of Li^+ at the LLZO||LLZO interfaces. Seo et al.[26] produced LLZO composite pellets by pressing a LLZO/PPC/$LiClO_4$ mixture, using DMF as a transient solvent, under 400 MPa at 120 °C for 1.5 h. They demonstrated the importance of DMF in the incongruent dissolution of the extreme surface of the LLZO particles. Furthermore, DMF has been shown to act as a plasticizer between LLZO/LLZO particles. Accordingly, it will improve the conductivity at the LLZO||PPC-$LiClO_4$ interface by both favoring the dissolution and precipitation processes and by increasing the free volume of PPC. The CSP composite pellet exhibits an ionic conductivity of 4.10^{-4} $S.cm^{-1}$ with a relative density of 80-90% while the CSP composite pellet without DMF was close to 10^{-9} $S.cm^{-1}$ at ambient temperature.

Kuhnert et al.[27] studied the interfacial resistance between LLZTO and PEO in composite electrolyte made by tap solution casting method. They demonstrated a decrease of this interfacial resistance by grafting PEO chains at LLZTO via epoxy groups. To achieve this, the surface-terminated oxygen on LLZTO particles is initially activated through plasma etching and followed by a sol-gel chemistry process involving (3-glycidyloxypropyl)trimethoxysilane (Si-R). This reaction facilitates the covalent attachment of Si-R layers onto the LLZTO particles. Subsequently, the surface layers, terminated with an epoxy group, react with the hydroxyl groups of the PEOs, thereby enabling the functionalization of the surface with PEO chains. This improvement is linked to a diminution of the free volume between the LLZTO particle and the solid polymer PEO electrolyte, probably due to a better rearrangement of the PEO chains at the LLZTO surface.

Inspired by this work, in the present paper, we will focus on the design of LLZO-PEO network composites rich in LLZO using CSP through an *in-situ* polymerization of a PEO like network. Interestingly our studies[28], on PEO network/LLZO/PEO network multilayers, have shown that *in-situ* polymerization induce a modification of the PEO arrangement at the LLZO interface. In contrast to previous studies, where the ceramic network is pre-formed, we have then studied how the polymer network formation during ceramic shaping was affected.

Accordingly, we have studied the assembly of PEO-network and LLZO ceramics under the effect of pressure and temperature, to manufacture an *Al*-LLZO composite. As we did before, we have selected Poly(ethylene glycol) methyl ether methacrylate (PEGM) and Poly(ethylene glycol) dimethacrylate (PEGDM) as precursors of the PEO network[29]. Besides to be

commercially available and in liquid form, these monomers allow a solvent-free synthesis that could be easily implemented in the CSP process. In our strategy, the liquid monomers are first mixed with the LLZO powder and the mixture is then introduced in the set-up of CSP to carry out a free-radical polymerization. We have chosen three different amorphous solid polymer electrolytes. The aim is to measure the impact of the polymer phase on the conductivity of the LLZO-PEO composite. According to Naboulsi et al.[29], LiTFSI dissolved in the solid polymer electrolyte (LiTFSI-SPE) exhibits a conductivity of 10^{-5} S.cm^{-1} at room temperature while a conductivity of 10^{-7} S.cm^{-1} was achieved when the TFSI group is grafted to the PEO network (solid polymer electrolyte called Si-SPE).

Using electrochemical impedance spectroscopy (EIS) measurements, we will try to understand the synergy between the PEO networks and the LLZO. The impact of the polymer and inorganic phases on ionic conductivity and activation energy will also be studied. Furthermore, this study has enabled us to highlight the favourable synergy between the PEO network and the Al-LLZO in the diffusion of Li^+, thanks to the CSP.

II. Experimental

II.1. Materials

Poly(ethylene glycol) methyl ether methacrylate (PEGM, M_n = 500 g.mol^{-1}, Sigma Aldrich), poly(ethylene glycol) dimethacrylate (PEGDM, Mn=750 g.mol^{-1}, Sigma Aldrich) and lithium 3-[(trifluoromethane)sulfonamidosulfonyl]propyl methacrylate (LiMTFSI, Specific Polymer) were dried at 25 °C under vacuum (10-15 mbar) before use. 2,2′-azobis(2-methylpropionitrile) (AIBN, initiator, 98%, Sigma Aldrich) was recrystallized in methanol before use. Bis(trifluoromethylsulfonyl) amine lithium salt (LiTFSI, > 99%, Sigma Aldrich), $Li_{6.25}Al_{0.25}La_2Zr_3O_{12}$ (*Al*-LLZO, 400 to 600 nm D50, Ampcera), $Li_{1.3}Al_{0.3}Ti_{1.7}(PO_4)_3$ (LATP, 300 nm, Ampcera), acetonitrile (ACN, anhydrous 99.8%, Sigma-Aldrich), silicon dioxide (SiO_2, 400-500nm synthesized by the Stober method and dried for 24 h in a vacuum at 150 °C) and dimethylformamide, N,N- (DMF, anhydrous 99.8%, package under inert gas, Alfa Aesar) were kept in the glove box (H_2O < 0.1 ppm). For the synthesis of Tetragonal $Li_7La_3Zr_2O_{12}$ (*tetra*-LLZO) Li_2CO_3 (ABCR, > 99 %), $La(OH)_3$ (Sigma-Aldrich, > 99.9 %) and ZrO_2 (Alfa Aesar, >99.5%) have been used.

II.2. Materials procedure

Procedure for solid polymer electrolyte without Li solution (PEO-network): PEGM, PEGDM and AIBN were introduced in a vial at the desired quantities (ratio PEGM/PEGDM: 80/20, 2 wt% AIBN by weight respect to the monomer) which was then degassed and flushed with nitrogen until the AIBN was dissolved.

Procedure for single-ion solid polymer electrolyte (Si-SPE) solution: PEGM, PEGDM and LiMTFSI were introduced in a vial according to the desired proportions (ratio PEGM/PEGDM: 80/20 and EO/Li = 24) and stirred until the total solubilization of LiMTFSI (2 h) at room temperature. 2% AIBN by weight with respect to PEGM, PEGDM and LiMTFSI were added to the mixture, which was then degassed and flushed with nitrogen until the AIBN was dissolved.

Procedure for solid polymer electrolyte (LiTFSI-SPE) solution: PEGM, PEGDM and AIBN were introduced in a vial at the desired quantities (ratio PEGM/PEGDM: 80/20, 2 wt% AIBN by weight respect to the monomer) which was then degassed and flushed with nitrogen until the AIBN was dissolved. The vial was then introduced in the glove box (H_2O < 0.1 ppm) and the required amount of LiTFSI was added to the mixture (EO/Li = 24). The mixture was stirred until the LiTFSI was dissolved.

Synthesis procedures for polymer membranes: the precursor mixtures were poured into a mold made with two glass plates separated by a Teflon gasket (thickness = 250 µm). The mold was then placed in an oven at 70°C for 2 h and then at 90°C for 1 h. The resulting polymer membranes were then dried under vacuum (10-15 mbar) at 70 °C in a glass oven (BUCHI B-585) for 12 h and then kept in a glove box (H_2O < 0.1 ppm) before use.

***Tetra*-LLZO Synthesis:** Tetragonal $Li_7La_3Zr_2O_{12}$ (*t-LLZO*) sample was prepared by solid-state reaction between Li_2CO_3, $La(OH)_3$ and ZrO_2 in 1.05/2.31/1 mass proportion (total mass 8 g), with 10 % excess (of total mass) of Li_2CO_3 to take into account Li evaporation. The precursors were ground using an agate mortar and pestle, were placed in an alumina crucible and heated at 950 °C for 12 hours, then cooled down to room temperature throughout 7 h. The heat treatment was done in tubular furnaces under dry-air conditions. This process was repeated once, with intermediate grinding to improve single phase purity of the final materials. The sample consists of light-yellow powder of tetragonal $Li_7La_3Zr_2O_{12}$ (Figure SI.V-1).

Procedure for cold-sintering preparation: Commercial *Al*-LLZO powder (or *t*-LLZO or LATP), DMF, ACN and polymer precursor solution were introduced in mortar to the desired

proportion (Table SI.V-1). ACN is used to homogenize the mixture. The amount of DMF and ACN introduced into the CSP set-up is 7 and 38 wt% respectively, with respect to the mass of inorganic[30]. The mixtures were ground manually with a pestle for 3 min in a glovebox. The powder mixture was introduced into the cold sintering machine (diameter: 12.7 mm) between two aluminum foils and compacted between 777-920 MPa and the following heat program was imposed: 70 °C for 2 h, 90 °C for 1 h and 120 °C for 30 min. The pellet was removed after heat treatment from the mold at 70 °C and put into the glove box. Solid self-standing pellets with a thickness ranging from 1 to 0.5 mm are obtained depending on the amount of inorganic introduced. The compacity of the composite pellets is determined using the ratio:

$$\frac{\rho_{experimental}}{\rho_{theoric}} \qquad \text{Equation 1}$$

$$\rho_{experimental} = \frac{m}{\pi * R^2 * t} \qquad \text{Equation 2}$$

with *m* is the mass (g), *R* the radius (cm) and *t* the thickness of the pellet (cm).

$$\rho_{theoric} = (\chi_{LLZO} * d_{LLZO}) + (\chi_{polymer} * d_{polymer}) \qquad \text{Equation 3}$$

with χ the volumetric fraction and *d* the density (g.cm^{-3}) of materials.

II.3. Characterization

Electrochemical impedance spectroscopy (EIS) was carried out using a 1260 Solartron FRA device between 10^7 Hz and 10^{-1} Hz, with a perturbation amplitude of 100 mV at the OCV (open circuit voltage). The sample was assembled in a Swagelok-type cell using two stainless-steel blocking electrodes (BE). The contact pressure was maintained with a spring (0.4 MPa).

To estimate the ionic conductivity of the samples, the intercept of the first semicircle was considered to correspond to the bulk resistance (R_{bulk}) from which the conductivity was estimated by using the following relation:

$$\sigma = \frac{e}{R_{bulk} * S} \qquad \text{Equation 4}$$

where *e* is the thickness (cm) and *S* is the surface area of the sample (cm²). The measurement was carried out every 10 °C between 30 °C and 80 °C. Temperature was controlled using an environmental chamber (Memmert). Cells were allowed to reach the thermal equilibrium for at least 30 min before measurement.

Calculation of the capacitance from the Constant Phase Element (CPE) by using the Zview software for the impedance data refinement, the CPE element includes two components, Q_o and α, respectively. The equivalent capacitance is calculated according to the following equation[31]:

$$C = \frac{(Q_o * R)^{(\frac{1}{\alpha})}}{R}$$ Equation 5

with R, the resistance in parallel to the CPE element in the electrical equivalent circuit.

The characteristic frequency (f_c) is calculated from the R and CPE of the equivalent circuits according to the following equation[32] :

$$f_c = \frac{1}{2 * \pi * R * C}$$ Equation 6

Thermogravimetric analysis (TGA) was performed using a NETZSCH STA 409 PC/PG. Samples with an average weight of ca. 20 mg were placed in a platinum pan and heated from 30 °C to 900 °C or 1000°C at 10 °C.min^{-1}. Synthetic air with a flow rate of 60 mL.min^{-1} was used as the sweeping gas.

III. Results and discussion

III.1. Contribution of polymer phase during cold-sintering on ionic conductivity

In this study, we have focused on the contribution of a cross-linked polymer phase to the fabrication of composite LLZO/PEO like network solid electrolyte by cold-sintering.

First, we have studied the impact of DMF in the process of densification of *Al*-LLZO ceramics. *Al*-LLZO powder was mixed with DMF and ACN to ensure a homogenous mixture. The mixture was then heated it up at 70 °C for 2 h then 90 °C for 1 h and finally 120 °C for 30 min under 777 MPa. This temperature profile was chosen, according to the one used for polymerization[29]. A supplementary heating step at 120°C has been added to ensure the cold sintering process. The *Al*-LLZO-CSP pellet exhibits a relative density of 60%. The impedance plot (Figure V-1, black) shows an ionic conductivity of 2.5.10^{-6} S.cm^{-1} (with a resistivity of 4.10^5 Ω.cm) for the *Al*-LLZO CSP-pellet.

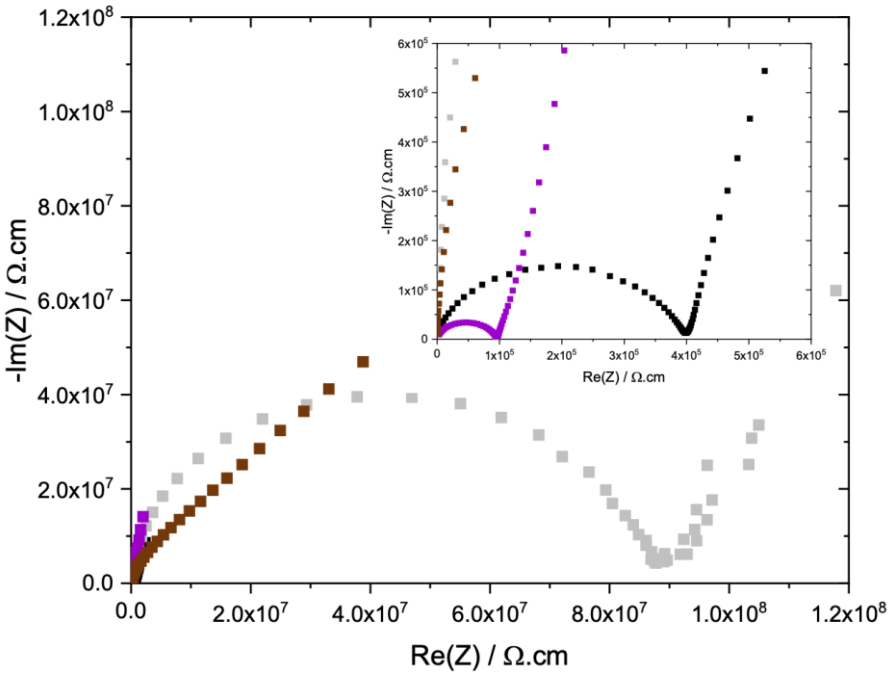

Figure V-1. (a) Impedance plot at 25 °C for (■) *Al*-LLZO CSP-pellet, (■) PEO network, *Al*-LLZO/PEO network CSP pellet (■) with and (■) without DMF.

The low ionic conductivity obtained for *Al*-LLZO CSP-pellet compared to sintered *Al*-LLZO (10^{-4} S.cm^{-1})[9] is probably linked to the low compacity of the pellet (60%, Equation 1). Consequently, a significant part of the pellet (porosity) hinders the transport of Li. Additionally, this low conductivity value compared to the one achieved on sintered LLZO shows that in these conditions the *Al*-LLZO powders are solely compacted but not sintered.

In an attempt to enhance the contact between the *Al*-LLZO particles, the PEGM-PEGDM polymer (PEO network) precursor solution was mixed with the inorganic particles in the presence of ACN and DMF, and the mixture followed the thermal treatment previously described. First, we observe an improvement in the compacity of the CSP pellet (74%, Equation 1). This improvement is linked to the additional polymer. Interestingly, the impedance plot (Figure V-1, purple) of the *Al*-LLZO/PEO network CSP pellet exhibits a smaller semi-circle, indicating a better ionic conductivity ($1.0.10^{-5}$ S.cm^{-1}). This improvement in ionic conductivity attests of the importance of adding the solid polymer electrolyte to improve the transport of Li at the particle||particle interface. Another interesting feature is the gain in ionic conductivity when compared to the ionic conductivity of the neat PEO network solid electrolyte (Figure V-1, grey). Indeed, the Nyquist plot of PEO network (Figure SI.V-2a) shows an important semi-circle, leading to an ionic conductivity of around 10^{-8} S.cm^{-1}. Accordingly, the ionic

conductivity of *Al*-LLZO/PEO network CSP pellet is higher than the *Al*-LLZO CSP pellets and the pure solid electrolyte polymer, indicating a positive synergy between the two components.

To explain this synergy and the role of DMF in our CSP system, an *Al*-LLZO/PEO network CSP pellet was synthesized without the addition of DMF under the same conditions. The Nyquist plot of *Al*-LLZO/PEO network CSP pellet without DMF (Figure V-1 (brown)) shows a very high resistance leading to an ionic conductivity of $4.5.10^{-8}$ S.cm^{-1}. This value is comparable to that of polymer alone indicating that, without DMF, the synergy between the components is different. Interestingly, a gain of three orders of magnitude in conductivity is measured for the *Al*-LLZO/PEO network CSP pellet with DMF (1.10^{-5} S.cm^{-1}). To check that the increase in conductivity on the CSP pellets in the presence of DMF and the PEO network was not due to swelling of the PEO network by DMF, a PEO network membrane was made with 27 wt% DMF using the polymer membrane preparation method. A conductivity of $1.4.10^{-8}$ S.cm^{-1} was measured (Figure SI.V-2b). This shows the importance of DMF in the dissolution process of the surface of *Al*-LLZO particles, as well as its role as a plasticiser[25]. If the DMF dissolves Li ions from the surface of *Al*-LLZO particles, the latter can then migrate towards the polymer phase and enrich it with free Li^+.

To check this assumption, we add Li-salts in the PEO-network either by dissolving LiTFSI in the PEO solid polymer (LiTFSI-SPE) or by grafting it to the PEO-network (Si-SPE). The impedance results represented in the Nyquist plot for *Al*-LLZO/LiTFSI-SPE and *Al*-LLZO/Si-SPE CSP are reported in Figure V-2.

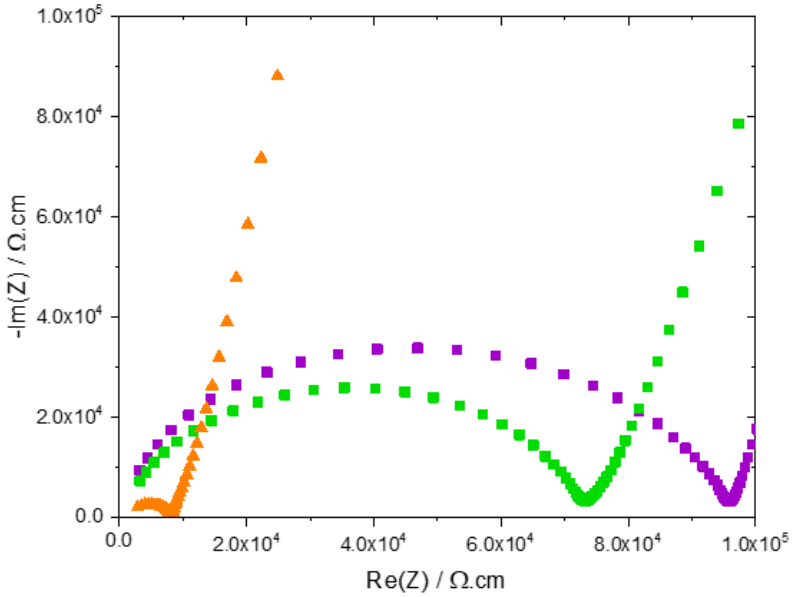

Figure V-2. Impedance plot at 25 °C for CSP composite pellet of (■) *Al*-LLZO/LiTFSI-SPE, (■) *Al*-LLZO/Si-SPE and (■) *Al*-LLZO/PEO network.

A conductivity of 1.10^{-5} S.cm^{-1} is found for the *Al*-LLZO/Si-SPE CSP pellet. Surprisingly, this value matches well with the one observed for the *Al*-LLZO/PEO network CSP pellet, where an enrichment in Li of the polymer network is supposed to happen during the CSP process. So, when the counter-anion is grafted onto the pendant chains of the PEO network, the Li^+ from the polymer precursor solution does not significantly contribute to ionic conductivity. Thus, as for PEO network, the design of a CSP pellet improves conductivity compared with the pure Si-SPE (10^{-7} S.cm^{-1}, Figure SI.V-2c) by a factor of 100. Interestingly, a conductivity of 1.10^{-4} S.cm^{-1} (Figure V-2, orange) is found for the *Al*-LLZO/LiTFSI-SPE CSP pellet, i.e. when the Li^+ and counter anion are more mobile in the PEO network and can concentrate at the interface. This is once again higher than the LiTFSI-SPE membrane (of 1.10^{-5} S.cm^{-1}, Figure SI.V-2d). This value compared well with the one found in the literature for LLZO/PPC-$LiClO_4$[25], but also for other oxides such as LATP and LAGP (10^{-4} S.cm^{-1})[22]. However, the *Al*-LLZO/LiTFSI-SPE CSP pellet ionic conductivity is one order of magnitude higher than the one found for *Al*-LLZO/PEO network and *Al*-LLZO/Si-SPE CSP pellets, which indicates that Li-salt is involved in conduction. As the inorganic network is solely compacted and not sintered, this tends to show that the polymer phase participates in conduction, potentially forming a continuous path within the composite CSP pellets. To highlight once again that the increase in ionic conductivity during CSP is not solely due to the addition of DMF to the polymer phase, a TGA analysis was carried out. Figure SI.V-3 shows a comparison of the TGA spectra for the *Al*-LLZO/LiTFSI-SPE CSP pellet, the LiTFSI-SPE membrane and the commercial *Al*-LLZO. A mass loss of 13% was observed for the *Al*-LLZO/LiTFSI-SPE CSP pellet and 9% for the commercial *Al*-LLZO. Decomposition of the polymer membrane occurs between 200°C and 600°C. When the mass loss of the commercial *Al*-LLZO is considered, approximately 4% by weight mass loss is observed for the *Al*-LLZO/LiTFSI-SPE CSP pellet. This value corresponds to the amount of LiTFSI-SPE precursor solution introduced during the CSP process (i.e. 13 vol%). Consequently, after CSP, no residual DMF remains. As the measured conductivity is not the same as for solid polymer electrolyte, this suggests that the CSP process might have modified the polymer or caused a different arrangement of PEO chains.

The impact of the inorganic phase volume proportion ranging from 0 to 90 vol% of *Al*-LLZO in the *Al*-LLZO/Si-SPE CSP pellet was studied. The evolution of the compacity (calculated with Equation 1) and the ionic conductivity as a function of the inorganic vol. fraction were reported in Figure V-3. First, a decrease of the compacity from 90 to 70% is observed with an increase of the vol. fraction of *Al*-LLZO from 50% to 90% (Figure V-3a).

Additionally, a compacity of 60%, i.e. a porosity of 40%, was measured on the *Al*-LLZO CSP pellet. To fill all the pores of CSP pellet, it is necessary to add more than 40 vol% of polymer phases. However, for a volume of 50 vol% of *Al*-LLZO (50 vol% of si-SPE), a compacity of 90% is measured. This is certainly due to the fact that the *Al*-LLZO particles have intrinsic porosity (probably due to aggregates) and therefore the polymer cannot fill them. We have then compared the compacity of composite made by CSP and by casting method for a composite containing 50 vol% of *Al*-LLZO and 20 vol% of *Al*-LLZO, respectively. The compacity is approximately the same (90%) for the two composites, confirming the presence of 10% of close porosity in both composites. Therefore, achieving 100% compacity will not be possible, and for a content of 87 vol% of *Al*-LLZO, the compacity will be around 75% according to our process parameters.

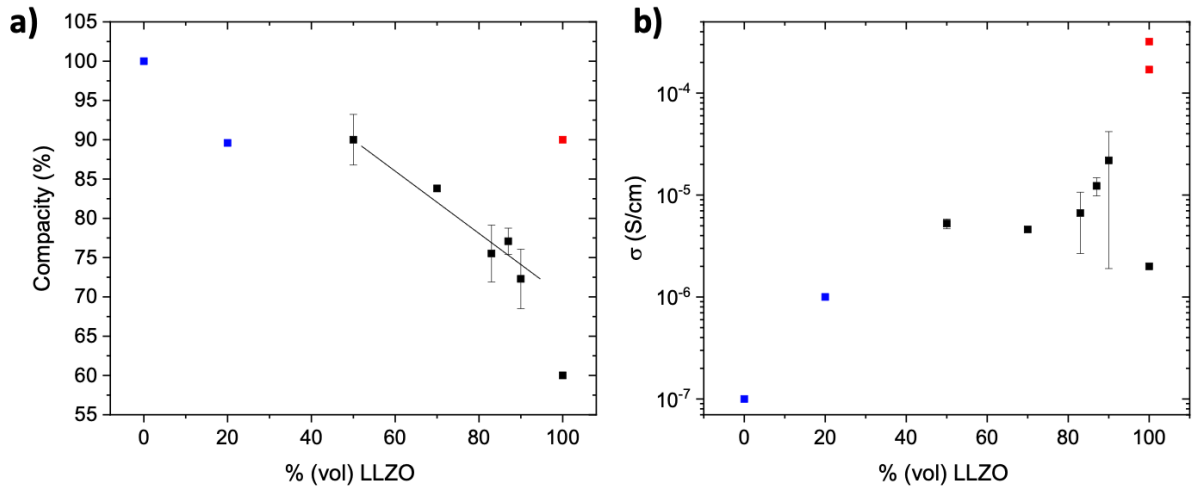

Figure V-3. Evolution of (a) compacity and (b) conductivity at 25 °C for composite pellet *Al*-LLZO/Si-SPE for different %vol of *Al*-LLZO. (blue symbol) Polymer synthesis method, (black symbol) CSP and (red symbol) sintering at high temperature.

The evolution of ionic conductivity as a function of % vol. of *Al*-LLZO (Figure V-3b) shows that the addition of 20% in vol. of *Al*-LLZO is sufficient to increase conductivity by an order of magnitude compared to the solid electrolyte polymer, Si-SPE (going from 10^{-7} S.cm^{-1} to 10^{-6} S.cm^{-1}). This enhancement may be explained by a preferential conductivity at the LLZO||PEO network interface. Then, the ionic conductivity is constant with a value of 5.10^{-6} S.cm^{-1} between 50 and 70% in vol. of *Al*-LLZO. An increase of the ionic conductivity by one order of magnitude (2.10^{-5} S.cm^{-1}) is then observed for a composite containing 90% in vol of *Al*-LLZO. This value in conductivity is not comparable either to the one for *Al*-LLZO CSP pellet ($2.5.10^{-6}$ S.cm^{-1}) or for Si-SPE polymer (1.10^{-7} S.cm^{-1}). To understand which phases

(LLZO, Si-SPE or LiTFSI-SPE, LLZO||PEO) conduce Li^+, we have then modeled our impedance data by an equivalent circuit.

III.2. Study of macroscopic conduction using EIS and equivalent circuit

To fit the impedance data of the composite *Al*-LLZO/PEO network, we proposed the equivalent circuit shown in Figure V-4.

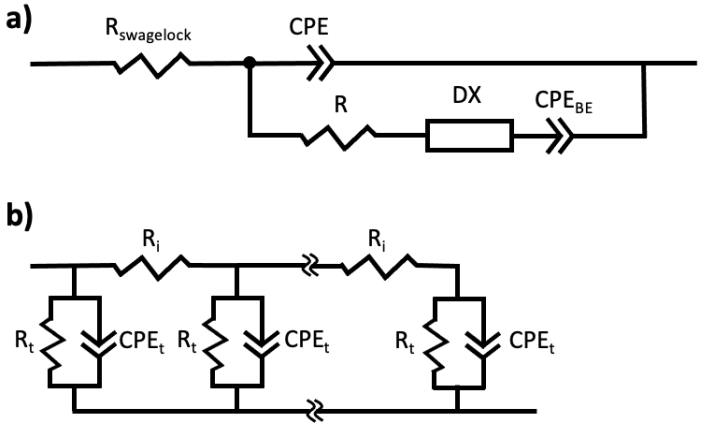

Figure V-4. (a) Equivalent circuit to fit impedance data of CSP pellet and (b) Representation of TLM (DX element in the equivalent circuit).

Inspired by our previous work on understanding the transport of Li at the *Al*-LLZO||PEO interface, the equivalent circuit is the following: $R_{swagelock}$ + CPE // (R + DX + CPE_{BE}), where the $R_{swagelock}$ is the resistance of the setup (cell, cables), CPE and R elements represent the conducting phase, Transmission Line Model (TLM; represented by DX in the equivalent circuit) is characteristic of the *Al*-LLZO||PEO network interface and CPE_{BE} represents the capacitive response of the blocking electrode. R_i corresponds to the resistance of the direct ionic path at the PEO network||*Al*-LLZO interface (macroscopic diffusion pathway), while R_t and C_t represent to the distributed resistance/capacitance for Li^+ transfer between the two electrolytes (hindered ionic transfer regions). This additional distributed $R_t//C_t$ element is actually the signature of a more tortuous (or an energetically costlier) path for the Li^+. The measured values of the elements of the fit are shown in Table SI.V-2.

Interestingly, from the R and CPE elements, we can estimate the characteristic frequency (f_c, calculated with Equation 6) of the semicircle that is intrinsically characteristic of the materials involved in the Li-ion transport[33]. All the values estimated from these impedance data are summarized in Table V-2.

Table V-2. Values of f_c at 30 °C for CSP pellets and solid polymer electrolyte.

Sample	f_c (Hz)
PEGM-PEGDM	9.10^2
LiTFSI-SPE	3.10^6
si-SPE	2.10^4
Al-LLZO	2.10^5
Al-LLZO/PEGM-PEGDM	8.10^5
Al-LLZO/LiTFSI-SPE	5.10^6
Al-LLZO/Si-SPE	8.10^5

First, we have estimated the f_c value of the semi-circle for *Al*-LLZO/PEO network CSP pellet at 8.10^5 Hz, which is different from the one of PEO network (9.10^2 Hz), and the one of *Al*-LLZO CSP pellet (2.10^5 Hz). This behavior is also observed for *Al*-LLZO/Si-SPE CSP pellet, where a f_c of 8.10^5 Hz is observed compared to 2.10^4 Hz for Si-SPE. Interestingly, f_c calculated for *Al*-LLZO/LiTFSI-SPE CSP pellet at 5.10^6 Hz is comparable to the one of LiTFSI-SPE polymer at 3.10^6 Hz. Importantly, the estimation of the f_c showed that neither the f_c value of *Al*-LLZO nor that of the polymer was found. This implies that another phase conducts the Li^+, which may be the interface or the polymer that has been modified.

To further explore the conduction path in the CSP composite pellet made with Si-SPE, we investigated two novel pellets where the inorganic *Al*-LLZO phase has been changed either by *tetra*-LLZO with an intrinsic ionic conductivity of 1.10^{-6} $S.cm^{-1}$ [8] or LATP with an ionic conductivity of 10^{-4} $S.cm^{-1}$ [22]. Interestingly, these phases exhibit either different ionic conductivity for *tetra*-LLZO or different surface chemistry for LATP. Based on the Nyquist plot (Figure V-5), a conductivity of ~ 3.10^{-5} $S.cm^{-1}$ was measured for the *tetra*-LLZO/Si-SPE and LATP/Si-SPE CSP pellets. Those values are comparable to the one found for *Al*-LLZO/Si-SPE CSP pellet ($1.5.10^{-5}$ $S.cm^{-1}$). Thus, the ionic conductivity is similar whatever the chemistry and the conductivity of the inorganic phase. This seems to indicate that the transport of Li^+ in the CSP composite is not supported by the inorganic phase, neither by the polymeric phase. It is important to note that the ionic conductivity of *tetra*-LLZO/si-SPE is higher than the conductivity of sintered *tetra*-LLZO. These results support the hypothesis that Li^+ from inorganic phase solubilizes into the polymeric phase to an optimum concentration, creating at the interface a new phase that is responsible for the conduction.

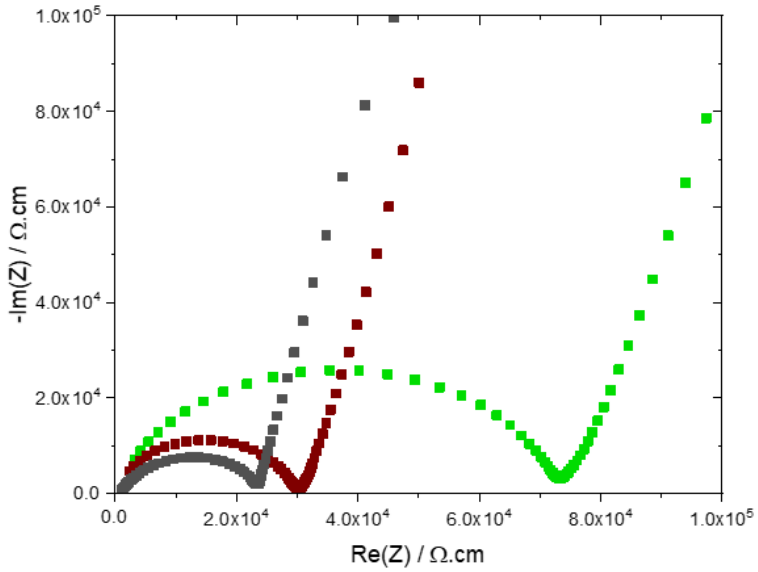

Figure V-5. Nyquist plot at 30 °C for (■) *Al*-LLZO/Si-SPE, (■) *tetra*-LLZO/Si-SPE and (■) LATP/Si-SPE.

The role of the polymer network was further studied by estimating the ε/σ ratio, which shows whether the polymer's conductivity changes during CSP process (Table V-3). ε is driven from ε = R × CPE, and the higher the ε/σ ratio, the more the material is perceived as an insulator to the diffusion of Li^+.

Table V-3. Values R_i, R_t and ε/σ of electrical circuit elements at 30°C for CSP pellets and PEO network.

Sample	R_i (Ω)	R_t (Ω)	ε/σ
PEGM-PEGDM			$2.0.\ 10^4$
LiTFSI-SPE			0.15
si-SPE			$1.1.10^3$
Al-LLZO/PEGM-PEGDM	15	$8.6.10^3$	0.18
Al-LLZO/LiTFSI-SPE	13	$1.4.10^3$	$7.4.10^{-4}$
Al-LLZO/Si-SPE (87/13) *	13	$5.2.10^3$	0.44
Al-LLZO/Si-SPE (50/50) *	12	$5.1.10^4$	1.58
tetra-LLZO/Si-SPE	15	$1.3.10^4$	0.02
LATP/Si-SPE	15	$8.7.10^5$	0.96

** % in vol.*

For the two polymer membranes (PEO network and Si-SPE), this ratio is $2.0.10^4$ and $1.1.10^3$, respectively. These values are then compared to the ones determined for the composite CST pellets (see Table V-3). *Al*-LLZO/PEO network (0.18) and *Al*-LLZO/Si-SPE CSP pellets (0.44) are similar values but not comparable to those of the pure polymers. However, they are

comparable to that of LiTFSI-SPE (0.15), which may indicate an enrichment of the polymer phase in free Li^+ during the CSP. Therefore, a decrease in this ratio is observed with the use of CSP. This is also the case for LiTSI-SPE and *Al*-LLZO/LiTFSI-SPE CSP pellets ($1.5.10^{-1}$ *vs.* $7.4.10^{-4}$ respectively). Based on the value of the ε/σ ratio, we concluded that the polymer network is noticeably modified during the CSP process.

This modification may result from an evolution in the Li concentration in the polymer phase due to the incongruent dissolution of the *Al*-LLZO particles, preferentially Li and Al ions. Accordingly, we synthesized a composite CSP pellet with 87% vol. SiO_2 (SiO_2/Si-SPE) under the same conditions. Interestingly, the CSP pellet exhibits a compacity of 79% (Equation 1) and an ionic conductivity of $1.4.10^{-8}$ $S.cm^{-1}$ at ambient temperature. This value is smaller than the one observed for *AL*-LLZO/Si-SPE CSP pellet, attesting the need of an inorganic phase containing Li and its incongruent dissolution to favor the dissolution of Li.

Finally, we have investigated the variation of the resistance R_i of the TLM, as it represents the resistivity of the direct macroscopic contact at the *Al*-LLZO||PEO network interface. R_i is indeed constant whatever the nature of the Li ion conducting inorganic and polymer phase. This tends to demonstrate that R_i varies only with the way the interface is created. Here, since the manufacturing process is the same, R_i remains unchanged (around 13 Ω, Table V-3).

We have then studied the variation of the values of R_t and C_t in the TLM (Table V-3 and Table SI.V-2), as they correspond to the distributed Li-ion transfer resistance/capacitance between the two electrolytes. These parameters should vary according to the difference in chemical composition and the energy gap for Li to pass from one dielectric material to the other (inorganic and polymer). First, we notice that the R_t value changes with the nature of the inorganic material (LATP *vs. tetra*-LLZO *vs. Al*-LLZO). and the vol. fraction of *Al*-LLZO in the CSP pellet. R_t is an order of magnitude higher for *tetra*-LLZO than for *Al*-LLZO, unfortunately the dielectric constants of these two materials are not known and cannot help explain this difference. On the other hand, we observe two orders of magnitude difference between the R_t value for the CSP composite with LATP *vs. Al*-LLZO ($8.7.10^5$ *vs.* $5.2.10^3$ Ω respectively). This difference may be due to different material dielectric constants, but also to surface chemistry. This confirms the role of the inorganic material and then its role in the modification of LLZO|| PEO network interface.

Finally, an order of magnitude increases of R_t with the decrease in % vol. from 87 to 50 of *Al*-LLZO suggests that the transport of Li^+ at the interface of LLZO|| PEO network depends

on the proportion of each of the compounds. This implies a different modification of the polymer and therefore a different ionic conductivity ($5.0.10^{-6}$ *vs.* $1.5.10^{-5}$ S.cm^{-1} for 50 and 87 vol% *Al*-LLZO respectively).

III.3. Understating the conduction mechanism with activation energy

To confirm that the Li ions move preferentially at the *Al*-LLZO||PEO interface, we have measured the energy of activation (E_a) of the different *Al*-LLZO-PEO composites (87% in vol. of *Al*-LLZO (Figure SI.V-4a). Values of 0.10, 0.13 and 0.11 eV for E_a were calculated for *Al*-LLZO/LiTFSI-SPE, *Al*-LLZO/Si-SPE and *Al*-LLZO/PEO network, respectively. These values are different from the ones measured for high-temperature sintered *Al*-LLZO (E_a are 0.32 and 0.62 eV for the bulk and grain boundaries respectively, Figure V-6) and for solid polymer electrolyte (E_a measured are 0.64 and 0.62 eV for SPE and Si-SPE respectively)[29]. This is an indication that the Li^+ transport in the composite is different from the one observed for SPE and *Al*-LLZO phases. He et al.[34] obtained an activation energy (E_a) of 0.15 eV for a composite electrolyte consisting of PEO-LiTFSI and 12 wt% LLZO, manufactured using a solution casting process.

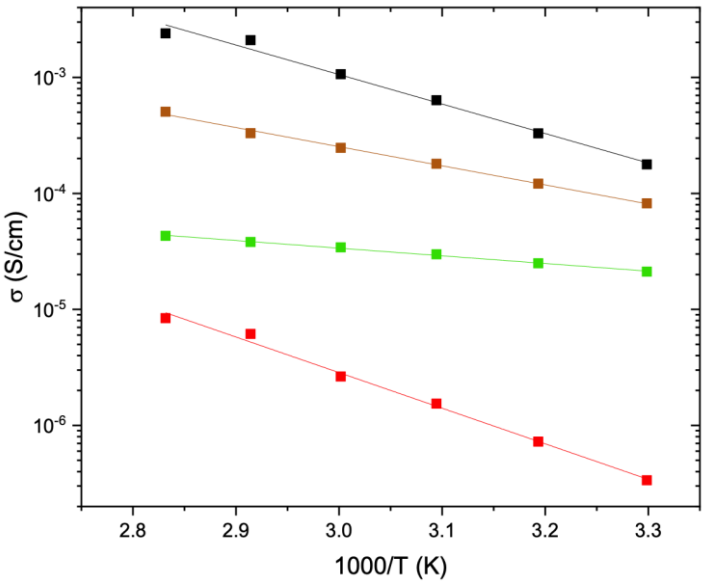

Figure V-6. Arrhenius plot for (■) Si-SPE membrane (■) *Al*-LLZO/Si-SPE (■) bulk and (■) Grain boundary of high temperature sintered *Al*-LLZO.

In addition, to check that our composites are temperature stable. The temperature conductivity was measured both when the composite was heated and when it was cooled (Figure SI.V-4b). No significant difference was observed, demonstrating the stability of our system after assembly.

IV. Conclusion and perspectives

In this work, *Al*-LLZO/PEO network composite is designed by combining CSP synthesis and *in-situ* polymerization of PEO network containing either ungrafted LiTFSI or grafted TFSI onto the PEO chain. First, we show that the conductivity of the hybrid CSP pellet changes with the nature of the PEO network, going from 10^{-5} S.cm^{-1} to 10^{-4} S.cm^{-1} for Si-SPE and LiTFSI-SPE. Interestingly, the ionic conductivity is not linked to the nature of the inorganic materials, as the conductivity is the same 10^{-5} S.cm^{-1} for CSP composite pellets containing LATP, *Al*-LLZO or *tetra*-LLZO. On the other hand, inorganic materials must contain Li (SiO_2/Si-SPE 10^{-8} S.cm^{-1}).

We have also demonstrated the importance of DMF in the CSP and its role in the enrichment of the polymer solid electrolyte with Li^+. Indeed, composite CSP pellet containing PEO network exhibits a conductivity of 10^{-5} S.cm^{-1} at the ambient temperature, which is three orders of magnitude higher than the one observed for pure PEO network solid electrolyte. Using inorganic material containing Li-ion is also important, as CSP composite pellet containing SiO_2 and Si-SPE exhibit poor ionic conductivity, an order of magnitude lower than the one observed for Si-SPE solid polymer electrolyte. Based on these observations and regarding the comprehensive EIS model, we have proposed that the Li-ion transport in these CSP composite electrolytes occurs mainly at the interface *Al*-LLZO||PEO network. More interestingly, we have demonstrated, by comparing the values obtained for R_i (representing the direct contact resistance of the *Al*-LLZO||PEO network) and R_t (transport of Li^+ from *Al*-LLZO to PEO network), a modification in the assembly of the PEO chains at the surface of *Al*-LLZO by the CSP, which was further highlighted by the very low E_a measured.

Supporting information

XRD patterns of *tetra*-LLZO; Table of sample composition and mains characteristic; Nyquist plot at 30 °C for all PEO network; TGA analysis of *Al*-LLZO/LiTFSI-SPE CSP pellet; Table of values R, CPE, f_c, Ri, R_t, CPE_t, α_t and ε/σ of electrical circuit elements at 30 °C for CSP pellets; Arrhenius plot for *Al*-LLZO/si-SPE (heating and cooling), *Al*-LLZO/LiTFSI-SPE and *Al*-LLZO/PEO network CSP pellet.

References:

(1) Murugan, R.; Thangadurai, V.; Weppner, W. Fast Lithium Ion Conduction in Garnet-Type Li7La3Zr2O12. *Angew. Chem. Int. Ed.* **2007**, *46* (41), 7778–7781. https://doi.org/10.1002/anie.200701144.

(2) Manthiram, A.; Yu, X.; Wang, S. Lithium Battery Chemistries Enabled by Solid-State Electrolytes. *Nat. Rev. Mater.* **2017**, *2* (4), 16103. https://doi.org/10.1038/natrevmats.2016.103.

(3) Yue, L.; Ma, J.; Zhang, J.; Zhao, J.; Dong, S.; Liu, Z.; Cui, G.; Chen, L. All Solid-State Polymer Electrolytes for High-Performance Lithium Ion Batteries. *Energy Storage Mater.* **2016**, *5*, 139–164. https://doi.org/10.1016/j.ensm.2016.07.003.

(4) Mauger; Julien; Paolella; Armand; Zaghib. Building Better Batteries in the Solid State: A Review. *Materials* **2019**, *12* (23), 3892. https://doi.org/10.3390/ma12233892.

(5) Pan, Q.; Zhang, W.; Pan, M.; Zhang, B.; Zeng, D.; Sun, Y.; Cheng, H. Construction of a Lithium Ion Transport Network in Cathode with Lithiated Bis(Benzene Sulfonyl)Imide Based Single Ion Polymer Ionomers. *J. Power Sources* **2015**, *283*, 279–288. https://doi.org/10.1016/j.jpowsour.2015.02.137.

(6) Bachman, J. C.; Muy, S.; Grimaud, A.; Chang, H.-H.; Pour, N.; Lux, S. F.; Paschos, O.; Maglia, F.; Lupart, S.; Lamp, P.; Giordano, L.; Shao-Horn, Y. Inorganic Solid-State Electrolytes for Lithium Batteries: Mechanisms and Properties Governing Ion Conduction. *Chem. Rev.* **2016**, *116* (1), 140–162. https://doi.org/10.1021/acs.chemrev.5b00563.

(7) Thompson, T.; Yu, S.; Williams, L.; Schmidt, R. D.; Garcia-Mendez, R.; Wolfenstine, J.; Allen, J. L.; Kioupakis, E.; Siegel, D. J.; Sakamoto, J. Electrochemical Window of the Li-Ion Solid Electrolyte $Li_7La_3Zr_2O_{12}$. *ACS Energy Lett.* **2017**, *2* (2), 462–468. https://doi.org/10.1021/acsenergylett.6b00593.

(8) Awaka, J.; Kijima, N.; Hayakawa, H.; Akimoto, J. Synthesis and Structure Analysis of Tetragonal Li7La3Zr2O12 with the Garnet-Related Type Structure. *J. Solid State Chem.* **2009**, *182* (8), 2046–2052. https://doi.org/10.1016/j.jssc.2009.05.020.

(9) Kotobuki, M.; Kanamura, K.; Sato, Y.; Yoshida, T. Fabrication of All-Solid-State Lithium Battery with Lithium Metal Anode Using Al2O3-Added Li7La3Zr2O12 Solid Electrolyte. *J. Power Sources* **2011**, *196* (18), 7750–7754. https://doi.org/10.1016/j.jpowsour.2011.04.047.

(10) Mori, D.; Sugimoto, K.; Matsuda, Y.; Ohmori, K.; Katsumata, T.; Taminato, S.; Takeda, Y.; Yamamoto, O.; Imanishi, N. Synthesis, Structure and Ionic Conductivity of Garnet Like

Lithium Ion Conductor $Li_{6.25+x}Ga_{0.25}La_{3-x}Sr_xZr_2O_{12}$. *J. Electrochem. Soc.* **2019**, *166* (3), A5168–A5173. https://doi.org/10.1149/2.0171903jes.

(11) Xiang, X.; Chen, F.; Shen, Q.; Zhang, L.; Chen, C. Effect of the Lithium Ion Concentration on the Lithium Ion Conductivity of Ga-Doped LLZO. *Mater. Res. Express* **2019**, *6* (8), 085546. https://doi.org/10.1088/2053-1591/ab2799.

(12) Yoon, S. A.; Oh, N. R.; Yoo, A. R.; Lee, H. G.; Lee, H. C. Preparation and Characterization of Ta-Substituted Li7La3Zr2-XO12 Garnet Solid Electrolyte by Sol-Gel Processing. *J. Korean Ceram. Soc.* **2017**, *54* (4), 278–284. https://doi.org/10.4191/kcers.2017.54.4.02.

(13) Cao, S.; Song, S.; Xiang, X.; Hu, Q.; Zhang, C.; Xia, Z.; Xu, Y.; Zha, W.; Li, J.; Gonzale, P. M.; Han, Y.-H.; Chen, F. Modeling, Preparation, and Elemental Doping of Li7La3Zr2O12 Garnet-Type Solid Electrolytes: A Review. *J. Korean Ceram. Soc.* **2019**, *56* (2), 111–129. https://doi.org/10.4191/kcers.2019.56.2.01.

(14) Geiger, C. A.; Alekseev, E.; Lazic, B.; Fisch, M.; Armbruster, T.; Langner, R.; Fechtelkord, M.; Kim, N.; Pettke, T.; Weppner, W. Crystal Chemistry and Stability of "$Li_7La_3Zr_2O_{12}$" Garnet: A Fast Lithium-Ion Conductor. *Inorg. Chem.* **2011**, *50* (3), 1089–1097. https://doi.org/10.1021/ic101914e.

(15) Adams, S.; Rao, R. P. Ion Transport and Phase Transition in $Li_{7-x}La_3(Zr_{2-x}M_x)O_{12}$ ($M = Ta^{5+}$, Nb^{5+}, $x = 0, 0.25$). *J Mater Chem* **2012**, *22* (4), 1426–1434. https://doi.org/10.1039/C1JM14588F.

(16) Tsai, C.; Thuy Tran, N. T.; Schierholz, R.; Liu, Z.; Windmüller, A.; Lin, C.; Xu, Q.; Lu, X.; Yu, S.; Tempel, H.; Kungl, H.; Lin, S.; Eichel, R.-A. Instability of Ga-Substituted $Li_7La_3Zr_2O_{12}$ toward Metallic Li. *J. Mater. Chem. A* **2022**, *10* (20), 10998–11009. https://doi.org/10.1039/D1TA10215J.

(17) Han, G.; Kinzer, B.; Garcia-Mendez, R.; Choe, H.; Wolfenstine, J.; Sakamoto, J. Correlating the Effect of Dopant Type (Al, Ga, Ta) on the Mechanical and Electrical Properties of Hot-Pressed Li-Garnet Electrolyte. *J. Eur. Ceram. Soc.* **2020**, *40* (5), 1999–2006. https://doi.org/10.1016/j.jeurceramsoc.2019.12.054.

(18) Guo, J.; Guo, H.; Baker, A. L.; Lanagan, M. T.; Kupp, E. R.; Messing, G. L.; Randall, C. A. Cold Sintering: A Paradigm Shift for Processing and Integration of Ceramics. *Angew. Chem. Int. Ed.* **2016**, *55* (38), 11457–11461. https://doi.org/10.1002/anie.201605443.

(19) Guo, H.; Guo, J.; Baker, A.; Randall, C. A. Hydrothermal-Assisted Cold Sintering Process: A New Guidance for Low-Temperature Ceramic Sintering. *ACS Appl. Mater. Interfaces* **2016**, *8* (32), 20909–20915. https://doi.org/10.1021/acsami.6b07481.

(20) Berbano, S. S.; Guo, J.; Guo, H.; Lanagan, M. T.; Randall, C. A. Cold Sintering Process of $Li_{1.5}Al_{0.5}Ge_{1.5}(PO_4)_3$ Solid Electrolyte. *J. Am. Ceram. Soc.* **2017**, *100* (5), 2123–2135. https://doi.org/10.1111/jace.14727.

(21) Jiang, P.; Guo, P.; Shi, Y.; Li, S.; Li, K.; Lu, X. Y.; Zhang, Z.; He, D.; Bian, J.; Lu, X. Solid-State Li Metal Battery Enabled by Cold Sintering at 120 °C. *Mater. Today Phys.* **2021**, *20*, 100476. https://doi.org/10.1016/j.mtphys.2021.100476.

(22) Lee, W.; Lyon, C. K.; Seo, J.; Lopez-Hallman, R.; Leng, Y.; Wang, C.; Hickner, M. A.; Randall, C. A.; Gomez, E. D. Ceramic–Salt Composite Electrolytes from Cold Sintering. *Adv. Funct. Mater.* **2019**, *29* (20), 1807872. https://doi.org/10.1002/adfm.201807872.

(23) Takashima, K.; Iwazaki, Y.; Randall, C. A. Cold Sintering for $Li_{1.5}Al_{0.5}Ge_{1.5}(PO_4)_3$ Using $LiNO_3$ -LiOH as a Transient Solvent. *Jpn. J. Appl. Phys.* **2021**, *60* (12), 126505. https://doi.org/10.35848/1347-4065/ac33cf.

(24) Wang, X.; Wang, J.; Li, F.; Zhu, F.; Ma, C. Influence of Cold Sintering Process on the Structure and Properties of Garnet-Type Solid Electrolytes. *Ceram. Int.* **2020**, *46* (11), 18544–18550. https://doi.org/10.1016/j.ceramint.2020.04.160.

(25) Seo, J.-H.; Fan, Z.; Nakaya, H.; Rajagopalan, R.; Gomez, E. D.; Iwasaki, M.; Randall, C. A. Cold Sintering, Enabling a Route to Co-Sinter an All-Solid-State Lithium-Ion Battery. *Jpn. J. Appl. Phys.* **2021**, *60* (3), 037001. https://doi.org/10.35848/1347-4065/abdd4c.

(26) Seo, J.-H.; Nakaya, H.; Takeuchi, Y.; Fan, Z.; Hikosaka, H.; Rajagopalan, R.; Gomez, E. D.; Iwasaki, M.; Randall, C. A. Broad Temperature Dependence, High Conductivity, and Structure-Property Relations of Cold Sintering of LLZO-Based Composite Electrolytes. *J. Eur. Ceram. Soc.* **2020**, *40* (15), 6241–6248. https://doi.org/10.1016/j.jeurceramsoc.2020.06.050.

(27) Kuhnert, E.; Ladenstein, L.; Jodlbauer, A.; Slugovc, C.; Trimmel, G.; Wilkening, H. M. R.; Rettenwander, D. Lowering the Interfacial Resistance in Li6.4La3Zr1.4Ta0.6O12|Poly(Ethylene Oxide) Composite Electrolytes. *Cell Rep. Phys. Sci.* **2020**, *1* (10), 100214. https://doi.org/10.1016/j.xcrp.2020.100214.

(28) Naboulsi, A.; Nguyen, G.; Franger, S.; Fichet, O.; Laberty-Robert, C. Understanding the Li-Ion Transport through the PEO-like Polymer//Al-LLZO Interface by Using Electrochemical Impedance Spectroscopy: In-Situ and Ex-Situ Approaches for the Fabrication of the PEO-like Polymer //Al-LLZO// PEO-like Polymer Multilayers. *Under submission*. 2023.

(29) Naboulsi, A.; Chometon, R.; Ribot, F.; Nguyen, G.; Fichet, O.; Laberty-Robert, C. Correlation between Ionic and Mechanical Properties of Solid PEO Polymer Electrolyte. *ACS Appl. Mater. Interfaces* **2023**, *Under revision*.

(30) Dussart, T. Batterie lithium tout solide : augmentation de la densité de courant critique et procédé innovant de fabrication. *Thèse* **2021**.

(31) Orazem, M. E.; Frateur, I.; Tribollet, B.; Vivier, V.; Marcelin, S.; Pébère, N.; Bunge, A. L.; White, E. A.; Riemer, D. P.; Musiani, M. Dielectric Properties of Materials Showing Constant-Phase-Element (CPE) Impedance Response. *J. Electrochem. Soc.* **2013**, *160* (6), C215–C225. https://doi.org/10.1149/2.033306jes.

(32) Huang, V. M.-W.; Vivier, V.; Orazem, M. E.; Pébère, N.; Tribollet, B. The Apparent Constant-Phase-Element Behavior of an Ideally Polarized Blocking Electrode. *J. Electrochem. Soc.* **2007**, *154* (2), C81. https://doi.org/10.1149/1.2398882.

(33) Wang, S.; Zhang, J.; Gharbi, O.; Vivier, V.; Gao, M.; Orazem, M. E. Electrochemical Impedance Spectroscopy. *Nat. Rev. Methods Primer* **2021**, *1* (1), 41. https://doi.org/10.1038/s43586-021-00039-w.

(34) He, K.; Cheng, S. H.; Hu, J.; Zhang, Y.; Yang, H.; Liu, Y.; Liao, W.; Chen, D.; Liao, C.; Cheng, X.; Lu, Z.; He, J.; Tang, J.; Li, R. K. Y.; Liu, C. In-Situ Intermolecular Interaction in Composite Polymer Electrolyte for Ultralong Life Quasi-Solid-State Lithium Metal Batteries. *Angew. Chem. Int. Ed.* **2021**, *60* (21), 12116–12123. https://doi.org/10.1002/anie.202103403.

Supporting information

Improvement of Ionic Conductivity of the *Al*-LLZO composite through *in-situ* synthesis of the PEO networks during the cold-sintering process

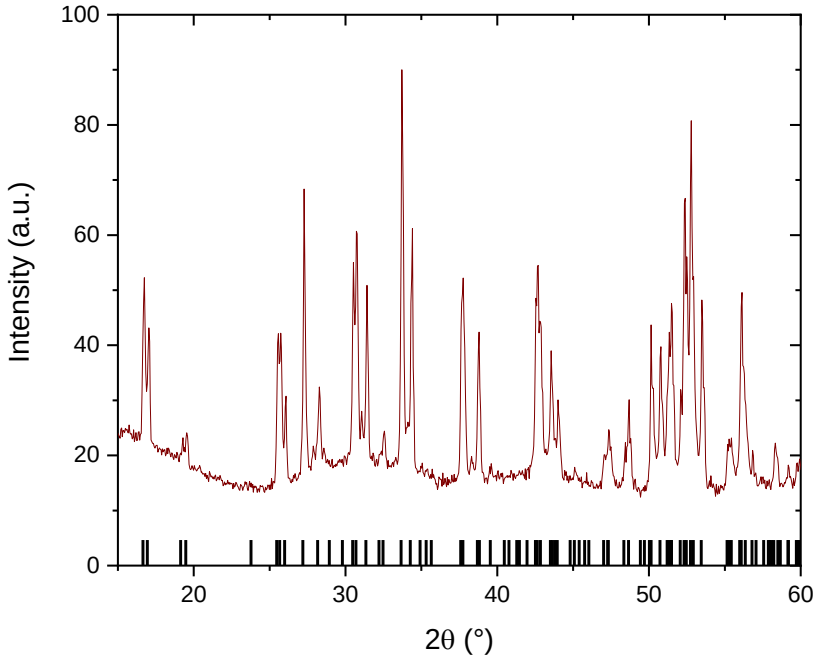

Figure SI.V-1. XRD patterns of *tetra*-LLZO with PDF#01-078-6708 (LLZO tetragonal) as a reference.

Table SI.V-1. Sample Compositions and main characteristics.

Pellet	%vol Inorganic	%vol Polymer	Volume DMF (µL)	Volume ACN (µL)	Compacity (%)	Conductivity @30°C (S.cm^{-1})
Al-LLZO	100	0	68	454	60	$2.5.10^{-6}$
Al-LLZO/PEGM-PEGDM	87	13	34	227	74	$1.0.10^{-5}$
Al-LLZO/SPE	87	13	34	227	73	$1.5.10^{-4}$
Al-LLZO/Si-SPE*	87	13	34	227	76	$1.5.10^{-5}$
tetra-LLZO/Si-SPE	87	13	34	227	82	$3.4.10^{-5}$
LATP/Si-SPE	87	13	22	114	77	$3.0.10^{-5}$
SiO_2/Si-SPE	87	13	68	454	79	$1.4.10^{-8}$

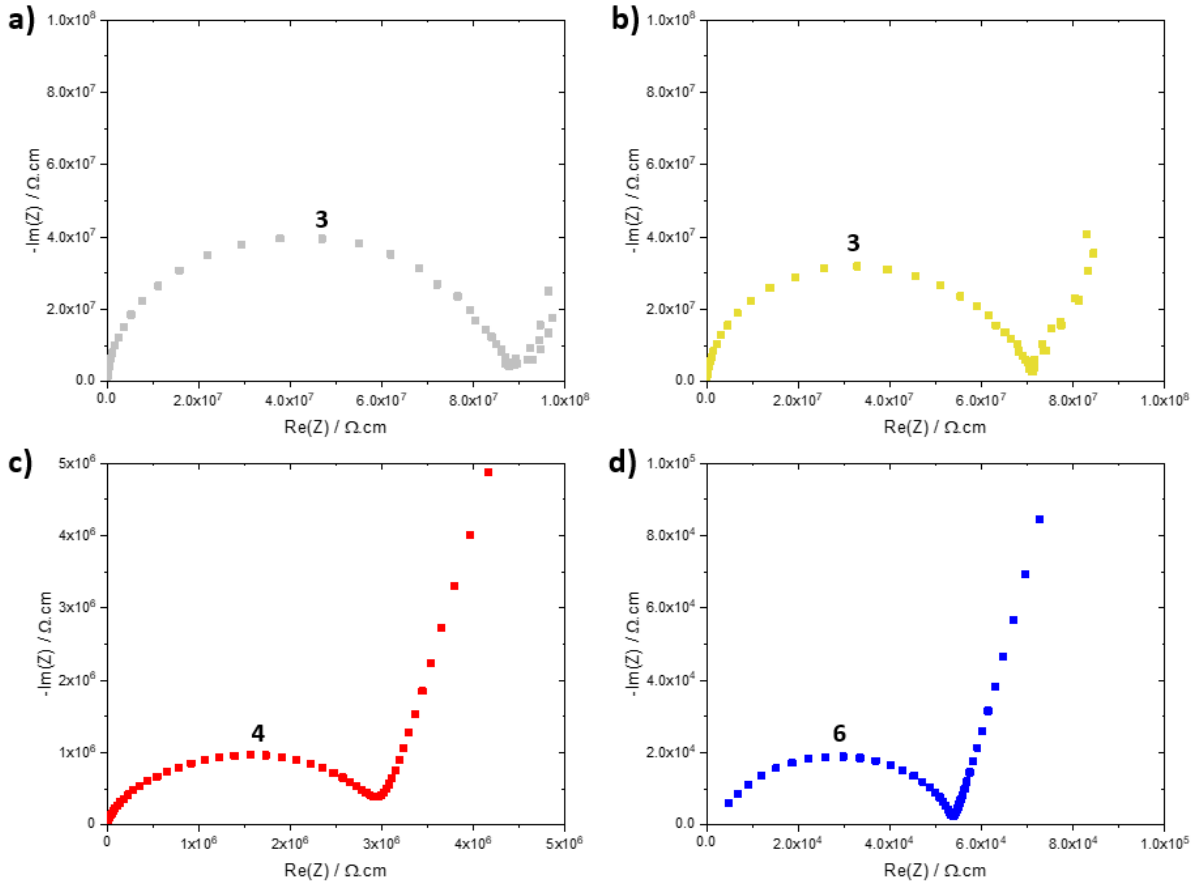

Figure SI.V-2. Nyquist plot at 30 °C for (a) PEO network, (b) PEO network with DMF, (c) Si-SPE membrane and (d) LiTFSI-SPE membrane. Numbers at the data points indicate power of frequency (Hz).

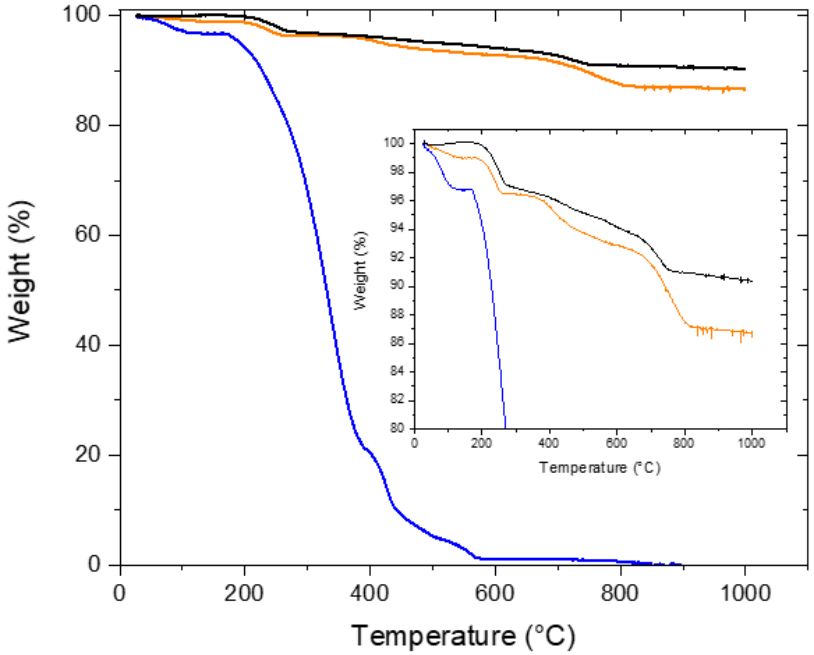

Figure SI.V-3. Thermogravimetric analysis of (—) commercial *Al*-LLZO, (—) LiTFSI-SPE membrane and (—) *Al*-LLZO/LiTFSI-SPE CSP pellet under air atmosphere at 10°C.min^{-1}.

Table SI.V-2. Values R, CPE, f_c, R_i, R_t, CPE_t, α_t and ε/σ of electrical circuit elements at 30 °C for CSP pellets.

Sample	R (Ω)	CPE (F)	α	f_c (Hz)	R_i (Ω)	R_t (Ω)	CPE_t (F)	α_t	ε/σ
Al-LLZO	$3.8.10^4$	$1.3.10^{-10}$	0.87	2.10^5					
Al-LLZO/PEGM-PEGDM	$4.2.10^3$	$6.6.10^{-10}$	0.83	8.10^5	15	$8.6.10^3$	$3.2.10^{-6}$	0.69	0.18
Al-LLZO/LiTFSI-SPE	$2.6.10^2$	$4.3.10^{-10}$	0.93	5.10^6	13	$1.4.10^3$	$1.5.10^{-5}$	0.66	$7.4.10^{-4}$
Al-LLZO/Si-SPE (87/13) *	$2.8.10^3$	$1.6.10^{-9}$	0.80	8.10^5	13	$5.2.10^3$	$1.8.10^{-7}$	0.96	0.44
Al-LLZO/Si-SPE (50/50) *	$9.5.10^3$	$1.6.10^{-9}$	0.80	3.10^5	12	$5.1.10^4$	$3.2.10^{-7}$	0.64	1.58
tetra-LLZO/Si-SPE	$1.1.10^3$	$6.6.10^{-10}$	0.88	2.10^6	15	$1.3.10^4$	$1.0.10^{-5}$	0.64	0.02
LATP/Si-SPE	$1.1.10^3$	$2.7.10^{-8}$	0.74	2.10^5	15	$8.7.10^5$	$1.1.10^{-7}$	0.98	0.96

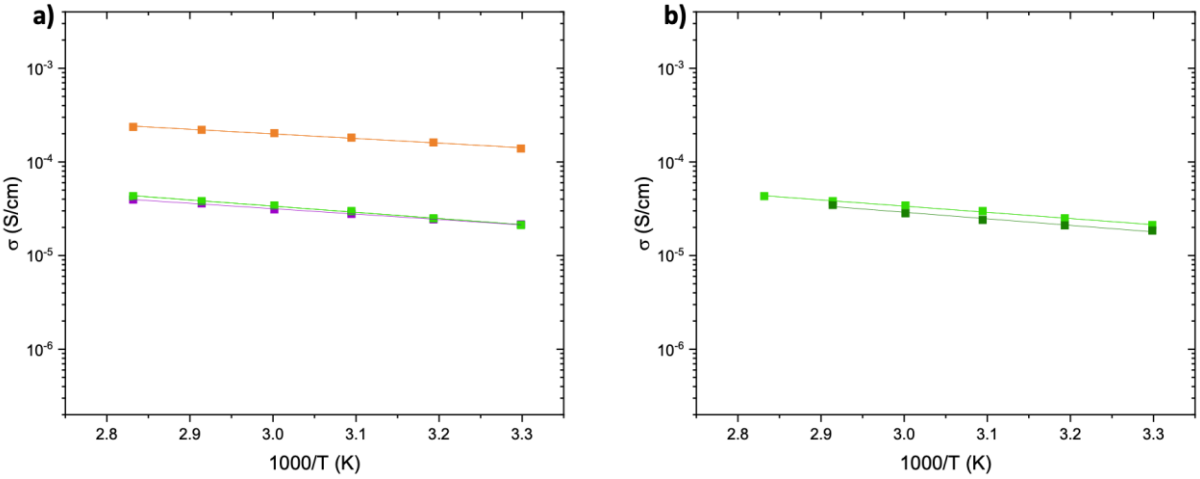

Figure SI.V-4. Arrhenius plot for (a) (■) *Al*-LLZO/Si-SPE, (■) *Al*-LLZO/LiTFSI-SPE, (■) for *Al*-LLZO/PEO network and (b) *Al*-LLZO/Si-SPE pellet (■) heating and (■) cooling.

General conclusion

All solid-state batteries (ASSB) are considered the next generation of batteries. Indeed, the safety provided by the non-flammable solid electrolyte (SE) and the increased energy density, achieved by utilizing Li-metal compared to Li-ion technology, make these technologies highly appealing[1]. The development of SE is at the heart of this advancement, and new avenues for more efficient and sustainable energy solutions are in progress. Throughout this study, we have explored various strategies in the design, synthesis, and characterization of SE, with a particular focus on polymer (SPE) and composite materials (SCE). The mechanical, thermal and electrochemical properties of these new solid electrolytes have been then investigated. This conclusion will highlight the key achievements of this study and underscore the remaining challenges as well as the prospects in this constantly evolving field.

The first area of study aimed at developing SPE that could be integrated into SCE. Understanding the parameters and mechanisms that impact the electrochemical properties and ionic conductivity of SPEs is crucial for their optimal integration into SCE design. To achieve this, two networks of poly(ethylene oxide) (PEO) were investigated from a solvent-free synthesis. The choice of a PEO network instead of a linear PEO was made to enhance the mechanical properties at high temperatures and to achieve an amorphous structure. The first involved a dissolved Li-salt (PEO-LiTFSI network), while the second incorporated a Li monomer allowing the grafting of the counter anion onto the PEO chains (PEO-LiMTFSI network). By varying the network cross-linking ratio, a correlation was established among glass transition temperature (T_g), storage modulus (E'), and ionic conductivity. The increase in the cross-linking ratio leads to a rise in both the T_g and the E', concomitant with a decrease in ionic conductivity. Increasing the cross-linking ratio enhances the elastic nature of the SPE, consequently reducing viscosity, which can modify the diffusion of Li^+. Interestingly, a transport number of 1 was measured for the PEO-LiMTFSI network using the Bruce and Vincent method,[2] and the measurement of diffusion coefficients through nuclear magnetic resonance. A transport number of unity holds significance in preventing the build-up of ion concentration gradients, which is particularly crucial for applications involving fast charging[3], but also, to suppress Li dendrites growth, which should then improve cycling stability and device safety[4]. The cycling stability of PEO network has indeed been demonstrated on a Li-metal symmetric cell. The cyclability of PEO-LiMTFSI network is better than that of PEO-

LiTFSI as we have demonstrated by 200 h of cycling *vs.* 70 h, respectively. The stability domain has also been extended up to 6 V for the PEO-LiMTFSI network, which suggests the possibility of using it in various formulations of high-voltage cathode materials. Despite the low conductivity measurement at RT for the PEO-LiMTFSI network (10^{-7} S.cm^{-1}) compared to the PEO-LiTFSI network (10^{-5} S.cm^{-1}), the PEO-LiMTFSI polymer exhibits several interesting parameters that make it a potential candidate in SCE fabrication.

Once the SPEs are optimized, they can be integrated into an SCE. For the inorganic materials, we have selected $Li_7La_3Zr_2O_{12}$ (LLZO) for its high ionic conductivity and its stability against Li. First to design SCE, we chose to examine the influence of incorporating $Li_{6.25}Al_{0.25}La_3Zr_2O_{12}$ (*Al*-LLZO) particles into optimized SPE on the mechanical properties and ionic conductivity of the SCE in comparison to the pristine one. The decision was made to exclusively focus on the PEO-LiTFSI network whose ionic conductivity is best among studied SPE. The synthesis of SCE was performed by the dispersion of *Al*-LLZO particles in liquid monomers, which were then polymerized. The addition of 7 vol% (24 wt%) of *Al*-LLZO particles did not demonstrate an enhancement in conductivity compared to that of the PEO-LiTFSI network (8.10^{-6} vs 1.10^{-5} S.cm^{-1}). In addition, no significant improvement in shear modulus was observed (0.11 MPa for the PEO-LiTFSI network and 0.16 MPa for SCE). Nevertheless, an improvement in mechanical property is achieved as SCEs flexible self-standing membrane with a thickness of 75 µm can be obtained, which is not the case for both the PEO-LiTFSI network (brittle unmanipulable membrane) nor the pure *Al*-LLZO (rigid brittle compact pellet). As a fraction in volume of 7% of *Al*-LLZO did not result in a percolated inorganic phase, a 3D *Al*-LLZO scaffold was designed using the electrospinning method to enhance the connected pathway of *Al*-LLZO, thus enabling the creation of a continuous Li^+ diffusion route. First, we have optimized the electrospun solution and the heat-treatment to obtain a cubic 3D *Al*-LLZO scaffold. Interestingly, this 3D scaffold allowed the fabrication of an SCE by a simple capillarity impregnation by the liquid precursors of network polymer. A 10 vol% of *Al*-LLZO SCE was synthesized in which a percolated network of inorganic material was achieved. Unfortunately, even with the pre-formation of a 3D *Al*-LLZO percolation pathway, the SCE conductivity is close to that of PEO-LiTFSI network (10^{-5} S.cm^{-1}). However, a self-standing object with a thickness of approximately 20 µm was obtained, which is highly interesting for reducing the ohmic resistance of the solid electrolyte. Furthermore, the influence of the *Al*-LLZO morphology (particles vs. scaffold) was highlighted by producing an SCE using linear polymer with dangling chains (PEO-LiTFSI brush). This PEO-LiTFSI brush forms a

viscous material, and the addition of 10 vol% of *Al*-LLZO particles does not result in a self-standing object. On the other hand, the utilization of the 3D *Al*-LLZO scaffold enables the achievement of self-standing membranes. Attempts to increase the inorganic density of the 3D *Al*-LLZO scaffold were conducted, resulting in an increased volume fraction of *Al*-LLZO (18-37 vol%) in the SCE. However, this led to a decrease in conductivity (10^{-6} $S.cm^{-1}$). In the literature, the decrease in ionic conductivity with the increase in the proportion of LLZO in the SCE is attributed to poor particle||particle contact, which obstructs the diffusion of Li^+. In our case, the particles appear to be sintered together[5] from FEG-SEM images, but this may not be enough. One possible reason for this decrease in conductivity in this condition could be attributed to the orientation of the fibers, which are not perpendicular to the applied current[6] or the poor connection of the polymer matrix in the SCE.

In a third approach, aiming to gain a better understanding of the phenomena involved in the transport at the PEO||*Al*-LLZO interface, we opted to develop multilayer structures to characterize the transport of Li^+ at the composite interface, employing the electrochemical impedance spectroscopy (EIS) method. An *in-situ* polymerization of the PEO-LiTFSI network at the surface of the *Al*-LLZO dense pellet was performed to mimic the reaction between *Al*-LLZO and PEO network, that will be encountered in the fabrication of SCE by "cold-sintering", thanks to the liquid monomer. Additionally, this design allows optimization of the PEO||*Al*-LLZO interface. First, the PEO-LiTFSI network was synthesized successively on both faces of the *Al*-LLZO pellet (*in-situ* copolymerization). For comparison, multilayers where the SPE was previously polymerized and applied on *Al*-LLZO pellet in the multilayer (*ex-situ*) was carried out. To extract the interface response in EIS, we opted to model it using a Transmission Line Model (TLM). We demonstrated that the transport of Li^+ can be represented by two elements: R_i, which accounts for the direct macroscopic passage of Li^+ at the PEO||*Al*-LLZO interface, and R_t and C_t, which account for the resistance/capacitance of the Li^+ transfer distribution between the two materials. Thus, R_t represents the energy gap to be overcome to pass from one electrolyte to the other. We demonstrated that *in-situ* copolymerization favors direct Li^+ transport with a very low activation energy (E_a = 0.38 eV). However, its effectiveness remains limited due to its higher resistance value compared to *ex-situ* polymerization (16 vs 2.3 $k\Omega.cm^2$). We concluded that *in-situ* polymerization could lead to secondary reactions that hinder Li^+ diffusion through static repulsion between the oxygen present on the LLZO surface and those of the PEO.

In a final approach, we chose to create a predominantly inorganic SCE involving a process that induces a dissolution and reprecipitation of the *Al*-LLZO surface. For this purpose, the cold-sintering process (CSP) enables the synthesis of an one-pot SCE and an *in-situ* polymerization of the PEO network by mixing the *Al*-LLZO particles with the solution of the monomer precursors. The pellets obtained through CSP are self-standing and have a thickness of approximately 500 µm. Reducing this thickness is challenging due to the high ceramic content in the pellets (~ 90 wt%). CSP allows for easy modulation of both the polymer and inorganic phases. Interestingly, a conductivity of 10^{-4} S.cm^{-1} at RT was achieved for a CSP pellet containing PEO-LiTFSI network/*Al*-LLZO, which is an order of magnitude higher than that of the PEO-LiTFSI network alone. Interestingly, two orders of magnitude increase in conductivity were observed for the CSP pellet containing PEO-LiMTFSI/*Al*-LLZO (10^{-5} S.cm^{-1}) compared to the PEO-LiMTFSI network. By replacing *Al*-LLZO with tetragonal LLZO (with lower conductivity, 10^{-4} vs 10^{-6} S.cm^{-1}, respectively), we observed that the ionic conductivity remained unchanged. Through equivalent circuit modeling of EIS measurements, we demonstrated a different organization of PEO chains at the interfaces of PEO||inorganic particles with the CSP, facilitating Li^+ conduction through this phase. This interface is highly favorable to Li^+ diffusion, as evidenced by a measured E_a of 0.1 eV.

In conclusion, we have highlighted the distinct synergies among the various SCE fabrication processes, emphasizing the importance of optimizing these approaches. The differences between capillary impregnation and the CSP method are not only in composition but also in the fact that *Al*-LLZO is sintered before capillary impregnation. This implies that the polymer might not aid in the conduction of grain boundaries and penetration between particles, unlike in CSP. During CSP, the particles||particles interface formation occurs in the presence of the polymer phase, leading to its modification and improved synergy.

The continuing development of solid electrolytes for ASSB inevitably drives research teams around the world into a frantic race for results and "innovations." Unfortunately, understanding the transport mechanism is performed by solely few groups. Throughout this work, we have endeavored to understand the transport mechanisms in our SCEs using impedance spectroscopy, coupled with data modeling using more advanced equivalent circuits. This step is essential for a better understanding of the interfaces involved in SCE fabrication.

Reference

(1) Janek, J.; Zeier, W. G. A Solid Future for Battery Development. *Nat. Energy* **2016**, *1* (9), 16141. https://doi.org/10.1038/nenergy.2016.141.

(2) Bruce, P.; Evans, J.; Vincent, C. A. Conductivity and Transference Number Measurements on Polymer Electrolytes. *Solid State Ion.* **1988**, *28–30*, 918–922. https://doi.org/10.1016/0167-2738(88)90304-9.

(3) Diederichsen, K. M.; McShane, E. J.; McCloskey, B. D. Promising Routes to a High Li^+ Transference Number Electrolyte for Lithium Ion Batteries. *ACS Energy Lett.* **2017**, *2* (11), 2563–2575. https://doi.org/10.1021/acsenergylett.7b00792.

(4) Ford, H. O.; Park, B.; Jiang, J.; Seidler, M. E.; Schaefer, J. L. Enhanced Li^+ Conduction within Single-Ion Conducting Polymer Gel Electrolytes via Reduced Cation–Polymer Interaction. *ACS Mater. Lett.* **2020**, *2* (3), 272–279. https://doi.org/10.1021/acsmaterialslett.9b00510.

(5) Zheng, J.; Hu, Y.-Y. New Insights into the Compositional Dependence of Li-Ion Transport in Polymer–Ceramic Composite Electrolytes. *ACS Appl. Mater. Interfaces* **2018**, *10* (4), 4113–4120. https://doi.org/10.1021/acsami.7b17301.

(6) Lancel, G.; Stevens, P.; Toussaint, G.; Marechal, M.; Krins, N.; Bregiroux, D.; Laberty-Robert, C. Hybrid Li Ion Conducting Membrane as Protection for the Li Anode in an Aqueous Li-Air Battery: Coupling Sol Gel Chemistry and Electrospinning. *Langmuir* **2017**, *33* (37), 9288–9297. https://doi.org/10.1021/acs.langmuir.7b00675.

Appendix

Appendix 1: Summary table of tests for 3D *Al*-LLZO scaffold synthesis.

Test	[reagent] ($mol.L^{-1}$)	%wt PVP	Solvent	solution aspect	Electrospinning condition	Aspect of as-spun	Heat treatment
1	0.12	7.5	EtOH:DMF:H_2O (0.67:0.22:0.11)	Homogenous	Drum Collector; d 15 cm; 650 RPM; 10%RH; 1.4-2 $mL.h^{-1}$; 17-20 kV		Calcination at 200 °C for 3h and 700 °C for 1 h
2	1.2	8	EtOH:DMF:H_2O (0.67:0.22:0.11)	The salts dissolve; PVP is added, it does not dissolve; additional solvent (5 and then 10 ml) is added, but it still does not dissolve		PVP is not dissolve	
3	1.2	5	EtOH:DMF:H_2O (0.67:0.22:0.11)				
4	0.65	6	DMF:Acetic acid (1:1)	Homogenous		Not working parameters	
5	0.56	3.8	DMF:Acetic acid (0.4:1)	Homogenous		Electrospray	
6	1.29	1.6	DMF:THF (1:1)			Not homogenous	
7*	1.19	4.4	EtOH:H_2O (1:1)	Homogenous	Drum Collector; d 15 cm; 600 RPM; 10%RH; 2-3 $mL.h^{-1}$; 20-25 kV		Calcination at 200 °C for 4h and 850 °C for 4 h

* Many attempts have been made to increase the [reagent] to improve the densification of the *Al*-LLZO scaffold, but they did not yield successful outcomes. Trials using double nozzles as well as core-shell nozzles were conducted without results.

Appendix 2: Summary table of sample thickness, shear modulus and aspect of SPE and SCE.

Sample	Thickness (µm)	Shear modulus (MPa)	Aspect
PEO-LiTFSI network	250	0.11	
PEO-LiTFSI network	75	-	
PEO-LiTFSI brush	250		
Al-LLZO$_{powder}$/PEO-LiTFSI network	250	0.16	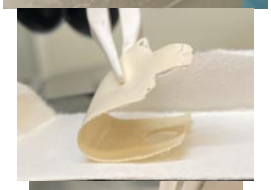
Al-LLZO$_{powder}$/PEO-LiTFSI network	75	-	
Al-LLZO$_{powder}$/PEO-LiTFSI brush	250		
Al-LLZO$_{scaffold}$/PEO-LiTFSI network	20-30		
Al-LLZO$_{scaffold}$/PEO-LiTFSI brush	40		
Al-LLZO$_{scaffold-densified}$/PEO-LiTFSI network	70-80		

Appendix 3: 3D images of ASSB cell.

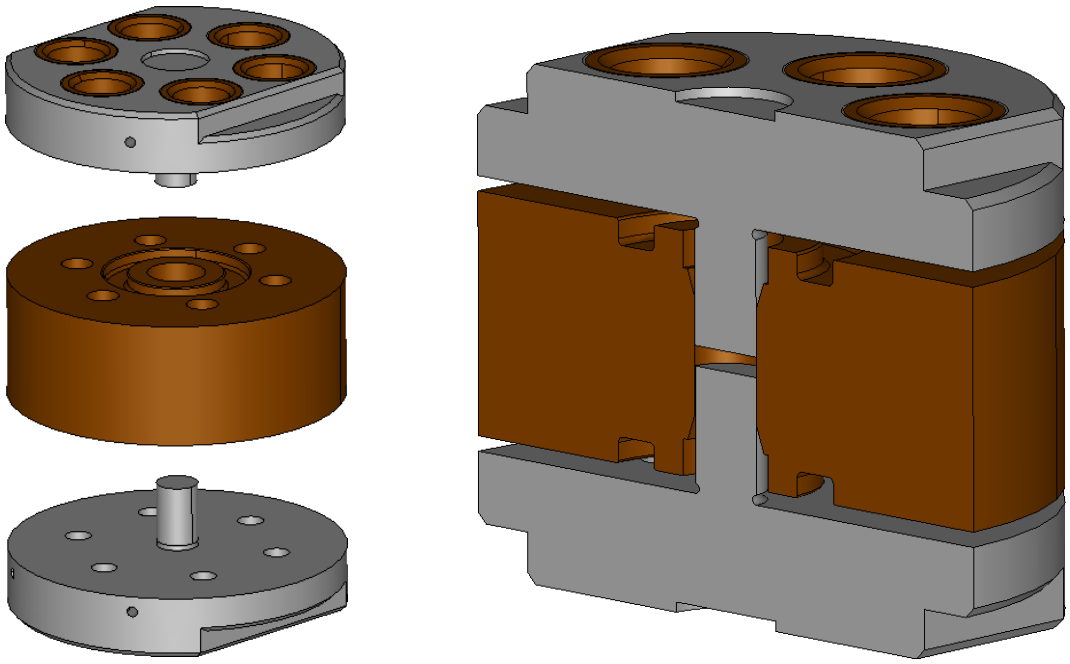

Appendix 4: Nyquist plot of *Al*-LLZO$_{particle}$/PEO-LiTFSI network.

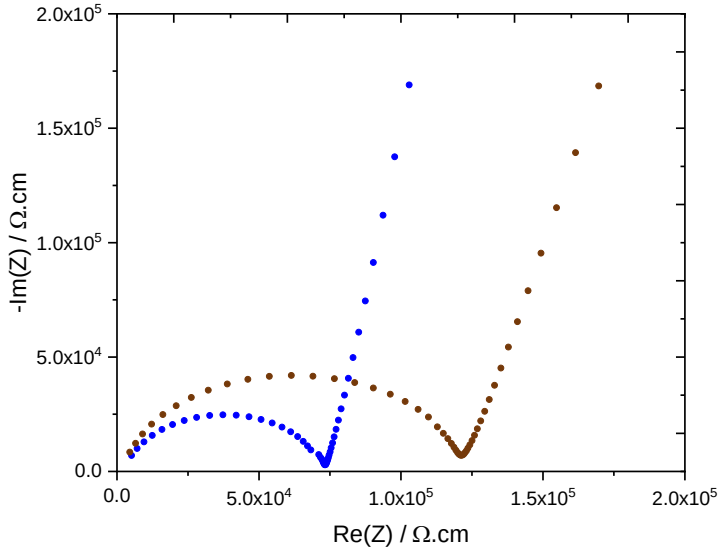

(●) PEO-LiTFSI network and (●) *Al*-LLZO$_{particle}$/PEO-LiTFSI network.

Appendix 5: Thermogravimetric analysis to determine the PVP's decomposition temperature.

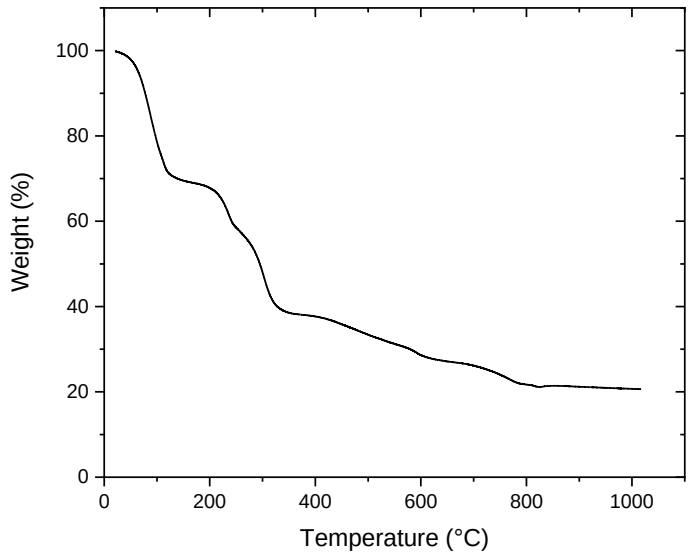

(—) *Al*-LLZO as-spun scaffold.

Appendix 6: Thermogravimetric analysis to determine the proportion of *Al*-LLZO in *Al*-LLZO$_{scaffod}$/PEO-LiTFSI network.

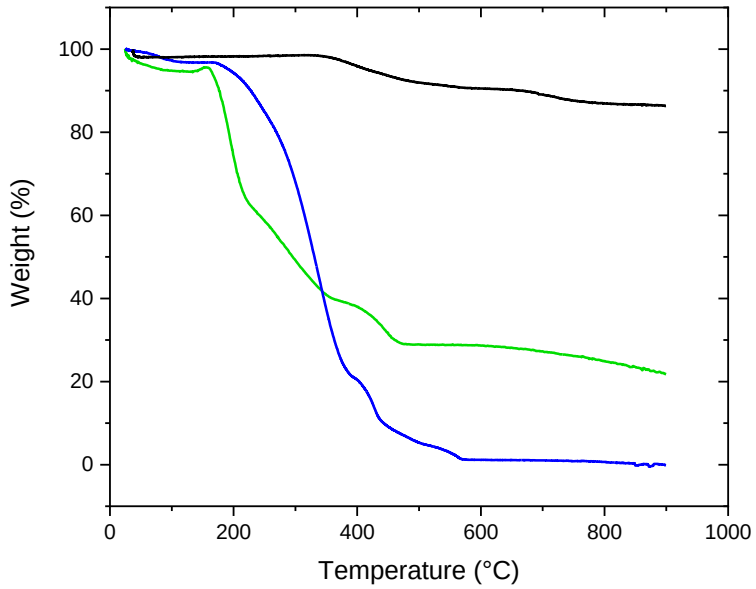

(—) *Al*-LLZO scaffold, (—) *Al*-LLZO$_{scaffod}$/PEO-LiTFSI network and (—) PEO-LiTFSI network.

Appendix 7: Nyquist plot at 25 °C of *Al*-LLZO$_{scaffold}$/PEO-LiTFSI network.

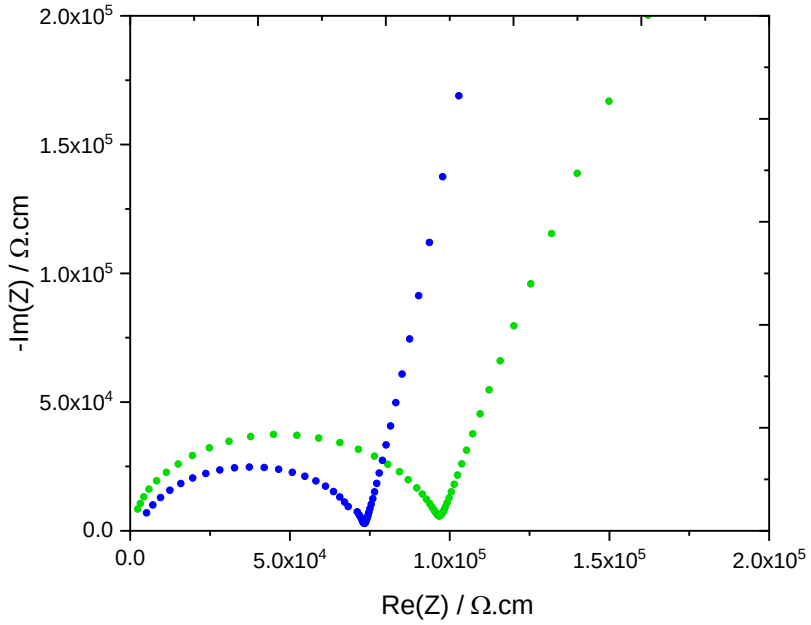

(●) PEO-LiTFSI network and (●) *Al*-LLZO$_{scaffod}$/PEO-LiTFSI network.

Appendix 8: Bruce et Vincent method for *Al*-LLZO$_{scaffold}$/PEO-LiTFSI brush to determine the transport number (t^+).

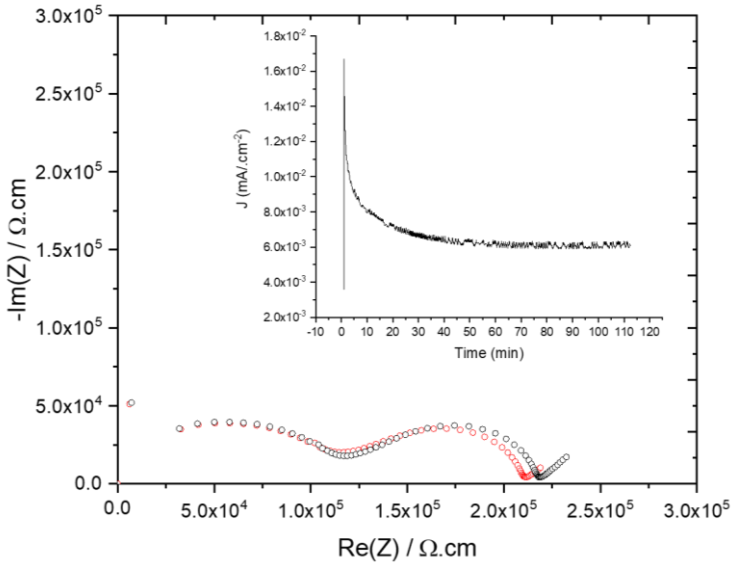

Determination of the lithium transport numbers by Bruce and Vincent method of *Al*-LLZO$_{scaffod}$/PEO-LiTFSI brush with polarization experiment and EIS spectra before (red) and after (black) polarization.

List of Figures

Chapter I.

Chapter II.

Chapter III.

Chapter IV.

Chapter V.

Appendix.

List of Tables

Chapter II.

Chapter IV.

Chapter V.

Abstract

The development of all solid-state batteries is essential if we are to make a success of the ecological transition and the deployment of all-electric vehicles. One way of developing this sector is to produce an all-solid electrolyte (SE). Poly(ethylene glycol)-based polymer SEs have the advantage of being adaptable to current Li-ion battery manufacturing processes. Unfortunately, their conductivity remains limited (10^{-6} - 10^{-9} S.cm^{-1}) at ambient temperature. Interestingly, inorganic SEs, such as $Li_7La_3Zr_2O_{12}$, are good ionic conductors (10^{-3} S.cm^{-1}), but they require costly and energy-intensive shaping processes. This thesis aimed to develop composite SEs that combine the advantages of these two materials. The work focused on the design of a high-performance composite SE and the study of transport mechanisms at the interface of these two materials. An in-depth study of a polymer SE was carried out in order to optimize its synthesis from liquid and commercial monomers. Taking advantage of this synthesis design, various composite SE shaping processes (low-temperature sintering, electro-assisted extrusion, evaporation casting) were explored in order to control the mixing of the two materials and their interface. Electrochemical impedance spectroscopy has been widely used to understand transport phenomena in composite SEs.

Résumé

Le développement de batteries tout solide est essentiel pour réussir la transition écologique et le déploiement de véhicules tout électriques. Le développement de cette filière pourra se faire, entre autres, par l'élaboration d'un électrolyte tout solide (SE). Les SE polymères à base de poly(éthylène glycol) présentent l'avantage d'être adaptables aux procédés actuels de fabrication des batteries Li-ion. Malheureusement, leur conductivité reste limitée (10^{-6} – 10^{-9} S.cm^{-1}) à température ambiante. Les SE inorganiques, comme le $Li_7La_3Zr_2O_{12}$, sont en revanche de bons conducteurs ioniques (10^{-3} S.cm^{-1}), mais ils nécessitent des procédés de mise en forme coûteux et énergivores. L'objectif de cette thèse était le développement de SE composites qui combinent les avantages de ces deux matériaux. Les travaux ont porté sur la conception d'un SE composite performant et l'étude des mécanismes de transport à l'interface de ces deux matériaux. Une étude approfondie sur un SE polymère a été menée afin d'optimiser sa synthèse à partir de monomères, liquides et commerciaux. En utilisant cette approche de synthèse, il a été possible de mettre en œuvre différents procédés de mise en forme de SE composite (frittage basse température, extrusion électro-assistée, coulée évaporation) afin de contrôler le mélange des deux matériaux et leur interface. La spectroscopie d'impédance électrochimique a été largement mise en œuvre pour comprendre les phénomènes de transport dans les SE composites.